UNICA

UNIVERSITÀ
DEGLI STUDI
DI CAGLIARI

**Ph.D. DEGREE IN PHYSICS**

Cycle XXXV

# Development of a new silicon pixel detector with 10 ps time resolution for high luminosity future experiments

Scientific Disciplinary Sectors
FIS/01, FIS/04

| | |
|---|---|
| Ph.D. Student: | Michela Garau |
| Supervisor: | Dr. Alessandro Cardini |

Final exam. Academic Year 2021/2022
Thesis defense: April 2023 Session

*Gutta cavat lapidem.*

# Table of contents

# Introduction

Many of the current High Energy Physics experiments need to operate at a higher instantaneous luminosity in order to increase the amount of collected data and fully exploit the discovery potential of such experiments. The High Luminosity Large Hadron Collider (HL-LHC) is a major upgrade of the LHC to increase the instantaneous luminosity from 2027, up to $5 \cdot 10^{34}\,\mathrm{cm}^{-2}\,\mathrm{s}^{-1}$, to fulfill the physics requirements of ATLAS and CMS experiments. This instantaneous luminosity increase poses some challenges at a technological level both for sensors and their electronics, in particular for tracking detectors close to the interaction point. These detectors have to operate in a harsh environment and sustain a high radiation damage and a large pile-up, which will be up to 140-200 interactions per bunch crossing for ATLAS and CMS experiments and about 40 for the LHCb experiment.
The development of new technologies, both in terms of sensors and electronics, is required to build experiments able to operate in these conditions. Simulation studies have shown that the introduction of an accurate time information to particle hits or tracks is fundamental to maintain the current tracking detector performances also in high luminosity conditions. In fact, an excellent time resolution allows to disentangle the proton-proton interactions that occur in the same bunch crossing. The LHCb VErtex LOcator (VELO) is one of the tracking detectors that requires a major upgrade to deal with the LHCb high luminosity phase, that will start after the Long Shutdown 4. Simulations performed by the LHCb collaboration have shown that the requirements to recover the same performances of the current VELO detector, but in the high luminosity conditions, are: a time resolution better than $50\,\mathrm{ps}$ per hit, a spatial resolution of the order of $10-20\,\mu\mathrm{m}$ and a radiation hardness up to $6 \cdot 10^{16}\,1\,\mathrm{MeV}\,\mathrm{n_{eq}}/\mathrm{cm}^2$.

This thesis work was done within the INFN-CSN5 R&D TimeSPOT project which aims to develop a new detector satisfying the LHCb VELO requirements for Run 5 and Run 6. TimeSPOT goals meet also the requirements of other detectors, e.g. the NA62 GigaTracker and the CMS Precision Proton Spectrometer. On the sensor side, new

3D silicon and diamond sensors have been developed. In this thesis, the development and characterization of the TimeSPOT 3D-trench type silicon sensors is described. These characterizations have been made in the laboratory and in several test beam campaigns, both on non-irradiated and highly irradiated devices. The structure of the thesis is described in the following.

Chapter 1 describes the scientific context of this work. The CERN accelerator complex is briefly described together with the scientific motivations of the LHC luminosity increase and the consequences on the experiments detectors. In particular three sub-detectors, requiring sensors with performance matching the TimeSPOT results and goals, are described: the LHCb VErtex LOcator, the CMS Precision Proton Spectrometer and the NA62 GigaTracker. In Chapter 2 the detection of charged particles with silicon sensors is described, starting from physical principles of radiation interaction with matter. The signal formation in silicon sensors hit by a charged particle and the damage induced on these sensors by the radiation are described. Finally, the state-of-the art of silicon sensors for timing applications is illustrated.

Chapter 3 is dedicated to the TimeSPOT project. The first steps of sensors design optimization and production are described. Moreover, the development of the TimeSPOT ASIC in 28 nm CMOS technology and first results are presented. In Chapter 4 the results of the first TimeSPOT test beam, conducted at the Paul Scherrer Institut (PSI) test beam facility, are shown. In addition to this, the laboratory characterization of the system of the two MCP-PMTs used at the test beam as time reference detector is described. Chapter 5 is dedicated to the deeper understanding of the first TimeSPOT test beam results through a simulation package developed within the TimeSPOT project. Moreover, the setup improvements in terms of electronics and time reference detector, made in light of test beam and simulation results, are shown. In Chapter 6 the TimeSPOT sensors laboratory characterization, performed with a $^{90}$Sr source, is presented. Moreover, results of a preliminary characterization of 3D-trench silicon sensors with three different pitch sizes, made with an infrared laser setup, are shown.

Chapter 7 shows the results from the test beam conducted at CERN Super Proton Synchrotron (SPS) H8 beamline, mainly concerning time resolution and efficiency performance of non-irradiated TimeSPOT sensors. Finally, Chapter 8 is dedicated to the characterization measurements made on highly irradiated TimeSPOT sensors, up to $2.5 \cdot 10^{16}\,1\,\mathrm{MeV}\,\mathrm{n_{eq}}/\mathrm{cm}^2$, both in the laboratory and in a test beam campaign at SPS.

# Chapter 1

# High luminosity experiments at CERN

This Chapter is an introduction about the context in which this PhD thesis work has been developed. The TimeSPOT sensors, whose development and characterization is described in this thesis, find their main application in some of the High Energy Physics (HEP) experiments located at CERN. Firstly the CERN accelerator complex is described. Particular attention is given to the future High Luminosity phase of the Large Hadron Collider (HL-LHC) that poses important challenges at a technological level for the detectors. Finally, the detectors for which the TimeSPOT sensors are a possible solution for their upgrades will be described: the LHCb VErtex LOcator, the CMS Precision Proton Spectrometer and the NA62 GigaTracker.

## 1.1 The Large Hadron Collider

The Large Hadron Collider (LHC) [1] is the world's largest and most powerful particle accelerator, located at CERN, in the tunnel that previously hosted the Large Electron Positron (LEP) collider which operated from 1989 to 2000. It first started up in 2008. The LHC sits in a 27 km long circular tunnel 100 m underground on the Franco-Swiss border near Geneva, Switzerland and it is the last element of the CERN accelerator complex, which consists of a chain of machines in which, at each stage, particle beams are accelerated at increasingly higher energies. The LHC is able to accelerate two counter-rotating bunches of protons or ions. The first case represents the main operation mode, since LHC experiments mainly investigate proton-proton (pp) collisions at the center of mass energy of $\sqrt{s} = 13\,\text{TeV}$, close to the maximum design value of 14 TeV. The CERN accelerator complex is shown in Figure 1.1, with highlighted the positions of the four interaction points in which the four main LHC experiments are located: ALICE [2], ATLAS [3], CMS [4] and LHCb [5]. First of all, protons are obtained by ionizing hydrogen gas with an electric discharge and are accelerated by a linear accelator, LINAC2, up to 50 MeV. The protons are then injected into the Proton Synchrotron Booster (PSB) in which the proton beam energy is increased up to 1.4 GeV. Then, the Proton Syncrotron (PS) accelerates protons up to 26 GeV that are injected into the Super Proton Synchrotron (SPS) accelerator, where the protons beam reaches the energy of 450 GeV and at this point it is split and the resulting two beams are injected into the two parallel tubes of the LHC, kept at ultrahigh vacuum. The beams are accelerated by radiofrequency cavities and their motion is guided by dipole magnets, used to bend their direction, and quadrupole magnets to ensure that the beam remain squeezed. The protons are not distributed continuously in the beams, but grouped together in *bunches*. Each proton beam at full intensity consists of 2808 bunches, spaced by 25 ns, resulting in a bunch crossing frequency of 40 MHz. Each bunch is filled with up to $1.15 \cdot 10^{11}$ protons. The two beams travel in opposite directions and collide with a center-of-mass energy of 14 TeV in the four interaction points where the four major LHC experiments are located.

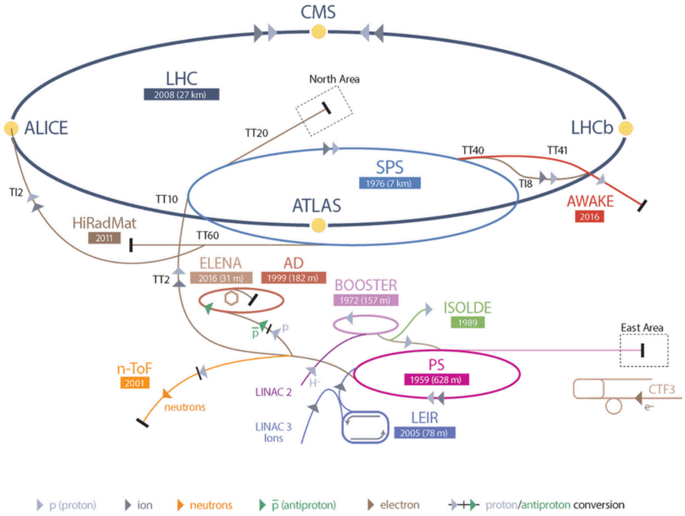

**Fig. 1.1** Schematic overview of the CERN accelerator complex [6].

The ATLAS and CMS experiments are general purpose detectors focused on the study of the electroweak and Higgs sector of the Standard Model (SM) and on direct search of New Physics (NP), in particular searching for production of beyond SM particles. The ALICE experiment mainly investigates the properties of QCD in high density regimes in heavy ion collisions. The LHCb experiment is dedicated to the measurement

of the properties of b-hadron and c-hadron decays.
The LHC operates at a nominal instantaneous luminosity of $1 \cdot 10^{34}\,\mathrm{cm}^{-2}\,\mathrm{s}^{-1}$, though the instantaneous luminosity is reduced at the LHCb and ALICE interaction points, in order to limit the number of interactions per bunch-crossing.

### 1.1.1 High Luminosity LHC

Figure 1.2 shows the projected performance of LHC until 2038 in terms of peak luminosity and integrated luminosity. After Long Shutdown 3 (LS3), the LHC machine will enter the High Luminosity phase (HL-LHC) [7]. Indeed, the statistical gain in running the accelerator without a significant luminosity increase after Run 3 would be marginal. To fully exploit the LHC discovery potential a major upgrade is needed in order to increase the luminosity, and consequently collision rate, by a factor of five beyond its design value of $1 \cdot 10^{34}\,\mathrm{cm}^{-2}\,\mathrm{s}^{-1}$. This upgrade of the machine requires about 10 years of prototyping, testing and realization of the new equipment.

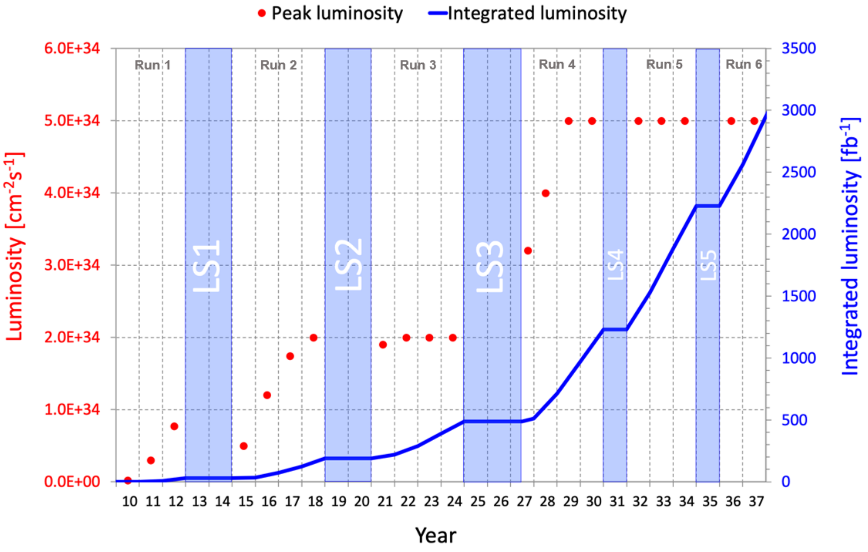

**Fig. 1.2** Projected LHC performance until 2037, showing the schedule for Run periods and Long Shutdowns (LS) of the LHC and projected luminosity values.

The High Luminosity phase poses important challenges at a technological level for the detectors of the LHC experiments, that have to cope with a higher collision rate and have also to minimize the *pile-up* problem effects. Operating at a luminosity of $5 \cdot 10^{34}\,\mathrm{cm}^{-2}\,\mathrm{s}^{-1}$ in the ATLAS and CMS experiments and at $2 \cdot 10^{34}\,\mathrm{cm}^{-2}\,\mathrm{s}^{-1}$ in LHCb will produce a pile-up of 140-200 [8] and 40 [9] respectively. This high pile-up (Figure 1.3) would cause inefficiencies to the current detectors, that for this reason have to be upgraded. A second issue introduced by the luminosity increase is the higher radiation damage caused by the larger number of collisions and by collision products on the sensors and on the read-out electronics. Therefore, a huge R&D work is needed to develop new technologies to deal with the high luminosity conditions.

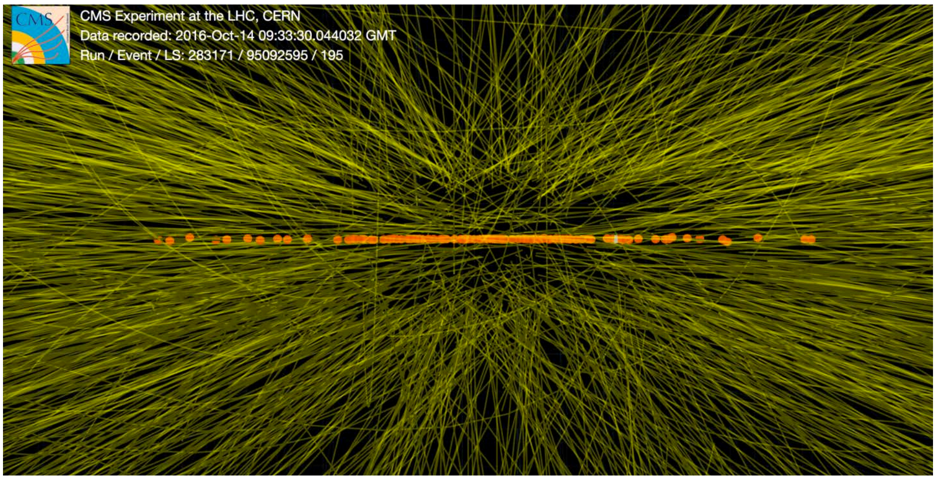

**Fig. 1.3** Collisions recorded by the CMS detector during a high pile-up fill (2016) at $\sqrt{s} = 13\,\text{TeV}$ [10]. The events are from isolated bunches with average pile-up roughly around 100.

## 1.2 High luminosity tracking detectors upgrades

One of the R&D projects started to provide a valid solution for the detectors to work in such challenging conditions is the INFN-funded TimeSPOT project [11]. TimeSPOT aims to develop a complete device consisting of an innovative silicon sensor and its read-out electronics able to satisfy the experiments requirements for the High Luminosity phase. In this section the detectors of CERN experiments for which the TimeSPOT developments represents a viable solution are described.

### 1.2.1 LHCb VErtex LOcator

As mentioned above, the LHCb experiment [5] is one of the four main LHC experiments and it is one of the most important experiments in the world performing high precision measurements in the heavy-flavour physics field, with a wide physics program based on *CP* violation, decay properties and search for NP in rare beauty and charm decays. The scheme of the current LHCb experiment (after LS2) is shown in Figure 1.4.

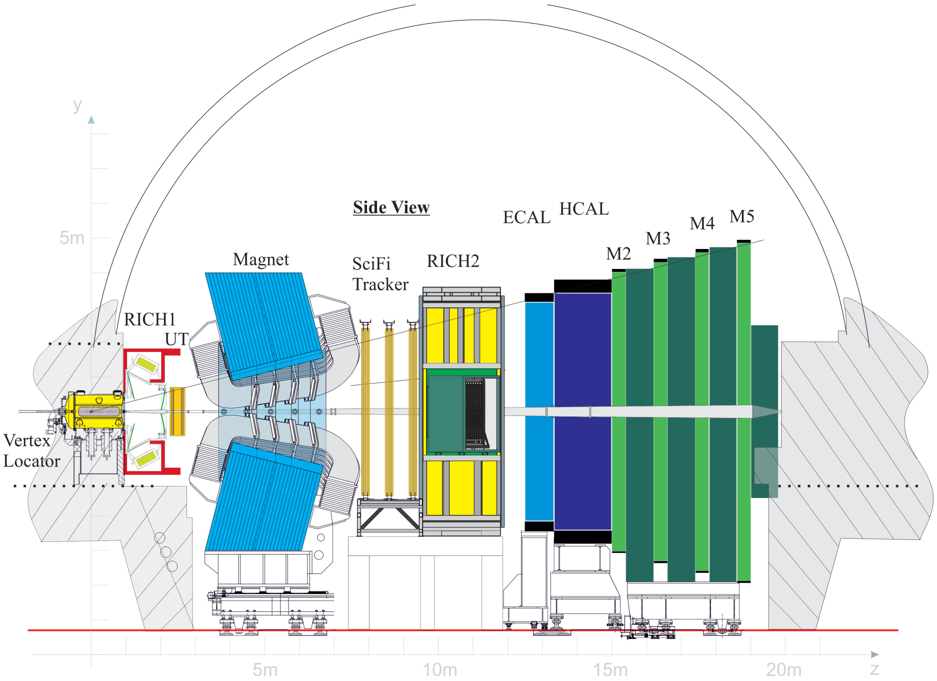

**Fig. 1.4** Schematic view of the Upgrade I LHCb detector done during LS2.

QCD-parton model can describe heavy-flavour production in proton-proton collisions at LHC. As a result of the strong interaction between partons in the $pp$ collision, $q\bar{q}$ pairs are created, mainly due to flavour creation processes, i.e. quark-antiquark annihilation $q\bar{q} \rightarrow b\bar{b}$ and gluon-gluon fusion $g\bar{g} \rightarrow b\bar{b}$. Because of the parton distribution functions of quarks and gluons inside the partons, the cross section of $b\bar{b}$ production depends on the polar angle to the beam axis. Figure 1.5 shows the polar angle distribution of the $b\bar{b}$ production cross section for $pp$ collisions at a centre-of-mass energy of 14 TeV, illustrating the production is mainly in the same direction close to the beam line.
The measured $b\bar{b}$ production cross section in $pp$ collisions at the center-of-mass energy of 13 TeV is [12]:

$$\sigma(pp \rightarrow H_b X)(13\,\text{TeV}) = (144 \pm 1 \pm 21)\,\mu\text{b} \tag{1.1}$$

To maximize the number of $b\bar{b}$ pairs detectable, the LHCb detector is built as a single-arm spectrometer in the forward region with respect to the proton-proton interaction (Figure 1.4). The layout is designed to cover the angular region from approximately 10 mrad to 300 mrad (250 mrad) in the x-y (y-z) plane, that translates in a pseudorapidity $\eta$ coverage of $2 < \eta < 5$, where the pseudorapidity is defined as

$$\eta = -ln(tan(\theta/2)) \tag{1.2}$$

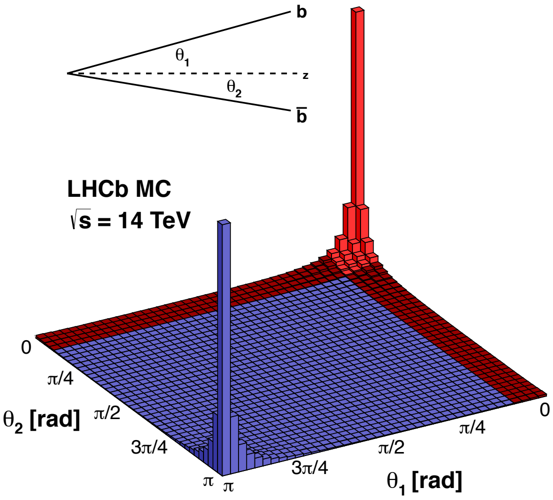

**Fig. 1.5** Cross section of $b\bar{b}$ pairs production as a function of their polar angle to the beam axis for $pp$ collisions at a center-of-mass energy of 14 TeV. The LHCb acceptance is shown in red. The plot is taken from [12].

and $\theta$ is the angle with respect to the beam axis. The LHCb acceptance covers about 27% of the total $b\bar{b}$ pairs produced [12].

As mentioned before, LHCb works at a luminosity lower than the nominal operating value of LHC, which was $4 \cdot 10^{32}\,\mathrm{cm}^{-2}\,\mathrm{s}^{-1}$ during Run 1-2 and has now become $2 \cdot 10^{33}\,\mathrm{cm}^{-2}\,\mathrm{s}^{-1}$ for Run 3 and Run 4. To work at a lower luminosity presents several advantages: the radiation damage is reduced and the number of primary vertices (PV) producing hadrons containing the $b$ quark decreases as well. This leads to a simpler reconstruction of the PV and of the particle decay vertex, called secondary vertex (SV), ensuring a better reconstruction of the tracks. The LHCb detector is built to have the following fundamental characteristics:

- a highly performing trigger system, optimised for the detection of b-hadrons;
- an excellent PV reconstruction system, essential for studying the oscillations of b-mesons and their CP violation
- an excellent particle identification, to reduce the presence of wrong-identified particles, essential in the measurement of rare decays.

During Long Shutdown 2 (LS2), LHCb has been upgraded according to the so-called *Upgrade I* program [13] in order to make the experiment able to work at a higher luminosity, fundamental to perform measurements that were not possible with Runs 1-2 data because of statistics limitations. The current LHCb detector (Figure 1.4) consists of two main types of detection systems:

- a **tracking system** composed of a vertex detector, called VErtex LOcator (VELO), the Upstream Tracker (UT) and the Scintillating Fiber tracker (SciFi);
- a **particle identification system** which includes two Cherenkov detectors (RICH1 and RICH2), an electromagnetic calorimeter (ECAL), a hadronic calorimeter (HCAL) and four muon detection stations (M2-M5).

Here only the VErtex LOcator (VELO) sub-detector will be discussed, since it represents one of the potential detector in which the silicon pixel sensors developed within the TimeSPOT project could be installed.
The VELO [14] is a crucial sub-detector, used for tracking and locating vertices. It is the system closest to the interaction point, surrounding it. The main purpose of the VELO is not only to identify tracks of the particles but also to separate the primary vertices of the beam collision from the secondary ones, originating from the short-lived decay of particles (b- and c- mesons). Important parameters of the VELO performance are the Impact Parameter (IP), the Primary Vertex and decay time resolutions. The IP is useful for the measurements of the long-lived particles as their decay occurs offset from the PV, so it provides an excellent selection variable in data for their identification. The IP resolution is affected by the multiple scattering in the material and the detector design. The original system (before LS2) consisted of silicon strip detectors, mainly made of 300 $\mu$m thick $n^+$-in-n sensors, arranged on half-moon shape modules to determine $r$ and $\phi$ coordinates of the passing particles. The VELO consisted of 21 sensitive planes on each side of the beam-pipe. The whole system was enclosed in a corrugated RF aluminium box, positioned 5 mm from the beam, with the main purpose to separate the VELO and beam vacuum, in addition to the protection of the sensitive electronics from the beam-induced charge. For safety, the detector is placed in position for data taking only once the stable beam conditions have been realized. The schematic of the assembled half detector is shown in Figure 1.6.

During LS2 the hardware trigger was replaced by a triggerless system with output rates of up to 40 MHz. This implied the need of changes to be made to the detector to allow for more complex pattern recognition requirements in high pile-up environment and cope with a higher integrated radiation dose. In particular, the upgraded detector was expected to be capable of accumulating 50 $\text{fb}^{-1}$ and the VELO, as all the LHCb

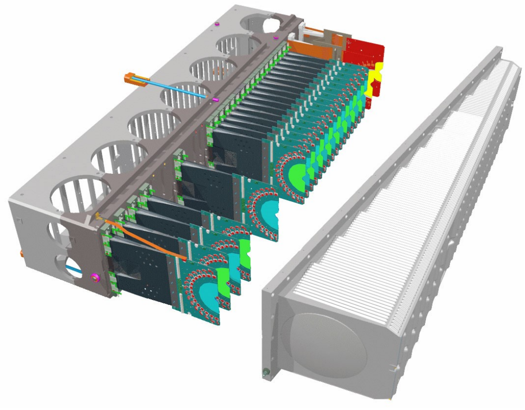

**Fig. 1.6** Schematic view of half VELO modules with the RF box [5].

subdetectors, must be qualified in performance up to a luminosity of $2 \cdot 10^{33}\,\mathrm{cm}^{-2}\,\mathrm{s}^{-1}$. To maintain or improve the VELO physics performance in Upgrade I, while delivering readout at 40 MHz, a complete replacement of the silicon sensors and electronics has been mandatory [15]. To satisfy this need, the collaboration has chosen to install a detector based on hybrid pixel sensors. A new radiation hard ASIC, named *VeloPix*, capable of coping with the upgrade data rates, has been developed. Moreover, the module cooling design has been upgraded in order to protect the tip of the silicon from thermal runaway effects after significant irradiation, and to cope with the high speed pixel ASIC power dissipation. Regarding the sensors, the silicon strips have been replaced by silicon pixel sensors increasing the effective number of channels from 180k up to almost 41M. The layout of the Upgrade I VELO is shown in Figure 1.7.

The sensors for the VELO Upgrade 1 are $55 \times 55\,\mu\mathrm{m}^2$ n-in-p planar silicon pixels with a thickness of $200\,\mu\mathrm{m}$. Each group of $768 \times 256$ pixels is bump-bonded to three ASICs. The VeloPix ASIC features a matrix of $256 \times 256$ active pixels, with cell dimensions of $55\,\mu\mathrm{m} \times 55\,\mu\mathrm{m}$. The sensor needs to feature a small gap of $165\,\mu\mathrm{m}$ between the matrices to allow the ASICs to be placed side by side. Then in order not to lose efficiency the pixels on either side of the gap are elongated from $55\,\mu\mathrm{m}$ to $137.5\,\mu\mathrm{m}$. This sensors provide a detection efficiency higher than 99% and can be operated up to 1000 V after the irradiation [17].

### VELO Upgrade II

After the Run 3 and Run 4 phases, just started in 2022, the LHCb experiment has planned, for Runs 5 and 6 (starting in 2033), to operate with a 7.5-fold increase in instantaneous luminosity. This scenario has a maximum instantaneous luminosity of

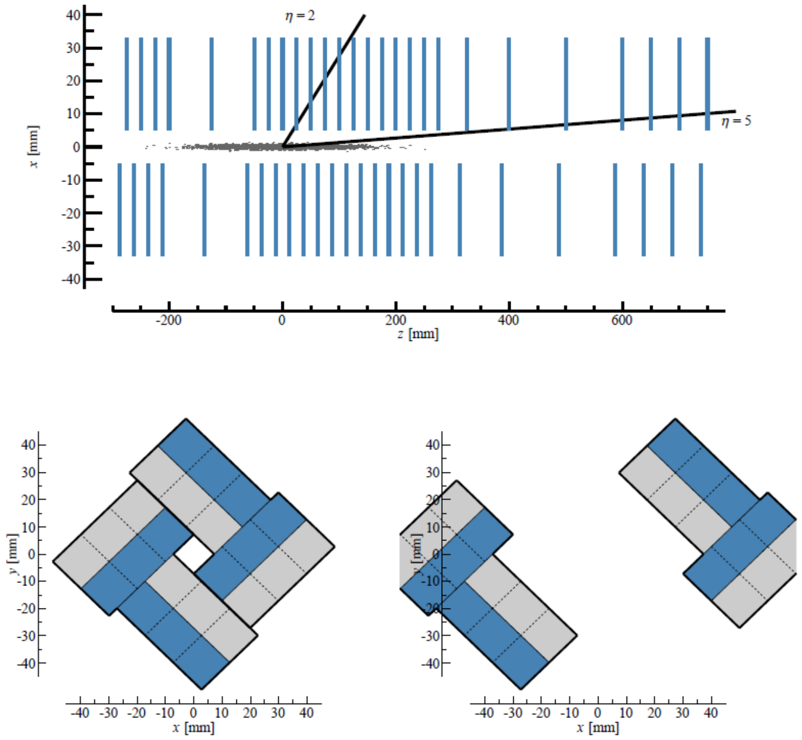

**Fig. 1.7** Layout of the Upgrade I VELO. (Top) Schematic cross-section at $y = 0$, together with illustrations of the z-extent of the luminous region and the nominal LHCb acceptance. (Bottom) Schematic layout in the $xy$ plane (left: VELO closed, right: VELO fully open). Taken from [16].

$1.5 \cdot 10^{34}\,\text{cm}^{-2}\,\text{s}^{-1}$ and an integrated luminosity of $50\,\text{fb}^{-1}$ per year, for a total of six years, and requires a second major upgrade, referred to as *Upgrade II* [9, 18]. With the same bunch scheme of Upgrade I, the mean pile-up will be of 42 collisions per event at the start of each fill. At a higher pile-up, it becomes more difficult to identify primary vertices maintaining the same previous resolution, as well as to associate the correct PV to a heavy flavour decay. In the current detector configuration, it is difficult to separate PVs which are closer than about 2 mm along the beam direction. Consequently, it is foreseen that in addition to excellent track impact parameter resolution, track timing information will also be needed to distinguish vertices. Moreover, to achieve the physics goals of LHCb, a precise secondary vertex (SV) reconstruction is fundamental. This information is used to obtain proper time measurements that are used in decay-time-dependent analysis, in addition to being used across LCHb's programme for combinatorial background discrimination. The usefulness of this information depends on the precision with which the distance between the PV and SV can be measured.

At such high multiplicities, the impact parameter resolution becomes progressively more important, as this variable is the key to associate particles with the correct PV. Secondary vertices from decays close to the beam line can be mistakenly reconstructed as (or merged with other) PVs, which lowers the overall efficiency for some physics channels of interest to the experiment, particularly for particles with sub-ps lifetimes. Conversely, partially reconstructed PVs can lead to a higher background for SV reconstruction.

The requirements on the temporal resolution of the VELO detector are mostly driven by the requirements of the tracking and primary vertex reconstruction. The PV reconstruction efficiency at different hit time resolutions with both 3D and 4D information is shown in Figure 1.8. The tracking efficiency under a proposed scenario with a lower peak luminosity of $\mathcal{L} = 1.0 \cdot 10^{34}\,\mathrm{cm}^{-2}\,\mathrm{s}^{-1}$ is also indicated. The efficiency is found to decrease continuously up to around 70 ps and then drops rather rapidly. In light of these results, the nominal requirement on the single hit temporal resolution is 50 ps, which balances a physics performance similar to Upgrade I with a resolution achievable on the Upgrade II timescale.

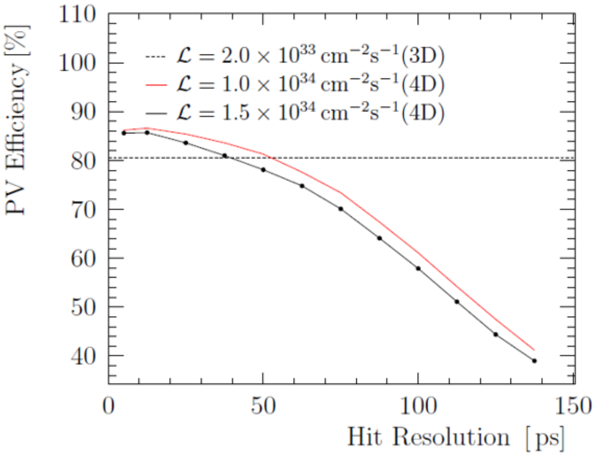

**Fig. 1.8** Primary vertex reconstruction efficiency as a function of the single hit time resolution for all vertices [18].

Two main different detector designs have been considered to cope with the Upgrade II pile-up density. Moreover, the long term accumulated radiation damage imposes restrictions on the detector design and replacement frequency. The two scenarios are referred to as *scenario A* ($S_A$) and *scenario B* ($S_B$). In Scenario A the layout is identical to Upgrade I, with a distance of the detector to the beam of 5.1 mm and the same RF-foil. In this scenario an hit resolution with a binary readout $55\,\mu$m pitch is considered. Since the yearly fluence reaches $1 \cdot 10^{16}\,1\,\mathrm{MeV}\,\mathrm{n_{eq}}\,\mathrm{cm}^{-2}$, while the total ionising dose would be 500 MRad, this scenario would require a replacement of the detectors every end-of-year shutdown, considering the radiation hardness of the current detector technologies. In addition, future ASIC would need to deal with a factor $\approx 10$ times higher hit rate. In Scenario B, instead, the sensors are placed further away from the beam at a distance of 12.5 mm, which needs a much lighter (or no) RF-foil. In this way, the fluence reaches $8 \cdot 10^{15}\,1\,\mathrm{MeV}\,\mathrm{n_{eq}}\,\mathrm{cm}^{-2}$ for a total delivered luminosity of $300\,\mathrm{fb}^{-1}$, comparable to that expected for $50\,\mathrm{fb}^{-1}$ with the VELO Upgrade I detector. On the other hand, this implies the requirement of a better spatial hit resolution (about $9\,\mu$m) in order to keep the same IP performance as in Upgrade I, for example using pixels with a pitch of $42\,\mu$m with binary readout. Moreover, in this scenario the material before the second hit needs to be dramatically reduced (about $0.5\%\,X_0$) in order to keep the same performance as in Upgrade I. This requires not only the RF-foil to be very light but also the sensor, ASIC and substrate materials. Also, the implementation of alternative scenarios with two technologies, one for precise spatial measurements and another with precise timestamps, but less granular pixel pitch is explored [18].

The main approach is the the so-called *4D-tracking* approach, which keeps the VELO Upgrade I detector layout with additional timing measurements associated to each spatial hit. The impact of various improvements to the VELO Upgrade I detector design has been studied, such as tracks reconstruction efficiency, purity, ghost rate, impact parameter resolution, PV reconstruction efficiency and resolution. In particular, two changes have been investigated: the addition of a per-hit time stamp on the order of 50 ps precision (i.e. $\mathcal{O}(20\,\mathrm{ps})$ per track), significantly thinning or removing the RF-foil. Some results of these studies are reported here. Figure 1.9 shows the tracking efficiency as a function of the transverse momentum of track ($p_T$), obtained for: 3D tracking in Upgrade I conditions and both the 3D and 4D tracking in Upgrade II conditions. The trends are essentially similar with significant improvements from the 4D tracking, that allows also to considerably suppress ghost tracks with respect to 3D tracking. Figure 1.10 shows the PV reconstruction efficiency as a function of the number of particles produced by a vertex, for the same three conditions above illustrated. The expected Upgrade I performance is nearly recovered by adding timing to the vertexing algorithm. The small remaining degradation could be reduced by tuning the parameters and further improving the reconstruction algorithm.

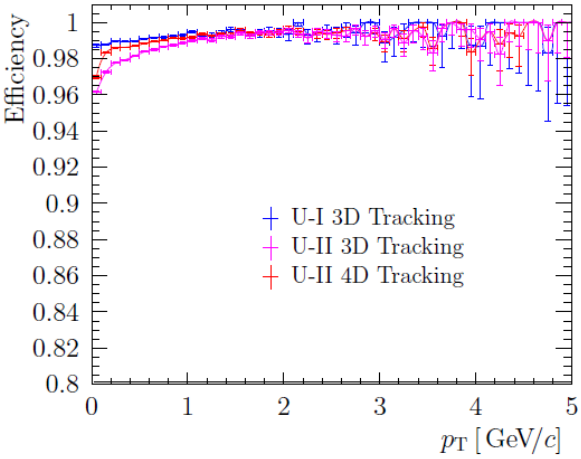

**Fig. 1.9** Tracking efficiency as a function of the track transverse momentum $p_T$, for Upgrade I conditions and Upgrade II conditions with both 3D and 4D tracking algorithms, with a 50 ps time resolution per hit in the 4D tracking case [18].

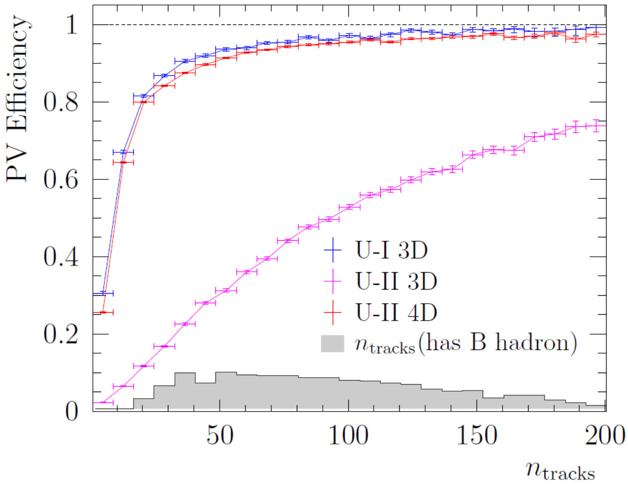

**Fig. 1.10** Primary vertex reconstruction efficiency vs the number of tracks per primary vertex, comparing the Upgrade I 3D reconstruction in both luminosity conditions and a variant using timing information, with a resolution of 50 ps per hit, to resolve the primary vertices [18].

Summarizing, and focusing on the sensors, since it is the main topic of this thesis work, the requirements for the sensors are:

- Radiation hardness of at least $1 \cdot 10^{16}\,1\,\mathrm{MeV}\,\mathrm{n_{eq}}\,\mathrm{cm}^{-2}$ with annual replacement of the detectors in $S_A$. No replacement would be necessary with a technology that could resist up to $6 \cdot 10^{16}\,1\,\mathrm{MeV}\,\mathrm{n_{eq}}\,\mathrm{cm}^{-2}$

- Hit resolution of 12 $\mu$m for scenario $S_A$, better than 9 $\mu$m for scenario $S_B$.
- Time resolution of at least 50 ps per hit, assuming that the combination of hits time-stamps would bring the track resolution to 20 ps.
- Material budget below 0.8% $X_0$ per detector plane.
- High detection efficiency (99%) for a particle in the LHCb acceptance. The efficiency also plays an essential role in the time measurements as the track resolution will improve when combining several hits.

This combination of requirements for the VELO detector in the Upgrade II is very challenging. Several options have been taken into account to satisfy these requirements. The silicon sensors technologies considered are: planar sensors, Low Gain Avalanche Diodes (LGADs), Monolithic Active Pixel Sensors and 3D sensors (including TimeSPOT sensors). All of them are described in detail in Chapter 3. A huge work also on the front-end electronics for the Upgrade II is needed. The main, and conflicting, challenges are the per-hit time measurement of the order of 50 ps (for the complete system of sensor and electronics) with pixel pitch of 55 $\mu$m or 42 $\mu$m, the enormous readout bandwidth and the severe radiation environment. In fact, in scenario $S_A$ ($S_B$) the ASIC has to sustain a pixel rate larger than 350 kHz (40 kHz) and a bandwidth per 2 cm$^2$ larger than 250 Gb/s (94 Gb/s), keeping the power budget at 1.5 W/cm$^2$. In Chapter 3 the development of the TimeSPOT ASIC, specifically designed for fast timing applications, is described.

### 1.2.2 CMS Precision Proton Spectrometer

The Precision Proton Spectrometer (PPS) of the CMS experiment is a near-beam magnetic spectrometer that measures protons surviving in the collision at the CMS interaction point (IP5). Protons that lose part of their energy in the interaction are bent outside the beam envelope by the LHC magnetic fields and can be detected. The PPS stations, located approximately 200 m away from the IP on both sides of CMS, provide a tracking and timing measurement of the outgoing protons, allowing to determine their kinematic properties. This information represents an unique extension of the physics capabilities of CMS, since it allows to reconstruct the entire final state of central exclusive production (CEP) events, which consist in processes that produce a central state with protons surviving the interaction. The central state kinematics, reconstructed with the CMS detectors, can be combined with the kinematics inferred from the proton measurement and used to effectively identify CEP events.

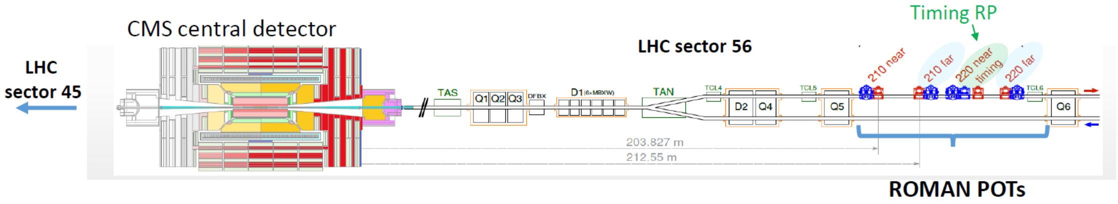

**Fig. 1.11** Schematic view of the beam line between the CMS interaction point (IP5) on the left and the PPS Roman Pot units on the right for LHC sector 56 [19]. The same structure, symmetric with respect to CMS, is present in LHC sector 45.

PPS has started the data taking during Run 2 (2016-2018), collecting more than 100 $\mathrm{fb}^{-1}$ of integrated luminosity.

In order to be able to detect the outgoing protons, the PPS sensors must be placed very close to the LHC beam, about 1.5 mm, thus they are inserted into the beam pipe thanks to movable structures called *Roman Pots* (RP). Inside the RPs, detectors are kept cool and in vacuum. The metallic structure is made of 2 mm thick stainless steel, which is thinner only in the region closest to the beam, the so-called *thin window*. Since PPS sensors (both tracking and timing sensors) are placed so close to the beam, they operate in a very high radiation environment and are required to have a very high radiation hardness, up to $3 \cdot 10^{15}\,1\,\mathrm{MeV}\,\mathrm{n_{eq}}\,\mathrm{cm}^{-2}$ for an integrated luminosity of 100 $\mathrm{fb}^{-1}$. As mentioned above, the PPS detector consists of a silicon tracking system to measure the position and direction of the protons, and a system of timing detectors to measure their time of arrival. Every arm contains three RP groups called *stations*. One station per arm contains one RP for timing detectors.

The measurement of the deflection of the proton from the beam direction is related to its fraction of momentum lost during the collision and hence to the amount of energy available for the $X$ system in the CEP production $pp \to pXp$. Therefore, the tracking system in PPS is fundamental to study the CEP events. At the beginning, in 2016, the tracking stations were made by silicon strip sensors of 66 $\mu$m pitch. In 2017, 3D silicon pixel modules were installed only in one station per sector, while they were installed in all the tracking stations in 2018. The size of the 3D sensor pixels installed is $150 \times 100\,\mu\mathrm{m}^2$.

Moreover, by measuring the time difference $\Delta t$ between the time of flights of the two protons, it is possible to reconstruct the longitudinal vertex position ($z_{vertex} = c\Delta t/2$), rejecting in this way all vertices that are incompatible with this measurement. For instance, detectors with a time resolution of $30 - 50$ ps are able to disentangle about 50 pile-up events. The main technology used for the timing in PPS during Run 2 relies on ultrapure single-crystal Chemical Vapour Deposition (scCVD) diamonds, each crystal with $4.5 \times 4.5\,\mathrm{mm}^2$ area and $500\,\mu$m thickness. A spatial resolution of about $130\,\mu$m and an overall station time resolution of $90 - 120\,$ps were measured [19]. An important upgrade program has started already for Run 3, with the main goal of reaching a time resolution better than 30 ps on each sector. To achieve this goal, an improvement on both the sensors and the electronics is needed. Moreover the program for the development of the new CMS PPS is ongoing.

### The HL-LHC upgrade of the CMS Precision Proton Spectrometer

An upgrade of the PPS detector is planned for operation in the High Luminosity LHC Phase starting from Run 4. Based on the HL-LHC goal of producing a total integrated luminosity of $3000\,\mathrm{fb}^{-1}$, the expectation of the new PPS project is to collect about a factor 10 more data than the present PPS system will until LS3 [20].

Focusing on the sensors, for the tracking part, pixel sizes between $100\,\mu$m and $200\,\mu$m are sufficient, so the tracking stations equipped with 3D silicon sensors already have an adequate space resolution. Moreover, to improve the timing measurement, three main options are taken into account: diamond sensors, 3D silicon sensors and LGADs. Diamond detectors have been already used in Run 2 for timing, in the so-called *Double Diamond* (DD) configuration and have shown time resolution in the range $90 - 120\,$ps and an excellent detection efficiency, reduced by the radiation damage only in a small portion and however greater than 95%. Diamonds could allow to reach a single-arm time resolution around 20 ps if each station is equipped with eight measuring planes of diamond detectors optimized for the new running conditions. The second option is to use 3D silicon pixel detectors, currently used for PPS tracking, also for timing. Future sensors are required to withstand $2 \cdot 10^{16}\,1\,\mathrm{MeV}\,\mathrm{n_{eq}}\,\mathrm{cm}^{-2}$ and 3D silicon sensors are intrinsically rad-hard devices (Section 2.5.3). This property has been confirmed by several measurements [21–23], together with excellent time resolution results [24, 25]. Some of these measurements, performed on TimeSPOT 3D sensors are illustrated in this thesis. The choice to install 3D silicon sensors also for PPS timing measurements would give the advantage of using exactly the same module providing simultaneous tracking and timing. Moreover, developments for the improvement of LGADs for timing applications, the Ultra Fast Silicon Detectors (Section 2.5.1) are ongoing.

### 1.2.3 NA62 GigaTracker

NA62 is a fixed-target experiment at the CERN SPS that started collecting data in 2014. It is dedicated to measurements of rare kaon decays, that could bring significant insights into new physics processes comparing the results with precise theoretical predictions. The main goal is to match the 10% theory precision for branching fraction of the ultra-rare kaon decay $K^+ \to \pi^+\nu\bar{\nu}$. For this purpose, innovative techniques have been developed, in particular in the domain of low-mass tracking devices [26]. The 400 GeV/c proton beam from the CERN SPS accelerator enables the production of a 75 GeV/c secondary kaon beam. The advantage of using a high-energy proton beam is the reduction of non-kaon-related accidental background due to the higher kaon production cross section. The disadvantage of high-energy protons and, consequently, of a high-energy secondary beam, is that pions and protons cannot be separated efficiently from kaons. The schematic of the NA62 experiment is shown in Figure 1.12. The main elements for the detection of the $K^+$ decay products are located along a 150 m long region starting 121 m downstream of the kaon production target. Useful $K^+$ decays are detected in a 65 m long decay region. The beam spectrometer GigaTracker (GTK), all detectors surrounding the decay region and the spectrometer detecting the final-state particles are placed in vacuum to avoid interactions and scattering of the beam and to obtain improved resolution for measured kinematic quantities.

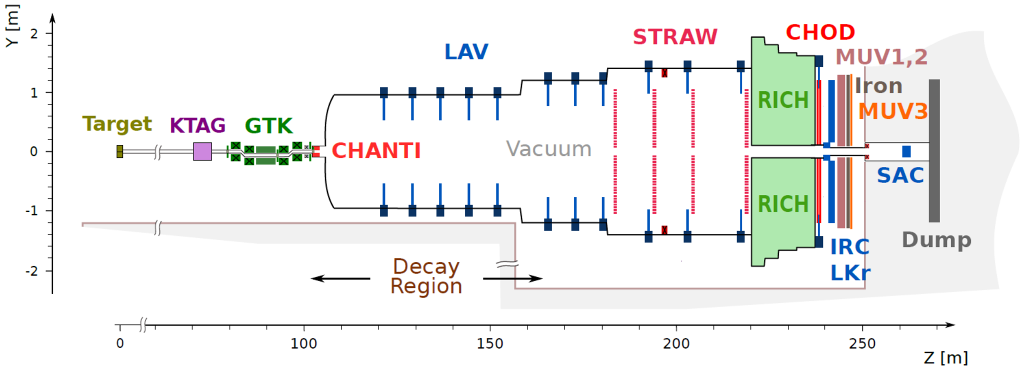

**Fig. 1.12** Schematic vertical section of the NA62 experimental setup [26].

In the following we will focus on the GTK detector since its requirements for the upgrade are met by the TimeSPOT sensors performance, as it will be shown later. The GTK is composed by three 60.8 mm × 27 mm planes of hybrid pixels, as shown in Figure 1.13. Its role is the tracking of particles in a beam with a flux up to 1.3 MHz/mm$^2$, providing at the same time a single-hit timing with 200 ps resolution for a total material budget lower than 0.5% $X_0$ per station. The matrix is made by $40 \times 45$ planar silicon pixels of $300\,\mu$m $\times$ $300\,\mu$m size and $200\,\mu$m thickness. The matrix is bump-bonded to the custom TDCPix ASIC. A GigaTracker module, complete with che cooling plate and mechanical support, is shown in Figure 1.14. Besides the material budget, another relevant constraint for the design of the GTK sensor is the intense radiation exposition with a fluence reaching $2 \cdot 10^{14}\,1\,\mathrm{MeV\,n_{eq}/cm^2}$ in 100 days of run.

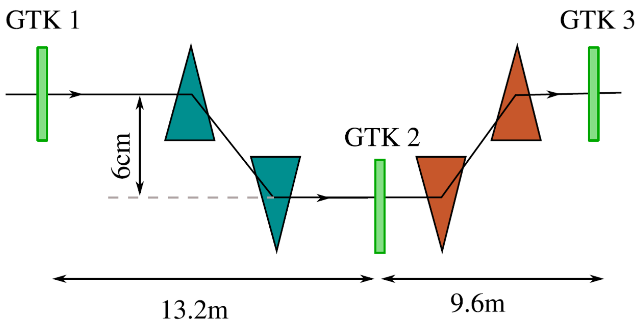

**Fig. 1.13** Layout of the GigaTracker [27], consisting of three stations (in green) inserted around two pairs of bending magnets (in blue and in orange) that displace the beam. The precise measurement of the vertical shift allows to measure the particle momentum.


(a) (b)

**Fig. 1.14** Picture of an assembled station looking at the sensor side (a) and at the cooling side (b) [26].

Time resolution measurements were initially performed on a demonstrator of the final system containing 45 pixels, with a 10 GeV/c $\pi^+$ beam from the PS [28]. The time resolution was found to be 160 ps at 300 V sensor bias. Prototype sensors made of $3 \times 3\,\mathrm{mm}^2$ n-in-p and p-in-n diodes were irradiated up to a fluence of $2 \cdot 10^{14}\,1\,\mathrm{MeV\,n_{eq}/cm^2}$ and showed a satisfying performance [29].

For the 2016 data taking, three stations were constructed and installed. They were all equipped with n-in-p sensors and mounted on cooling plates with thickness of 380 $\mu$m for GTK1 and GTK2 and and 280 $\mu$m for GTK3. The material budget in the beam acceptance is therefore 0.73% $X_0$ for GTK1 and GTK2 and and 0.62% $X_0$ for GTK3. The time resolution values obtained are 132.0 ps for GTK1, 127.1 ps for GTK2 and 129.2 ps for GTK3, that result in a time resolution for the track of 74.7 ps, assuming that the track time coordinate is the average of the three hits time coordinate [29]. Increasing the sensor bias voltage from 100 V to 250 V, an improvement of the station time resolution of 20 ps was observed. Then, operating the sensors at 250 V, a track resolution of 65 ps was achieved. A degradation of the time resolution with the irradiation was observed, showing, at the end of the 2017 data taking period, a time resolution of $146 - 158$ ps.

### The GTK Upgrade

The NA62 experiment is approved for data taking up to LHC Long Shutdown 3 (LS3), but in the longer term, fixed-target runs in the SPS North Area are scheduled at least through 2040. The HIKE program (High Intensity Kaon Experiments) [30] is foreseen to include three experimental phases for the high-precision study of rare kaon decays during the period from the end of LS3 to the Future Circular Collider (FCC) era. For instance, Phase 1 is based on a $K^+$ experiment running at four times the intensity of NA62 to measure the branching fraction of the decay $K^+ \to \pi^+\nu\bar{\nu}$ to 5% precision and to perform other studies of lepton universality, number and flavour violation. In the Phase 1, the intensity increase requires an improvement of the time resolution of the detectors by a factor of four in order to maintain the loss of events from accidental coincidence to acceptable levels ($\leq$ 25%), while maintaining other performance specifications such as space-time reconstruction performance and low material budget. To satisfy these requirements, most detectors will need to be rebuilt or extensively upgraded. In particular, the GigaTracker will need to be upgraded. A time resolution of better than 50 ps will be required and the detector will have to be able to handle rates of 8 MHz/mm$^2$ and be radiation resistant up to $2 \cdot 10^{15}$ 1 MeV n$_{\mathrm{eq}}$/cm$^2$ per year. TimeSPOT sensors represent an excellent candidate for the upgrade of the GigaTracker, as it will be shown in next chapters.

# Chapter 2

# Particle detection with silicon sensors

This Chapter is focused on the description of silicon sensors for charged particles detection used for timing applications. An initial introduction on the charged particles interaction with matter is presented, before describing the signal formation in silicon sensors, and discussing in particular the time resolution of these devices and on factors affecting it. Finally, an up-to-date overview of the silicon sensors developed and used for timing applications is presented.

## 2.1 Interaction of radiation with matter

The operation of any radiation detector basically depends on the manner in which the radiation to be detected interacts with the material of the detector itself. An understanding of a specific type of detector response must therefore be based on a familiarity with the fundamental mechanisms by which radiations interact and lose their energy in matter [31–33]. For reasons that will be clarified later, it is necessary to separate charged particles into two classes: (1) electrons and positrons, and (2) heavy particles, i.e. particles heavier than the electron. This latter group includes muons, pions, protons, $\alpha$ particles and other light nuclei. Particles heavier than this, i.e. heavy ions, are excluded in this discussion because of additional effects which arise.

### 2.1.1 Heavy charged particles

The passage of charged particles through matter causes a loss of energy by the particle and a deflection of the particle from its incident direction. These two effects are mainly the result of two processes:

1. inelastic collisions with the atomic electrons of the material;
2. elastic scattering from nuclei.

Of these two electromagnetic processes, the interaction is mostly through Coulomb force with the orbital electrons of the absorber atom. In these collisions, a small fraction of its kinetic energy is transferred from the particle to the atom causing an excitation or ionization of the latter. These collisions are usually divided in: *soft* collisions in which results only an excitation and *hard* collisions in which the transferred energy is sufficient to cause ionization. In some of the hard interactions, the electron itself may have energy enough to cause secondary ionizations. These high-energy recoil electrons are referred to as *$\delta$-rays* and have a small range compared with the incident particle range, so the consequent ionizations occur close to the primary track.
Elastic scattering from nuclei occurs rarely with respect to electron collisions and very little energy is transferred in these collisions since the nuclei masses are usually large compared to the incident particle. Consequently, these interactions are not normally significant in the response of radiation detectors and the operation of charged particle detectors is based on the results of the interactions with electrons for their response.
The maximum energy which can be transferred from a charged particle of mass $M$ to an electron of mass $m_e$ in a single collision is:

$$W_{\max} = \frac{2m_{\mathrm{e}}c^2\eta^2}{1 + 2s\sqrt{1+\eta^2} + s^2} \tag{2.1}$$

where $s = m_{\mathrm{e}}/M$ and $\eta = \beta\gamma$, with $\beta = v/c$ and $\gamma = 1/\sqrt{1-\beta^2}$. Moreover, if $M >> m_{\mathrm{e}}$:

$$W_{\max} \simeq 2m_{\mathrm{e}}c^2\eta^2 \tag{2.2}$$

The energy loss per path length, called *stopping power* ($S$) or simply $dE/dx$, was first calculated by Bohr using classic approach [34]. The first correct quantum-mechanical calculation was performed by Bethe, Bloch and other authors. The formula obtained, known as *Bethe-Bloch formula*, is:

$$-\frac{dE}{dx} = 2\pi N_{\mathrm{a}} r_{\mathrm{e}}^2 m_{\mathrm{e}} c^2 \rho \frac{Z}{A}\frac{z^2}{\beta^2}\left[ln\left(\frac{2m_{\mathrm{e}}\gamma^2 v^2 W_{\max}}{I^2}\right) - 2\beta^2\right] \tag{2.3}$$

with $r_{\mathrm{e}}$ classical electron radius, $N_a$ Avogadro's number, $I$ mean excitation potential of the absorber, $Z$ and $A$ atomic number and atomic mass of absorbing material, $\rho$ density of absorbing material, $z$ charge of incident particle in units of $e$, $W_{\max}$ maximum energy transfer in a single collision. The unit of measurement of $S$ is $[MeV\, cm^2/g]$. Two corrections are normally added to Equation 2.3: the density effect correction $\delta$ and the shell correction $C$, so that

$$-\frac{dE}{dx} = 2\pi N_{\mathrm{a}} r_{\mathrm{e}}^2 m_{\mathrm{e}} c^2 \rho \frac{Z}{A}\frac{z^2}{\beta^2}\left[ln\left(\frac{2m_{\mathrm{e}}\gamma^2 v^2 W_{\max}}{I^2}\right) - 2\beta^2 - \delta - 2\frac{C}{Z}\right] \tag{2.4}$$

The density ($\delta$) and shell ($C$) corrections are important at high and low energies respectively. The density correction takes into account the fact that the electric field of the particle also tends to polarize the atoms along its path. Consequently, electrons far from the path of the particle will be shielded from the full electric field intensity and collisions with these outer lying electrons will contribute less to the total energy loss than predicted by the Bethe-Bloch formula (Equation 2.3). The shell correction arises from the fact that when the velocity of the incident particle is comparable or smaller than the orbital velocity of the bound electrons, the assumption that the electron is stationary with respect to the incident particle is no longer valid. The shell correction is generally small. In Figure 2.1 the stopping power $-dE/dx$ for positive muons in copper as a function of $\beta\gamma$ is shown, while Figure 2.2a shows the stopping power as a function of kinetic energy for different particles. At non-relativistic energies, the energy loss is dominated by the $1/\beta^2$ factor and decreases with increasing velocity until about $v \simeq 0.96\, c$, where a minimum is reached. A particle at this minimum point is known as *minimum ionizing particle* (MIP) and the minimum value of $dE/dx$ is almost the same for all particles of the same charge. As the energy increases, the term $1/\beta^2$ becomes almost constant and the energy loss rises again due to the logarithmic dependence on $\gamma$ (see Equation 2.3). Figure 2.2b shows the stopping power curve for different materials. In Figure 2.3 the most probable energy loss, scaled to the mean loss at minimum ionization, for several silicon detector thicknesses is shown. The mean energy loss of a MIP in silicon is about 387 eV/$\mu$m and the energy needed to create an electron-hole pair ($eh$) in silicon is 3.6 eV, then the mean number of pairs is $\sim 108\, eh/\mu$m, while the most probable number is $\sim 72\, eh/\mu$m.

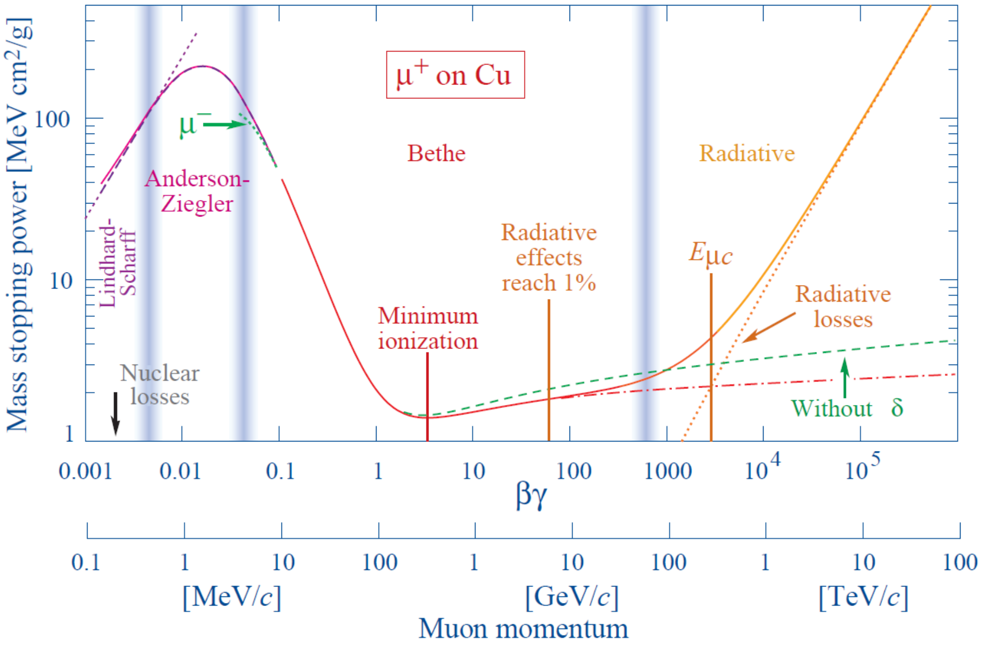

**Fig. 2.1** Stopping power for positive muons in copper as a function of $\beta\gamma$ over nine orders of magnitude in momentum [33].

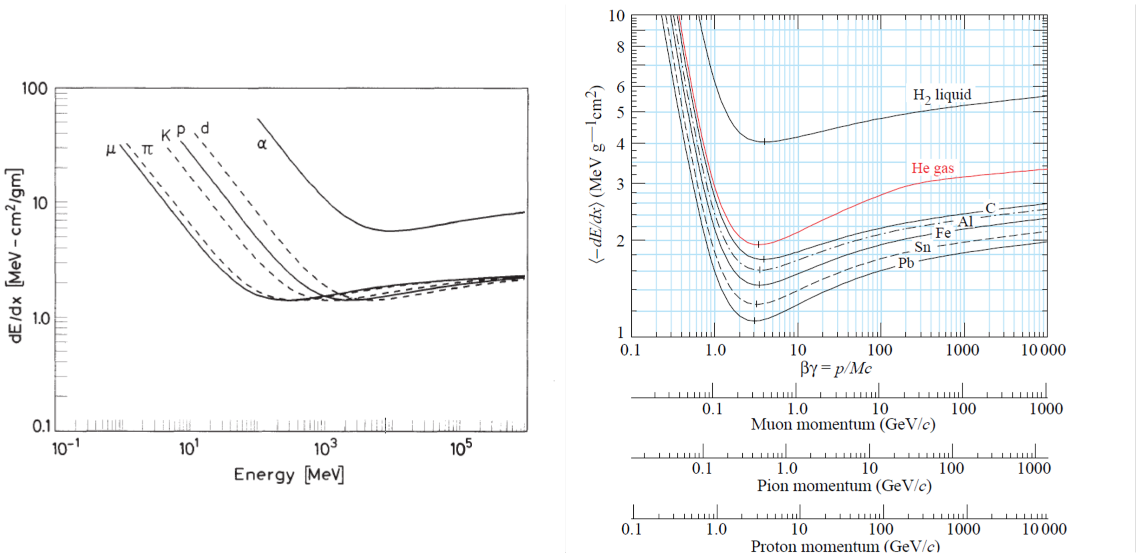

**(a)** **(b)**

**Fig. 2.2** (a) Stopping power $dE/dx$ as a function of energy for different particles [31]. (b) Mean energy loss rate in liquid hydrogen, helium, carbon, aluminum, iron, tin and lead [33].

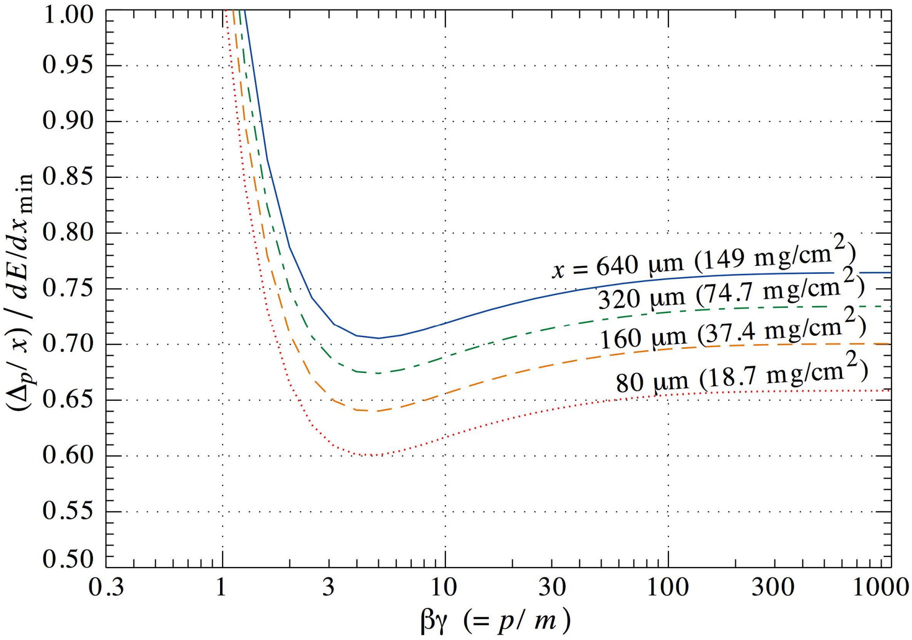

**Fig. 2.3** Most probable energy loss in silicon, scaled to the mean loss of a minimum ionizing particle, 387 $eV/\mu m$ (1.66 MeVg$^{-1}$cm$^2$), for different sensor thicknesses ($x$) [33].

## 2.1.2 Electrons and positrons

Like heavy charged particles, also electrons (and positrons) lose energy per collisions when passing through matter. However, another energy loss mechanism becomes relevant: the emission of electromagnetic radiation (*bremsstrahlung*) arising from scattering in the electric field of a nucleus. At energies of a few MeV, this process is still a relatively small factor, but it becomes comparable to or greater than the collision loss when the energy reaches a few 10's of MeV. Then, the total energy loss of electrons is composed of two parts:

$$\left(\frac{dE}{dx}\right)_{tot} = \left(\frac{dE}{dx}\right)_{rad} + \left(\frac{dE}{dx}\right)_{coll} \tag{2.5}$$

The energy loss by *bremsstrahlung* is proportional to the inverse of the particle squared mass:

$$-\left(\frac{dE}{dx}\right)_{rad} \propto \frac{1}{m^2} \tag{2.6}$$

and this explains the negligibility of radiative term for heavy charged particles. The Bethe-Bloch formula (Equation 2.3) must be slightly modified for electrons and positrons, for two reasons. One is their small mass, so the assumption that the incident particle is undeflected during the collision is invalid. The second is that for electrons the collisions are with identical particles, so the calculation must take into account their indistinguishability. The Bethe-Bloch formula becomes:

$$-\frac{dE}{dx} = 2\pi N_a r_e^2 m_e c^2 \rho \frac{Z}{A}\frac{1}{\beta^2}\left[ln\left(\frac{\tau^2(\tau+2)}{2(I/m_e c^2)^2)}\right) + F(\tau) - \delta - 2\frac{C}{Z}\right] \tag{2.7}$$

where $\tau$ is the kinetic energy of particle in units of $m_e c^2$, and for electrons

$$F(\tau) = 1 - \beta^2 + \frac{\tau^2/8 - (2r+1)ln2}{(\tau+1)^2} \tag{2.8}$$

while, for positrons

$$F(\tau) = 2\,ln2 - \frac{\beta^2}{12}\left(23 + \frac{14}{\tau+2} + \frac{10}{(\tau+2)^2} + \frac{4}{(\tau+2)^3}\right) \tag{2.9}$$

Figure 2.4 shows both the collision loss and the radiation loss for electrons in copper. The energy at which the two contributions are equal is called *critical energy.*

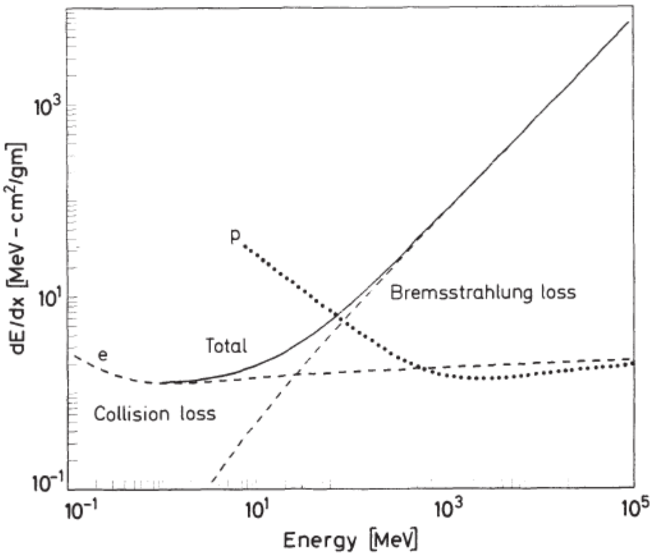

**Fig. 2.4** Collision loss and radiation loss for electrons in copper; also the stopping power for protons is shown, for comparison [31].

### 2.1.3 Multiple Coulomb scattering

As already mentioned in Section 2.1.1, in addition to inelastic collisions with the atomic electrons, charged particles passing through matter also suffer several elastic Coulomb scattering from nuclei. This scattering from nuclei is described by the Rutherford formula:

$$\frac{d\sigma}{d\Omega} = z_2^2 z_1^2 r_e^2 \frac{(m_e c/\beta p)^2}{4 sin^4(\theta/2)} \tag{2.10}$$

The effect of these collisions is that the charged particle traversing a medium is deflected by many small-angle scatters and the cumulative effect is a deflection from the original particle direction, as shown in Figure 2.5. For many applications it is sufficient to use a Gaussian approximation for the central 98% of the projected angular distribution, with an RMS width given by [35]

$$\theta_0 = \frac{13.6\,\mathrm{MeV}}{\beta c p} z \sqrt{x/X_0}\,[1 + 0.038\,ln(x/X_0)] \tag{2.11}$$

where $p$, $\beta c$ and $z$ are the momentum, velocity and charge number of the incident particle, while $x$ is the thickness of the scattering medium and $X_0$ is its radiation length, defined as the distance over which the electron energy is reduced by a factor 1/e due to radiation loss only.

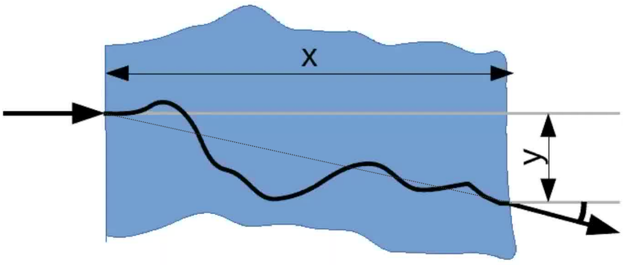

**Fig. 2.5** Representation of the multiple Coulomb scattering effect deviating the trajectory of a particle traversing a medium.

### 2.1.4 Energy loss distribution

A particle traversing a material undergoes a series of single interactions, each one contributing to the total energy loss. The energy loss is subject to statistical fluctuations which occur in the number of collisions and in the energy transferred in each collision. The calculation of the energy loss distribution is divided into two cases: thick absorbers and thin absorbers. For thick absorber in which the number of collisions is large, by the Central Limit Theorem, the energy loss distribution follows a Gaussian distribution. On the other hand, the number of collisions in a thin absorber (or in gases) is too small and the Central Limit Theorem can not be applied because of the possibility of large energy transfers in a single collision. For thin absorbers, the mean energy loss is displaced with respect to the peak because of the high energy tail, while the peak position defines the most probable energy loss. Depending on the thickness of the absorber, there are different theories to describe the distribution. The distinguishing parameter is the ratio between the mean energy loss ($\bar{\Delta}$) and the maximum energy transferable in a single collision ($W_{\text{max}}$):

$$\kappa = \bar{\Delta}/W_{\text{max}} \tag{2.12}$$

For very thin absorbers ($\kappa \leq 0.01$) the energy loss distribution is well described by the Landau theory, while the region of intermediate $\kappa$ values was treated by Symon and Vavilov. Already for $\kappa = 1$, the distribution resembles a Gaussian shape. Figure 2.6 shows the energy loss distribution for 500 MeV pions passing through different thickness silicon detectors.

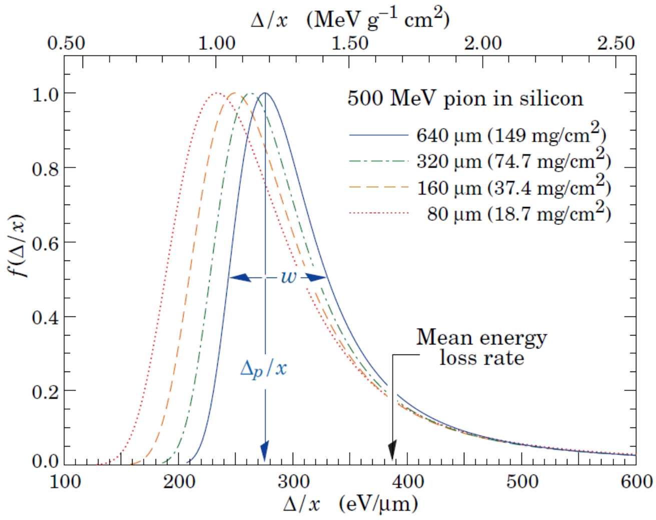

**Fig. 2.6** Energy loss distribution for 500 MeV pions incident on silicon detectors with different thickness [33]. Distributions are normalized to the most probable value $\Delta/x$. The width $w$ is the full width at half maximum.

## 2.2 The p-n junction as particles detector

Silicon is the most used and studied semiconductor for radiation detection, but intrinsic silicon can not be used as particle detector and it is necessary to realize a special silicon device, named *p-n junction*, for the reasons illustrated in the following. In pure silicon the carrier concentration $n_i$ is about $10^{10}\,\text{cm}^{-3}$ at room temperature, corresponding to a resistivity $\rho \approx 400\,\mathrm{k\Omega\,cm}$ [36]. The silicon lattice includes $5 \cdot 10^{22}\,\mathrm{atoms/cm^3}$ but crystal imperfections and minor impurities concentrations limit Si carrier concentrations to about $10^{11}\,\mathrm{cm^{-3}}$ at room temperature, corresponding to a resistivity $\rho \approx 40\,\mathrm{k\Omega\,cm}$. These resistivity values are too low for use in a simple crystal detector, since signal currents are typically of order of $\mu$A, so if the quiescent current has to be small compared to the signal current, the resistance between the electrodes has to be $\gg 30\,\mathrm{M\Omega}$. For instance, in pure silicon substrates, with a typical silicon sensor $1\,\mathrm{cm^2}$ area and $300\,\mu$m thickness, there are about $3 \cdot 10^8$ electron-hole pairs at room temperature, whereas a MIP would normally generate about $2 \cdot 10^4$ electron-hole pairs, four orders of magnitude less than the thermal ones. So the signal would be completely lost in the free-charge carriers. It is therefore essential to reduce the thermal pairs by several orders of magnitude and the most effective solution is to obtain a silicon volume depleted by free charge by using a reverse-biased p-n junction. The key is the replacement of silicon atoms with other atoms of a specific element, to control the conductivity of semiconductors. This process is called *doping*. Required concentrations are in the range $10^{12} - 10^{18}\,\mathrm{cm^{-3}}$.

The doping of a semiconductor can be an *n-type* or a *p-type* doping. In the first case the impurity has one more valence electron with respect to the semiconductor element and it is called *donor*, while in the second case the doping element has one less valence electron with respect to the semiconductor and it is called *acceptor*. Silicon belongs to the group 4 of the periodic table, so it has four valence electrons. So n-type doped silicon is obtained by replacing a silicon atom by an atom with five valence electrons (for example P, As, Sb), so leaving one valence electron without a partner, that contributes an excess electron to the lattice. On the other hand, introducing a group 3 atom (for example B, Al, Ga, In) leaves one impurity valence electron without a partner and p-type silicon is obtained. The donor level lies in the forbidden gap close to the conduction band edge, so thermal excitation can promote electrons into the conduction band. On the other side, the acceptor level lies in the forbidden gap just above valence band edge. Thermal excitation can promote electrons from the valence band to fill the acceptor state, leaving a hole in the valence band.

The p-n junction is a two-terminal device made of the junction of an n-type and a p-type semiconductor. Figure 2.7 shows a p-n junction and its internal potential and electric field. Due to the large concentration difference of charge carriers between the two regions, electrons (holes) will diffuse across the junction, leaving a positive (negative) charge in the n-side (p-side). As a result, a volume free of mobile charges is created across the junction, called space charge region or depletion region. The resulting electric field across the depletion region represents the so-called *built-in potential* ($V_{bi}$), which depends on the doping concentrations ($N_a$, $N_d$) of the two regions:

$$V_{bi} = \frac{kT}{q} ln \left( \frac{N_a \, N_d}{n_i^2} \right) \tag{2.13}$$

where $k$ is the Boltzmann's constant and $T$ the temperature. As explained before, to use a p-n junction as a particle detector, it is necessary to fully deplete the bulk and this is achieved by applying an external potential. The total depletion region width is equal to:

$$w_{depl} = x_p + x_n = \sqrt{\frac{2\varepsilon_0 \varepsilon_{Si}(N_a + N_d)}{qN_a N_d}(V_{bi} + V_{bias})} \tag{2.14}$$

where $x_p$ and $x_n$ are the widths of the depletion regions in the p- and n-side of the junction, respectively, $\varepsilon_0$ and $\varepsilon_{Si}$ are the vacuum and silicon dielectric constant. Since typically one side of the junction is much more heavily doped than the other and the built-in potential is generally considerably lower than the applied bias voltage, assuming an n-type bulk material, Equation 2.14 can be simplified as:

$$w_{depl} \cong x_n = \sqrt{\frac{2\varepsilon_0 \varepsilon_{Si}}{qN_d} V_{bias}} \tag{2.15}$$

The depletion voltage that has to be applied to have a fully depleted detector of thickness $d$ is:

$$V_{FD} = \frac{qN_d d^2}{2\varepsilon_0 \varepsilon_{Si}} \tag{2.16}$$

To avoid excessive reverse bias voltage, a particular detector configuration is used: the *p-i-n* (PIN diode), where $i$ stands for *intrinsic* semiconductor.

## 2.3 Signal formation in silicon sensors

As described before, charged particles traversing matter lose a fraction of their energy through collisions with the atomic electrons, leading in this way to excitation or ionization of the atoms. In a silicon diode, when an external electric field is applied, a current is induced on the electrodes, due to the motion of electrons ($e$) and holes ($h$) formed by ionization. As established by the Shockley-Ramo theorem [37, 38], the signal is determined by the instantaneous current $i$ induced at the electrodes by the

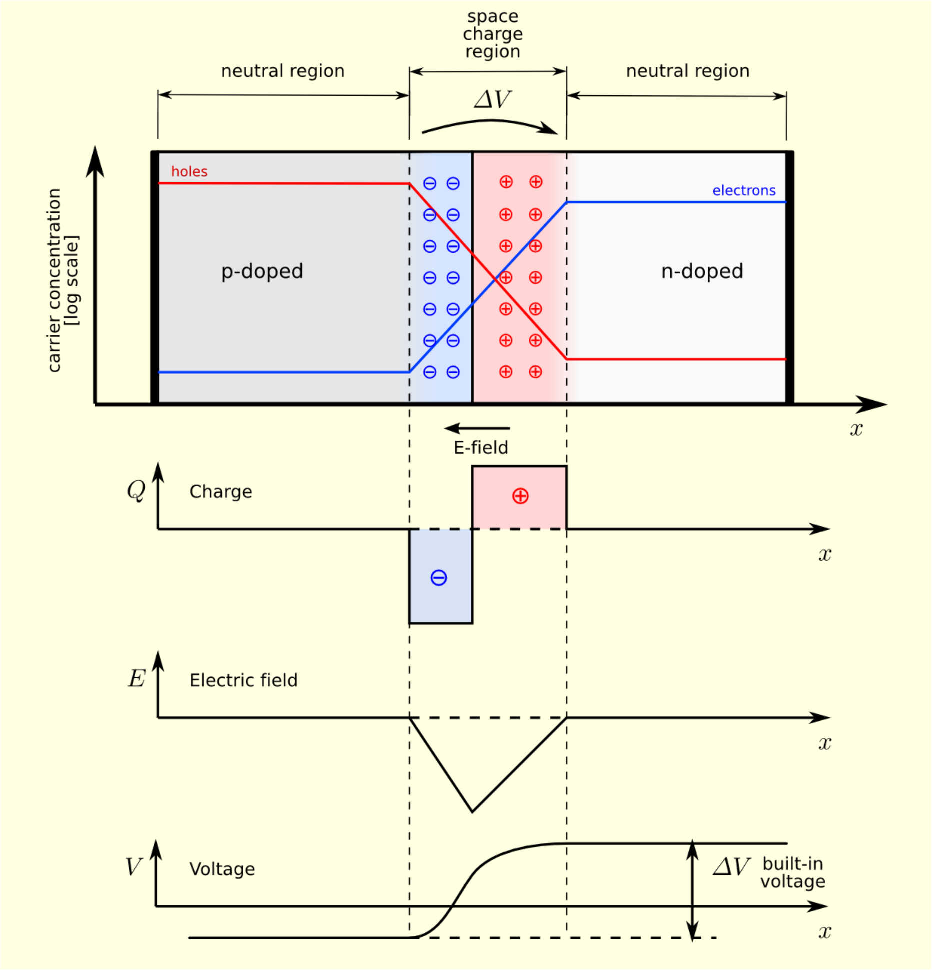

**Fig. 2.7** A p-n junction at thermal equilibrium. The charge distribution, the electric field and the internal potential are shown, both in the depletion region and in the charge-neutral regions.

charge carriers moving along their drift paths, according to this formula

$$i = q\,\mathbf{E_w} \cdot \mathbf{v_d} \tag{2.17}$$

where $\mathbf{E_w}$ is the weighting field and $\mathbf{v_d}$ is the charge carriers drift velocity. The weighting field $\mathbf{E_w}$ is the electric field that would exist in a given position $x$ if the given electrode, for which the induced charge has to be calculated, is at unitary potential, while the other electrodes are at zero potential and if the electron inducing the current would be removed.

As a significant example, the case of a reverse-biased p-n junction (Figure 2.8) is considered. According to the Shockley-Ramo theorem, the induced current on one electrode is

$$i = q\,v\,E_w \tag{2.18}$$

where the weighting field is $E_w = 1/d$ and the charge carrier velocity can be expressed in terms of the mobility ($\mu$) and the electric field ($E$) in this way $v_d = \mu E = \mu V_{bias}/d$. Then, the current induced by a single charge carrier is

$$i = q\,\mu\,\frac{V_{bias}}{d^2} \tag{2.19}$$

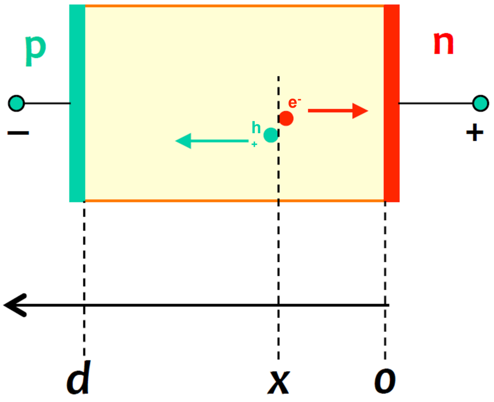

**Fig. 2.8** Scheme of a reverse-polarised p-n junction.

If the electron-hole pair is created in the position $x$ between the two electrodes, as illustrated by Figure 2.8, the drift time of electrons ($t_e$) and holes ($t_h$) is:

$$t_e = \frac{x}{v_e} = \frac{x}{\mu_e E} = \frac{x\,d}{\mu_e V_{bias}} \tag{2.20}$$

$$t_h = \frac{d-x}{v_h} = \frac{d-x}{\mu_h E} = \frac{(d-x)\,d}{\mu_h V_{bias}} \tag{2.21}$$

In the specific case in which the electron-hole pairs are created in the middle between the two electrodes ($x = d/2$), the current induced by the electrons lasts about 1/3 of that induced by the holes, due to the different mobility of electrons and holes in silicon ($\mu_e \sim 1450\,\mathrm{cm^2/(V\,s)}$, $\mu_h \sim 450\,\mathrm{cm^2/(V\,s)}$). Figure 2.9 shows a scheme of the current induced by the two charge carriers when a charged particle hits the sensor of Figure 2.8 in three particular positions: $x = 0$, $x = d/2$ and $x = d$.

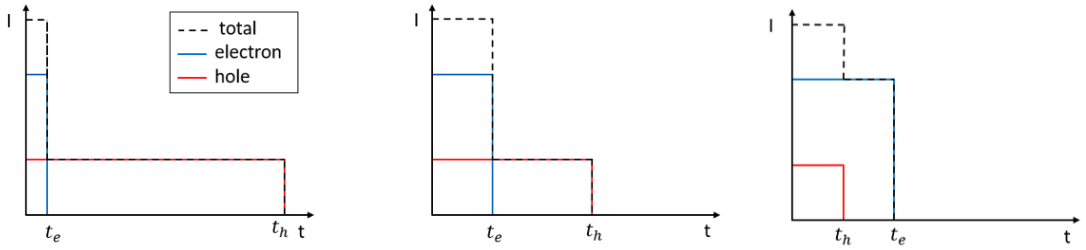

**Fig. 2.9** Scheme of the current induced by the electrons (in blue), the holes (in red) for three different positions of charge generation, $x = 0$, $x = d/2$, $x = d$ (from left to right). The total current is indicated by the black dashed line.

This simplified model indicates that the signal shape is influenced by the position where the incident particle hits the sensor, due to the different charge carriers velocity, and this affects the time resolution of the sensor.

## 2.4 Radiation damage of silicon sensors

Silicon sensors highly exposed to radiation (e.g. in high energy physics experiments) undergo severe damage to their structure, since the radiation causes the formation of defects both in the bulk and in the surface of the sensor [39, 40]. The three main effects introduced by radiation are:

- displacement of atoms from their position in the lattice (bulk)
- transient and long-term ionization in insulator layers (surface)
- formation of interface defects (surface)

### 2.4.1 Bulk damage

The bulk damage causes modifications in terms of leakage current, depletion voltage and Charge Collection Efficiency (CCE). This damage depends on the type of radiation particle and on its energy range. In silicon sensors used in tracking detector of HEP experiments, the damage to the bulk is caused by charged hadrons (protons, pions), neutrons or highly energetic leptons (electrons, muons). This damage is mainly due to the Non Ionizing Energy Loss (NIEL) mechanism, in which the incident particle undergoes to multiple collisions with the silicon atoms causing the displacement of an atom. These displacements translate into the creation of new energy levels in the band

gap, behaving like acceptors or donors and resulting in macroscopic property changes of leakage current, depletion voltage and charge collection efficiency.
The creation of additional energy levels in the forbidden band gap causes an increase of the generation-recombination processes in silicon, that, in a reverse-biased *pn* junction means an increase of the reverse leakage current. Many experiments found that there is a linear behaviour of leakage current with the fluence (Figure 2.10):

$$\Delta I = \alpha \, \Phi_{eq} \, V \tag{2.22}$$

where $\alpha$ is the current-related damage parameter, $\Phi_{eq}$ is the 1 MeV neutron equivalent fluence and $V$ the total depleted sensor volume. The increase of the leakage current affects both the signal-to-noise ratio of the detector and the system power budget [41].

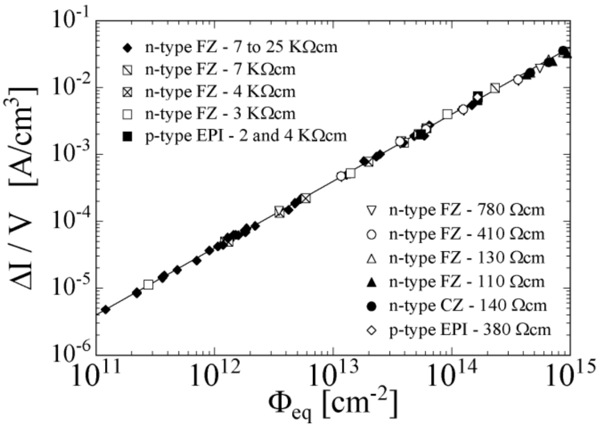

**Fig. 2.10** Leakage currents of devices produced by various process technologies from different silicon materials versus fluence after an annealing treatment for 80 min at 60°C [41].

Figure 2.11 shows the effective doping concentration as a function of the fluence. Starting with an *n*-type doped silicon bulk, a constant removal of donors together with an increase of acceptor-like levels shifts the space charge first down to an intrinsic level and then up to a more *p*-type material proportionally to radiation fluence. This material *type inversion* causes a change in the depletion voltage, that drops first and starts rising later.
Above a fluence of $1 \cdot 10^{15}$ 1 MeV $\mathrm{n_{eq}/cm^2}$, the signal loss becomes the fundamental problem of silicon detectors. This signal degradation is due to the defects acting as very efficient trapping centers for free charge carriers. When free carriers, generated from an impinging particle, are captured, they are usually not released before hours or longer [42], leading to a CCE degradation.

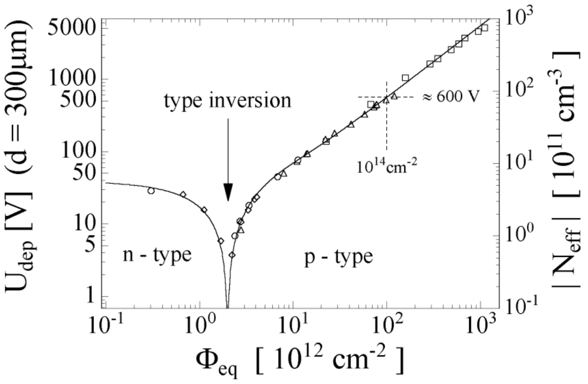

**Fig. 2.11** Depletion voltage and absolute effective doping concentration at different irradiation fluences. Plot from [41].

### 2.4.2 Surface damage

Surface damage depends on ionisation effects on the insulator material (mainly silicon dioxide $SiO_2$) used to protect the detector surface from external agents and from any possible mechanical damage. This damage refers both to damage in the $SiO_2$ passivation layer and in its interface with the silicon bulk. In this case damage is introduced by ionization and the resulting generation of electron-hole pairs. Most of these recombine instantly, but a fraction of them will not. The mobility of electrons in silicon dioxide ($\mu_e \sim 20\,\mathrm{cm}^2/(\mathrm{V}\cdot\mathrm{s})$) is several orders of magnitude higher than that of the holes ($\mu_h \sim 2\cdot 10^{-5}\,\mathrm{cm}^2/(\mathrm{V}\cdot\mathrm{s})$), so electrons quickly drift to the metal electrode while holes diffuse to the $Si - SiO_2$ interface, where they get trapped. As a result, positive static charges accumulate at the interface. Then, the main macroscopic effects of the surface damage are an increase of inter-pixel capacitance, leading to a noise increase, and a decrease of inter-pixel resistance that leads to an increase of cross-talk effects, but also the breakdown voltage might be affected.

## 2.5 Silicon sensors for timing applications

The particle arrival time, $t_0$, measured by a silicon sensor is subject to fluctuations, that arise from different phenomena each one contributing with a time jitter term to the global time resolution of the sensor, $\sigma_t$. The time resolution of the sensors is then given by the sum in quadrature of these jitter contributions:

$$\sigma_t = \sqrt{\sigma_{un}^2 + \sigma_{ej}^2 + \sigma_{tw}^2 + \sigma_{Landau}^2 + \sigma_{TDC}^2} \tag{2.23}$$

The $\sigma_{\mathbf{un}}$ jitter term is due to the non-uniformities in weighting field $E_w$ and charge carriers drift velocity, that lead to differences in the signals shape depending on the incident particle hit position.

The electronic jitter $\sigma_{\mathbf{ej}}$ is due to the noise fluctuations that modulate the instantaneous signal level, as illustrated in Figure 2.12 by the shaded band. Assuming to use a discriminator to measure the time at which the signal reaches the threshold $V_T$, we have that the fluctuations in signal amplitude translate into timing fluctuations. By geometrical projection, the jitter due to the electronics is obtained:

$$\sigma_{ej} = \frac{\sigma_n}{\left.\frac{dV}{dt}\right|_{V_T}} \approx \frac{\sigma_n}{\frac{V}{t_r}} = \frac{t_r}{\frac{S}{N}} \tag{2.24}$$

where $t_r$ is the signal rise time and $S/N$ the signal-to-noise ratio. Since usually the signal $V(t)$ is not linear, the optimum trigger level is the point of maximum slope.

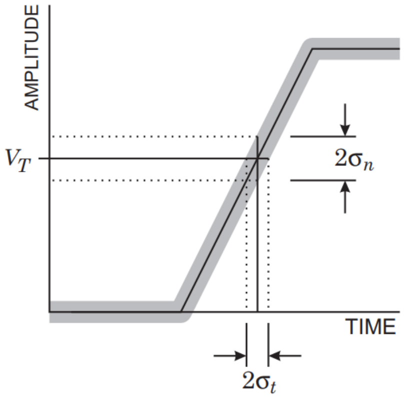

**Fig. 2.12** Fluctuations in signal amplitude ($\sigma_n$) crossing a threshold $V_T$ translate into timing fluctuations ($\sigma_t$) [36].

Another time jitter source is due to the signal amplitude variations, $\sigma_{\mathbf{tw}}$. Indeed, the time at which the signal crosses a fixed threshold depends on pulse amplitude and the timing signal shifts as the amplitude varies, causing the broadening of the time distribution. This effect, illustrated in Figure 2.13, is called *time-walk*. The time-walk jitter can be mitigated by setting the threshold to the lowest possible level or using time-picking methods that compensate for amplitude variations, such as a Constant Fraction Discriminator (CFD) or a Leading Edge discriminator with a correction of the time of the signal for the Time Over Threshold (TOT) that is related to the signal amplitude.

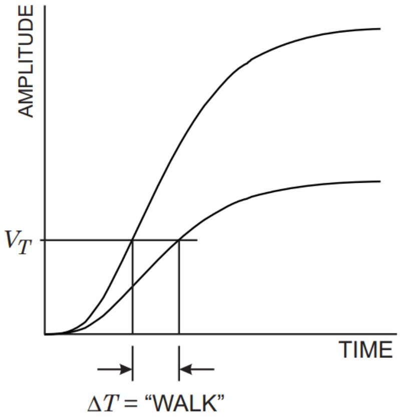

**Fig. 2.13** The time at which a signal crosses a fixed threshold depends on the signal amplitude, leading to *time-walk* phenomenon [36].

The $\sigma_{\mathbf{Landau}}$ term is the jitter due to the amplitude variations depending on the sensor thickness crossed by the charge carriers inducing the signal. Finally, the $\sigma_{\mathbf{TDC}}$ is the jitter due to the resolution of the Time to Digital Converter (TDC) used to make time intervals measurements.

All the jitter contributions in Equation 2.23, apart from the $\sigma_{TDC}$, must be taken into account in the design of a sensor developed to have excellent timing performance. Silicon sensors developed and used for timing applications are described in the following sections.

### 2.5.1 Ultra Fast Silicon Detectors

Ultra Fast Silicon Detectors (UFSDs) are silicon sensors based on the Low Gain Avalanche Detector (LGAD) technology and optimized for precise time measurements. A LGAD sensor is shown in Figure 2.14. The LGAD design relies on a modification of a traditional planar silicon sensor with the addition of another doping layer, that is obtained with a $p^+$ material, like silicon doped with boron or gallium, in the case of a *n-in-p* sensor. This additional doping layer leads to a large increase in doping concentration in close proximity to the junction and consequently a modification of the electric field profile along the thickness of the sensor with a very high intensity ($\sim 3 \cdot 10^5$ V/cm) in the first few microns of the sensor, inducing the low gain avalanche mechanism.

Two fundamental aspects to be considered to ensure good timing performance of UFSDs are the gain and the thickness. The requirements are to have a gain sufficient

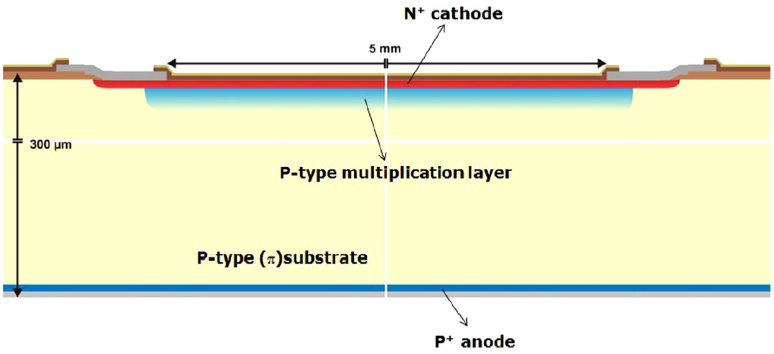

**Fig. 2.14** Schematic cross section of a LGAD pad design [43].

to perform accurate time measurements and thin enough sensors to have a faster rising edge that implies better timing performance. However too thin sensors have larger capacitance values and a smaller signal, thus it is required a high gain to generate signals that are large enough to be measured accurately by the read-out electronics. The combination of experimental measurements and simulations indicated as optimum performance parameters a thickness of about 50 $\mu$m and a gain of about 20 [44].
After the irradiation, the gain layer multiplying capability starts to decrease. This problem can be mitigated at production level by using carbon enriched wafers, while it is operatively overcome increasing the bias voltage to increase the bulk electric field and gain. However, it is not possible to increase the bias voltage indefinitely without reaching the breakdown and causing the *auto-triggering* phenomenon, which is the problem of noise reaching high enough levels to be falsely registered as a signal by a sensor. The bias voltage at which the auto-trigger rate starts to increase varies with the radiation fluence and with the doping element used [45].
A lot of R&D work has been done in the study and optimization of the UFSD sensors. For example, different thickness sensors, from 35 $\mu$m to 80 $\mu$m, have been produced and characterized. These studies have shown that the $\sigma_{Landau}$ term is dominant in the time resolution of these devices, with a value of about 25 ps for the 35 $\mu$m thickness sensor and about 36 ps, for the 35 $\mu$m and the 80 $\mu$m thickness sensors, respectively [46]. However, at an irradiation fluence of $2.5 \cdot 10^{15}$ 1 MeV $\mathrm{n_{eq}}/\mathrm{cm}^2$, because of a significant decrease of the gain, thicker sensors have better time resolution as they have an higher initial signal. The time resolution measured for not irradiated UFSD is in the range $(25-35)$ ps and also devices irradiated up to $1.5 \cdot 10^{15}$ 1 MeV $\mathrm{n_{eq}}/\mathrm{cm}^2$ have shown a comparable time resolution, while a worsening is observed at higher irradiation fluences [46, 47]. Such a feature makes them inadequate to be used in tracking detectors exposed to high radiation fluences such as the LHCb VELO. Also the spatial resolution

of current LGADs, having pad areas of $1-2\,\mathrm{mm}^2$, is not sufficiently good for LHCb VELO and other detectors working in high luminosity conditions. A huge R&D work to improve both the radiation hardness and the spatial resolution of such devices is in progress [48–50].

### 2.5.2 Monolithic silicon sensors

Monolithic Complementary Metal-Oxide Semiconductor sensors (abbreviated in *CMOS*) are pixellated devices in which the sensor and front-end electronics are processed on the same wafer. The main difference to other solid state sensors used in high energy physics experiments is the lack of any depletion voltage - we are not considering the High Voltage CMOS and the High Resistivity CMOS here. A shallow depletion layer created purely by the p-n junction collects charges right away. Charges created in the epitaxial layer are collected via diffusion in the $N$-wells. The EPI layers thickness is in the order of $15-20\,\mu$m, but the low signal is compensated for by very low capacitance value, hence very small noise, resulting in signal-to-noise ratio up to 30. In Figure 2.15 the cross section of a Monolithic Active Pixel Sensor (MAPS) is shown. MAPS were shown as a promising technology for high-granularity and light in material budget detectors [51]. They represent several advantages over traditional hybrid pixel detector technologies, as they can be inexpensively built, even in large array sizes, thinned to the needs, offer individual pixel readout, reasonable radiation hardness ($10^{12}-10^{13}\,1\,\mathrm{MeV}\,\mathrm{n_{eq}}\,\mathrm{cm}^{-2}$), and operated at high speeds with low power consumption.

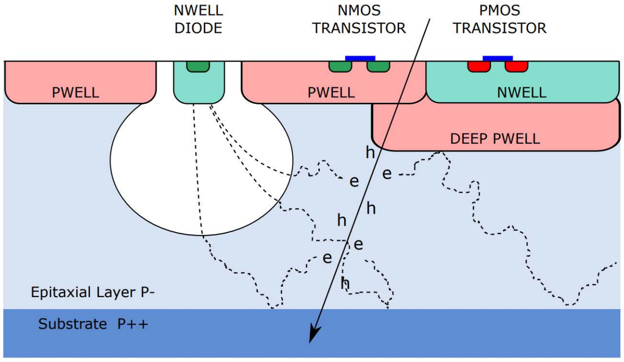

**Fig. 2.15** Schematic cross section of a Monolithic Active Pixel Sensor [52].

Until now monolithic pixel sensors with nanosecond time resolution are adopted in Belle-II [53], while MAPS are used in STAR [54], Mu3e [55] and in the upgraded ALICE tracker [56] installed to take data during the LHC Run3. A lot of R&D work

has been done to develop monolithic sensors for 4D-tracking measurements, with very good time resolution. After a demonstrator with discrete components which reached a time resolution of 100 ps [57], the first monolithic silicon pixel detector prototype in the SG13G2 IHP 130 nm process with 100 $\mu$m pitch was fabricated and it allowed to measure a time resolution of 50 ps [58], while with an improved second prototype a time resolution of 36 ps and an efficiency of 99.9% were achieved [59]. Both these prototypes were realized without an avalanche gain mechanism.
A recent project, the MONOLITH H2020 ERC Advanced project, has the aim to develop a novel monolithic silicon sensor, named *Picosecond Avalanche Detector* (PicoAD), that provides both picosecond timing and high spatial resolution. The novel idea is to develop a sensor with a fully depleted multi-junction containing a continuous deep gain layer which separates a few $\mu$m thick absorption region in which the primary electrons are generated from the region where the electrons drift (Figure 2.16).

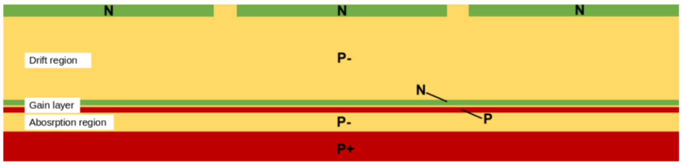

**Fig. 2.16** Schematic cross section of the PicoAD detector. The sensor presents N-type pixels on a high-resistivity epitaxial layer. A second junction is used to produce a continuous avalanche gain layer [60]. The epitaxial layer and the deep junction are operated in full depletion.

This structure allows to decouple the pixelated structure from the continuous gain layer. A PicoAD proof-of-concept prototype, consisting of a matrix of hexagonal pixels with a pitch of 100 $\mu$m, was recently produced and characterized both in laboratory [61, 60] and in a test beam [62]. At a bias voltage of 125 V, a detection efficiency of 99.9% has been measured. A time resolution of about 17 ps was measured in the full active area, including the inter-pixel regions.

## 2.5.3 3D silicon sensors

3D silicon pixel sensors belong to the hybrid pixel sensors category in which the sensor and the readout chip are produced in two separate wafers and then connected to each other through the bump bonding technique (Figure 2.17).
3D sensors were proposed for the first time by Sherwood Parker in 1997 [63–65] as an alternative to the planar sensors. In Figure 2.18 a scheme of both a planar and a 3D sensor is shown. In a planar sensor the electrodes are implanted on the top and on

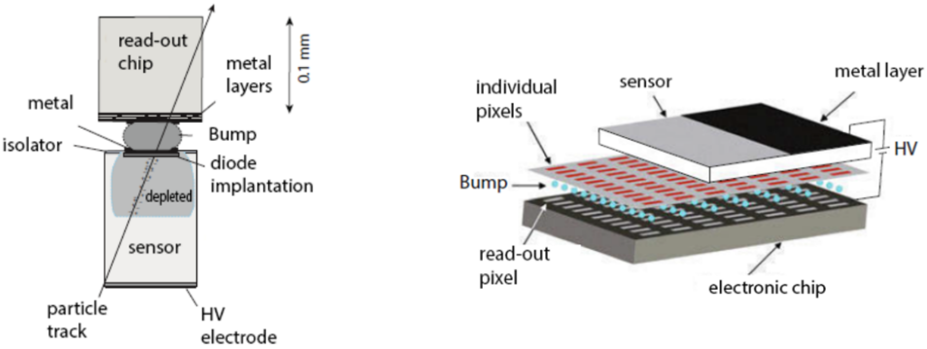

**Fig. 2.17** (Left) Scheme of a hybrid pixel bump-bonded to the front-end electronics. (Right) Scheme of a sensor pixels matrix bump-bonded to the front-end electronics.

the bottom surfaces of the wafer, while in a 3D sensor the electrodes are implanted perpendicularly to the wafer surface.

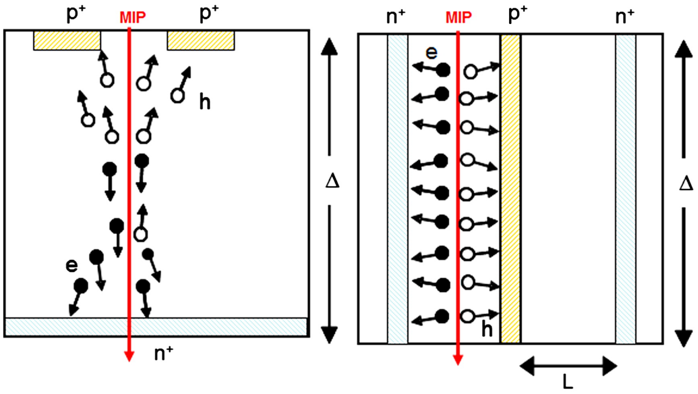

**Fig. 2.18** Schematic cross section of a silicon planar sensor (left) and a silicon 3D sensor.

One of the main feature of the 3D geometry is that it decouples the wafer thickness ($\Delta$) from the distance between the electrodes ($L$). This allows to make $L$ much smaller than $\Delta$ by design, so that the full depletion voltage $V_{dep}$ can be significantly reduced with respect to the planar one of the same thickness. Moreover, a smaller inter-electrode distance allows to have a shorter charge collection distance, to reach high electric fields and charge carriers velocity saturation already at low bias voltage, so the charge collection times can be much shorter. This is possible without losing in signal amplitude, since the amount of charge generated in a silicon sensor due to a MIP crossing it depends on the sensor thickness (Section 2.1), so the charge generated in a planar and in a 3D sensor with the same thickness is the same (in both cases about 72 electron-hole pairs per $\mu$m are generated). The short inter-electrode distance also implies that the induced signal are very fast and that the $\sigma_{Landau}$ term in Equation 2.23 is significantly reduced. Moreover, this geometry can counteract the charge loss from trapping induced by the radiation damage, as the distance travelled by the charge carriers is shorter than in a planar sensor.

However, 3D sensors present also some disadvantages compared to planar sensors. The first one is that the small inter-electrode distance causes an high sensor capacitance that could increase the noise and degrade the time resolution, so a dedicated work on the electronics is needed. Another disadvantage is that in a 3D sensor very low field regions are present in the active volume, in particular between electrodes of the same doping type. This means that charge carriers generated in these regions diffuse until they reach a region with a sufficiently high electric field, causing a delay of the signal response and thus a worsening of the time resolution. It is possible to face this problem optimizing the design of the 3D sensor in order to optimize the uniformity of the sensor response, reducing the low field regions size.

So far, 3D sensors have been installed in some LHC experiments, in ATLAS IBL [66] and in CMS-PPS [67], for example, but not for timing applications. The radiation hardness of 3D silicon sensors with columnar electrodes has been tested up to a radiation fluence of $3 \cdot 10^{17}\,1\,\mathrm{MeV\,n_{eq}/cm^2}$ [22]. At perpendicular particle incidence, 3D sensors suffer of a geometrical inefficiency when a particle crosses an electrode, since the electrodes are non-sensitive areas. This disadvantage can be easily overcome by tilting the sensors to form an angle between the incoming particle and the vertical electrodes, as done for the ATLAS IBL detector, where 3D sensors are mounted at 15° with respect to the perpendicular particles incidence.

In 2017 an INFN-funded project, the TimeSPOT project, has started to develop 3D sensors optimized for timing applications, with a trench electrodes configuration, turning out to be the best design from simulations results. The main topic of this thesis is the characterization of TimeSPOT sensors, whose design, fabrication and characterization will be described in next chapters.

# Chapter 3

# The TimeSPOT project

This Chapter is dedicated to an overview of the project *TIME and SPace real-time Operating Tracker*, TimeSPOT. TimeSPOT is a 4-year INFN-funded project born to develop devices with excellent time and space resolution and very high radiation hardness, both for the sensor and for the read-out electronics. The final goal is to realize a tracker system composed by at least four TimeSPOT tracking layers. The sensors development concerned both silicon and diamond devices, but in this thesis only silicon sensors are discussed since their characterization is the main topic of this work. More details about 3D diamonds sensors developed within the TimeSPOT project can be found in Refs. [68–71]. In this chapter the simulation work done to optimize the geometry of the sensor, the fabrication process and the development of an ASIC optimized for TimeSPOT sensors in CMOS 28 nm technology are described.

## 3.1 Sensor design optimization

As explained in Section 2.5.3, the 3D-sensors technology enables the design and optimization of the sensor active volume and electrodes for a precise purpose, as the timing application for TimeSPOT. In fact the electrodes geometry in a 3D sensor has a large impact on its time resolution. For this reason the first step of the TimeSPOT project has been the design of the sensor through simulations studies of several 3D geometries, in order to choose the best option for timing purposes. The time jitter term $\sigma_{\mathrm{un}}$ (Equation 2.23), due to the non-uniformity in the signals shape, depends only on the sensor active volume geometry and so it can be minimized by design. According to the Shockley-Ramo theorem 2.17, the signal is determined by the instantaneous current $i$ induced at the electrodes by the charge carriers moving along their drift paths, that depends on both the weighting field ($\mathbf{E_w}$) and the charge carriers drift

velocity ($\mathbf{v_d}$). Hence, an high uniformity both in weighting field and in electric field is fundamental to achieve a good time resolution, as well as to reach the charge carrier velocity saturation regime, that is easier to reach in a 3D sensors, thanks to the short inter-electrode distance, with respect to a planar sensor.
Within the TimeSPOT project, a total of 20 3D-pixel geometries have been designed and simulated [72] with the Synopsys Sentaurus TCAD simulation package [73], using square and hexagonal shapes with trench or column electrodes. Here two geometries are taken into account and are shown in Figure 3.1, where the bias electrodes, $p^+$ doped, are represented in blue, while the collection electrodes, $n^{++}$ doped, are shown in red. The first one is a square geometry pixel with four column bias electrodes in the corners and a central collection electrode, while in the second geometry the bias and collection electrodes are trenches parallel to each other. In Figure 3.2 the weighting field and the electric field maps obtained at a bias voltage of $-150\,\mathrm{V}$ for the two geometries considered are shown. The five-columns geometry presents a very high electric field close to the electrodes, that radially decreases moving away from the columns, and very low electric field between the bias columns corresponding to a null weighting field. On the other hand, the trench geometry shows a weighting field and electric field much more uniform, especially in the region between the readout trench and the bias trenches, with small regions at lower weighting field in the pixel corners.

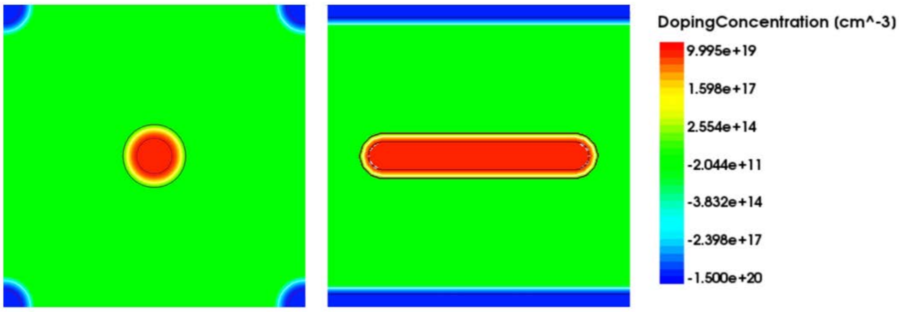

**Fig. 3.1** TCAD 2D model simulation showing the electrode geometries and doping profiles for (left) the five columns geometry and (right) the trench geometry [24].

In addition to this, another analysis, based on quasi-stationary simulation, named *Ramo maps*, was used to evaluate the induced current $i(t)$ due to a charge moving in each point of the sensitive volume, computed according to Equation 2.17. Figure 3.3 shows the Ramo maps obtained for the squared 5-columns geometry and for the trench geometry pixels at different bias voltages. The advantages of the trench geometry are evident, since in the column geometry large contributions to the induced current are

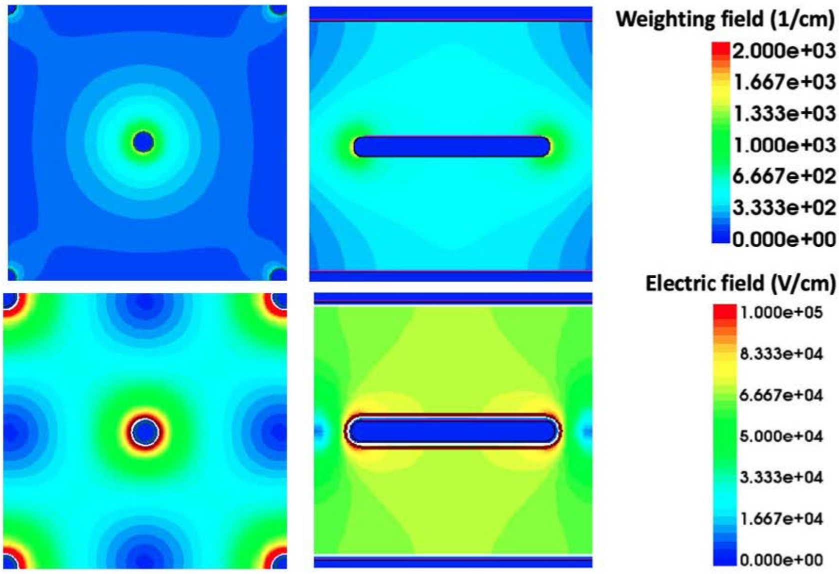

**Fig. 3.2** (Top) Weighting field and (bottom) electric field maps for (left) the five columns geometry and (right) the trench geometry at $V_{\text{bias}} = -150\,\text{V}$.

given only in the proximity of the collecting electrode, while they extend to almost the complete volume in the trench case.

An important parameter in the development of sensors optimized for timing is the charge collection time and, in particular, its uniformity in the active area of the sensor. To estimate this quantity, a simulation chain has been developed. The static sensor properties (electric field, weighting field and charge carriers velocity maps) were simulated with TCAD, while the energy deposit in the sensor volume was obtained using a `Geant4`-based Montecarlo simulating charge deposits from $O(10^3)$ MIPs perpendicularly impinging on the sensor surface at random positions. Then, the carrier dynamics was entirely simulated by means of the TIMESPOT Code for Detector (*TCoDe*) software [74], developed within the TimeSPOT project collaboration to increase processing speed of induced signal calculations. In Figure 3.4 a comparison of the charge collection time in the two geometries considered is shown. The charge collection time distribution obtained with the trench geometry shows smaller values and, most importantly, a more uniform behaviour with respect to the 5-columns geometry. This implies a better timing response uniformity of the trench pixel sensor, in which the time distribution is peaked and appears as a Gaussian with a tail at larger times, due to the slightly slower areas.

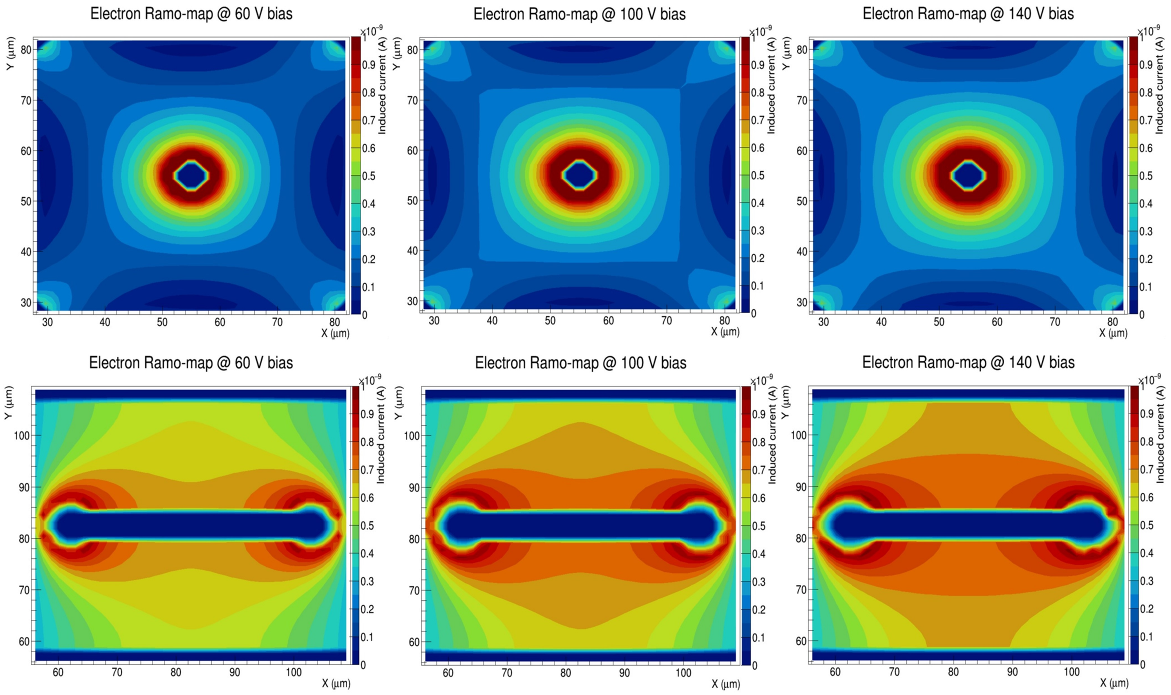

**Fig. 3.3** Ramo maps for electrons at $V_{\text{bias}} = -60\,\text{V}$, $-100\,\text{V}$, and $-140\,\text{V}$ for the five columns geometry (top) and the trench geometry (bottom) [24].

For all these reasons, the 3D-trench geometry has been chosen for the TimeSPOT silicon pixel sensor, that is shown in Figure 3.5. The TimeSPOT pixel has a size of $55 \times 55\,\mu\text{m}^2$ and an active thickness of $150\,\mu$m, which ensures an efficient detection of a MIP (depositing about 2 fC). The collecting trench electrode is $40\,\mu$m long and $5\,\mu$m wide and $135\,\mu$m deep, while the ohmic electrode, providing the bias voltage to the pixel, extend throughout the entire sensitive thickness. The pixel dimensions were chosen in order to have a sensor pitch compatible with the TIMEPIX readout and processing ASIC family [75]. Moreover, in the two TimeSPOT batches produced, several test structures with different pitch and trenches size have been designed and fabricated.

## 3.2 TimeSPOT sensors production

Two batches of TimeSPOT sensors were produced at Fondazione Bruno Kessler (FBK) foundry (Trento, Italy) in 2019 and 2020 using a single-sided fabrication process. Before TimeSPOT sensors production, several fabrication tests were performed to develop a fabrication procedure [76], since trench electrodes had never been produced before at

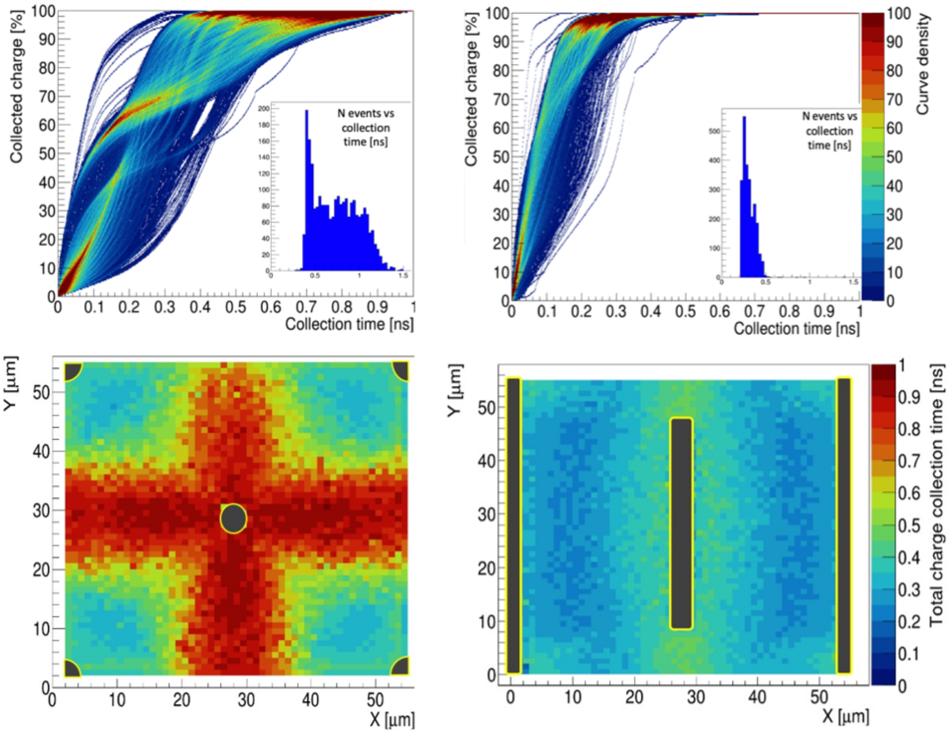

**Fig. 3.4** Simulated timing performance comparison among two different 3D geometries at $V_{\text{bias}} = -100\,\text{V}$: from left to right the five columns and the trench geometry. About 3000 MIP tracks are simulated. (Top) Charge collection time curves and distribution for the two geometries. (Bottom) Spatial distribution of the total charge collection time for the same geometries. [24]

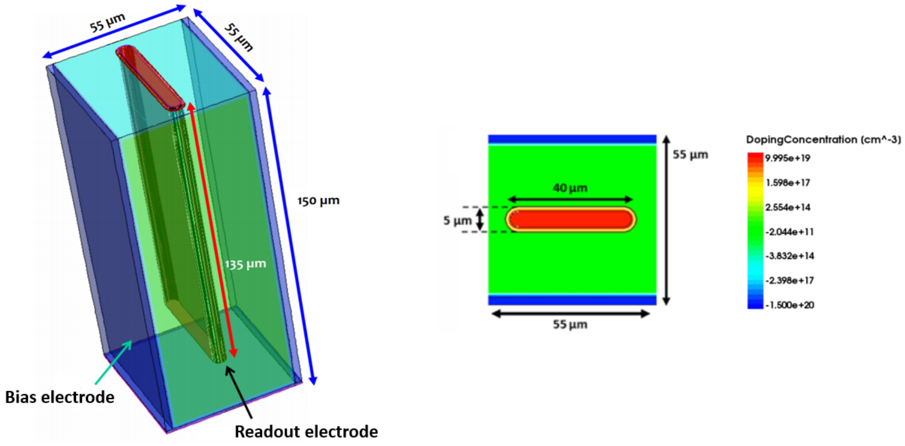

**Fig. 3.5** Geometry of the designed TimeSPOT pixel, showing dimensions and doping profiles (red for $n^{++}$ doping, green for $p^{-}$ doping and blue for $p^{+}$ doping).

FBK, while some tests were carried out in 2013 at IBM-CNM (Barcelona, Spain) [77]. The starting material used is p-type silicon-silicon direct wafer bonded, which consist of a 150 $\mu$m thick, high-resistivity Float Zone active layer bonded to 500 $\mu$m thick low-resistivity silicon support wafer. Figure 3.6 shows the schematic of the structure of the 3D-trench silicon sensor. 3D electrodes were made using the Deep Reactive Ion Etching (DRIE) MEMS technique [78, 79].

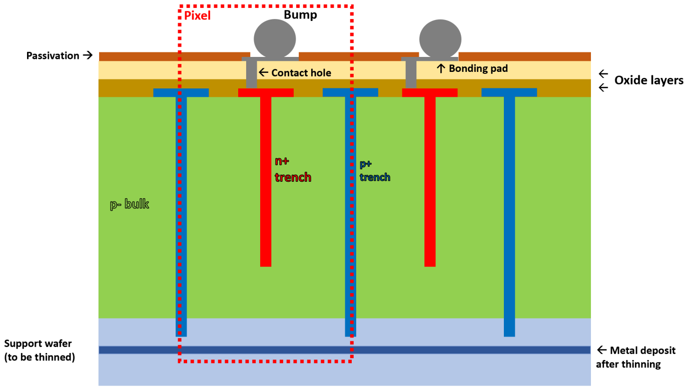

**Fig. 3.6** Schematic cross-section of a 3D sensor.

Several geometries with different trench lengths and widths or with different electrodes grouping and read-out configurations were fabricated. The layout of some of these test devices is shown in Figure 3.7. A picture of one of the TimeSPOT wafers produced and some test structures seen at the microscope are shown in Figure 3.8 and Figure 3.9, respectively, while Figure 3.10 shows the view of a section of one of the 3D-trench structures produced using a Scanning Electron Microscope (SEM).
After the production, the current-voltage (IV) characteristics of matrices test structures were measured, using a temporary metal of the wafer to connect the matrix pixels [79]. From these measurements, considering the number of pixels in the matrix, a leakage current of about 10 pA per pixel is obtained, comparable to the leakage current of a silicon 3D-pixel with columnar electrodes fabricated at FBK [80]. For several test structures characterized, as for example single pixels, double pixels and pixel-strip test structures, the breakdown voltage has been observed in a range between $-150$ V and $-200$ V. Also, capacitance-voltage measurements have been performed on pixel-strip sensors, resulting in a capacitance per pixel of about $110-160$ fF, depending on the trench length [79]. Comparable results were obtained for sensors from the second batch.

This thesis work is focused on the detailed characterization of TimeSPOT sensors, both in laboratory and in test beam campaigns. The results of the performed measurements, including time resolution and geometrical detection efficiency are reported in detail in the following chapters.

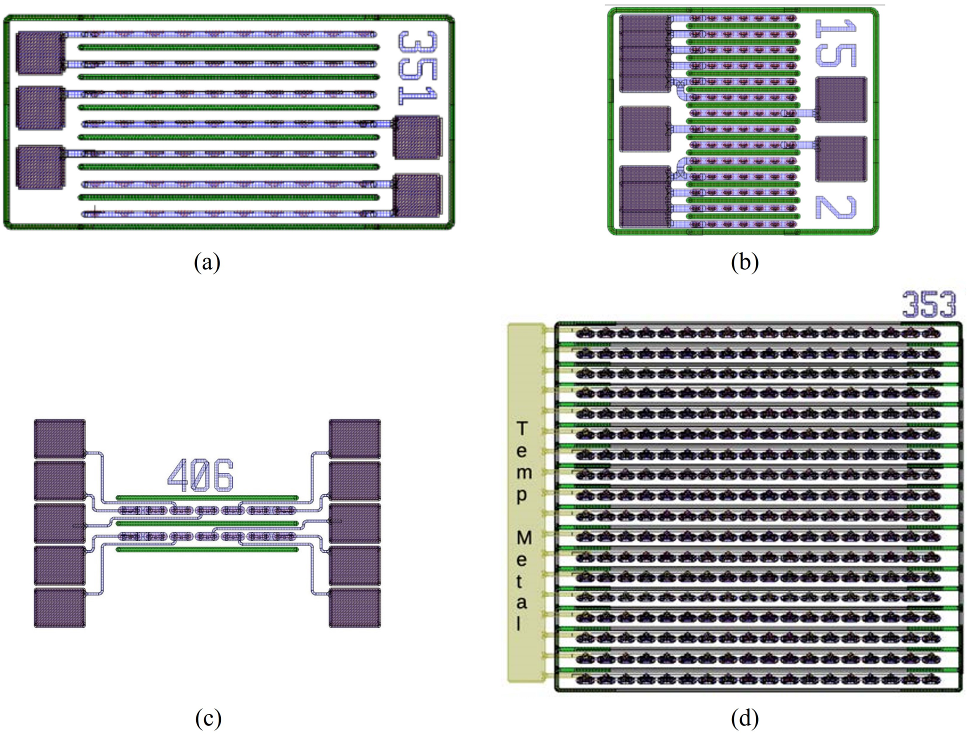

(a) (b) (c) (d)

**Fig. 3.7** Layout of TimeSPOT test structures: pixel-strips, each one consisting of (a) ten $55 \times 55\,\mu\text{m}^2$ pixels or (b) seven $27.5 \times 27.5\,\mu\text{m}^2$ pixels shorted together, (c) single and double pixels and (d) $18 \times 18$ pixels matrix.

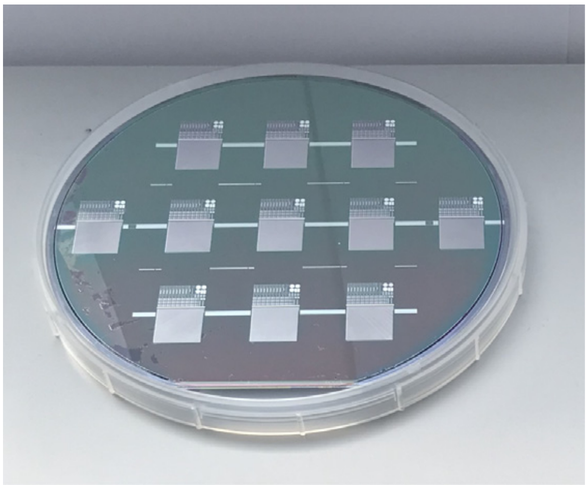

**Fig. 3.8** Picture of a wafer from the first batch of TimeSPOT sensors.

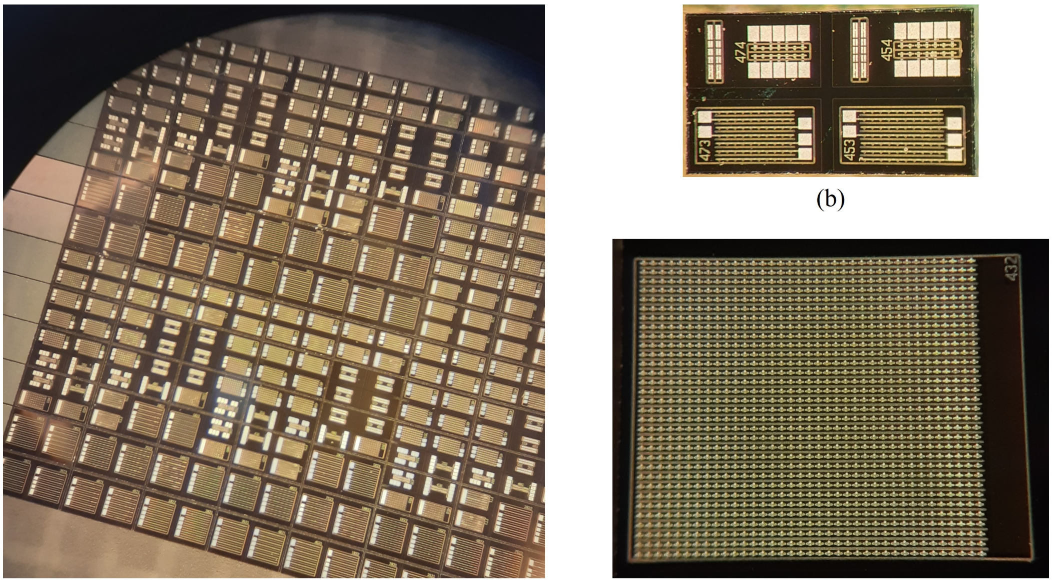

(b)

(a)

(c)

**Fig. 3.9** Picture of TimeSPOT sensors taken with the microscope. (a) A cut of the wafer. (b) Test structure with pixel-strips, single and double pixels. (c) 32 × 32 pixels matrix. This is the matrix to be bump-bonded to the TimeSPOT ASIC.

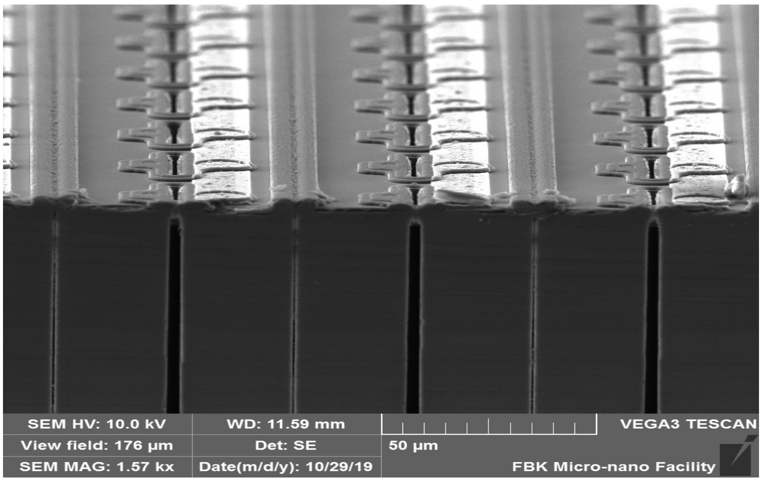

**Fig. 3.10** Scanning Electron Microscope picture of a section of a TimeSPOT test structure from the first batch.

## 3.3 TimeSPOT ASIC development in 28 nm CMOS technology

Within the TimeSPOT project the *Timespot1* ASIC has been designed and produced in order to readout TimeSPOT pixel matrices with characteristics capable to satisfy LHCb Upgrade II requirements for the VELO (Section 1.2.1). Timespot1 is the first ASIC conceived in 28 nm CMOS technology to readout small pixels with single-hit time resolution below 50 ps [81]. As explained in Section 1.2.1, several requirements have to be satisfied at the same time: small pitch, excellent time resolution, high pixel hits rate, high data bandwidth, high radiation hardness and low power consumption. Each pixel of Timespot1 is provided with a charge amplifier, a discriminator and a Time-to-Digital Converter (TDC) for the digitization of the timing information, with a maximum readout rate per pixel of 3 MHz. The power budget per pixel has been kept below 40 $\mu$W to comply with the constraint of a power consumption of about 50 $\mu$W per pixel, given by the power dissipation system employed by the experiments.
The Timespot1 ASIC is specifically designed for the readout of a 32 × 32 TimeSPOT pixels matrix. Its block architecture is shown in Figure 3.11.

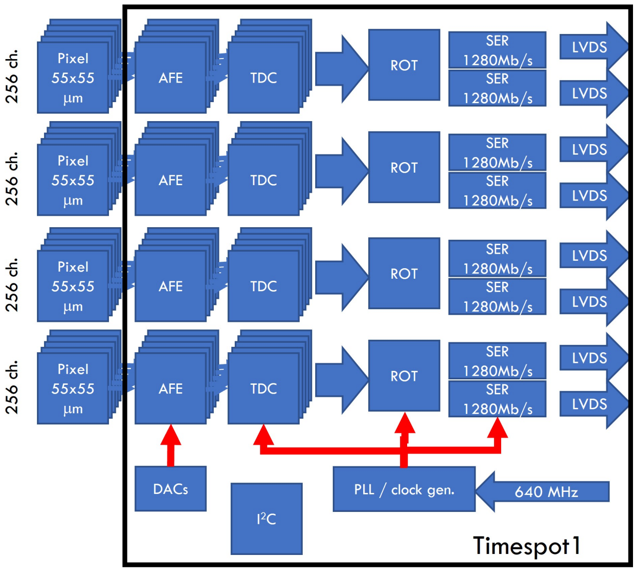

**Fig. 3.11** Block architecture of the Timespot1 ASIC [81]. The 1024 channels are organized in four groups of 256 channels each. For each group, a Read Out Tree sends the data collected to the serializers (SER).

The 1024 channels are organized in four blocks consisting of 256 channels. Each group is connected to one Read Out Tree (ROT) block, that collects data from the active channels, assigns them a global timestamp and sends them to one of the two serializers connected to LVDS drivers. The ASIC configuration is made using an slow-control interface via I$^2$C protocol. The layout and a picture of the Timespot1 ASIC are shown in Figure 3.12. The Analog Front End (AFE) consists a Charge Sensitive Amplifier (CSA) and a leading edge discriminator for each channel. The CSA is connected both to the sensor bonding pad and to its own charge-injection circuit used to generate current pulses for electrical tests. The TDC is based on a Vernier architecture with two identical Digital Controlled Oscillators (DCOs) working at slightly different frequency. It measures the Time of Arrival (ToA) of the output signal of the AFE and the Time Over Threshold (TOT) of the signal in order to correct the time jitter due to the time walk.

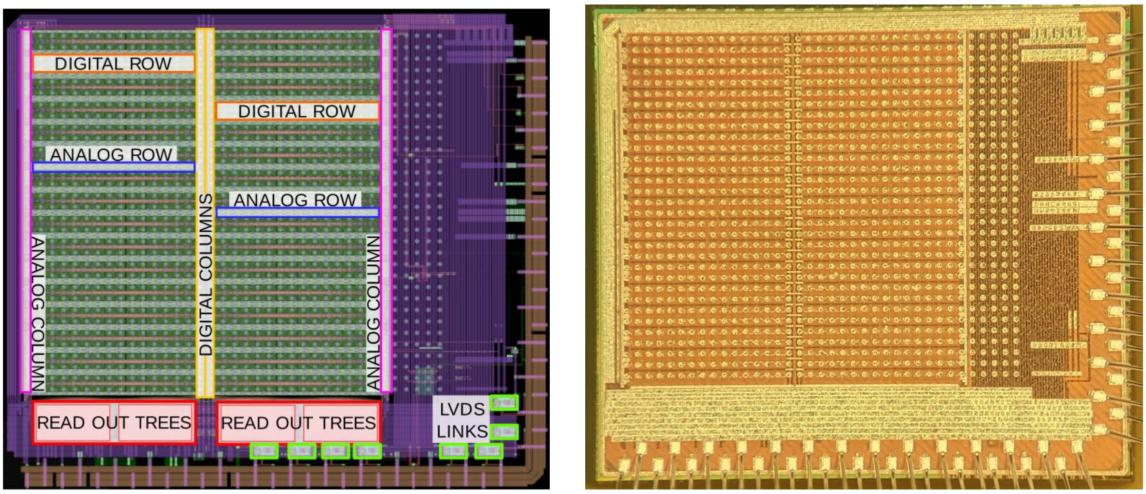

**(a)** **(b)**

**Fig. 3.12** (a) Full chip layout with the main structures highlighted. Its total size is $2.618 \times 2.288\,\text{mm}^2$ [81]. (b) Picture of the Timespot1 silicon die seen at the microscope.

The circuit performance of the Timespot1 ASIC have been tested on a dedicated PCB named TSPOT1 (Figure 3.13). First of all, tests of the ASIC before the bump-bonding of the sensors matrix have been performed, by using internal test pulses on each of the 1024 channels in order to evaluate the uniformity around the matrix. The AFE output, when each channel is pulsed through a charge injection circuit, is a digital pulse that is then measured by the TDC. Repeating several time the measurement for each channel, it is possible to evaluate the convoluted time resolution of the AFE and the TDC. Then, the AFE time resolution is evaluated by subtracting in quadrature the time jitter contribution of the TDC, that can be individually measured. These tests have shown a good uniformity across all the matrix, with a small geometry effect on the right sub-matrix. The measured AFE time resolution for a 2 fC signal is 43 ps with a dispersion across the matrix of about 18 ps, at a power consumption of about 13 $\mu$W per channel. The average TDC time resolution is 22.6 ps with a dispersion of 5.5 ps across the matrix. A design bug in the AFE has been identified and solving it there is the possibility to improve its time resolution.

The ASIC has been hybridized with a TimeSPOT pixel matrix and the tests are ongoing. The ultimate goal is to realize a small-scale tracking demonstrator consisting of 4 or more tracking layers, each one consisting of a Timespot1 ASIC hybridized with both silicon and diamond TimeSPOT 3D sensors.

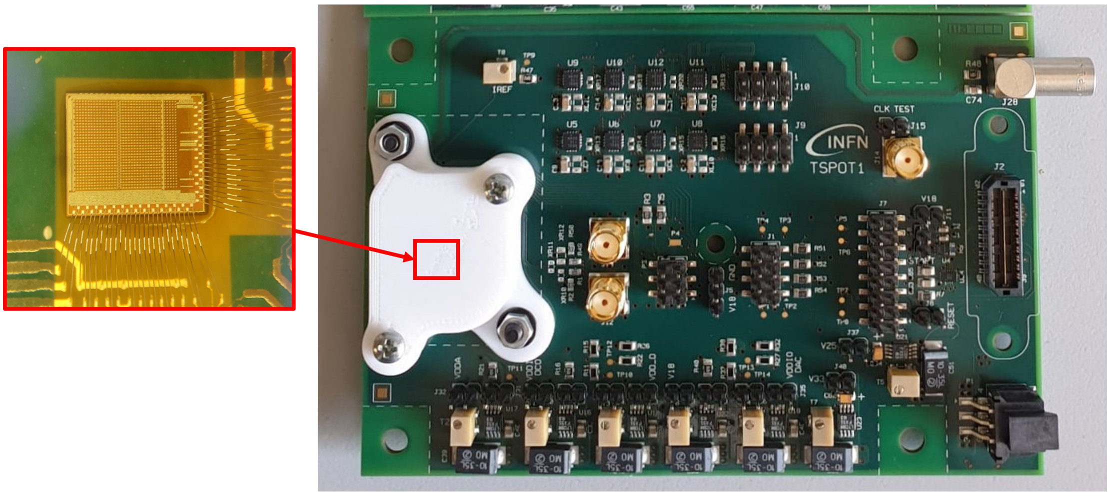

**Fig. 3.13** Picture of the TSPOT1 PCB for the test of the Timespot1 ASIC. The ASIC is wire-bonded to the board in the area protected by the white box and indicated by the red box.

# Chapter 4

# First TimeSPOT test beam

This Chapter is dedicated to the first test beam characterization of TimeSPOT sensors [24] at the Paul Scherrer Institut (PSI) test beam facility. Tests were conducted at the $\pi$M1 beamline with a 270 MeV/c positive particles beam, mainly composed by pions with a small contamination of muons, positrons and protons. The experimental setup, the analysis strategies and results are reported, including the first measurement of the time resolution of a TimeSPOT sensor with minimum ionizing particles.

## 4.1 Test beam setup

The setup used to characterize TimeSPOT sensors at the PSI test beam facility is shown in Figure 4.1. It is composed by one TimeSPOT sensor under study, that is our Device Under Test (DUT), and two Cherenkov detectors, that are used as time reference of our measurements, all mounted inside a light-tight box on the pion beamline. The silicon sensor is attached to the front-end electronic (FEE) board by means of conductive tape, it is wire bonded to the input of the front-end amplifier (Figure 4.5) and biased by supplying a negative voltage to the pad where it is attached. All the detectors were mounted perpendicular to the beam direction and the silicon sensor could be aligned with an accuracy of 1 mm. Signals from the silicon sensor and from the two MCP-PMTs were acquired by means of an 8 GHz analogue bandwidth, 20 GSa/s, 4-channels digital oscilloscope Rhode & Schwartz RTP084. The oscilloscope trigger condition required a signal from the 3D-trench silicon sensor in coincidence with a signal from the downstream MCP-PMT. The recorded waveforms were then analyzed offline. Since the transverse size of the beam was approximately 40 mm × 40 mm FWHM at the focal point where the sensor was located, only a small fraction of the particles crossed both the silicon sensor and the MCP-PMTs, so the beam intensity was adjusted, by means of collimators, to achieve a data acquisition trigger rate of the order of 100 Hz. Also the radio-frequency signal coming from the PSI Ring Cyclotron was acquired and used to further improve the pion beam purity by selecting a proper delay between the MCP-PMTs signals and the phase of the RF. The oscilloscope screenshot with the four signals in persistence mode is shown in Figure 4.2. In this test beam the sensor under test consists of two pixels connected to the same front end channel, referred to as *double pixel*, so it was not possible to measure the pixel geometrical efficiency or the charge sharing between adjacent pixels.

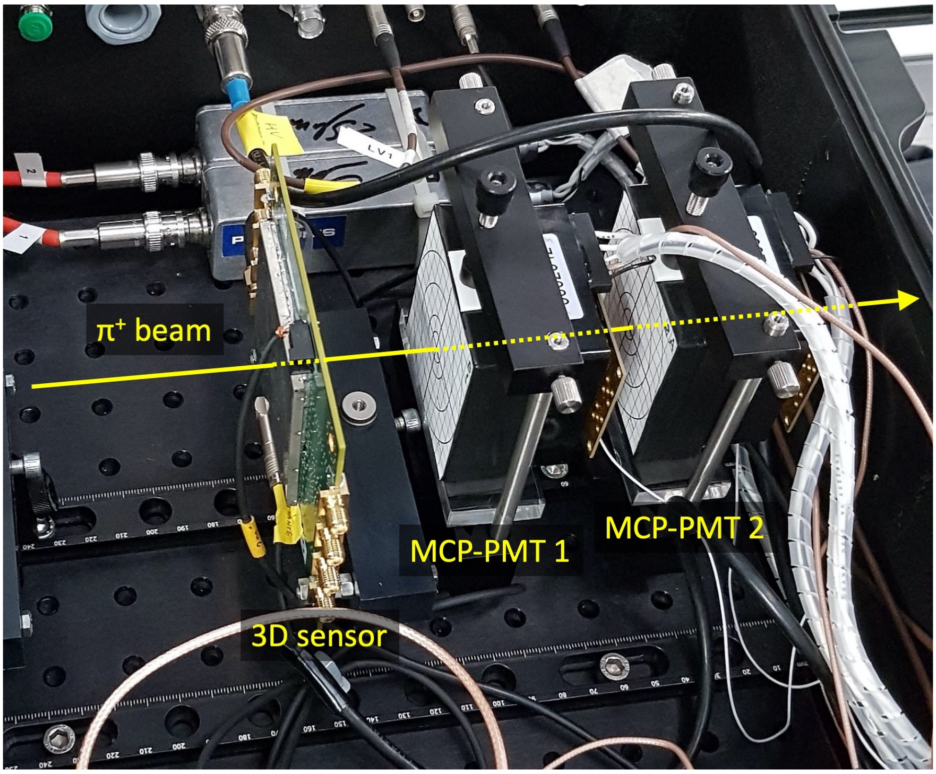

**Fig. 4.1** Setup used during the test beam at PSI. The front-end electronics board in which a 3D-trench silicon sensor is mounted and the two MCP-PMTs used to provide the time reference are visible in the picture.

### 4.1.1 Time reference detector

As mentioned before, the time reference of this setup, named *Time-Tagger*, is composed by two Cherenkov detectors, each one consisting in a 20 mm thick quartz radiator attached by means of an optical silicon to a 53 mm × 53 mm active window Micro-Channel Plate Photo-Multiplier Tube (MCP-PMT) Planacon, model XP85112 and

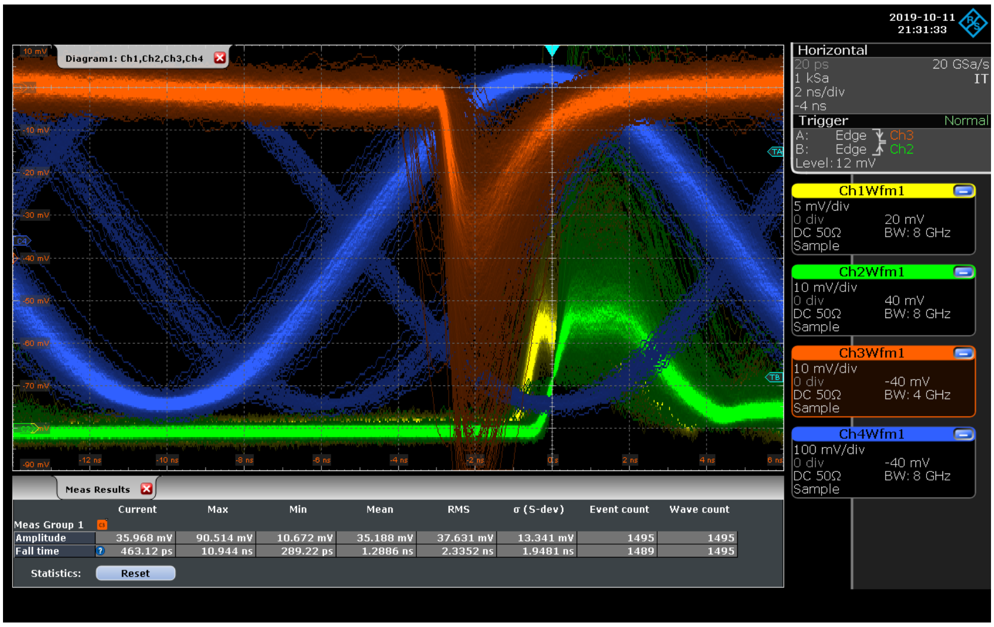

Horizontal
20 ps 20 GSa/s
1 kSa IT
2 ns/div
-4 ns

Trigger Normal
A: Edge Ch3
B: Edge Ch2
Level: 12 mV

Ch1Wfm1
5 mV/div
0 div 20 mV
DC 50Ω BW: 8 GHz
Sample

Ch2Wfm1
10 mV/div
0 div 40 mV
DC 50Ω BW: 8 GHz
Sample

Ch3Wfm1
10 mV/div
0 div -40 mV
DC 50Ω BW: 4 GHz
Sample

Ch4Wfm1
100 mV/div
0 div -40 mV
DC 50Ω BW: 8 GHz
Sample

| | Current | Max | Min | Mean | RMS | σ (S-dev) | Event count | Wave count |
|---|---|---|---|---|---|---|---|---|
| Meas Group 1 | | | | | | | | |
| Amplitude | 35.968 mV | 90.514 mV | 10.672 mV | 35.188 mV | 37.631 mV | 13.341 mV | 1495 | 1495 |
| Fall time | 463.12 ps | 10.944 ns | 289.22 ps | 1.2886 ns | 2.3352 ns | 1.9481 ns | 1489 | 1495 |

Statistics: Reset

**Fig. 4.2** Waveforms acquired with the oscilloscope: the signal from the 3D-trench silicon sensor (orange), the signals from the two MCP-PMTs (yellow and green) and the radio-frequency from the PSI Ring Cyclotron (blue). The three different RF phases correspond to the various components of the beam.

XP85012, referred to as MCP-PMT1 and MCP-PMT2, respectively. The Time-Tagger detector was extensively studied preliminarly in laboratory, both with a red laser and with cosmic rays [82], in an previous configuration with plexiglass radiators (Figure 4.3a) instead of quartz radiators, which were mounted before the test beam to increase the amount of Cherenkov photons produced in the radiators themselves.

For the time resolution performance measurement, the Time-Tagger was tested with cosmic rays. The two detectors were mounted on a light-tight black box, one after the other, and the box was placed vertically, on top of a 5 cm thick block of lead, below which a scintillator coupled to a PhotoMultiplier Tube (PMT) was positioned, in order to make a particle energy selection (Figure 4.4b). Two signals from each MCP-PMT were acquired: the signal coming from all 64 pads of the PMT and the signal coming from the four central pads (Figure 4.3b), while the other pads were grounded. Waveforms were recorded and analyzed offline by fitting the rising edge of each signal in order to measure the time of arrival of each MCP-PMT, $t_1$ and $t_2$, and to extract, from the $\Delta t = t_2 - t_1$ distribution, the time resolution of the system. Selecting the events in which a signal in the four central pads was present, that is the most similar condition to that of a test beam, a time resolution $\sigma_{\Delta t} = 24.4 \pm 0.5\,\mathrm{ps}$ was measured. Therefore, using the average time measured with them, a time resolution of about 12 ps was expected at the test beam.

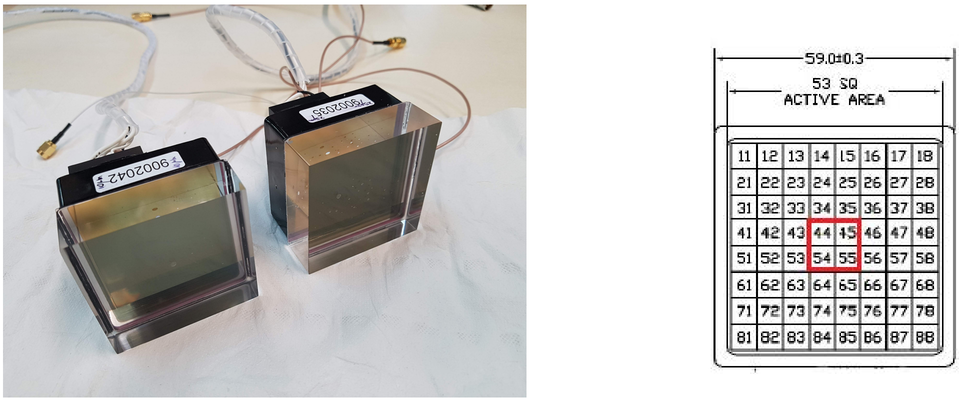

**(a)** **(b)**

**Fig. 4.3** (a) The two MCP-PMTs Planacon XP85112 and XP85012 each one coupled to a 20 mm thick plexiglass radiator. (b) The scheme of the 64 pads of the two detectors with the four central pads readout in our setup in the red box.

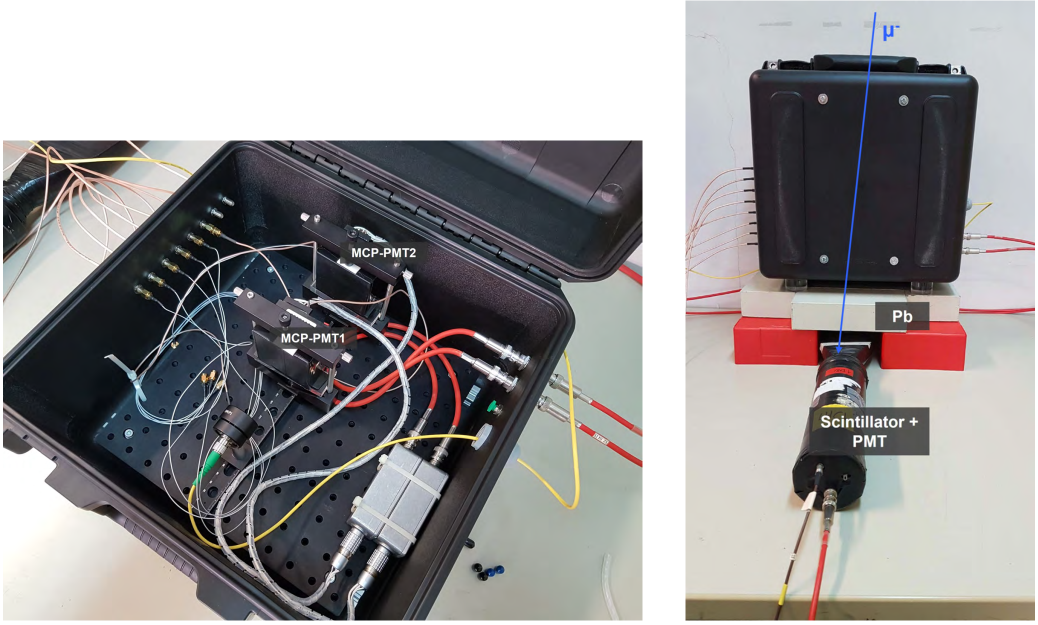

**(a)** **(b)**

**Fig. 4.4** (a) The two MCP-PMTs mounted one after the other on the rail inside the light-tight black box. (b) The box in vertical on top of a 5 cm thick block of lead, below which a scintillator coupled to a PMT was placed to make a particles energy selection.

### 4.1.2 FEE board and test structure

The silicon sensor readout board is based on a two-stage signal amplification scheme acting as an inverting transimpedance amplifier, implemented on a custom-made circuit. The first amplification stage consists of an AC-coupled silicon-germanium bipolar transistor designed for high bandwidth (up to 5 GHz) and low noise applications, featuring a gain of nearly 30 dB at 2 GHz and an integrated output noise of 260 $\mu$V. This design was optimised for sensors with capacitance $\mathcal{O}(10\,\mathrm{pF})$, producing signals with charge $\mathcal{O}(10\,\mathrm{fC})$ and a rise time of about 200 ps. These values of capacitance and charge are rather different from those typical for a TimeSPOT sensor, nevertheless the board performed satisfactorily also on the TimeSPOT sensor signals. Protection from external electromagnetic noise is ensured by metal shields (Figure 4.5). The second amplification stage consists of a current amplifier with 2 GHz bandwidth and provides 20 dB gain factor.
As mentioned before, the 3D trench silicon sensor tested is a *double pixel*, consisting of two pixels connected to the same readout channel, and it is shown on the top right of Figure 4.5a and in Figure 4.5b.

## 4.2 Data analysis

The data analysis of this test beam had the main purpose of measuring, for the first time, the time resolution of a TimeSPOT 3D-trench silicon sensor with Minimum Ionizing Particles (MIPs). To take into account the attenuation of the 10 m low-loss cable used during data acquisition, the cable's transfer function, measured in laboratory, was deconvoluted from the silicon sensor waveforms. Figure 4.6 shows the average shape of the two MCP-PMTs and the silicon sensor waveforms. The typical rise time values (20-80% of the signal) are 370 ps, 490 ps and 200 ps, respectively. For each detector, the signal amplitude $A$ is given by the maximum of the waveform, corrected by the baseline, that is evaluated just before the beginning of the signal (Figure 4.7a). To measure the Time of Arrival (ToA) of the silicon sensor signal, three methods have been implemented:

1. The **Leading Edge (LE)** is the simplest algorithm, consisting on taking the ToA of the signal as the time at which the signal crosses a fixed threshold of $-10$ mV (optimized for these specific silicon sensor signals) and interpolating the waveform in the range ±40 ps around the threshold. This method is affected by *time-walk*

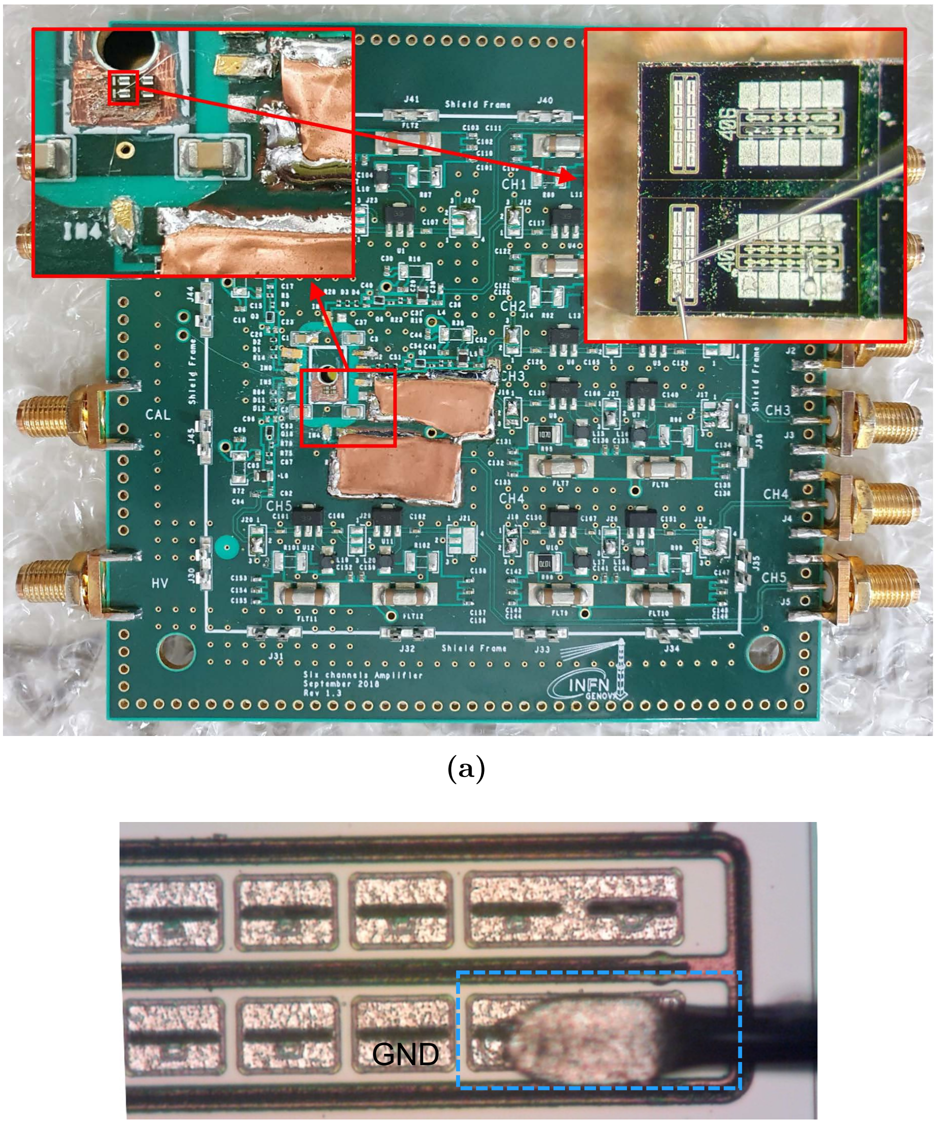

(a)

(b)

**Fig. 4.5** (a) The six-channels front-end electronics board used for the first stage amplification of the silicon sensor signal. The amplifier is located underneath the copper shielding. The 3D-trench silicon sensor characterized at the test beam is shown in the top right picture. (b) A double pixel sensor outlined in the dashed blue box. In the test structure used at the test beam, the side pixel was grounded.

effect, that in this case was not possible to correct with an amplitude-dependent correction of the ToA.

2. The **PSI method** is an implementation of a Constant Fraction Discriminator (CFD), in which the ToA of each waveform is set as the value corresponding to

35% of the signal amplitude and it is calculated from a linear interpolation of the signal in the 20-80% rising edge.

3. The **Reference** method is based on the amplitude and rise time compensated (ARC) algorithm [83, 32] in which the signal is processed by subtracting to it an identical contribution delayed by about half of the signal's rise time and the ToA is set to the time at which the resulting waveform exceeds 50% of its amplitude, determined with a linear fit of the signal rising edge, as illustrated in Figure 4.7b.

The ToA of the two MCP-PMTs was determined by means of the PSI algorithm at a 35% fraction of the signal amplitude.

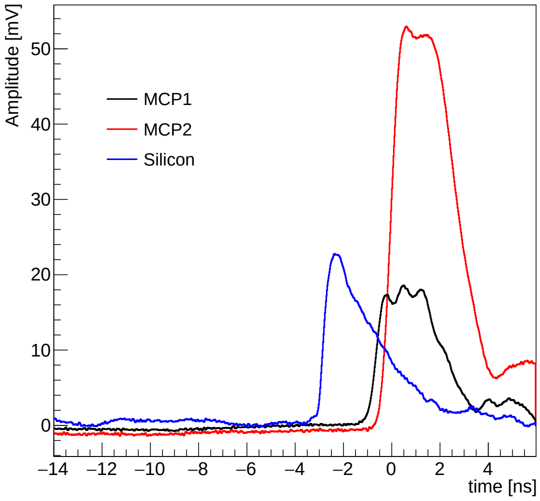

**Fig. 4.6** Average waveforms of the MCP-PMT1 (black), MCP-PMT2 (red) and silicon sensor (blue). In this plot the 3D-trench silicon sensor signal is reversed for convenience. The average is made on fifty signals.

## 4.3 Results

The sensor signal amplitude distribution obtained at a bias voltage $V_{\text{bias}} = -140\,\text{V}$ is shown in Figure 4.8. It follows a Landau distribution convoluted with a Gaussian down to the smallest amplitudes, indicating that, in this case, to have the DUT in the trigger does not bias the amplitude distribution of the sensor signals. Moreover, the most probable value and the width of the Landau are in agreement to what is expected for the energy deposit of a MIP in 150 $\mu$m of silicon [84], providing an important check of the proper operation of the 3D-trench silicon sensor.

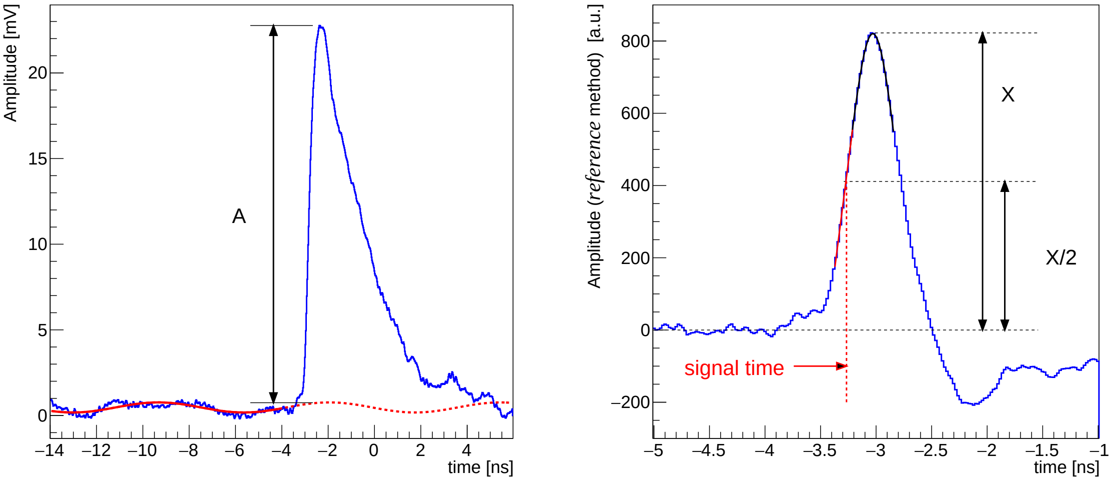

**(a)** **(b)**

**Fig. 4.7** (a) Average 3D-trench silicon sensor waveform and (b) resulting waveform after the Reference method is applied. The Gaussian fit used to determine the signal amplitude in the reference method is shown in black, while the linear fit in the rising edge of the signal is shown in red.

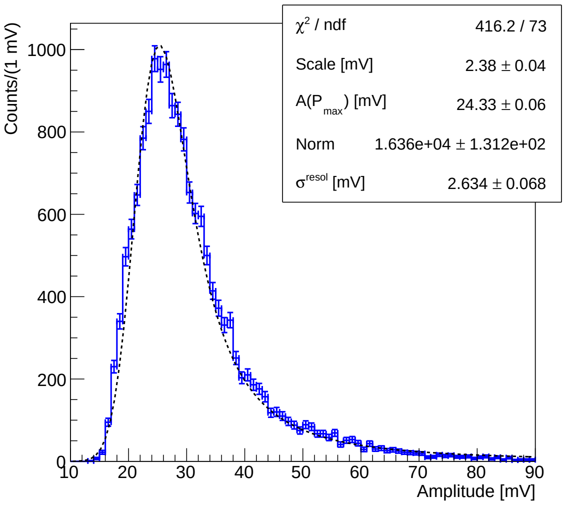

**Fig. 4.8** Distribution of the signal amplitudes for the silicon sensor. The superimposed blue curve is the result of a fit with a Landau distribution convoluted with a Gaussian.

The time resolution of the 3D-trench double pixel was evaluated by measuring the delay of the sensor signal with respect to the pion time of arrival measured using the average time of the two MCP-PMTs signals, $\langle t_{MCP-PMT} \rangle$. The accuracy of the system of the two MCP-PMTs is measured from the distribution of their time difference,

$t_{MCP-PMT1} - t_{MCP-PMT2}$, shown in Figure 4.9a. Fitting this distribution with a Gaussian function, a time uncertainty (sigma) of $24.8 \pm 0.2$ ps is obtained, resulting in a timing accuracy of about 12.4 ps using the average time of the two devices. Figure 4.9b shows the distribution of the time difference between the 3D-trench silicon sensor signal ToA and the average time of the two MCP-PMTs signals, $t_{Si} - \langle t_{MCP-PMT} \rangle$, applying the Reference method to the silicon sensor signals. The distribution has a principal peaking structure with a Gaussian core and a tail of late signals, partially expected from simulation (Section 3.1) and partially due to a feature of the test structure, that will be discussed in Chapter 5. The time distribution is fitted by means of an Exponentially Modified Gaussian (EMG), with the Gaussian and the exponential contributions describing the Gaussian core and the tail of the distribution, respectively.

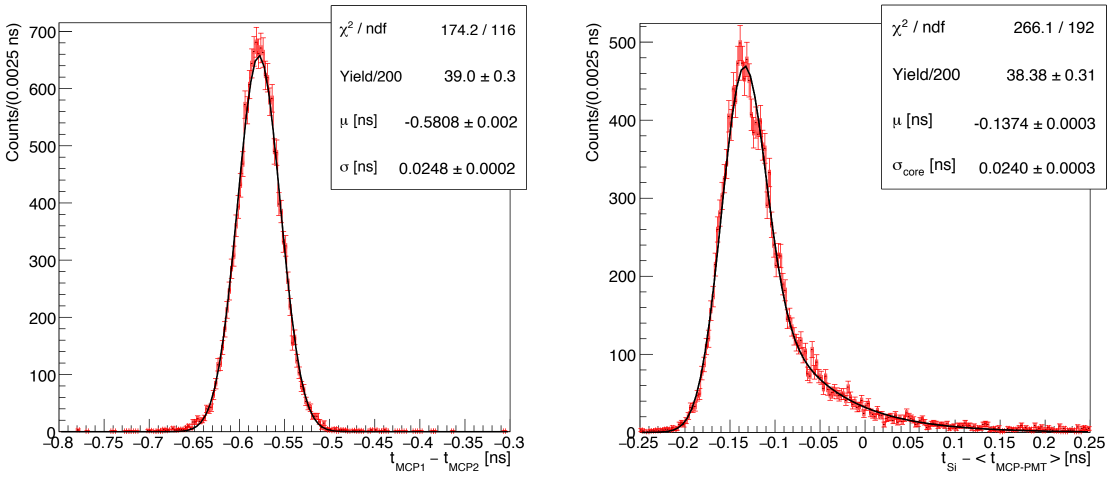

**(a)** **(b)**

**Fig. 4.9** (a) Distribution of the time difference between the two MCP-PMTs with a Gaussian fit overlaid. (b) Distribution of the time difference between the 3D-trench silicon sensor and the average time measured by the two MCP-PMTs with the result of the fit overlaid.

Assuming that the Gaussian core provides a good estimate of the performance of the largest fraction of the sensor active area, the time resolution for the 3D-trench silicon sensor, measured with the most performing Reference method, is $\sigma_t^{Si} = 20.6 \pm 0.4$ ps, after subtracting in quadrature the time reference accuracy. This deconvolution of the time reference jitter is possible if no correlations among the signals are present, therefore laboratory measurements have been performed in order to legitimate this procedure and are reported in Section 4.4.

**Table 4.1** Average signal-to-noise ratio, noise, slew rate (dV/dt) and time resolution of the 3D-trench silicon sensor for different bias voltages and for different analysis methods. The time resolution values reported are obtained after the subtraction in quadrature of the Time-Tagger accuracy.

| | method | | | | | | | | |
|---|---|---|---|---|---|---|---|---|---|
| | *reference* | | | | *PSI* | | | | *leading edge* |
| $V_{\text{bias}}$ [V] | S/N | N [mV] | dV/dt [mV/ps] | $\sigma_{\text{t}}^{\text{Si}}$ [ps] | S/N | N [mV] | dV/dt [mV/ps] | $\sigma_{\text{t}}^{\text{Si}}$ [ps] | $\sigma_{\text{t}}^{\text{Si}}$ [ps] |
| $-20$ | 12.2 | 2.22 | 0.097 | $24.2 \pm 0.5$ | 14.8 | 2.13 | 0.070 | $32.7 \pm 0.7$ | $46.4 \pm 0.5$ |
| $-50$ | 13.0 | 2.24 | 0.114 | $21.9 \pm 0.4$ | 13.1 | 2.38 | 0.086 | $30.3 \pm 0.4$ | $37.6 \pm 0.3$ |
| $-80$ | 13.3 | 2.26 | 0.121 | $22.7 \pm 1.2$ | 12.2 | 2.56 | 0.095 | $30.0 \pm 1.1$ | $34.2 \pm 1.0$ |
| $-110$ | 13.6 | 2.26 | 0.125 | $20.9 \pm 0.4$ | 12.3 | 2.57 | 0.098 | $27.8 \pm 0.4$ | $34.7 \pm 0.3$ |
| $-140$ | 13.9 | 2.25 | 0.128 | $20.6 \pm 0.4$ | 12.6 | 2.56 | 0.100 | $27.1 \pm 0.4$ | $35.3 \pm 0.4$ |

The results obtained at different sensor bias voltages are reported in Table 4.1. In Figure 4.10 the time resolution measured with the three different methods and at different sensor bias voltages are shown. Despite the simplicity of the Leading Edge method, without any correction for the time walk effect, applying it, a very good time resolution of 35 ps is obtained at $-140$ V. Both the PSI and the Reference methods show that a mild dependence of the time resolution on the bias voltage is present. The first method results are about $(20-25)\%$ worse than those of the Reference method, since the latter reduces the time jitter due to signals rise time fluctuations.

A rough estimate of the contribution of the electronic jitter, $\sigma_{ej}$, to the time resolution has been computed from the average sensor signals slew rate and noise, as $\sigma_{ej} \sim N/(dV/dt)$, using the values in Table 4.1, that has resulted to be in a range from 18 ps to 20 ps and this is a clear indication that the electronics noise was a relevant contribution in the measured time resolution, implying that an improvement in the front-end electronics was crucial to fully exploit the sensor timing performance.

### 4.3.1 Time-Tagger characterization at the test beam

The Time-Tagger performances were measured at the test beam also with dedicated runs at lower beam intensity, in order to avoid the saturation of the two MCP-PMTs. An high voltage (HV) scan of each MCP-PMT was performed and the measured signals amplitude as a function of the HV is shown in Figure 4.11. Then, the high voltage of one of the two MCP-PMTs was fixed and a voltage scan of the other MCP-PMT was performed, to measure the time resolution of the Time-Tagger at different high voltages, and viceversa by changing the role of the two detectors. In the two type of

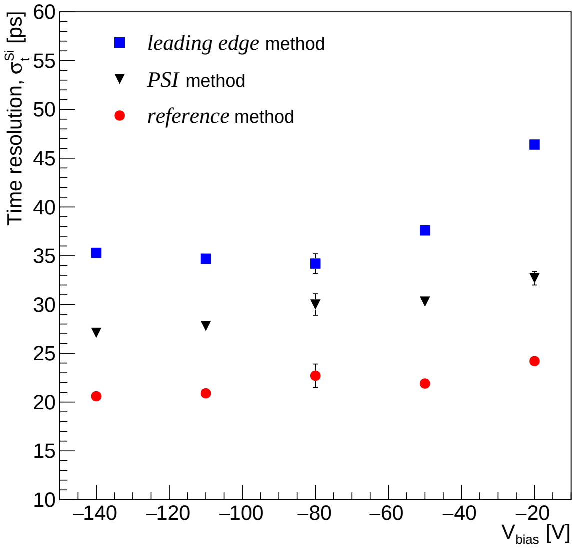

**Fig. 4.10** Time resolution of the TimeSPOT double pixel, $\sigma_t^{Si}$, as a function of the sensor bias voltage for the different analysis methods considered. The contribution due to the time reference accuracy is subtracted.

measurements the MCP-PMT operated at fixed voltage was supplied at the maximum allowed value, which is 2800 V for MCP-PMT1 and 2400 V for MCP-PMT2.

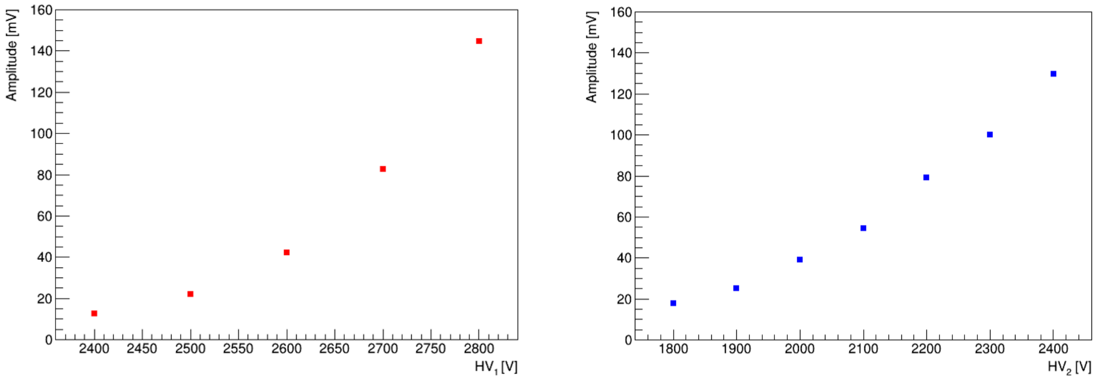

(a) (b)

**Fig. 4.11** Signals amplitude as a function of the high voltage (a) for the MCP-PMT1 and (b) for the MCP-PMT2.

The time resolution measured as a function of the high voltage supplied to the two photomultipliers is shown in Figure 4.12. It is observed a large dependence of the time resolution on the MCP-PMT1 high voltage, while the time resolution measured at different MCP-PMT2 voltages is almost constant except for the lowest voltage. In this conditions the best time resolution measured is $22.1 \pm 0.3\,\text{ps}$, that means a time reference accuracy of about 11 ps when the average time measured by the two PMTs is used as time of arrival of the particle. This value is quite close to the expected time resolution of the 3D-trench silicon sensor with an improved front-end electronics board, a reason why it became necessary to improve also the Time-Tagger detector for further TimeSPOT studies (see Section 5.2.2).

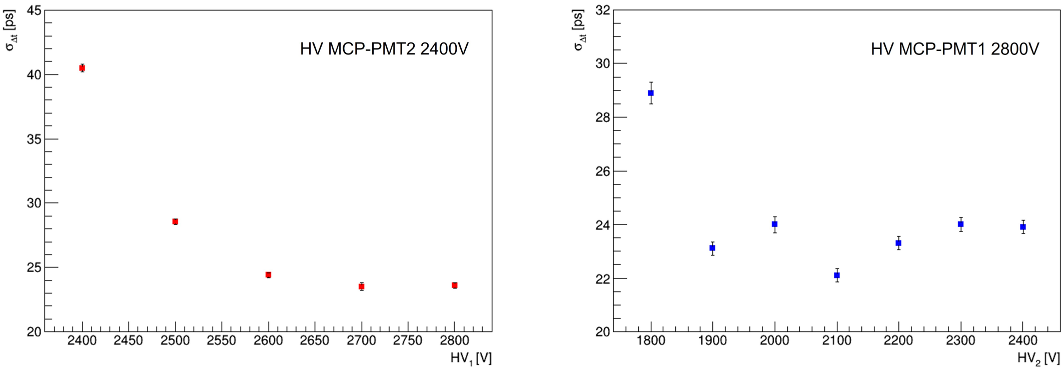

**(a)** **(b)**

**Fig. 4.12** (a) Time resolution of the Time-Tagger as a function of the MCP-PMT1 high voltage, with the MCP-PMT2 supplied voltage fixed at 2400 V and (b) viceversa, with the MCP-PMT1 high voltage fixed at 2800 V.

## 4.4 Cross-talk measurements

In this section the measurements made to verify the presence of correlation between the two Planacon MCP-PMTs (referred to also as MCP1 and MCP2) and between them and the silicon sensor are described. These measurements have been performed in order to demonstrate that the subtraction in quadrature of the Time-Tagger jitter contribution, applied to extract the time resolution of the TimeSPOT sensor under test (Section 4.3), is legitimate.

To perform these measurements the MCP-PMTs have been illuminated with a PicoQuant LDH-P-C-650 [85] red laser with a wavelength of $(655 \pm 10)\,\text{nm}$. The laser intensity is controlled by means of a driver PDL 200-B, that was used in external trigger mode in order to reduce the repetition frequency at 100 Hz, by means of a pulse generator. The laser and the driver are shown in Figure 4.13a. Figure 4.13b shows the setup inside the light-tight black box.

The optical fiber is coupled to an holder for Neutral Density (ND) filters, used to properly attenuate the light that reaches the detector. A filter is placed between the

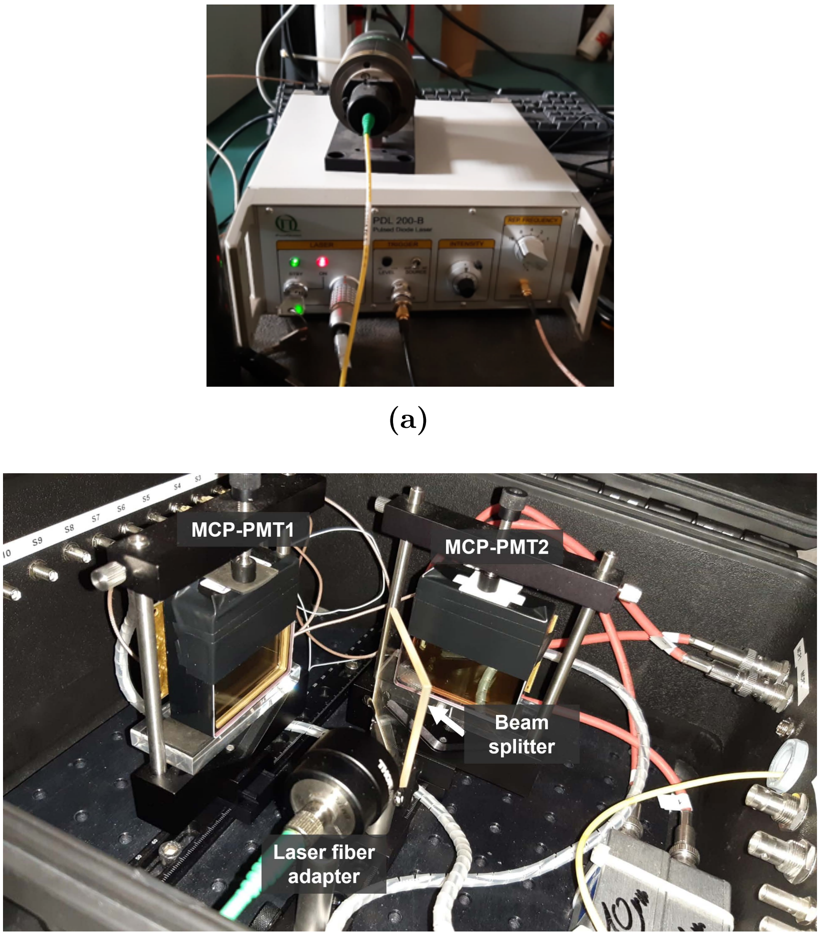

**(a)**

**(b)**

**Fig. 4.13** (a) PicoQuant red laser LDH-P-C-650 with a wavelength of $(655 \pm 10)$ nm and its driver PDL 200-B. (b) Setup used to illuminate MCP-PMT1 and MCP-PMT2 at the same time with the laser using a filter to split the beam.

two MCP-PMTs to split the light beam and illuminate at the same time the two devices, that are mutually perpendicular mounted. The intensity of the laser was chosen on the basis of measurements performed on this laser, at different intensities, using a streak camera [82], while the ND filters have been chosen in such a way that the MCP-PMTs signals amplitude was about the same measured at the test beam. Attempts were made to reproduce test beam conditions as much as possible (same 10 m-long cables and signal attenuators used at the test beam, for example). The waveforms of the laser reference and the two MCP-PMTs are acquired by means of a 4 GHz analogue bandwidth, 20 GSa/s, 4-channels digital oscilloscope Rhode & Schwartz RTO1044 (Figure 4.14) and analyzed offline applying the PSI algorithm at 50% and 35% of the amplitude to the laser signal and the MCP-PMTs signals, respectively.

By illuminating the two photodetectors at the same time, the time resolution of each MCP-PMT with respect to the laser reference, $t_{MCP1} - t_{laser}$ and $t_{MCP2} - t_{laser}$, and the time resolution of one MCP-PMT relative to the other one, $t_{MCP2} - t_{MCP1}$, can be measured. In general, the time resolution $\sigma_{12}$ of a system of two detectors, each one with a time resolution $\sigma_1$ and $\sigma_2$, is given by

$$\sigma_{12} = \sqrt{\sigma_1^2 + \sigma_2^2 + 2\rho_{12}\sigma_1\sigma_2} \tag{4.1}$$

where $\rho_{12}$ is the correlation factor between $\sigma_1$ and $\sigma_2$. Therefore, if no correlations are present, $\rho_{12}$ is close to zero, then the measured $\sigma_{12}$ extracted from the $t_{MCP2} - t_{MCP1}$ distribution is equal to $\sigma_{12} = \sqrt{\sigma_1^2 + \sigma_2^2}$.

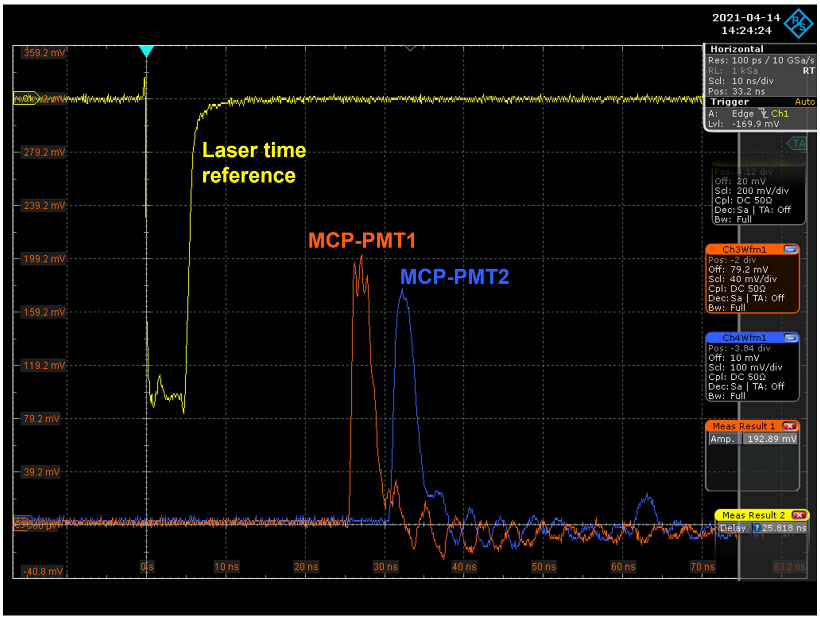

Horizontal
Res: 100 ps / 10 GSa/s
RL: 1 kSa RT
Scl: 10 ns/div
Pos: 33.2 ns
Trigger Auto
A: Edge Ch1
Lvl: -169.9 mV

Pos: 4.12 div
Off: 20 mV
Scl: 200 mV/div
Cpl: DC 50Ω
Dec: Sa | TA: Off
Bw: Full

Ch3Wfm1
Pos: -2 div
Off: 79.2 mV
Scl: 40 mV/div
Cpl: DC 50Ω
Dec: Sa | TA: Off
Bw: Full

Ch4Wfm1
Pos: -3.84 div
Off: 10 mV
Scl: 100 mV/div
Cpl: DC 50Ω
Dec: Sa | TA: Off
Bw: Full

Meas Result 1
Amp. 192.89 mV

Meas Result 2
Delay 25.818 ns

**Fig. 4.14** Laser reference (in yellow), MCP-PMT1 (in orange) and MCP-PMT2 (in blue) signals seen at the oscilloscope.

In Figure 4.15 the three time distributions mentioned before are shown. Considering the standard deviation of the histograms as time resolution, it results that the sum in quadrature of $\sigma_1$ and $\sigma_2$ is equal to 17.9 ps, while $\sigma_{12}$ measured is equal to 17.7 ps. Therefore it follows that the correlation factor is $\rho_{12} = -0.026$, so this measurement demonstrates that the correlation factor between the two MCP-PMTs is negligible. This can be seen also from the distribution of the average time of the two MCP-PMTs (Figure 4.16), whose standard deviation is 9.2 ps, equal to half of $\sigma_{12}$ within 0.4 ps, in agreement with what expected for non-correlated variables.

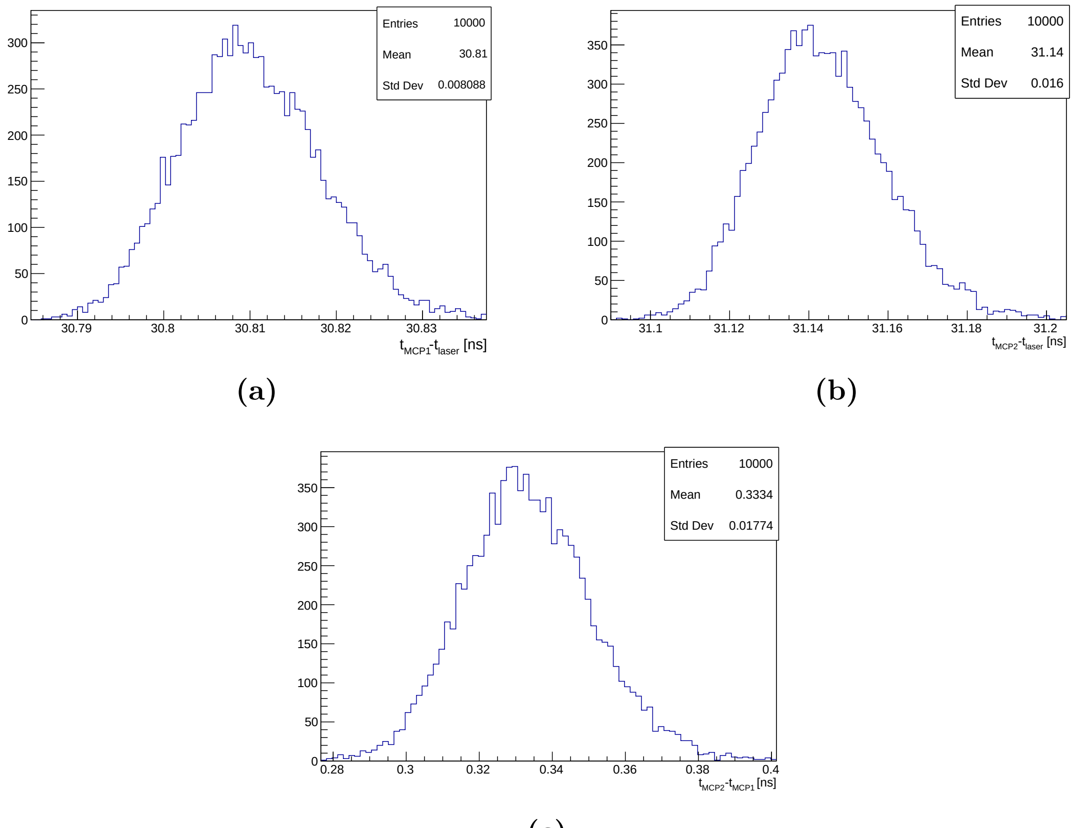

**(a)** **(b)**

**(c)**

**Fig. 4.15** Time distribution of (a) MCP1 with respect to the laser, $t_{MCP1} - t_{laser}$, (b) MCP2 with respect to the laser, $t_{MCP2} - t_{laser}$ and (c) MCP2 relative to MCP1, $t_{MCP2} - t_{MCP1}$.

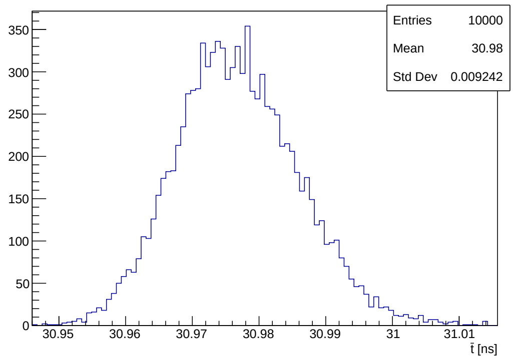

**Fig. 4.16** Time distribution of the average time measured by the two MCP-PMTs, $\bar{t} = (t_1 + t_2)/2$.

Secondly, the cross-talk induced on the silicon sensor FEE board by the two MCP-PMTs was studied. In fact, this induction could introduce a correlation of the silicon sensor with the photomultipliers and if it happens, it is not mathematically correct to subtract in quadrature the time reference accuracy, since the correlation term is not negligible. Therefore, the same FEE board with the silicon sensor used at the test beam has been added to the setup of Figure 4.13 and both the low voltage of the board and the bias of the sensor have been powered on. A small induced signal of about $(1-2)\,\mathrm{mV}$ maximum amplitude was observed on the board (Figure 4.17a), but, most importantly, it was delayed of about 4 ns with respect to the position of a real signal coming from the sensor when illuminated by the red laser (Figure 4.17b), so it does not affect the sensor signals.

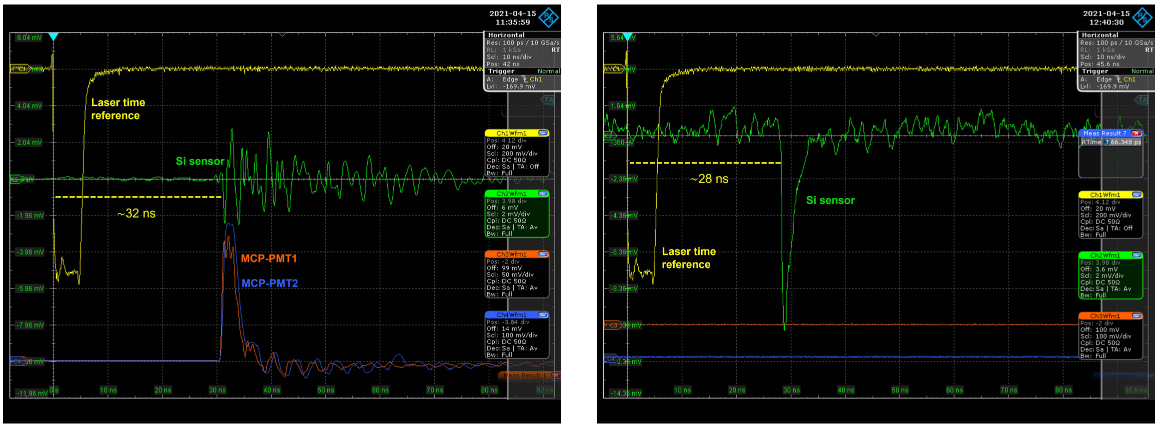

**(a)** **(b)**

**Fig. 4.17** (a) Laser reference (yellow), MCP-PMT1 (orange), MCP-PMT2 (blue) signals and signal from the silicon sensor FEE board (green) when the two MCP-PMTs are illuminated. (b) Laser reference signal (yellow) and signal of the silicon sensor (green) when it is stimulated by the red laser.

## 4.5 Summary and outlook

In this chapter, the first TimeSPOT test beam, conducted at the PSI in 2019, and the results obtained have been presented. In particular the time resolution of a double pixel sensor has been measured by using three different software algorithms to determine the time of arrival of each signal event by event. A time resolution of about 20 ps was achieved with a constant-fraction based algorithm and it was also shown that this time resolution includes an important electronic jitter contribution, indicating the need of an improved front-end electronics to fully exploit the sensor performances. Moreover, laboratory measurements performed on the two MCP-PMTs used as time reference at the test beam have been described: (i) the preliminary characterization of the system by using cosmic rays and (ii) the measurements aimed to study the correlations between the two devices and with the silicon sensor.

After this test beam it was clear that some improvements of the setup were possible and necessary. First of all, it would have been better to characterize a single pixel, since the double pixel test structure presented also a *side region* where the electric field is lower, impacting the time resolution performance, which deviates from the one expected from a real pixel structure. Then, the development of an improved front-end circuit optimized for TimeSPOT sensors would have allowed to better exploit the sensor timing performance. Finally, the Time-Tagger used had a time resolution comparable to the expected TimeSPOT sensor resolution, then an improvement also on the time reference detector was needed. All these aspects have been addressed and the details will be found in the next chapter.

# Chapter 5

# Detailed simulation and setup improvements

This Chapter is dedicated to the detailed study of the first TimeSPOT test beam results described in Chapter 4 and to the description of the improvements made on the setup on the basis of the test beam measurements. A detailed simulation has been developed to fully simulate the device physics response and better understand test beam results, using the combination of several software tools (TCAD, Geant4, TCoDe and TFBoost). The test beam measurements and the estimation of the intrinsic time resolution of TimeSPOT sensors have revealed the need of a new front-end electronics board and a better time reference detector, that will be discussed in this chapter.

## 5.1 Detailed TimeSPOT sensors simulation

In this Section, the detailed simulation of the double-pixel sensor tested at the PSI test beam is illustrated [86]. Firstly, a summary of the simulation procedure, that can be applied also to different sensors with different front-end electronics, is provided. Then, after a comparison between simulation and data, some important results coming from the simulation are shown.

### 5.1.1 Double pixel test structure modelling

The test structure characterized at the first TimeSPOT test beam (Figure 4.5b) has been simulated in order to study in more depth the test beam results and to develop a detailed simulation tool. The layout of the sensor, designed using the Synopsys Sentaurus TCAD simulation package [73], is shown in Figure 5.1. It consists of two standard TimeSPOT pixels ($55 \times 55\,\mu m^2$ each) connected to the same readout electrode, referred to as double pixel and a third adjacent pixel, connected to ground to properly define the boundary conditions of the double pixel in terms of electric and weighting fields. On the opposite side of this third pixel there is an additional active region, referred to as *side region* in the following, that is critical for the timing performance of this particular test structure, while it is not present in a conventional TimeSPOT pixel.

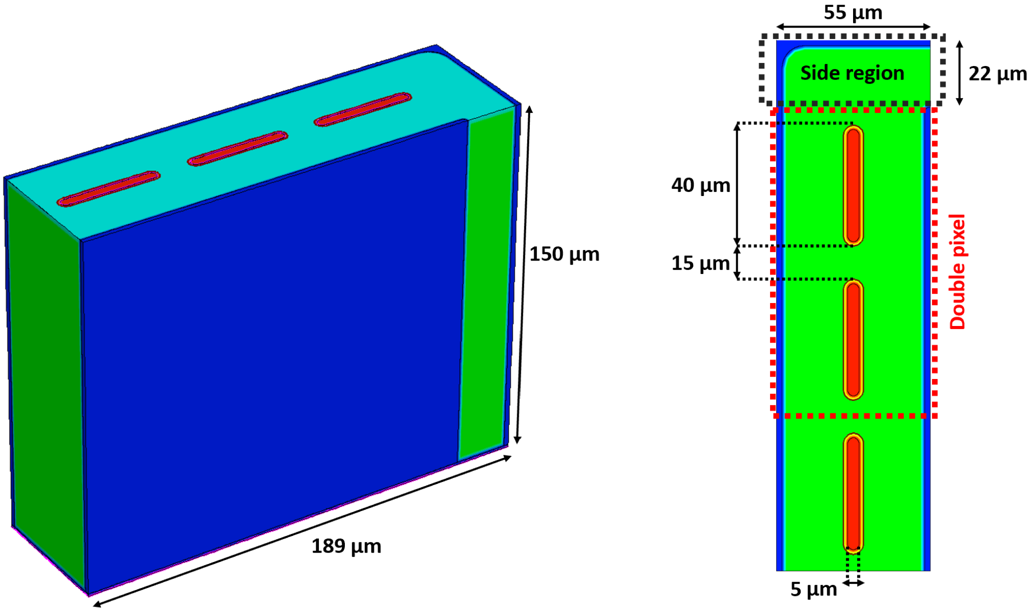

**Fig. 5.1** TimeSPOT double-pixel layout, including sections and sizes, designed using the Synopsys Sentaurus TCAD simulation package.

Figure 5.2a shows the electric field maps at the bias voltages of $-50\,V$, $-100\,V$ and $-150\,V$, while Figure 5.2b shows the weighting field map. The simulated sensor presents an uniform electric field between the ohmic and readout electrodes, that is smaller in the inter-pixel regions between two neighbouring readout electrodes and in the side region. The side region is the main critical region for the timing performances of this particular test structure, because of the lower and less uniform electric and weighting fields that cause larger charge collection times and a more diversified current signals depending on the position, also due to the difference in the charge carriers drift velocities.

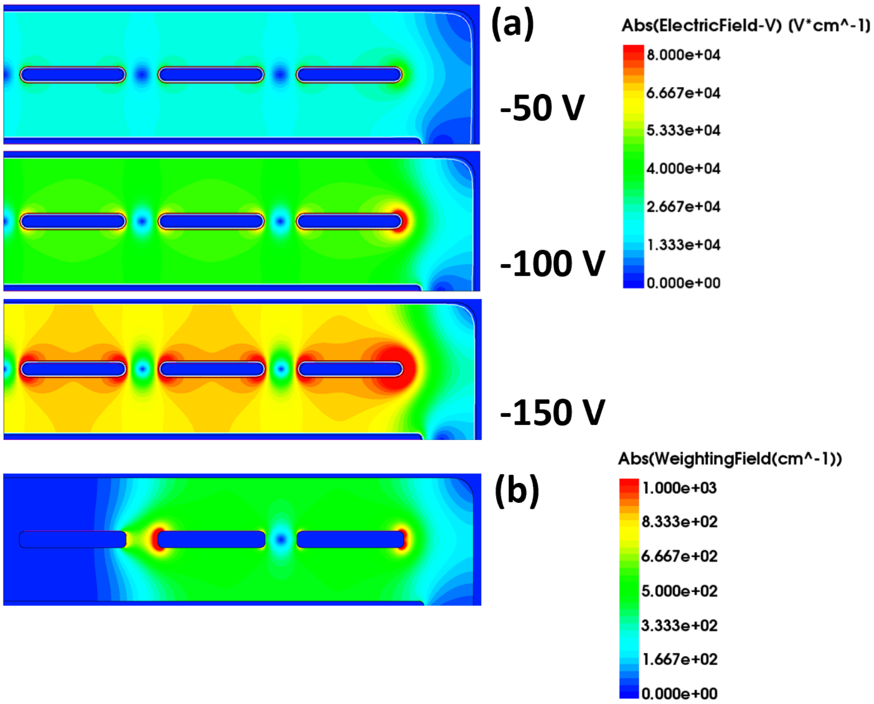

**Fig. 5.2** (a) Electric field map at different bias voltages and (b) weighting field map for the double-pixel test structure.

### 5.1.2 Energy deposit simulation

The studies described in this chapter are based on precise simulations of the energy deposit in silicon from both high-energy ionising particles and laser beams, since also an ultra-fast infrared (IR) laser and a red laser are used in the characterization of TimeSPOT sensors.

To model the energy deposit in the sensor due to an ionising particle, the `Geant4` [87] Monte Carlo simulator is used. A sequence of positive pions with momentum 270 MeV/c (equal to the pion momentum at PSI test beam) hitting the detector surface with an uniform spatial distribution and with an angular distribution in agreement with the characteristics of the PSI $\pi$M1 beam line is generated. The energy deposits, the trajectories of the incoming pion and all the secondary particles produced in the pion interaction with the silicon are saved and then used by the TCoDe simulation package [74] to compute the charge carrier deposits and the currents induced on the readout electrodes due to the drift of the charge carriers. Concerning the laser beam simulation, the energy deposition is simulated with a specific tool developed within the TCoDe package. The algorithm takes into account the Gaussian shape of the laser beam, the wavelength, the light absorption in the material and the position of the focus. For each photon of the laser beam, electron-hole pairs are generated along the laser direction at a depth that follows an exponential distribution, to account for the light absorption in silicon. Figure 5.3 shows the different projections of the charge carrier distributions generated by different laser sources.

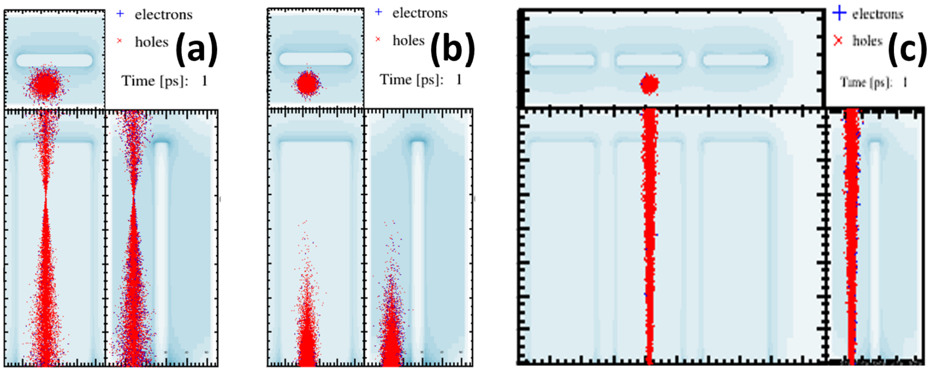

**Fig. 5.3** Examples of simulated energy deposit shapes from laser inside the TimeSPOT test structure, illuminated from the top surface. (a) Deposit with focus inside the active bulk. (b) Deposit shape due to high absorption (655 nm wavelength). (c) Deposit of IR laser source (1030 nm wavelength).

The TCoDe simulator receives in input the TCAD-generated physics maps, containing spatial information of the charge carrier mobility, the electric and weighting field of the interested device, and the energy deposits in the sensor material obtained from `Geant4` or the laser simulation. The output consists of the induced current signals for the electron and hole contributions as well as for primary and secondary particles.

### 5.1.3 Front-end electronics response simulation

In order to perform a quantitative comparison with measurements, the TCoDe output, consisting of the induced current signals, needs to be convoluted with the front-end electronics response. To do this, an open-source application, named TFBoost (TIMESPOT Front-End Booster) [88], has been developed and used. In our specific case, TFBoost computes the convolution of the TCoDe output signals with the response function of the FEE board used at the test beam, adds the noise to the signal (using an analytical model or noise samples provided by the user) and, finally, it applies a digitization to the output signal simulating the 8 bit ADC of the oscilloscope used at the test beam. As done for the PSI test beam data acquisition, only simulated signals with an amplitude larger than 15 mV are recorded for the analysis. An example of the result of the front-end simulation for a single input current is shown in Figure 5.4.

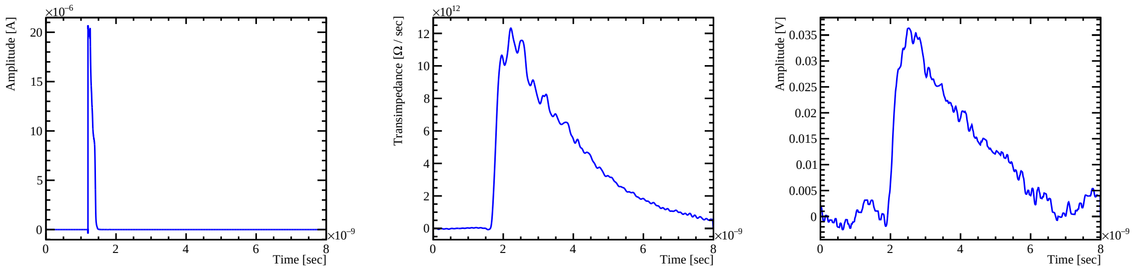

**Fig. 5.4** Example of the result of the front-end simulation for a single input current from the double pixel test structure, at $V_{bias} = -150\,\text{V}$. (Left) input current for a MIP deposition in the sensor, (center) simulated transimpedance and (right) output waveform with real noise.

Two methods for the determination of the front-end transfer function have been developed: a semi-empirical and an analytical method. Only the first method is described here. This is, indeed, the main method since the transfer function acting on the transient signals generated in the sensor is characterized not only by the front-end electronics itself but also by the sensor capacitance and the impedance of the sensor-electronics connection (e.g. wire-bonding). In order to accomplish this, the double-pixel sensor characterized at the PSI test beam, connected to the same FEE board, is illuminated using a 200 fs width, 1030 nm wavelength laser with a minimum spot size of 1.8 $\mu$m FWHM (Section 6.2). The laser intensity is adjusted to obtain an energy deposition in the sensor corresponding to 1 MIP. The output signals are obtained by averaging 3000 single waveforms to suppress the noise and reach a signal-to-noise ratio (SNR) of about 54 dB.

The laser irradiation is repeated in different positions within the active area of the sensor (Figure 5.5a) and at different bias voltages. The FEE board output signals are then deconvoluted with TFBoost using the simulated currents obtained from TCoDe at the corresponding laser positions and bias voltages. Figure 5.5b shows the transfer functions obtained at different laser irradiation positions at $V_{\text{bias}} = -150\,\text{V}$, that ideally depend only on the electronics response, and they are in a very good agreement, especially in the rising edge.

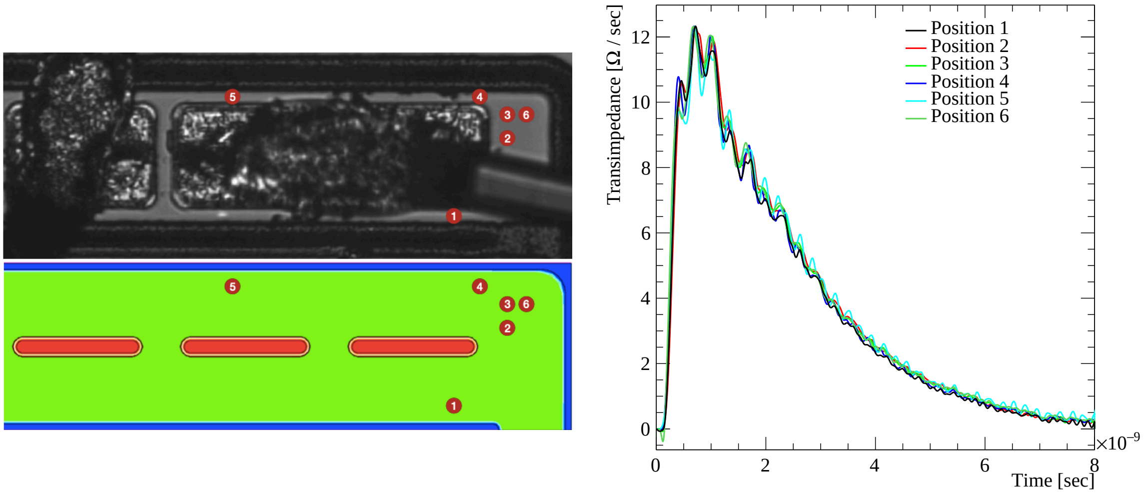

**(a)** **(b)**

**Fig. 5.5** (a) Illustration of the six irradiation positions within the active area of the actual double pixel test structure (top) and the corresponding positions in the simulated structure (bottom). (b) Comparison of semi-empirical transfer functions obtained in different irradiation positions with the laser setup, for the $V_{bias} = -150\,\mathrm{V}$ sample.

### 5.1.4 Comparison with test beam measurements

The simulated waveforms of the 3D-trench test structure are analysed using the same procedure applied to data and described in Chapter 4. The use of a semi-empirical transimpedance allows to reproduce with very good accuracy the different structures of the real average waveform observed at the test beam, as illustrated by Figure 5.6. The good agreement between data and simulation is also visible by comparing the single waveforms in terms of amplitude, rise time and noise fluctuations. A qualitative comparison is shown in Figure 5.7, while, quantitatively, the agreement between data and simulation is within 5% looking at the main quantities representing the signal properties reported in Table 5.1. Figure 5.8 shows the sensor amplitude distribution for data at $V_{\mathrm{bias}} = -140\,\mathrm{V}$ and simulation at $V_{\mathrm{bias}} = -150\,\mathrm{V}$. The simulation reproduces the data distribution characterized by a Landau probability density function shaped by the trigger acceptance function at low amplitudes. Residual differences between data and simulation are present, but they do not affect the results that are discussed in the following.

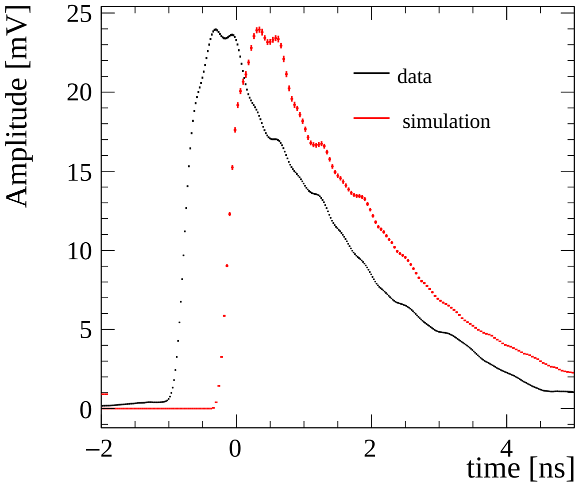

**Fig. 5.6** Silicon sensor average waveform from (black) data and (red) simulation. An arbitrary time shift between the two signals is applied to allow a qualitative comparison.

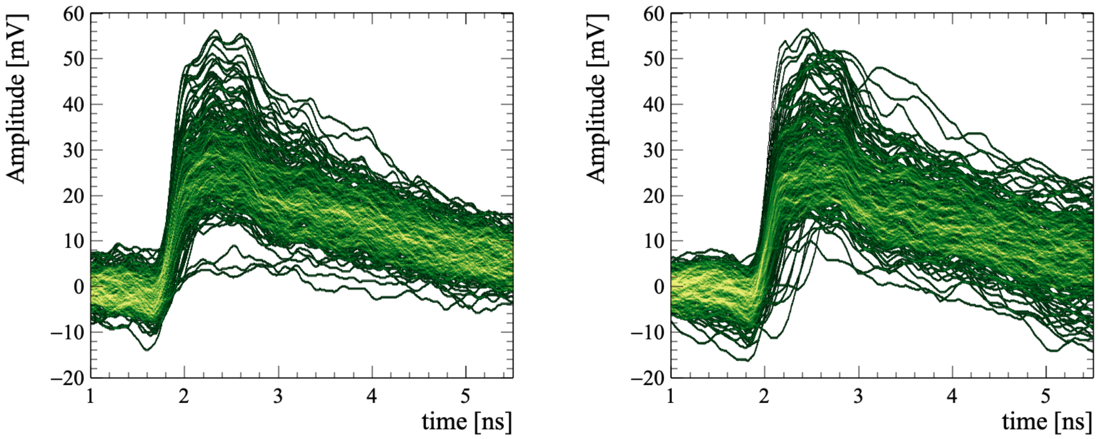

**(a)** **(b)**

**Fig. 5.7** Overlap of 200 silicon sensor waveforms for (a) simulation and (b) test beam data.

**Table 5.1** Maximum amplitude, average signal-to-noise ratio, noise and rise time (20-80)% of the 3D-trench silicon sensor response at different values of bias voltage for simulation and data. The statistical uncertainties are below 1%.

| | $V_{\text{bias}}$ [V] | Amp($\text{P}_{\text{max}}$) [mV] | $\langle$S/N$\rangle$ | $\langle$N$\rangle$ [mV] | rise time [ps] |
|---|---|---|---|---|---|
| Simulation | −50 | 25.0 | 14.6 | 2.11 | 247 |
| | −100 | 24.5 | 14.3 | 2.17 | 224 |
| | −150 | 24.4 | 14.2 | 2.19 | 217 |
| Data | −50 | 24.1 | 14.3 | 2.19 | 258 |
| | −110 | 24.4 | 13.9 | 2.30 | 221 |
| | −140 | 24.7 | 14.2 | 2.29 | 217 |

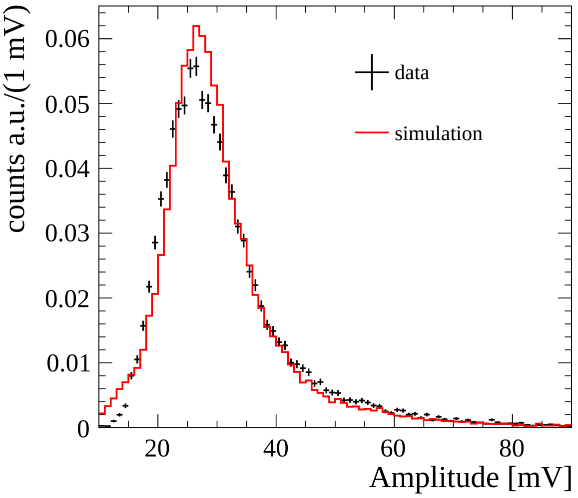

**Fig. 5.8** Distribution of the silicon sensor amplitudes in data at $V_{\text{bias}} = -140\,\text{V}$ and simulation at $V_{\text{bias}} = -150\,\text{V}$.

For the TimeSPOT sensor time resolution measurements, a time reference composed by two MCP-PMTs was used at the test beam, with a measured accuracy of 12.4 ps (Section 4.3) using the average time of the two photomultipliers. The ToA of the silicon sensor is determined by means of the Reference method (Section 4.2). Figure 5.9 shows the distribution of the time difference between the silicon sensor signal and the average time of the two MCP-PMTs, $t_{\text{Si}} - \langle t_{\text{MCP-PMT}} \rangle$, for data and simulation at two different values of $V_{\text{bias}}$. In the simulation the uncertainty in the time reference is accounted by adding to the ToA of the silicon sensor a random value generated according to the measured time reference resolution. The two distributions are in very good agreement, both in the region of the peak and of the tail. A detailed study of the tail is reported in Section 5.1.5.

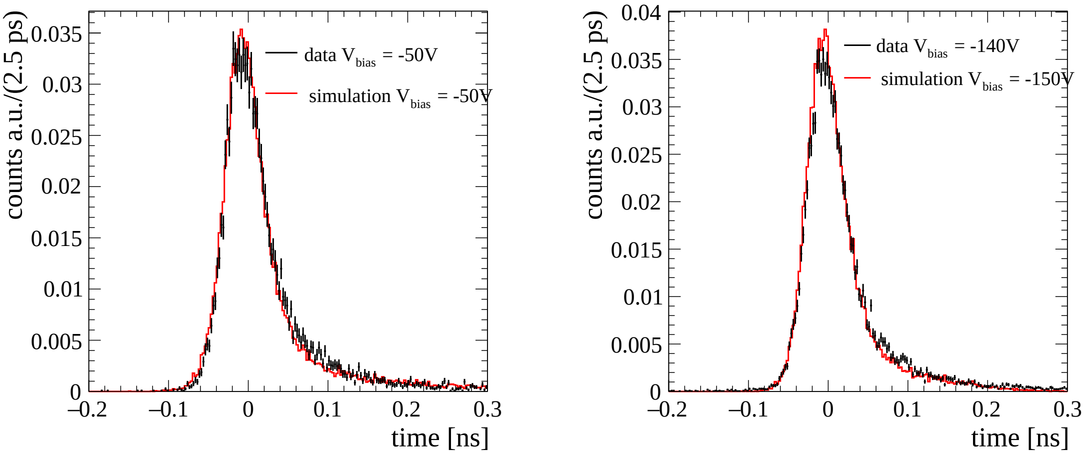

**(a)** **(b)**

**Fig. 5.9** The distribution of the time difference between the 3D-trench silicon sensor signal and the pion arrival time at (a) $V_{\text{bias}} = -50\,\text{V}$ and (b) $-150\,\text{V}$ for data and simulation.

### 5.1.5 Results from simulation

Thanks to the good agreement between data and simulation, the simulation was used to study in detail several characteristics of the 3D-trench silicon sensor used at the PSI test beam, in particular the spatial distribution of the time of arrival. Figure 5.10 shows the ToA distribution with respect to the particle impact point coordinates for different bias voltages, $V_{\text{bias}} = -50\,\text{V}$, $-100\,\text{V}$ and $-150\,\text{V}$. It is clear that a large number of slower events are produced in the *side region* on the right of the double pixel, in the X-coordinate interval $[165\,\mu\text{m}, 189\,\mu\text{m}]$. In fact, in this region the electric field is lower but sufficient to produce a signal that exceeds the threshold. The ToA are typically larger than those from the double-pixel core and vary as much as 200 ps. In a real detector made of a 3D-trench pixels matrix, the contribution of the *side region* might possibly affect only the pixels located at the borders of the matrix. Since this zone is not representative of a double pixel sensor, it has to be excluded in the timing characterization of the real double pixel.

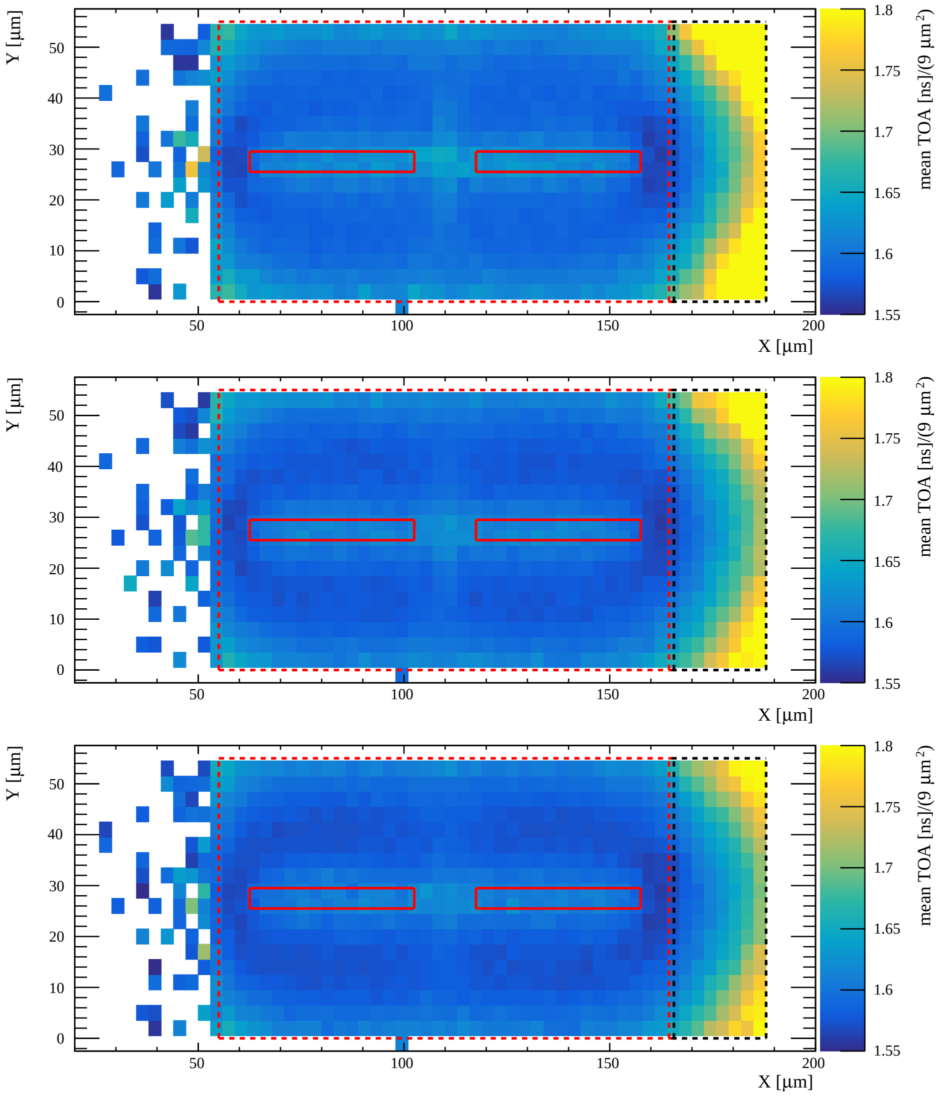

**Fig. 5.10** Distribution of the signal mean time of arrival with respect to the (X,Y) track impact point coordinates. The double pixel region is limited by the red-dashed line, while the *side region* is limited by the black-dashed line. The readout trenches are indicated by the full-red lines. The displayed range of ToA values are chosen to emphasise the different values in the double pixel region. Plots correspond to simulated samples at (from top to bottom) $V_{\text{bias}} = -50,\ -100,\ -150\,\text{V}$.

Focusing on the double pixel region, between $X = 55\,\mu\text{m}$ and $X = 165\,\mu\text{m}$, an increase of the ToA distribution uniformity is observed. The Y projection of the mean ToA, shown in Figure 5.11, has a dependency on the distance from the trenches and it changes with the bias voltage. In particular, in the regions closer to the bias or the readout trenches, where one of the two charge carriers contributes mostly to the current induction, the charge carriers drift path is longer with respect to the region in the middle of the two trenches and so the signals are slower. The pattern is not symmetric because of the different velocities of the two charge carriers. The small region between the two readout trenches of the double pixel, with X-coordinate in the range $[105\,\mu\text{m}, 115\,\mu\text{m}]$ and Y-coordinate in the interval $[22.5\,\mu\text{m}, 32.5\,\mu\text{m}]$, has a smaller electric field (Figure 5.2) and signals produced in this region are typically slower than those produced in the rest of the double pixel.

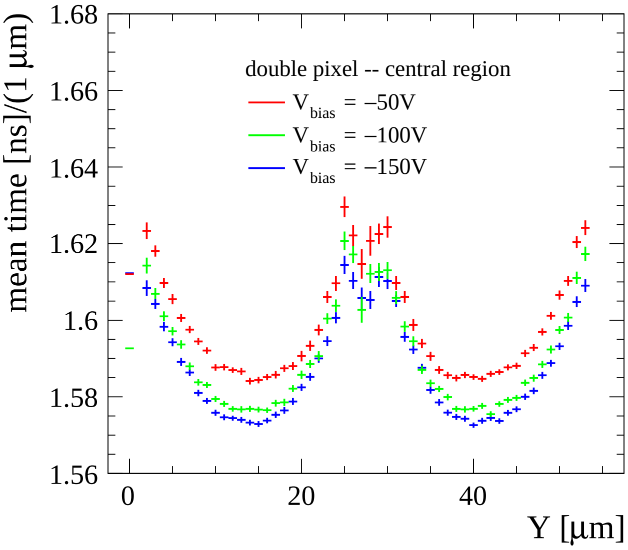

**Fig. 5.11** Y projection of the mean time of arrival at different bias voltages. Only signals originated in the central part of the double pixel, excluding the regions in X at the border of each pixel ($70\,\mu\text{m} < \text{X} < 95\,\mu\text{m}$ and $125\,\mu\text{m} < \text{X} < 150\,\mu\text{m}$), are considered.

An important result of this simulation work is the understanding of where the unexpected long tail of the time distribution, observed at the PSI test beam, arises from. In fact, the simulation makes it possible to factor the contributions from the double pixel region and the side region, as illustrated in Figure 5.12. It allows to understand that the tail is mainly due to signals coming from the side region, while the signals originated in the double pixel contribute to the peaking structure, originating a low asymmetric distribution.

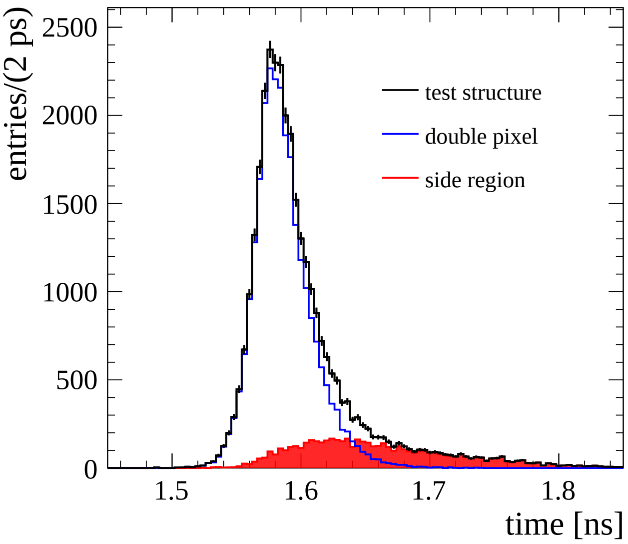

**Fig. 5.12** Distributions of the time of arrival for simulated signals at a bias voltage of $-150\,\mathrm{V}$. All reconstructed signals in the test structure are included, the contributions due to signals originated in the double pixel ($55\,\mu\mathrm{m} < \mathrm{X} < 165\,\mu\mathrm{m}$) and in the low-field *side region* ($\mathrm{X} > 165\,\mu\mathrm{m}$) are overlaid.

## 5.2 Test beam setup improvements

In Chapter 4 a remark was made on the fact that the front-end electronics was a limiting factor to the measurement of the TimeSPOT sensor time resolution and this resulted in the development of a different circuit, optimized for TimeSPOT sensors. In this perspective, also a more performing time reference detector is needed, since the time accuracy of the Time-Tagger used at the PSI test beam is close to the expected time resolution of the TimeSPOT sensor. In this Section, the new FEE board and the new Time-Tagger characterization are presented.

### 5.2.1 New front-end electronics board

A different circuit schematic, optimized to process the fast current signals output from TimeSPOT sensors, was developed by means of an analytic model and Spice-based simulations [89]. The circuit consists of a two stages of transimpedance amplifier with ultra low-noise Silicon-Germanium bipolar junction transistors, having transition frequency of about 85 GHz. It has an RMS noise of about 4 mV, a signals (20-80)% rise time of about 100 ps and a signal to noise ratio of about 20 for a charge deposit of

1 MIP in a TimeSPOT sensor. Two versions of the circuit, shown in Figure 5.13, have been produced, capable to readout either one or four sensor channels. Finally, the pad for the sensor has a 500 $\mu$m diameter hole to allow to illuminate the sensor with an infrared laser also from the back and to avoid low energy particles, used for laboratory characterizations (see Chapter 6), to lose energy in the printed circuit board (PCB).

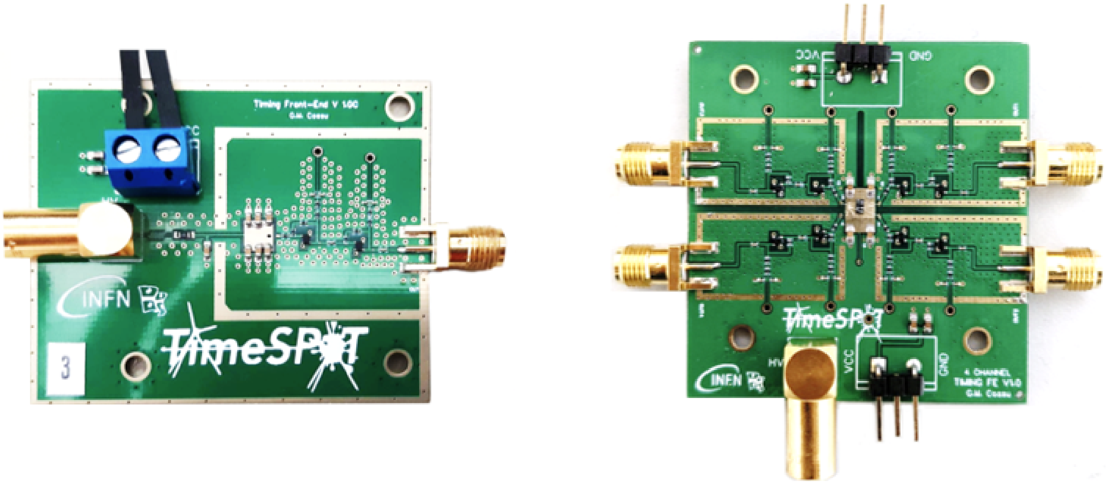

(a) (b)

**Fig. 5.13** The front-end boards produced *ad hoc* for TimeSPOT sensors in the (a) single-channel and (b) four-channels version.

### 5.2.2 New MCP-PMTs characterization

In order to have a better Time-Tagger to be used as time reference in a test beam, two new optimized MCP-PMTs were purchased. The two MCP-PMTs are two Photonis model PP2365Y, with a 18 mm diameter, 6 $\mu$m diameter pores and 5.5 mm thick quartz input window (Figure 5.14). From now on we will refer to them as MCP3 and MCP4. The two MCP-PMTs were characterized in laboratory with the red laser used also for the measurements of the former ones (see Section 4.4). Figure 5.15 shows the setup used for the characterization of MCP3 and MCP4, consisting of the MCP-PMT under test, the optical fiber and the holder for the Neutral Density (ND) filters used to regulate the light intensity coming on the photomultiplier entrance window. The characterization of these MCP-PMTs was made at different light intensities, starting from the condition of single photon, to which these kind of devices are sensitive.

Figure 5.16 shows the signals coming from the laser driver and from the MCP-PMT, seen at the Rohde & Schwarz RTO1044 oscilloscope used for the measurements. The

**Fig. 5.14** Picture of one of the two Photonis PP2365Y MCP-PMT.

laser signal represents the time reference with respect to which the delay of the MCP-PMT signal is measured, in order to extract the time resolution of the photomultiplier. In fact, this laser signal provides an excellent time reference for timing measurements, having an estimated time jitter of $3-4\,\mathrm{ps}$. At each laser pulse emitted, several variables of the MCP-PMT waveform are measured, including in particular the amplitude and the delay from the laser reference. These measurements are performed by the oscilloscope and controlled by a data acquisition system developed in LabVIEW.

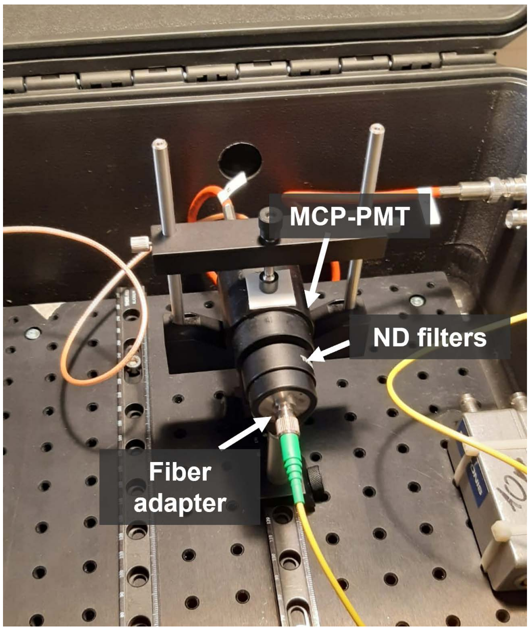

**Fig. 5.15** Setup inside the light-tight black box. The fiber adapter and the holder for ND filters are placed in front of the MCP-PMT under test.

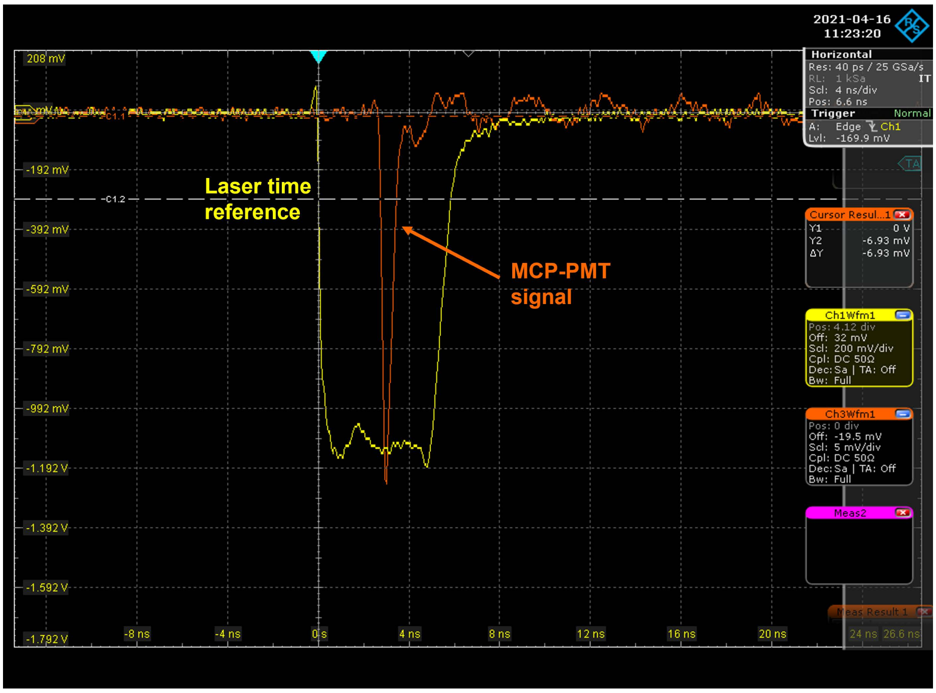

```
2021-04-16
11:23:20
Horizontal
Res: 40 ps / 25 GSa/s
RL:  1 kSa              IT
Scl:  4 ns/div
Pos: 6.6 ns
Trigger             Normal
A:   Edge  Ch1
Lvl:  -169.9 mV

Cursor Resul...1
Y1              0 V
Y2        -6.93 mV
ΔY        -6.93 mV

Ch1Wfm1
Pos: 4.12 div
Off:  32 mV
Scl:  200 mV/div
Cpl: DC 50Ω
Dec: Sa | TA: Off
Bw:  Full

Ch3Wfm1
Pos: 0 div
Off:  -19.5 mV
Scl:  5 mV/div
Cpl: DC 50Ω
Dec: Sa | TA: Off
Bw:  Full
```

**Fig. 5.16** Laser time reference (yellow) and MCP-PMT (orange) signals seen at the oscilloscope.

The amplitude distribution obtained with MCP3 in a single photon condition is shown in Figure 5.17a, where it is possible to observe the pedestal due to no photons detected and the bump at about 9 mV due to a single photoelectron emitted by the MCP-PMT, at a supply voltage of 2800 V. Figure 5.17b shows the distribution of the delay of the MCP3 signal from the laser time reference signal at 2800 V. The time distribution is fitted with an Exponentially Modified Gaussian (EMG) distribution, with the exponential contribution used to describe the distribution tail due to back-scattered photoelectrons. The MCP3 single-photon time resolution measured at 2800 V is $\sigma_t = 24.4 \pm 0.8$ ps, including the laser time reference jitter, which in this case can be considered negligible. As a comparison, the single-photon time resolution of the Planacon XP85112 (MCP1) used at the PSI test beam is about 43 ps. This result gives a first indication of the better timing performances achievable using these more performing MCP-PMTs.

Moreover the single-photon time resolution of the MCP3 has been measured at different supply voltages. The results, reported in Figure 5.18, show a slight deterioration of the time resolution as the voltage decreases. A time resolution of about 28 ps have been found at a supply voltage of 2600 V. Finally, the timing performances of the two MCP-PMTs have been evaluated for different number of detected photoelectrons by varying the laser degree of attenuation with the ND filters. The results of these studies

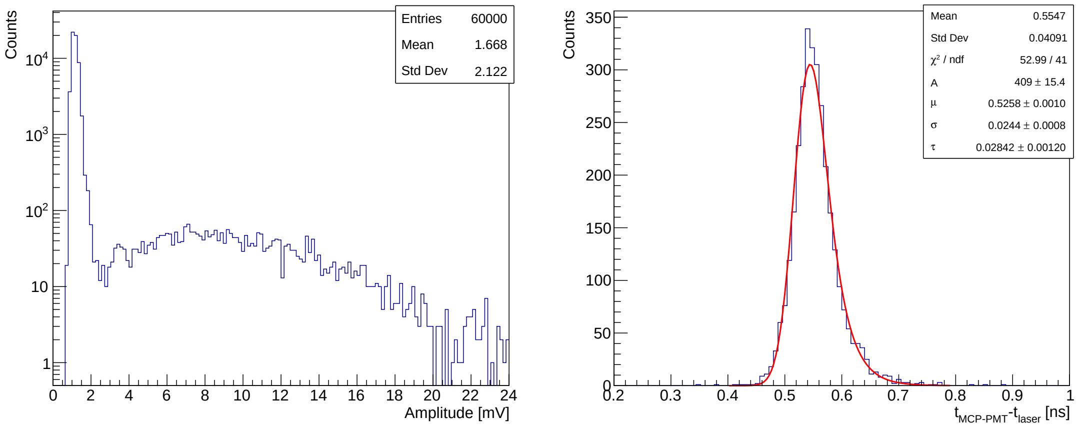

**(a)** **(b)**

**Fig. 5.17** (a) Distribution of MCP3 signals amplitude in single-photon condition. (b) Distribution of the delay between MCP3 signal and the laser time reference at 2800 V.

are reported in Figure 5.19, where the time resolution of both the MCP-PMTs is shown as a function of the signals amplitude (Figure 5.19a) and as a function of the detected photoelectrons (Figure 5.19b). These measurements revealed a bad functioning of MCP4, which showed a low gain and a consequent worse time resolution with respect to MCP3. For this reason MCP4 was sent to repair before being used at the upcoming test beam (see Chapter 7). Focusing on MCP3 results, an improvement of the time resolution as the light intensity increases is observed. A time resolution of about 8 ps with 27 photoelectrons detected, including the laser time jitter, has been measured.

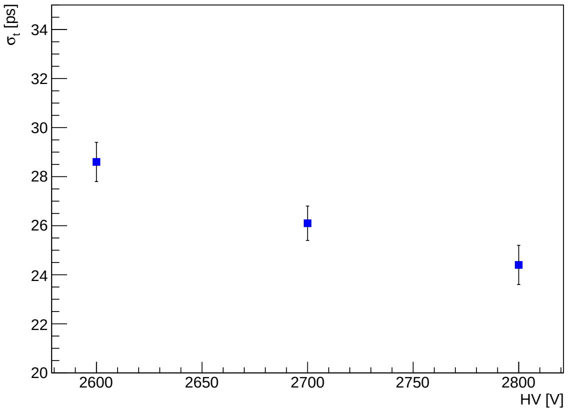

**Fig. 5.18** Time resolution of MCP3 measured in single-photon condition at different supply voltages.

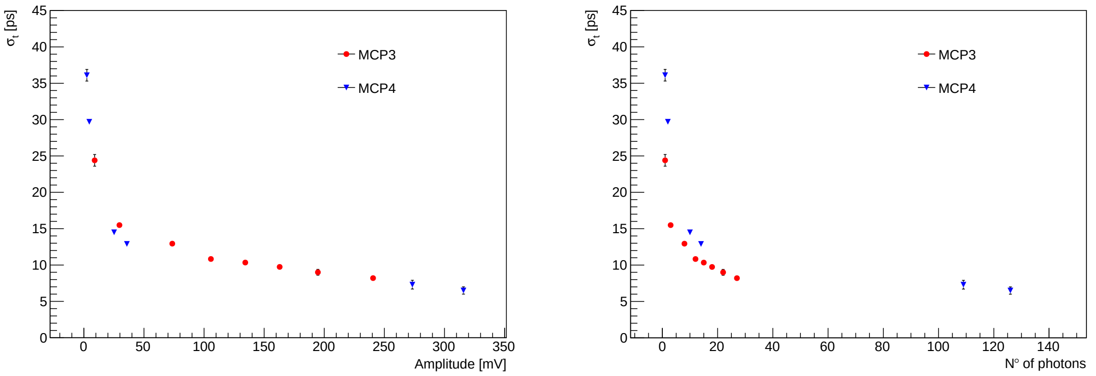

**(a)** **(b)**

**Fig. 5.19** Time resolution of MCP3 and MCP4 at 2800 V (a) as a function of the signal amplitude and (b) as a function of the number of photoelectrons detected.

These measurements allowed to estimate the performances of a time reference detector composed of MCP3 and MCP4. In fact, at the test beam, for 180 GeV/c positive pions beam (SPS/H8 beamline), about 15-20 Cherenkov photons per MIP are expected in a 5.5 mm thick quartz window, corresponding to a time resolution of MCP3 lower than 10 ps. Assuming that, after the MCP4 reparing, the two MCP-PMTs have the same timing performance, a time reference accuracy lower than 5 ps is expected using the average time measured by the two devices, which is about half the time accuracy of the former Time-Tagger (12.4 ps).

# Chapter 6

# TimeSPOT sensors laboratory characterization

The characterization of silicon sensors needs two complementary studies: an overall response of the sensor and a sub-pixel level response measurement. For the TimeSPOT sensors characterization, two laboratory setups have been developed, one using a $^{90}$Sr radioactive source to perform testbeam-like characterizations directly in the laboratory, the other one using an infrared laser to characterize the sensors at a sub-pixel level. In this Chapter the two setups are described, with the main focus on the measurements made with the $^{90}$Sr source on two different TimeSPOT test structures: the single pixel and the pixel-strip. This setup allows to perform time resolution measurements with minimum ionizing particles directly in the laboratory, despite the limits of the setup given mostly by the multiple scattering in silicon for low energy electrons emitted by the $^{90}$Sr source and illustrated in this chapter by means of a `Geant4` simulation. Finally, a comparison between three different test structures with different pitch sizes characterized with the infrared laser setup is shown. For all these characterizations the sensor is glued with conductive tape and wire-bonded (Figure 6.1) to the preamplifier input pad of the custom-made single-channel front-end electronics board, designed and built for TimeSPOT sensors [89], described in Chapter 5.

## 6.1 Sensors characterization with $^{90}$Sr source setup

A laboratory setup, emulating a testbeam-like setup, was developed in order to characterize TimeSPOT sensors with Minimum Ionizing Particles (MIPs) in the laboratory, in particular to measure their timing performance. In this setup, a $^{90}$Sr $\beta$-source is used. $^{90}$Sr decays in $^{90}$Y which in turn decays in $^{90}$Zr, that is stable. The complete

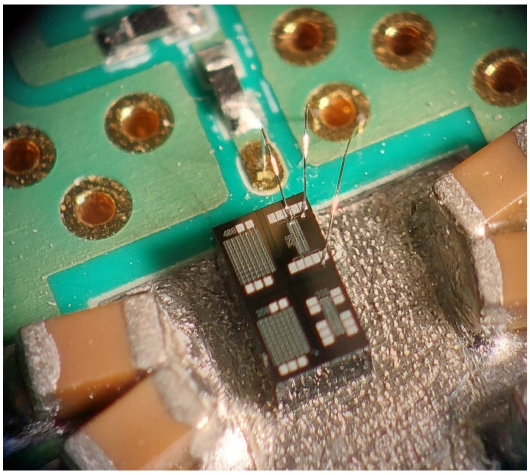

**Fig. 6.1** Picture of a wire-bonding of a TimeSPOT single pixel to the test board, seen at the microscope.

decay is given by

$$^{90}_{38}Sr \rightarrow ^{90}_{39} Y + e^- + \bar{\nu} + E_{e^-,Sr} \tag{6.1}$$

$$^{90}_{39}Y \rightarrow ^{90}_{40} Zr + e^- + \bar{\nu} + E_{e^-,Y} \tag{6.2}$$

where $E_{e^-,\mathrm{Sr}}$ and $E_{e^-,\mathrm{Y}}$ indicate the continuously distributed decay energy shared between the electron ($e^-$) and the anti-neutrino ($\bar{\nu}$). The cumulative spectrum of $^{90}$Sr and $^{90}$Y calculated using the simplified Fermi function [90, 91] is shown in Figure 6.2. The maximum energy of the electrons is about 2.2 MeV, that corresponds to the end-point energy of the $\beta$-decay, while the average energy is 0.3 MeV.

The setup with the $^{90}$Sr source is shown in Figure 6.3. The device under test is put in front of the $^{90}$Sr source and a Micro-Channel Plate Photo-Multiplier Tube (MCP-PMT) used as time reference detector is placed downstream. The MCP-PMT used is the Photonis PP2365Y (named MCP3), whose characterization has been illustrated in Section 5.2.2. It is an MCP-PMT with a 1.8 mm diameter and 5.5 mm thick quartz input window, 6 $\mu$m pores diameter and a measured single-photon detection time resolution of about 24 ps. The MCP-PMT is used both to provide a good time reference to the setup and to allow the selection of higher energy electrons emitted by the $^{90}$Sr source. Signals from the silicon sensor and the MCP-PMT are acquired by means of a 4 GHz analog bandwidth 20 GSa/s 4 channels digital oscilloscope (Rohde & Schwarz RTO1044). The oscilloscope acquisition trigger condition is the coincidence of a signal from both the silicon sensor and the MCP-PMT, with a proper trigger threshold, that for the silicon sensor has been chosen in such a way that also a fraction of noise events is included in

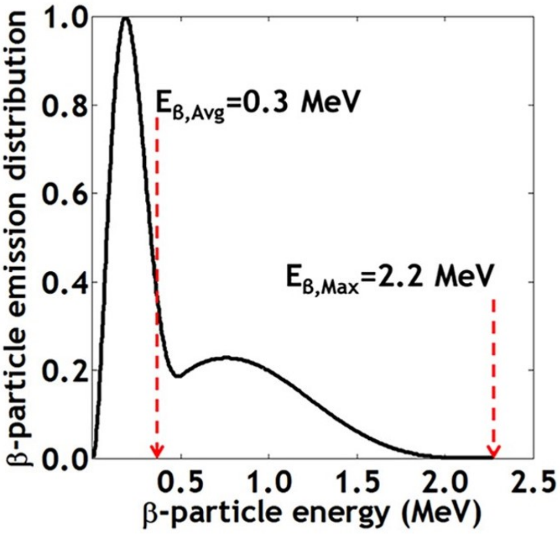

**Fig. 6.2** Normalized energy spectrum of $\beta$-particles emitted by the serial decay of $^{90}$Sr and $^{90}$Y [91].

the acquired amplitude range. A typical event acquired with this setup is shown in Figure 6.4. The waveforms are saved and analysed offline.
To select events in which there is a signal both from the silicon sensor and the MCP-PMT means that the electron has produced Cherenkov light in the MCP-PMT input window, thus it translates into a selection of electrons with energies higher than 0.7 MeV. The energy spectrum of the electrons emitted by the $^{90}$Sr source is such that the multiple scattering in silicon becomes an important effect to be taken into account. In fact, because of this, the energy deposited in the DUT is lower than that deposited by an high energy particle, that goes straight through the sensor, and smaller signals lead to an higher time jitter and thus to a worse time resolution with respect to that measurable at a test beam. Moreover, the presence of the device under test in the trigger can bias the measurements, and this is one of the criticalities of this setup, which is unavoidable due to the presence of the multiple scattering that makes impossible to align the DUT to another sensor that, as done at the beam tests (see Chapter 7 and Chapter 8), could be used as a trigger.

### 6.1.1 Simulation

The electrons emitted by the $^{90}$Sr radioactive source have energies up to 2.2 MeV (Figure 6.2), which are much lower than the particles energy at PSI and SPS beam test facilities where TimeSPOT sensors have been tested. Because of this, as already

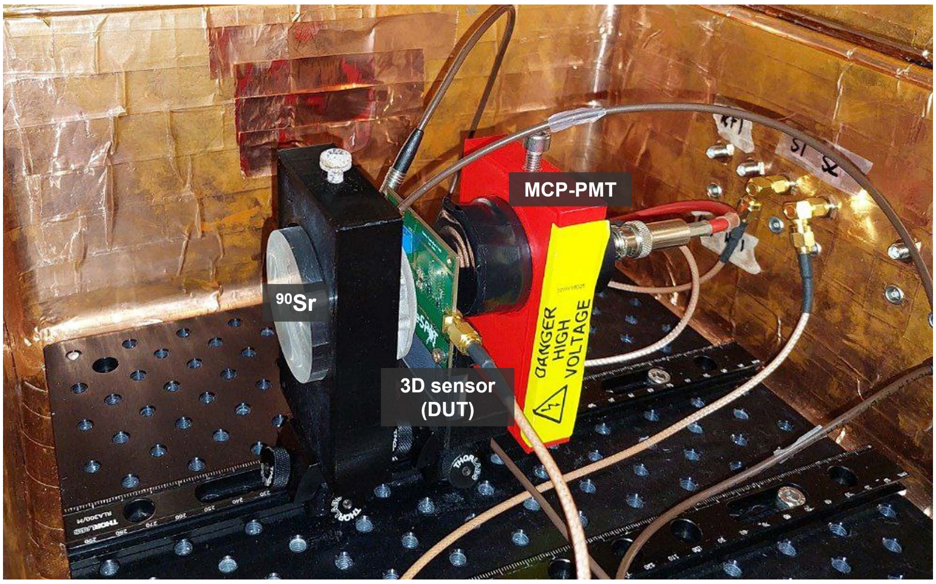

**Fig. 6.3** The setup with $^{90}$Sr source. The silicon sensor under test and the MCP-PMT are placed one after the other along the emission direction of the source.

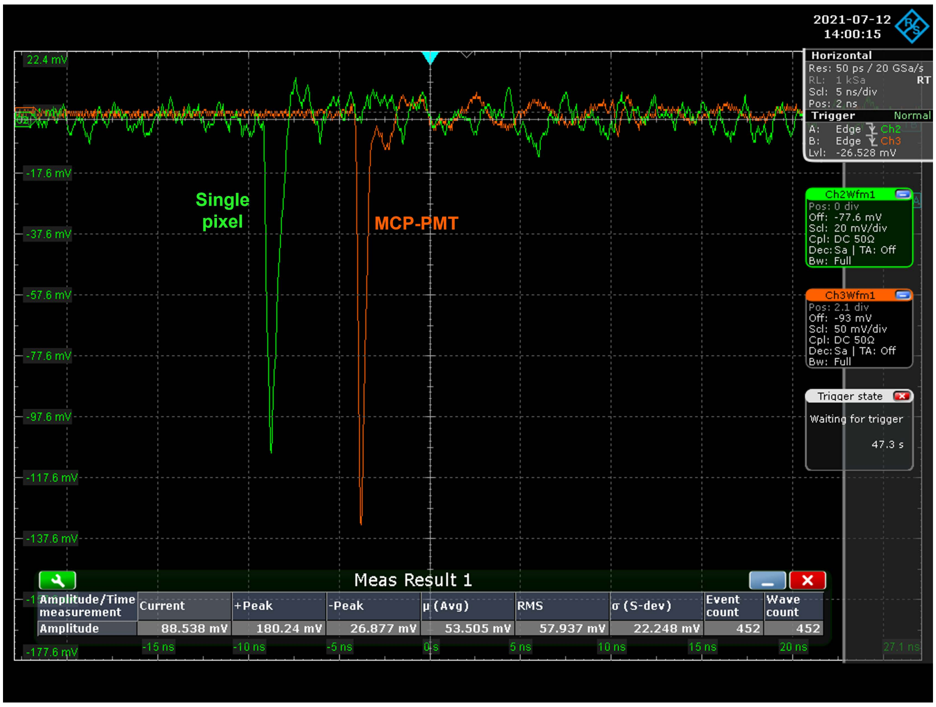

2021-07-12
14:00:15

Horizontal
Res: 50 ps / 20 GSa/s
RL: 1 kSa RT
Scl: 5 ns/div
Pos: 2 ns

Trigger Normal
A: Edge Ch2
B: Edge Ch3
Lvl: -26.528 mV

Ch2Wfm1
Pos: 0 div
Off: -77.6 mV
Scl: 20 mV/div
Cpl: DC 50Ω
Dec: Sa | TA: Off
Bw: Full

Ch3Wfm1
Pos: 2.1 div
Off: -93 mV
Scl: 50 mV/div
Cpl: DC 50Ω
Dec: Sa | TA: Off
Bw: Full

Trigger state
Waiting for trigger
47.3 s

Meas Result 1

| Amplitude/Time measurement | Current | +Peak | -Peak | μ (Avg) | RMS | σ (S-dev) | Event count | Wave count |
|---|---|---|---|---|---|---|---|---|
| Amplitude | 88.538 mV | 180.24 mV | 26.877 mV | 53.505 mV | 57.937 mV | 22.248 mV | 452 | 452 |

**Fig. 6.4** Typical coincidence event of a TimeSPOT single pixel (in green) and the MCP-PMT (in orange).

mentioned, the multiple scattering in the silicon is a relevant phenomenon in the $^{90}$Sr source setup. To study this effect, a simple `Geant4` simulation has been implemented.

A $55 \times 55 \times 150\,\mu\mathrm{m}^3$ silicon block, representing a TimeSPOT pixel, is simulated and surrounded by a $275 \times 275 \times 150\,\mu\mathrm{m}^3$ external silicon ring, as illustrated by Figure 6.5. This simulated device allows to know the amount of energy deposited inside and outside our pixel. The study is made for electrons with energies 0.5 MeV, 0.7 MeV, 1 MeV, 2 MeV, that are in the energy spectrum of electrons emitted by $^{90}$Sr, and for the 180 GeV/c pions of the SPS/H8 beamline at CERN. The 0.7 MeV energy was chosen as it is the Cherenkov threshold for electrons in quartz, so in our setup energies lower than this are filtered by the MCP-PMT. For each run, $1 \cdot 10^5$ particles are generated with direction perpendicular to the pixel surface. Figure 6.6 shows 50 simulated events for 0.5 MeV and 1 MeV electrons and for 180 GeV pions, illustrating the different impact of multiple scattering in silicon at different incident particle energies.

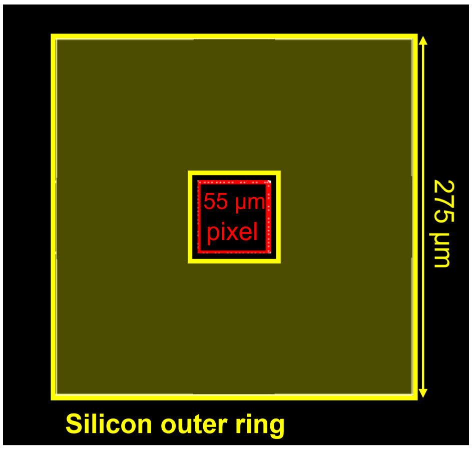

**Fig. 6.5** Simulated silicon block of $275 \times 275 \times 150\ \mu\mathrm{m}^3$ (yellow box) with an internal smaller block of $55 \times 55 \times 150\ \mu\mathrm{m}^3$ (red frame), representing the TimeSPOT pixel.

The energy deposit distributions in the $55 \times 55 \times 150\ \mu\mathrm{m}^3$ silicon pixel and in the external silicon ring are shown in Figure 6.7a and in Figure 6.7b, respectively. For 180 GeV pions a clear Landau distribution is observed inside the pixel, while no energy deposit is present in the outer ring. On the other hand, for the electrons up to 2 MeV, the charge deposit distribution in the pixel is broader, because a large amount of charge is deposited outside the pixel. Figure 6.8 shows the sum of the energy deposited in the pixel and in the outer ring by each particle. For 2 MeV electrons, the distribution obtained with 180 GeV pions is reproduced, while, for lower energies, a larger amount of charge is deposited in the pixel but the distribution assumes a Landau-like shape. These results bring to the consideration that this setup with the $^{90}$Sr source allows to measure only an upper limit of the time resolution of TimeSPOT silicon sensors, that is expected to be better if measured in a test beam with high energy particles, where the

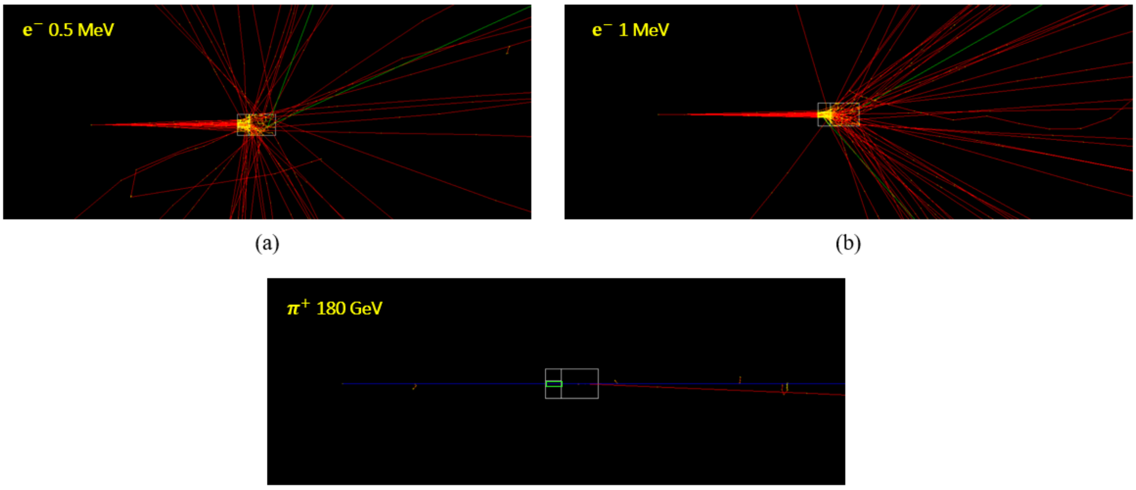

(a) (b) (c)

**Fig. 6.6** Simulation of 50 (a) 0.5 MeV electrons, (b) 1 MeV electrons and (c) 180 GeV pions hitting the simulated silicon block consisting on a $55 \times 55 \times 150\ \mu m^3$ (highlighted in green in the bottom figure) and the external silicon ring.

multiple scattering is negligible. However, this setup allows to make preliminary time resolution measurements and to compare different test structures or sensors irradiated at different fluences in the laboratory.

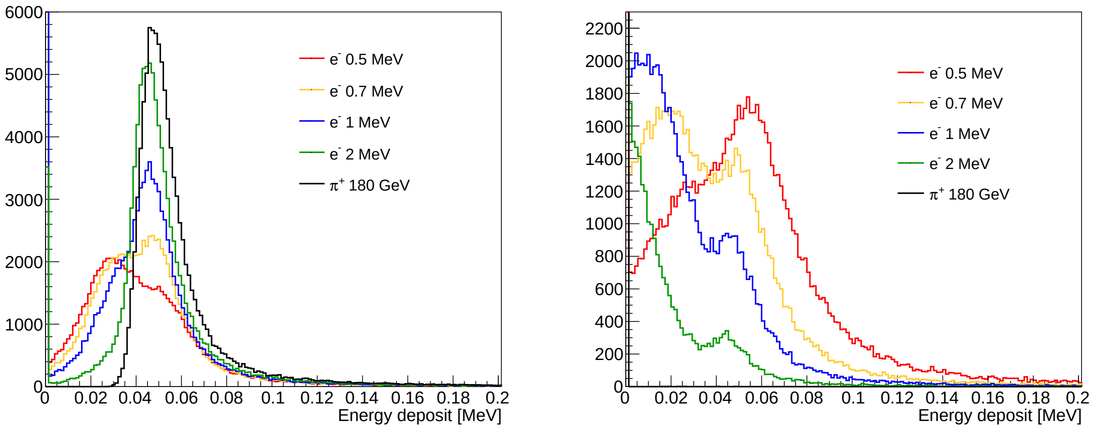

**(a)** **(b)**

**Fig. 6.7** (a) Distribution of the energy deposit in a $55 \times 55 \times 150\ \mu m^3$ silicon pixel and (b) in the outer silicon ring for 0.5 MeV, 0.7 MeV, 1 MeV, 2 MeV electrons and 180 GeV pions.

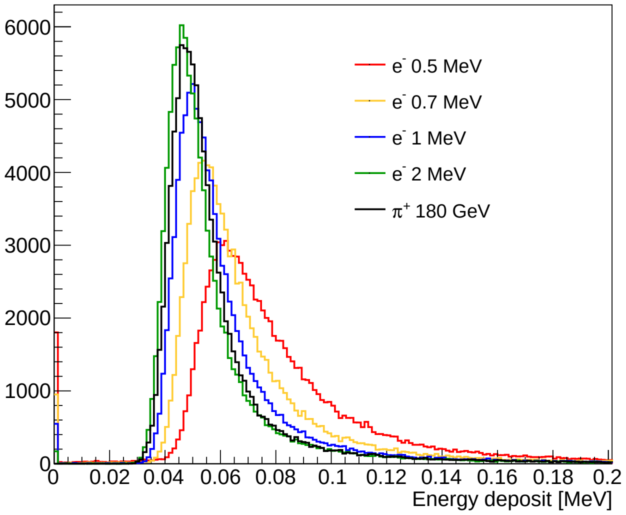

**Fig. 6.8** Distribution of the sum of the charge deposit in the pixel and in the outer ring for 0.5 MeV, 0.7 MeV, 1 MeV, 2 MeV electrons and 180 GeV pions.

### 6.1.2 Data analysis

The analysis of the acquired waveforms consists of two main steps: the measure of both the amplitude and the Time of Arrival (ToA) of each signal. The signal amplitude is measured with respect to the baseline, while for the ToA measurement, different algorithms for the silicon sensor signals, in part already described in Section 4.2, have been developed and used. These methods are:

1. The **Leading Edge (LE)** with a fixed threshold of $-15$ mV (Figure 6.9a), optimized for the signals coming from the new front-end electronics board.

2. The **Spline** method, which replaces the *PSI* method (Section 4.2). It is a constant fraction algorithm that interpolates the waveform with cubic splines, with a granularity of 1 ps, and defines the ToA as the time at which the signal exceeds a fraction of the signal amplitude (Figure 6.9b). An optimization of this fraction was performed for each sensor characterized, resulting in an amplitude fraction of 20% for the single pixel sensor and 35% for the pixel-strip sensor, concerning the measurements shown in this chapter.

3. The **Reference** method, in which the signal is processed by subtracting to it an identical contribution delayed by about half of the signal rise time and the ToA is set to the time at which the resulting waveform exceeds 50% of its amplitude (Figure 4.7b).

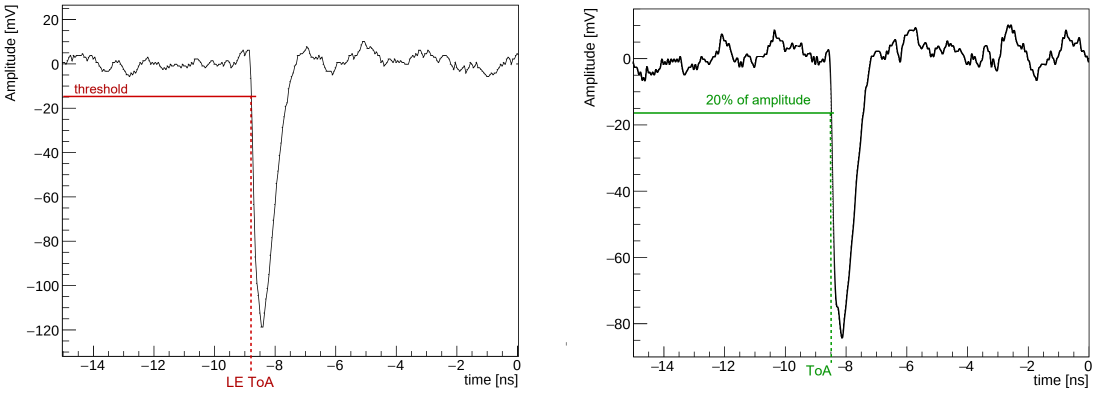

**(a)** **(b)**

**Fig. 6.9** Illustration of (a) the Leading Edge (LE) method and (b) the Spline method at 20% fraction of the signal amplitude applied to signals from a TimeSPOT single pixel.

All methods parameters are optimized with real data, from both laboratory and test beam measurements, in order to guarantee the best detection efficiency and timing performances. These parameters depend on the front-end electronics and on the sensor used, that determine signals characteristics (rise time, amplitude and noise). The ToA of the MCP-PMT signal is determined by applying the Spline method.

### 6.1.3 Measurements and results

As explained in Section 6.1.1 above, this setup with the $^{90}$Sr source allows to measure an upper limit of the sensor time resolution and thus to have a first estimation of its timing performance directly in laboratory. The test structures characterized with this setup are a single pixel and a pixel-strip (Figure 6.10), and the acquisition trigger condition used is that explained before.

#### Single pixel characterization

The single pixel and the MCP-PMT signals amplitude distributions are shown in Figure 6.11. As expected, the single pixel amplitude distribution (Figure 6.11a) is not Landau-like because of the relevant multiple scattering of electrons with energy in the range $(0.7-2)\,\mathrm{MeV}$ in silicon, as already illustrated by the simulation. An amplitude selection on the MCP-PMT signals is applied ($|A| > 30\,\mathrm{mV}$), in order to select electrons with at least $1\,\mathrm{MeV}$ energy and to have a sufficiently good time reference resolution.

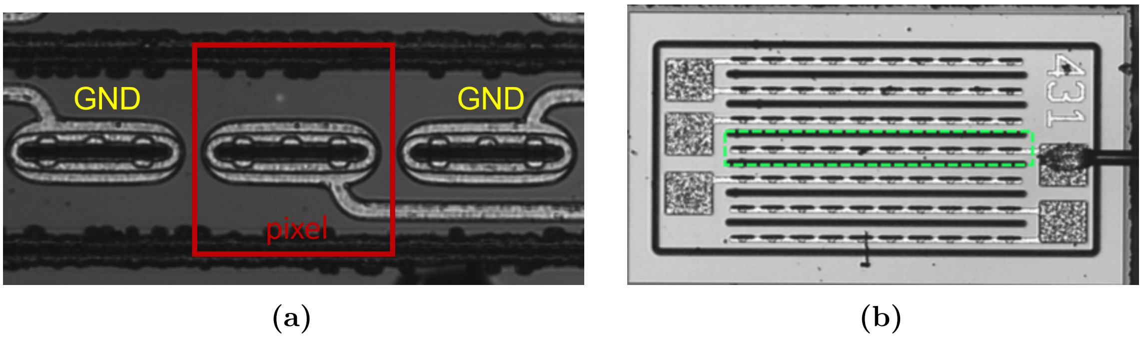

**Fig. 6.10** Two of the TimeSPOT sensors tested with this setup: (a) a single pixel and (b) a pixel-strip. The single pixel test structure consists of seven adjacent pixels, where the three innermost, visible in the picture, can be individually readout; for the measurements described here the side pixels are grounded and the central one (in the red box) is connected to the FEE input. The pixel-strip (in the green dashed box) consists of ten pixels shorted together.

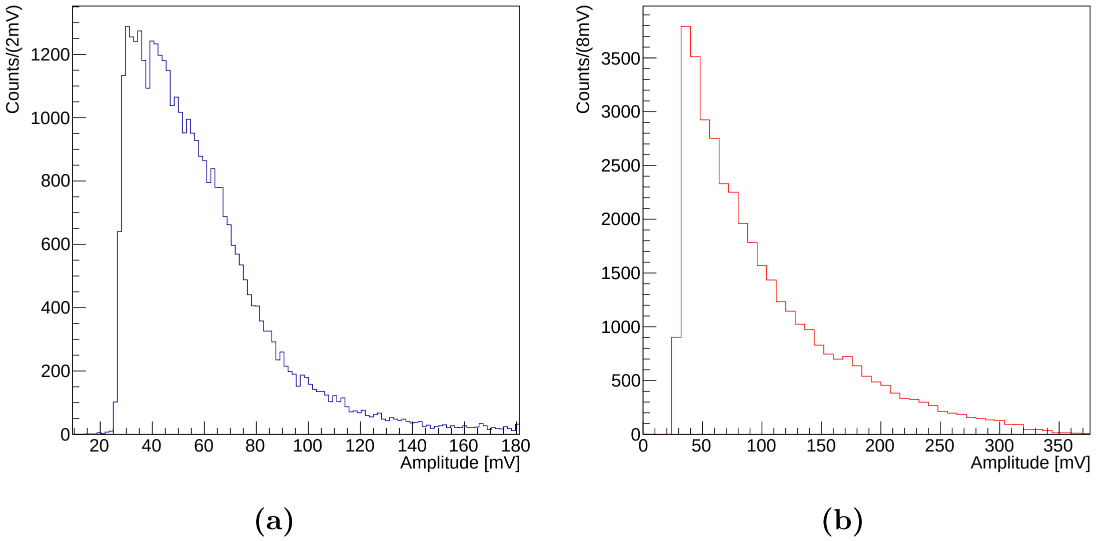

**Fig. 6.11** (a) Single pixel signals amplitude distribution at $V_{\text{bias}} = -50$ V. (b) MCP-PMT signals amplitude distribution at 2800 V.

Figure 6.12 shows the distribution of the difference between the ToA of the single pixel and the MCP-PMT, $t_{\text{pixel}} - t_{\text{MCP-PMT}}$, from which the time resolution of the single pixel is extracted. The distribution consists of a peaking structure, due to energy deposits in the single pixel, and a constant contribution, due to noise events. The peak is described by the sum of two Gaussian functions: the Gaussian core accounts for the contribution of the signals originated in the central region of the sensor, while the secondary Gaussian describes the contribution of the signals originated close to the trenches that feature a slightly larger ToA due to the longer charge collection time of one of the two charge carriers, as accurately demonstrated with simulation studies [86]. Their contributions are combined to compute the effective resolution as

$$\sigma_{\text{eff}}^2 = f_1(\sigma_1^2 + \mu_1^2) + (1 - f_1) \cdot (\sigma_2^2 + \mu_2^2) - \mu^2 \tag{6.3}$$

where $f_1$ is the fraction of the Gaussian core and $\mu$ is defined as

$$\mu = f_1\mu_1 + (1 - f_1) \cdot \mu_2 \tag{6.4}$$

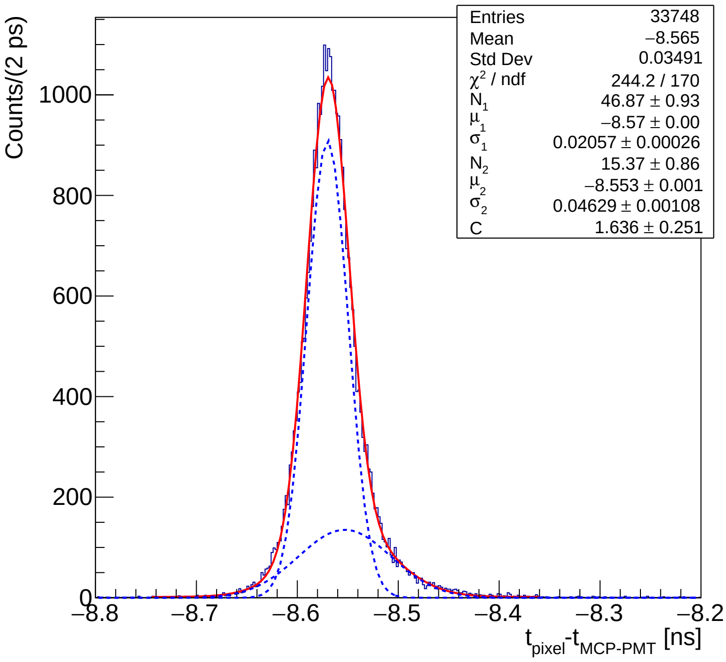

**Fig. 6.12** Distribution of the single pixel ToA with respect to the MCP-PMT, $t_{\text{pixel}} - t_{\text{MCP-PMT}}$, at $V_{\text{bias}} = -50\,\text{V}$. The distribution is fitted with the sum of two Gaussian and a constant (in red). The two Gaussian are also shown (blue dashed lines).

A comparison between the time distributions obtained with the three different methods (Leading Edge, Spline and Reference), at a bias voltage of $-75\,\text{V}$ for the pixel, is shown in Figure 6.13. As expected, the distribution obtained applying the Leading Edge algorithm to the silicon sensor signals is larger than those obtained with the CFD-like algorithms. However, the distributions resulting by applying the Spline and the Reference methods to the single pixel signals are similar to each other, showing an effective time resolution of $29.2\pm0.5$ ps and $31.2\pm0.5$ ps, respectively. This is in contrast to what observed at the PSI test beam (Section 4.3), where the Reference algorithm led to a significant improvement in the time resolution measurement. This hasn't been completely understood but one possible explanation is that in these measurements, differently to test beam ones, the charged particle path in the silicon is not straight, thus each signal is a mixture of signals coming from sensor regions where the electric field value is different. This means that in this setup the signals rise time values are more uniformly distributed, hence the Reference algorithm, that mitigates the jitter due to rise time fluctuations, has no effect.

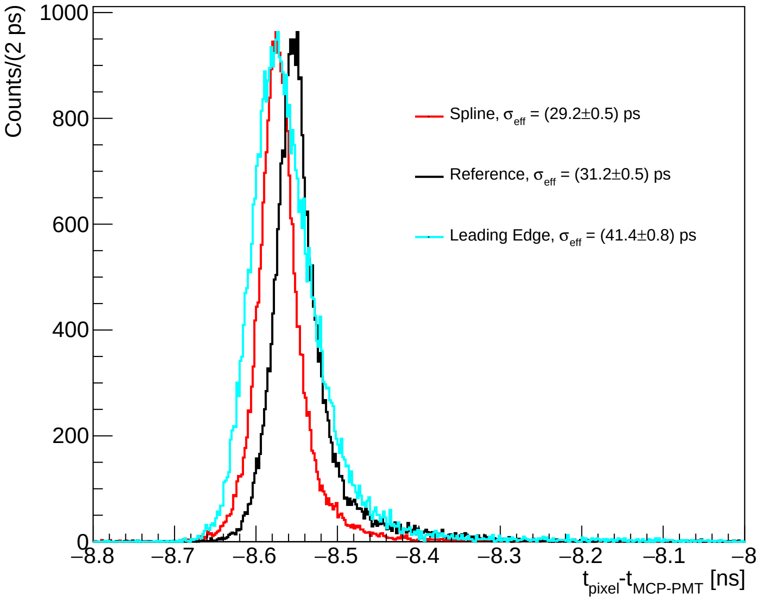

**Fig. 6.13** Distribution of the single pixel ToA with respect to the MCP-PMT, $t_{\text{pixel}} - t_{\text{MCP-PMT}}$, obtained at $V_{\text{bias}} = -75\,\text{V}$ with three different time-picking methods: Leading Edge, Spline and Reference. The effective time resolution $\sigma_{\text{eff}}$ in the legend includes the time jitter contribution of the MCP-PMT. Histograms are normalized to the distribution maximum.

Figure 6.14 shows the time distributions obtained at different bias voltages in a range from $-10\,\text{V}$ to $-100\,\text{V}$ with the Spline algorithm, normalized at the histograms integral. It is possible to observe that a wider distribution is obtained at $-10\,\text{V}$ and $-25\,\text{V}$, while for $V_{\text{bias}} \leq -50\,\text{V}$ the distributions are more similar to each other. Moreover, a shift of the time distribution to the left is observed as the bias voltage increases, as can be seen in Figure 6.15, where the mean value $\mu$ of the distribution, obtained from the fit, as a function of the bias voltage, is shown. The value of $\mu$ itself is not important, since a constant quantity has been added to each value for more clarity, while it is important to see the relative difference of each value with the other values. This shift of $\mu$ with the bias voltage is due to the increase of the electric field intensity which leads to a smaller charge collection time and thus to a smaller ToA.

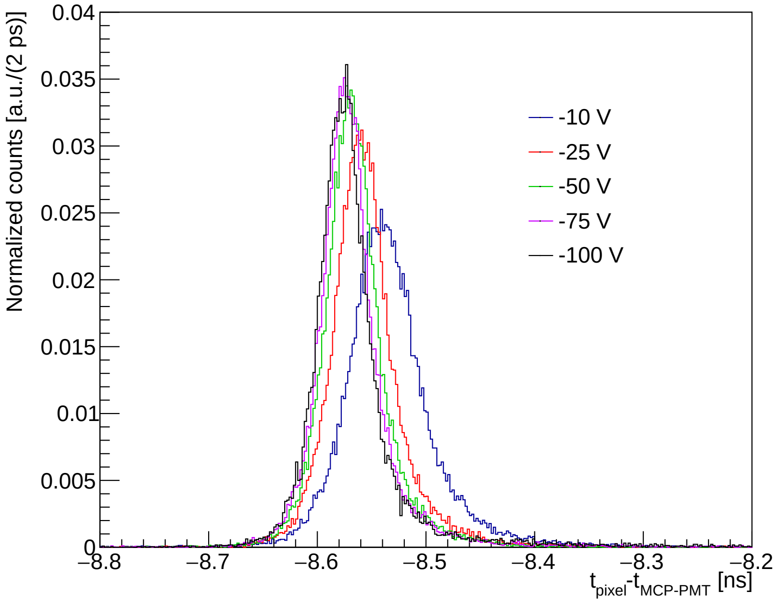

**Fig. 6.14** Distribution of the single pixel ToA with respect to the MCP-PMT, $t_{\text{pixel}} - t_{\text{MCP-PMT}}$, obtained with the Spline method, at different bias voltages and normalized to the integral of the histograms.

To obtain the single pixel time resolution, the time jitter contribution of the MCP-PMT, measured with a red laser (Section 5.2.2), is subtracted in quadrature from the effective time resolution calculated with the two Gaussian fit results, according to Equation 6.3. The single pixel time resolution measured for several bias voltage is reported in Figure 6.16 for the three different algorithms applied. An improvement of the time resolution is observed increasing the bias voltage (absolute value) up to $-50\,\text{V}$, while no improvement is observed further increasing the bias. At $-100\,\text{V}$ the measured single pixel time resolution with the different methods is $39.2 \pm 1.0\,\text{ps}$ with the LE, $25.6 \pm 0.6\,\text{ps}$ with the Spline and $25.8 \pm 0.7\,\text{ps}$ with the Reference. These values can not be compared with the PSI test beam results (Section 4.3) because of the different front-end electronics board and also test structure used, namely a single pixel instead of double pixel with the side region problem (Section 5.1.5). A comparison between this setup and test beam results will be done in the next chapter, dedicated to the TimeSPOT test beam campaigns conducted at the SPS/H8 beamline at CERN, notwithstanding the limits of this setup.

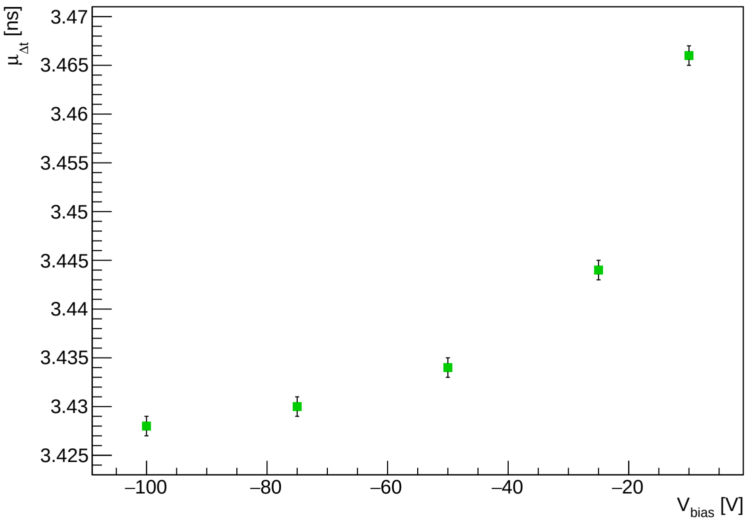

**Fig. 6.15** Mean value $\mu$ of the ToA distributions obtained with the Spline method as a function of the single pixel bias voltage. The $\mu$ value itself is not relevant, but it is important the trend with the bias voltage.

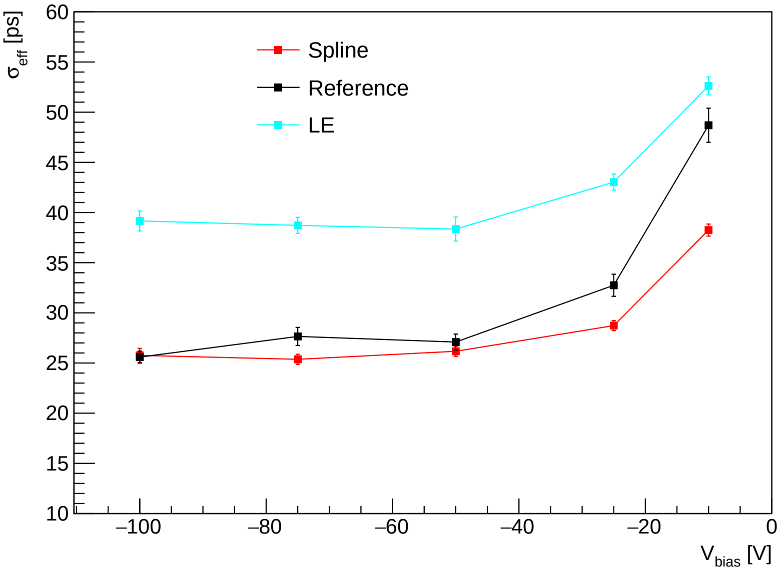

**Fig. 6.16** Effective time resolution of the single pixel as a function of the bias voltage with Leading Edge, Spline and Reference algorithms. The MCP-PMT time jitter contribution has been subtracted in quadrature.

### Pixel-strip characterization

The pixel-strip signals amplitude distribution measured with the $^{90}$Sr source setup is shown in Figure 6.17. This sensor shows a different amplitude distribution with respect to the single pixels having, as expected, a lower amplitude. This is due to the ten times higher capacitance of the pixel-strip structure with respect to a single pixel. In Figure 6.18 the distribution of the difference between the ToA of the pixel-strip and the MCP-PMT, $t_{\mathrm{strip}} - t_{\mathrm{MCP-PMT}}$, with the two Gaussian fit, is shown. The effective time resolution is calculated according to Equation 6.3. Figure 6.19a shows the ToA distributions obtained at different pixel-strip bias voltages applying the Spline method to the sensor signals. As observed for the single pixel, a progressive narrowing of the distribution with the increase of the bias voltage is observed, together with a shift of the distribution at lower time values as the bias voltage increases. This shift of the distributions with the bias voltage is quantified in Figure 6.19b where the mean, $\mu$, of the distribution as a function of the bias voltage applied is shown.

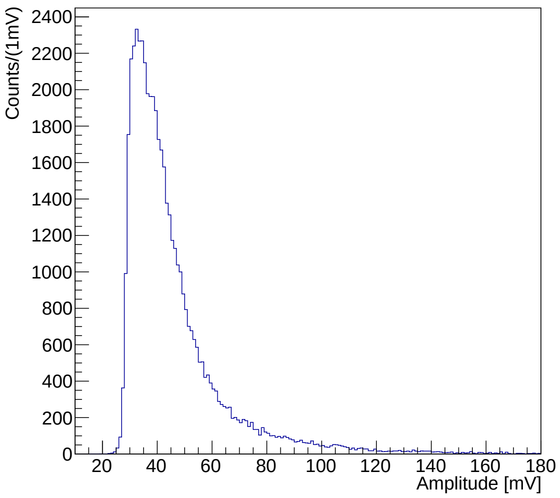

**Fig. 6.17** Pixel-strip signals amplitude distribution at $V_{\mathrm{bias}} = -50\,\mathrm{V}$.

Figure 6.20 shows the effective pixel-strip time resolution measured at different bias voltages, after the subtraction in quadrature of the MCP-PMT jitter contribution. Only the Leading Edge and the Spline algorithms results are shown, since the Reference method gives results comparable to those obtained with the Spline. An improvement of the time resolution with the increase of the bias voltage is observed. At a bias voltage of $-100\,\mathrm{V}$ a time resolution of $40.9 \pm 1.0\,\mathrm{ps}$ and $27.2 \pm 0.6\,\mathrm{ps}$ has been measured with the LE and with the Spline methods, respectively.

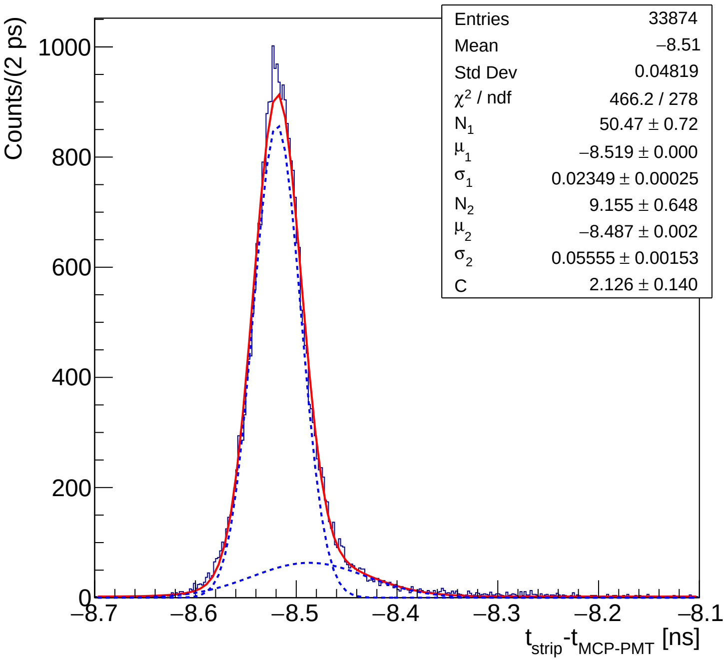

**Fig. 6.18** Distribution of the single pixel ToA with respect to the MCP-PMT, $t_{\text{strip}} - t_{\text{MCP-PMT}}$, at $V_{\text{bias}} = -50\,\text{V}$. The distribution is fitted with the sum of two Gaussian and a constant (in red). Also the two Gaussian are shown (blue dashed lines).

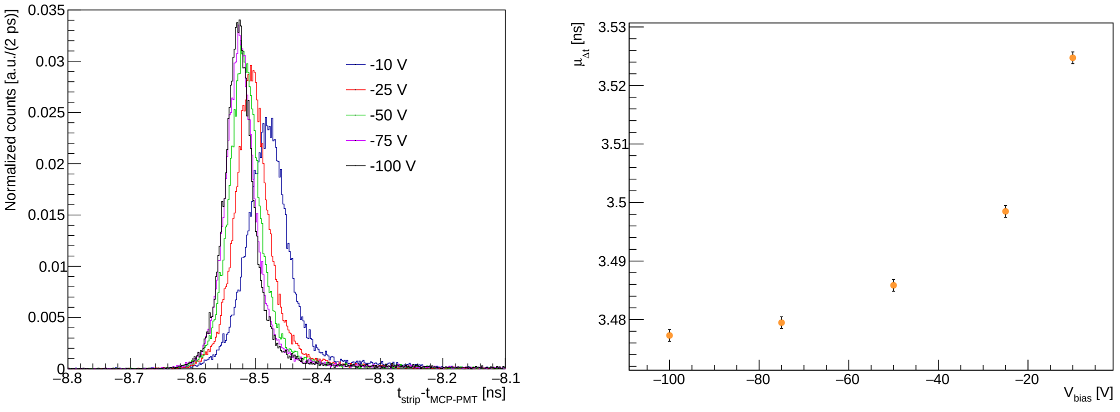

**(a)** **(b)**

**Fig. 6.19** (a) Distribution of the pixel-strip ToA with respect to the MCP-PMT, $t_{\text{strip}} - t_{\text{MCP-PMT}}$, obtained with the Spline method, at different bias voltages and normalized to the integral. (b) Mean value $\mu$ of the ToA distributions obtained with the Spline method as a function of the pixel-strip bias voltage. The $\mu$ value itself is not relevant, but it is important the trend with the bias voltage.

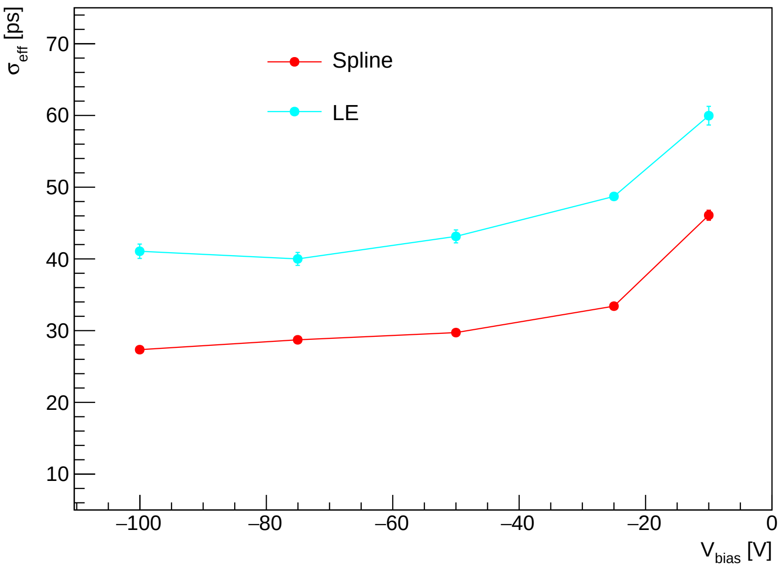

**Fig. 6.20** Effective time resolution $\sigma_{\text{eff}}$ of the pixel-strip as a function of the bias voltage, estimated with the Leading Edge and the Spline methods. The MCP-PMT time jitter contribution has been subtracted in quadrature.

The ToA distribution of the pixel-strip is a little wider with respect to that of the single pixel. In particular, the tail is longer in the pixel-strip, as shown in Figure 6.21a. In Figure 6.21b the results of the effective time resolution as a function of the bias voltage measured for the two sensors are summarized, displaying a similar behaviour of the time resolution with the bias voltage and a slightly better performance of the single pixel with respect to the pixel-strip. This is due to the presence in the pixel-strip of the *side region*, whose impact to the time resolution has been studied in detail for the double pixel test structure (Section 5.1.5).

### 6.1.4 Summary

In this section, the laboratory setup to test TimeSPOT sensors with minimum ionizing particles and some of the measurements performed have been presented. The setup is composed by a $^{90}$Sr source, emitting electrons up to 2.2 MeV, the DUT and an MCP-PMT used as time reference and also as energy selector of the electrons. The behaviour of the electrons emitted by this radioactive source in silicon has been studied through a `Geant4` simulation, showing how strong the impact of multiple scattering is in this setup, while it is negligible at the test beam energies. Because of this, this setup allows to measure only an upper limit of the sensors time resolution, which can

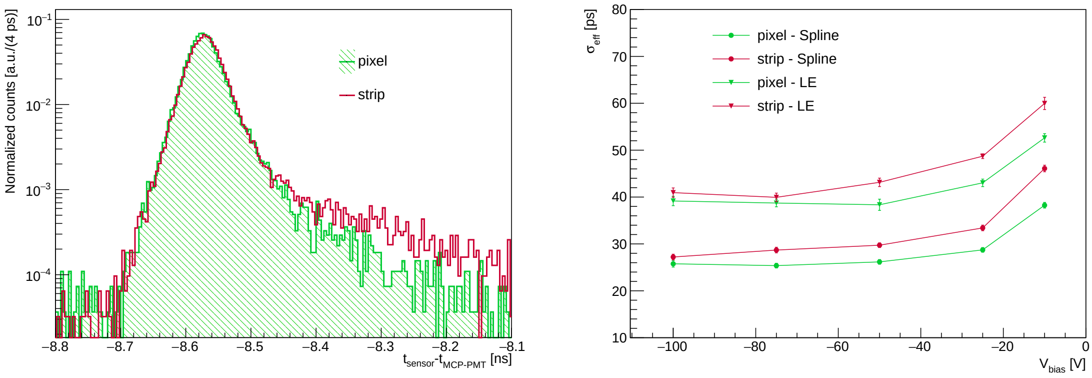

**(a)** **(b)**

**Fig. 6.21** (a) Distribution of the ToA with respect to the MCP-PMT of the single pixel (in green) and the pixel-strip (in magenta) at $V_{\text{bias}} = -75\,\text{V}$ normalized to the histograms integral. (b) Effective time resolution $\sigma_{\text{eff}}$ of the single pixel and the pixel-strip at different bias voltages, obtained with the LE and the Spline methods.

be more precisely measured at the test beam. Moreover, it presents the issue of having the DUT in the trigger and this could bias the measurement rejecting signals with an amplitude below the trigger threshold. But nevertheless it represents an important tool for the characterization of silicon sensors directly in the laboratory, allowing to make preliminary measurements of time resolution and to compare different test structures. Here, measurements of time resolution of a TimeSPOT single pixel and of a pixel-strip have been presented. Both test structure resulted to have a time resolution better than 30 ps at $V_{\text{bias}} = -100\,\text{V}$, with time resolution of the single pixel systematically slightly better than that of the pixel-strip at the different bias voltages applied, which presents a longer tail in the time distribution, due to the presence of the side region.

## 6.2 Sensors characterization with infrared laser

A preliminary comparison of TimeSPOT sensors with different pitch sizes with respect to the nominal pitch of 55 $\mu$m is presented in this Section. These studies have been done in order to explore the possibility of using these sensors for the same 4D-tracking applications or similar. A larger pitch size, for example, could be easier to produce, while a smaller pitch size is potentially more rad-hard and could have an even better resolution with respect to the 55 $\mu$m pitch.

These measurements have been performed by using a laser-based setup developed in Cagliari within the TimeSPOT project and used to characterize these 3D-trench silicon sensors in laboratory. This setup, shown in Figure 6.22 [92], provides the opportunity to excite the sensor and measure its response at a sub-pixel level [93], which is a characterization complementary to that done with the $^{90}$Sr source setup or in a test beam, that instead allow to measure the overall sensor response from all its active area.

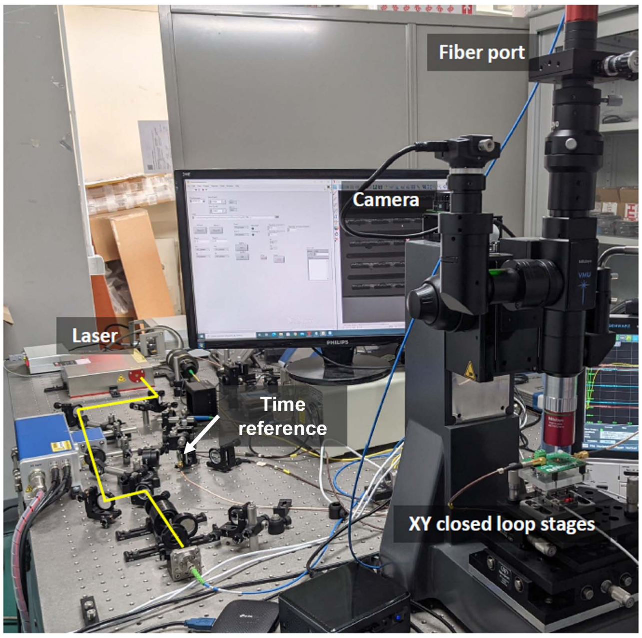

**Fig. 6.22** Laser-based test station realized in our laboratory, in Cagliari, within the TimeSPOT project.

The setup consists of an infrared (IR) laser, OneFive Origami 10 [94], with a duration pulse lower than 200 fs, a wavelength of 1030 nm and a repetition frequency of 40 MHz. The laser beam travels in open space, then it is focused on a fiber port and transported to the microscope by means of a mono-mode optical fiber. The microscope allows to focus the light on a very small spot of 1.8 $\mu$m FWHM, on the sensor active area. A digital camera is used to visualize the sensor and the laser light spot, while $x$-$y$ piezoelectric closed loop stages allow to move the sensor with respect to the laser spot. The light attenuation length in silicon at a wavelength of 1030 nm is about 330 $\mu$m so the laser pulse energy is deposited almost uniformly in the TimeSPOT sensor 150 $\mu$m thickness, as shown by the plot of the beam propagation in the sensor thickness in Figure 6.23. This allows to use this laser to emulate the passage of a minimum ionizing particle in the sensor active volume. The time reference used in this setup consists of another TimeSPOT sensor mounted on a FEE board and illuminated by a laser spurious reflection, and it is able to provide a laser pulse time stamping with an accuracy better than 1 ps [92]. This represents the accuracy of the system in measuring the ToA of sensor signals.

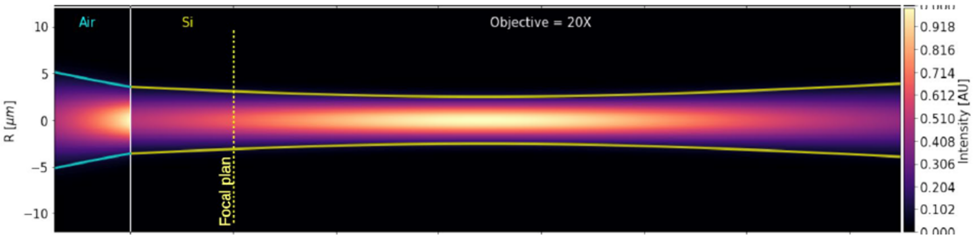

**Fig. 6.23** The 1030 nm laser beam spot size and intensity at each point in 150 $\mu$m silicon thickness.

The measurements shown in this section are spatial laser scans of the silicon sensor under test. In particular a comparison between three different pitch sizes is illustrated. To make a spatial laser scan, the sensor is moved with respect to the laser beam with a 1 $\mu$m step and 1000 signal waveforms are recorded in each position, from both the sensor under test and the time reference, by using an 8 GHz analog bandwidth 20 GSa/s, 4-channels digital oscilloscope Rohde & Schwarz RTP084. The movement system and the data acquisition is controlled by means of a LabVIEW program, then the acquired waveforms are analyzed offline. Sensors can be illuminated from the front or from the back (Figure 6.24), allowing, in this second scheme, to avoid some metallized areas that are present on the surface of the sensors.

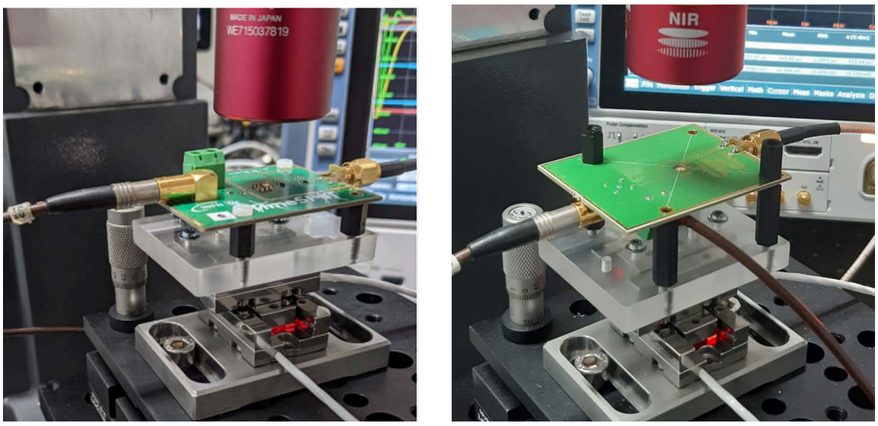

**Fig. 6.24** Silicon sensor illuminated from the front (left) and from the back (right) by the laser beam.

### 6.2.1 Results

In this section a comparison between TimeSPOT sensors with a different pitch size is presented. The three test structures tested are shown in Figure 6.25. All the three structures are pixel strips, consisting of seven or ten pixels connected to the same readout pad and they differ from each other for the pixel dimensions: $27.5 \times 27.5\,\mu\text{m}^2$, $55 \times 55\,\mu\text{m}^2$ and $110 \times 55\,\mu\text{m}^2$.

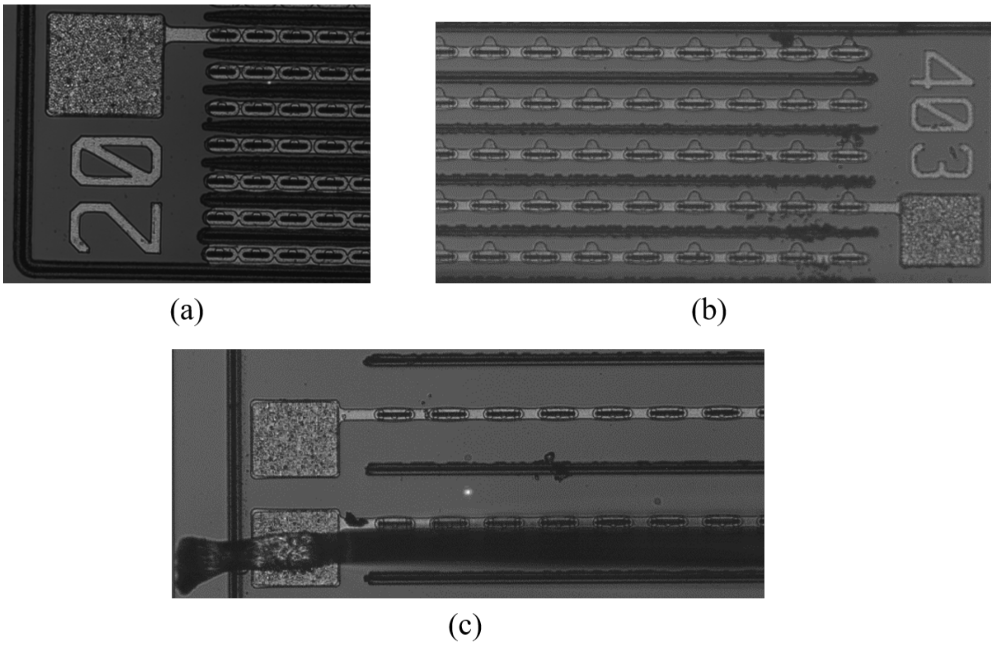

(a) (b)

(c)

**Fig. 6.25** (a) Strip of seven $27.5 \times 27.5$ $\mu\text{m}^2$ pixels. (b) Strip of ten $55 \times 55$ $\mu\text{m}^2$ pixels. (c) Strip of ten $110 \times 55$ $\mu\text{m}^2$ pixels.

Taking into account the different distance between readout and bias trenches in the three sensors, we applied an appropriate bias voltage in order to have a similar electric field in three structures, achieved by increasing the bias voltage with the increase of the pitch size. In the $27.5\,\mu$m pitch sensor, it was not possible to apply the proper bias voltage of $-25\,\text{V}$ to have similar electric field conditions in the three sensors, because of the high leakage current of the particular test structure used, so a $V_{\text{bias}} = -15\,\text{V}$ was applied. The $27.5\,\mu$m pitch and the $55\,\mu$m pitch sensors were illuminated from the back, while the $110\,\mu$m pitch sensor was illuminated from the front, so in this last case the inter-pixel region is not visible because of the metallization connecting the ten readout trenches of the strip. In Figure 6.26 the ToA maps obtained illuminating the three strips under test are shown, with the readout trenches marked with a dashed red box. The inactive trenches areas are cut off from the map by applying a signal

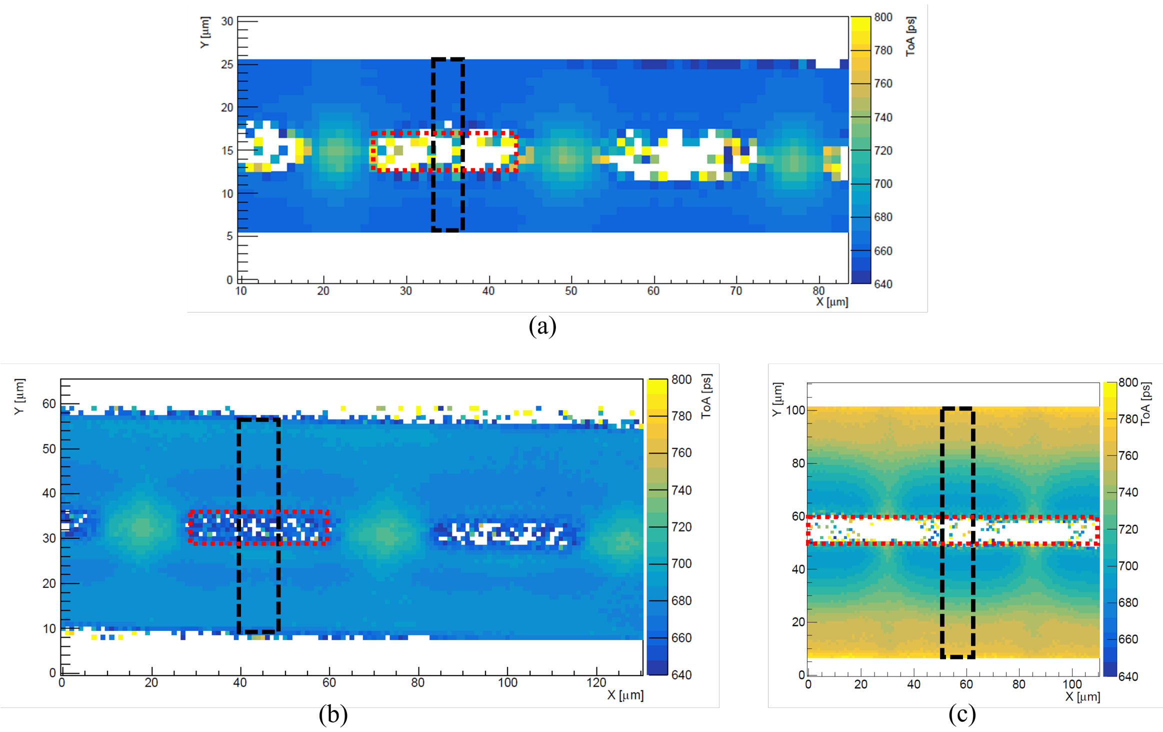

(a)

(b)

(c)

**Fig. 6.26** Map of the average ToA per position for (a) a strip of seven $27.5 \times 27.5\,\mu\text{m}^2$ pixels at $-15$ V bias voltage, (b) a strip of ten $55 \times 55\,\mu\text{m}^2$ pixels at $-50$ V bias voltage and (c) a strip of ten $110 \times 55\,\mu\text{m}^2$ pixels at $-100$ V bias voltage. For each position in the map the average ToA is calculated on 1000 waveforms. The dashed black box indicates the central slice of the pixel, used to evaluate the residual non-uniformity of the sensors disregarding inter-pixel regions, while the dashed red box indicates the position of the readout trenches.

amplitude selection in order to focus only on the active region of the sensors. The sensors with a pitch of 27.5 $\mu$m and 55 $\mu$m show a very uniform ToA map and, as expected, the smaller the pitch the greater the uniformity, especially in the central region of the pixel. On the other hand, the pixel with 110 $\mu$m pitch shows very slow regions that make this pixel dimension present a worse time resolution, at least in this electric field condition. Focusing on the central slice of the pixel of each sensor, defined by the black box in Figure 6.26, and taking the average ToA for each position inside the slice, it is possible to evaluate the residual non-uniformity of the sensor without considering inter-pixel regions. Since averages of the measured ToA are performed for each position, the electronic jitter can be considered negligible, allowing to evaluate the intrinsic sensor response [93]. The standard deviation of the average ToA distribution in the central slice decreases as the pitch of the sensor decreases, from about 30 ps for 110 $\mu$m pitch to 5 ps for 55 $\mu$m pitch and down to 2 ps for the smallest pitch of 27.5 $\mu$m.

These results confirm the excellent performance of the $55\,\mu$m pitch size sensors and show potential and drawbacks of the other pitch sizes investigated. The $110\,\mu$m pitch size presents a worse time resolution because of the less uniformity and intensity of the electric field. However, in the event that it is possible to operate such devices at an higher bias voltage ($< -100\,$V) to get closer to the velocity saturation condition, this sensor could be an option for detectors that have less stringent requirements in terms of spatial resolution, such as the NA62 GigaTracker in the HIKE program, which requires a pitch size $\leq 300\,\mu$m. The $27.5\,\mu$m pitch sensor, instead, has a better time resolution and a higher radiation hardness, but as disadvantages it has a higher capacitance and a larger portion of dead volume, since trenches have the same dimensions of the $55\,\mu$m pitch sensor ones. The measurements reported in this section show that the $55\,\mu$m pitch size sensor is the most performing and appropriate sensor for the upgrades of the high luminosity experiments mentioned in Chapter 1.

# Chapter 7

# TimeSPOT sensors test beam before irradiation

Two test beam campaigns at the CERN Super Proton Synchrotron (SPS) H8 beamline for non irradiated TimeSPOT sensors characterization were conducted in October 2021 and in May 2022. Tests have been made with a 180 GeV/c positive hadrons beam, mainly composed by pions. In this Chapter, the setup designed and realized is described, the analysis method and the performed measurements of detection efficiency, timing performance and charge sharing between two pixels are illustrated. Also, a comparison with measurements made with the $^{90}$Sr source setup, regarding timing performance, is shown.

## 7.1 Test beam setup

The test beam setup designed and realized is shown in Figure 7.1a. Two TimeSPOT sensors, wire-bonded to their own FEE boards are mounted inside an electromagnetically shielded and light-tight box, one after the other along the beam line direction, $z$. One of the two 3D sensors is installed on a fixed mount, while the other one is mounted on two closed-loop piezoelectric linear stages [95] (Figure 7.1b) that allow up to 16 mm movements with 10 nm position accuracy in the transversal directions $(x, y)$ with respect to the beamline. There is also the possibility to mount one of the two silicon sensors on a manually rotating mount around the vertical direction to measure sensor performance at non-normal beam incidence (Figure 7.1b).

As time reference detector of our setup, two 18 mm diameter and 5.5 mm thick quartz input window microchannel plate photomultiplier tubes (MCP-PMTs) are used, providing a particle timestamp with a precision in the range of $(3-4)$ ps using the average

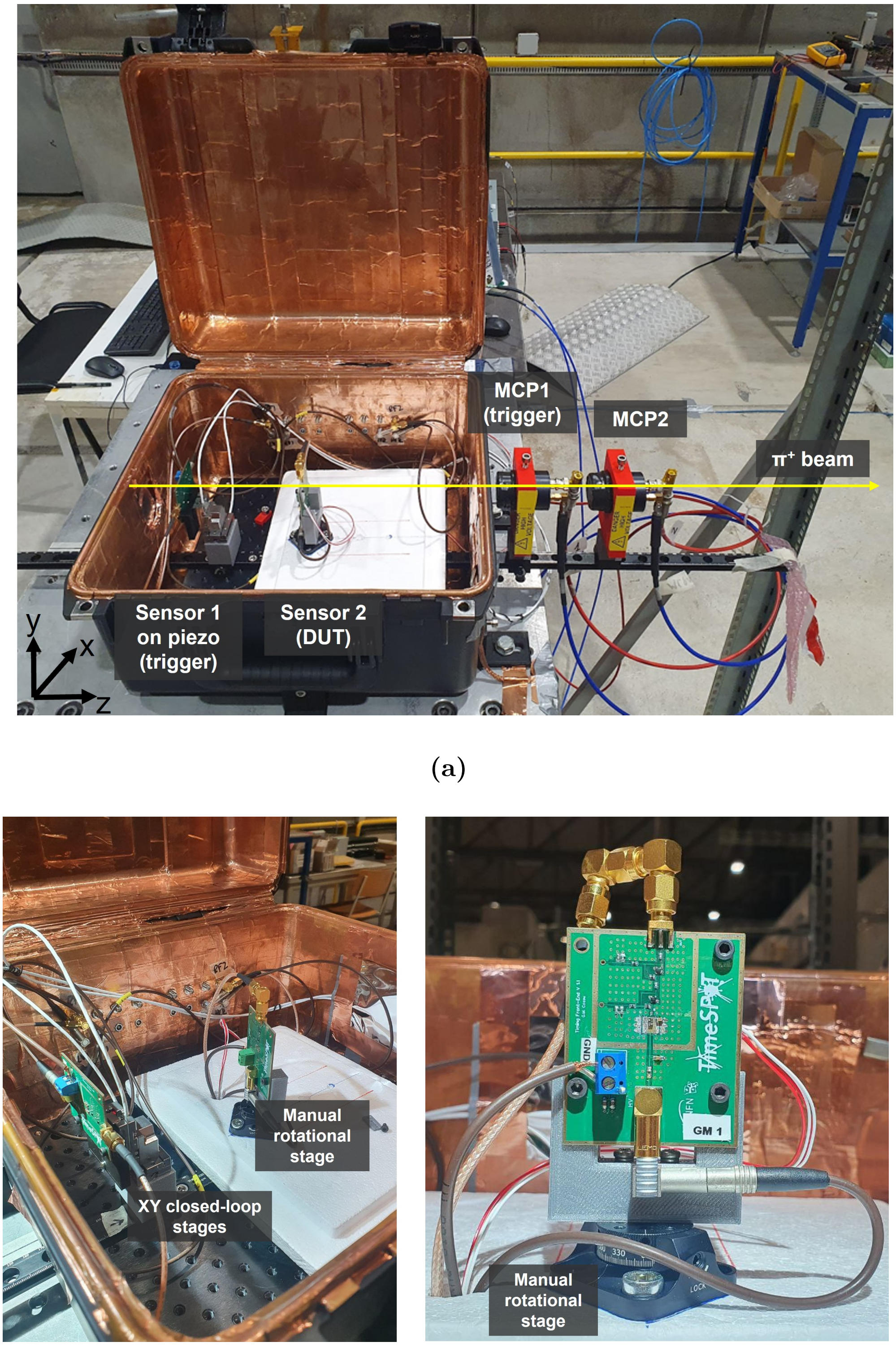

(a)

(b)

**Fig. 7.1** The setup used for the two test beam campaigns at CERN SPS/H8 beamline. (a) The sensors mounted on their FEE boards inside the electromagnetically shielded and light tight box and the two MCP-PMTs downstream. (b) The upstream board mounted on piezoelectric stages and the second board mounted on a manual rotational stage.

time of the two. The data acquisition (DAQ) system consists on an 8 GHz analog bandwidth 20 GSa/s 4 channels digital oscilloscope Rhode & Schwartz RTP084, used to acquire the signals from the silicon sensors and the two MCP-PMTs. The oscilloscope trigger condition is chosen on the basis of the measurement performed. A typical event acquired with this setup and seen at the oscilloscope is shown in Figure 7.2. The specific configuration of the setup and the oscilloscope trigger for each measurement is described in the results Section 7.3.

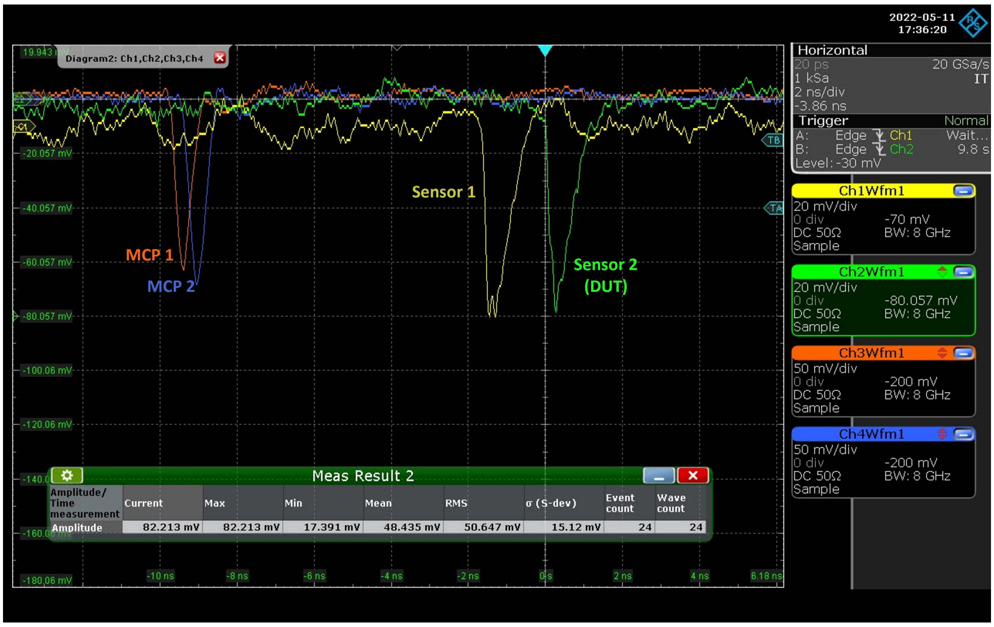

Horizontal
20 ps 20 GSa/s
1 kSa IT
2 ns/div
-3.86 ns
Trigger Normal
A: Edge Ch1 Wait...
B: Edge Ch2 9.8 s
Level: -30 mV

Ch1Wfm1
20 mV/div
0 div -70 mV
DC 50Ω BW: 8 GHz
Sample

Ch2Wfm1
20 mV/div
0 div -80.057 mV
DC 50Ω BW: 8 GHz
Sample

Ch3Wfm1
50 mV/div
0 div -200 mV
DC 50Ω BW: 8 GHz
Sample

Ch4Wfm1
50 mV/div
0 div -200 mV
DC 50Ω BW: 8 GHz
Sample

Meas Result 2

| Amplitude/ Time measurement | Current | Max | Min | Mean | RMS | σ (S-dev) | Event count | Wave count |
|---|---|---|---|---|---|---|---|---|
| Amplitude | 82.213 mV | 82.213 mV | 17.391 mV | 48.435 mV | 50.647 mV | 15.12 mV | 24 | 24 |

**Fig. 7.2** A typical event acquired during the data taking. The signals from the two silicon sensors are shown in yellow and green and the signals from the two MCP-PMTs are shown in orange and blue. The relative timing between silicon sensors and MCP-PMTs signals is digitally adjusted to optimize the trigger condition used.

On average, $10^6$ particles are extracted every 30 seconds in a 4 seconds-long spill and are focused on an approximately circular spot of $(6-8)$ mm sigma radius measured immediately before our setup location.

An initial alignment of the setup with the beam was performed using a laser level and adjusting the moving table $(x, y)$ position to center the two targets mounted on the red holders in Figure 7.3a so that the detectors were aligned with the beam direction. This guarantees the relative alignment between the beam line and the optical rail. An USB microscope mounted on a sliding support was used to measure the position of the downstream silicon sensor and to perform a pre-alignment of the silicon sensor mounted on remote controllable $x$-$y$ piezoelectric stages (Figure 7.3b) with respect to the downstream silicon sensor. The final alignment between silicon sensors was made with the beam, moving the sensor on the piezoelectric stages to maximize the coincidence rate with the reference sensor. The coincidence counts measured in a single pixel $x$ and $y$ scan are shown in Figure 7.4. It is important to underline that thanks to this system for the alignment of two TimeSPOT sensors, it was possible to not put the DUT on the acquisition trigger (unlike in the first test beam), allowing to avoid to bias the measurements.

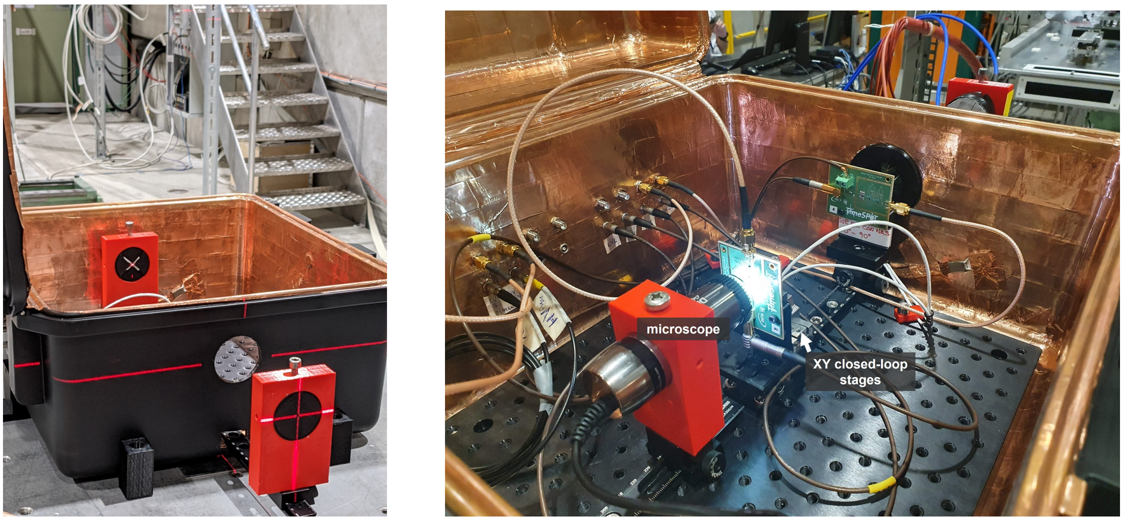

**(a)** **(b)**

**Fig. 7.3** (a) Picture of the black box placed on the moving table. The laser level is visible and centered on the two targets used to align the rail with the sensors with the beam line direction. (b) Picture of the pre-alignment procedure with the microscope in front of the board mounted on x-y closed-loop stages in order to move this board such that the silicon sensor is in the position of the downstream sensor.

## 7.2 Data analysis

The Time of Arrival (ToA) of each silicon sensor signal is determined by means of the three algorithms described in Section 6.1.2: *Leading Edge* (LE), *Spline* and *Reference* methods. For the two MCP-PMTs the Spline method is used, since no improvements are observed applying the Reference method. All methods parameters are the same as those used in the analysis of data taken with the $^{90}$Sr source setup.

Moreover, in this test beam data analysis, an amplitude-dependent correction of the Leading Edge method has been applied, in order to remove the time-walk effect. This *Leading Edge amplitude corrected* method is based on the correlation between the ToA of the signal measured with the LE algorithm and the signal amplitude $A$, that is

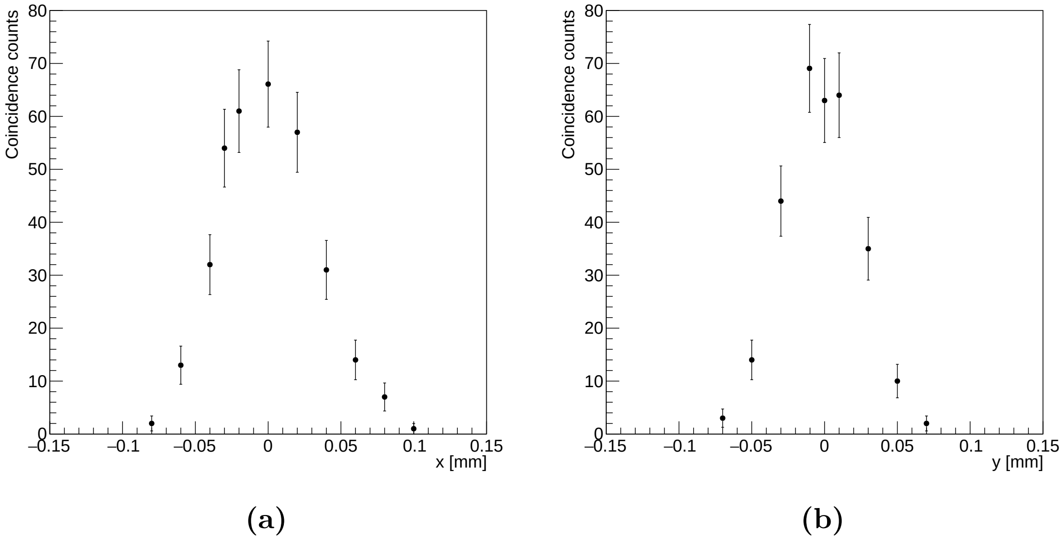

**(a)** **(b)**

**Fig. 7.4** Coincidence counts between two single pixels in a scan along (a) $x$ and (b) $y$ direction.

shown in Figure 7.5. A fifth order polynomial function is used to fit this dependence and the ToA corrected for the amplitude is calculated as

$$t_{LE,corr} = [t_{LE} - (p_0 + p_1A + p_2A^2 + p_3A^3 + p_4A^4 + p_5A^5)] - \langle t_{MCP-PMTs} \rangle \quad (7.1)$$

where $t_{LE}$ is the ToA measured with the LE before the correction, $p_i$ are the fit parameters and $\langle t_{MCP-PMTs} \rangle$ is the average of the time measured by the two MCP-PMTs.

## 7.3 Results

In this section the results of the two test beam campaigns at SPS/H8 beamline are illustrated, in particular the studies reported are: detection efficiency, timing performance and charge sharing between two adjacent pixels.

Several preliminary measurements, not shown here, have been performed at the beginning of the test beam, like the optimization of the High Voltage (HV) applied to the two MCP-PMTs and the fine alignment of the table making an $x$-$y$ scan of the rate in a silicon sensor. After the MCP-PMTs HV optimization, the distribution of the time difference between the two devices in Figure 7.6 is obtained, from which it follows

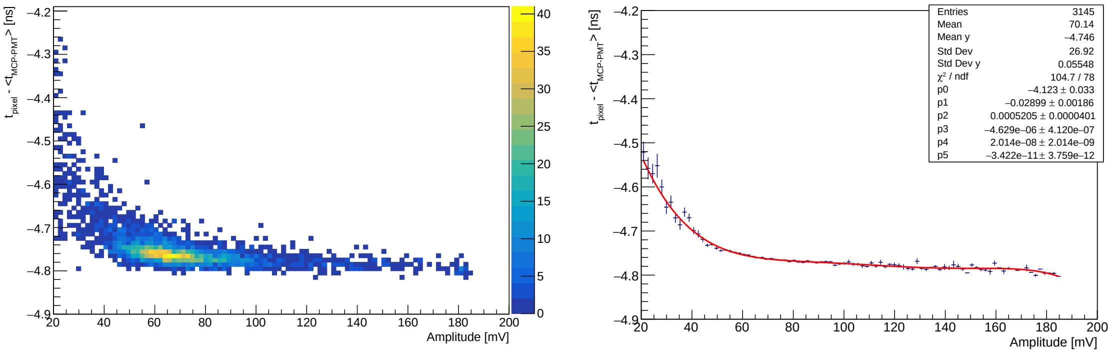

**(a)** **(b)**

**Fig. 7.5** (a) Distribution of the time of arrival of the single pixel measured with the LE method with respect to the time reference $t_{pixel} - \langle t_{MCP-PMT} \rangle$ as a function of the pixel signal amplitude. (b) Profile of the single pixel ToA as a function of its signal amplitude with the $5^{th}$ order polynomial fit, used for the amplitude-dependent correction of the method, shown in red.

that the precision of our time reference, using the average time measured by the two photodetectors, was in the range of $(3-4)$ ps.

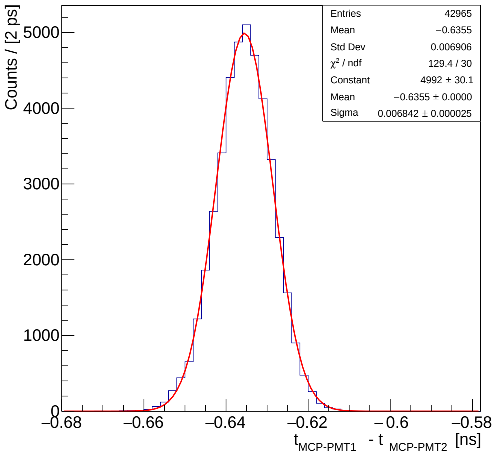

**Fig. 7.6** Distribution of the time difference measured between the two MCP-PMTs, $t_{MCP-PMT1} - t_{MCP-PMT2}$.

### 7.3.1 Single pixel timing performance at 0°

The energy deposit inside the sensor active area depends on the track length, that in the case of 0° incident beam angle (normal incidence), is equal to the sensor thickness, 150 $\mu$m for a TimeSPOT sensor. For an angled beam (see Section 7.3.2), instead, the track length distribution widens, since the length of the particle path in the sensor active volume increases or decreases depending on the impact point on the pixel surface. In Figure 7.7 the amplitude distributions of the single pixel at beam normal incidence, obtained at different bias voltages in the range $(-7, -100)$ V, are shown. The peaking contribution above 20 mV is associated to sizeable energy deposits in the sensor, while the contribution that populates the region below 20 mV is due to the noise. The amplitude distributions follow the characteristic Landau shape. For $V_{\text{bias}} \leq -50$ V the distributions overlap almost perfectly, while for $V_{\text{bias}} > -50$ V the distributions are shifted to lower amplitude values. The reduced signal amplitudes observed at low absolute bias voltages are due to the effect of the fast front-end electronics on the slower signals (ballistic deficit). Anyway, the sensor shows very good performance also at low absolute bias voltages.

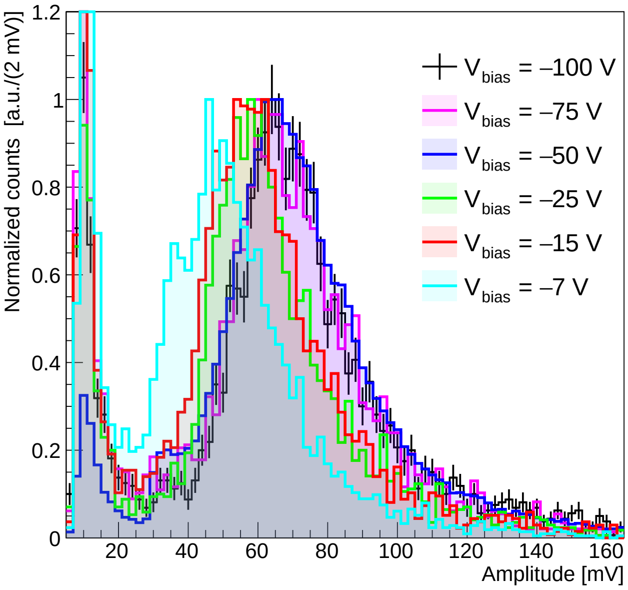

**Fig. 7.7** Amplitude distribution of the single pixel at normal beam incidence and for different bias voltages. The distributions are normalized at the Landau peak.

The setup for the measurement of TimeSPOT sensors timing performance consists in: two single pixels, one of which is our device under test, and the two MCP-PMTs. The acquisition trigger condition is the coincidence of the other single pixel and one of the two MCP-PMTs, indicated as *Sensor 1* and *MCP 1* in Figure 7.1a. A single pixel test structure is shown in Figure 7.8. The time resolution of the DUT was measured at different bias voltages, in a range from $-7\,\mathrm{V}$ and $-100\,\mathrm{V}$.

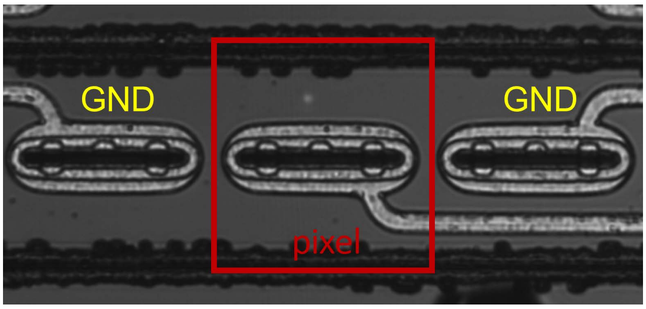

**Fig. 7.8** Single pixel test structure consisting of seven adjacent pixels, where the three innermost, visible in the picture, can be individually readout. For the measurements here described the central pixel is that one under test, while the two adjacent pixels are grounded to guarantee the central pixel proper electric field conditions.

Figure 7.9a shows the distribution of the difference between the ToA of the single pixel and the Time-Tagger, $t_{\mathrm{pixel}} - \langle t_{\mathrm{MCP-PMT}} \rangle$, at a bias voltage of $-100\,\mathrm{V}$. The distribution consists of a peaking structure, due to particles crossing the DUT and releasing energy inside it, and a constant contribution due to noise events. The distribution is described by the sum of two Gaussians, for the peak, and a constant contribution, for the background, for the reasons explained in Section 6.1.2. At the maximum bias voltage applied of $-100\,\mathrm{V}$ and with the most performing Reference method, the effective time resolution of the single pixel is $\sigma_t^{\mathrm{pixel}} = 12.4 \pm 1.3\,\mathrm{ps}$, after the subtraction in quadrature of the time reference jitter contribution.

In Figure 7.9b the measured effective time resolution of a 3D trench single pixel at different bias voltages with the four different methods described before, is shown. The pixel shows an almost constant time resolution for $V_{\mathrm{bias}} \leq -25\,\mathrm{V}$, while it worsens at higher (absolute value) bias voltages. This worsening is related to both the specific fast front-end electronics used for these measurements, that is less efficient in collecting the full charge from slow signals, and to the increase of differences in velocity between the two types of charge carriers at low absolute bias voltage, that affects the sensor uniformity. The best single pixel timing performances are obtained using the Reference method, that allows to mitigate the time jitter contribution due to rise time fluctuations.

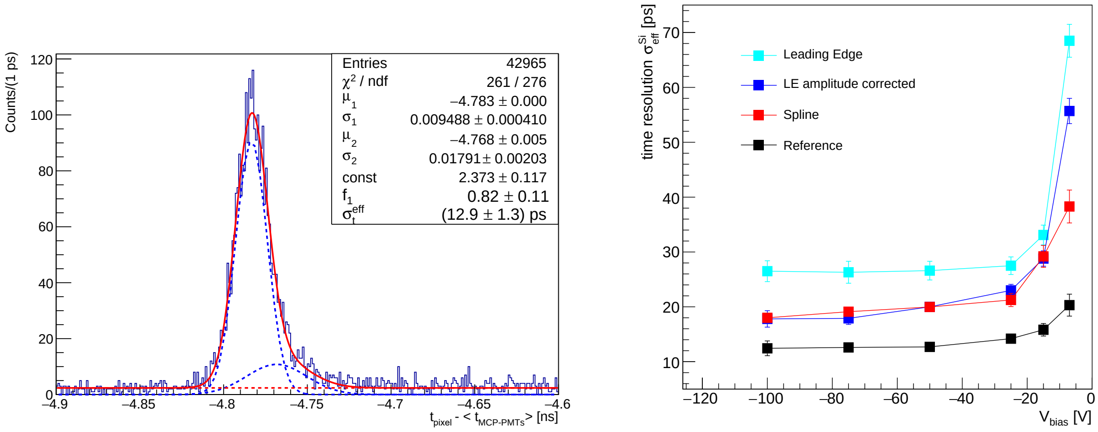

**(a)** **(b)**

**Fig. 7.9** (a) Distribution of the difference between the TOA of the single pixel and the time reference, $t_{\mathrm{pixel}} - \langle t_{\mathrm{MCP-PMT}} \rangle$, for the single pixel at $V_{\mathrm{bias}} = -100$ V with the *reference* method. The distribution is fit with the sum of two Gaussian functions (blue dashed lines) describing the signal, and a constant (red dashed line) modelling the background. (b) Effective time resolution of the single pixel at different bias voltages for different analysis methods. Here the contribution due to the resolution of the time reference is subtracted.

The Leading Edge method, despite its simplicity, provides time resolutions lower than 30 ps for $V_{\mathrm{bias}} \leq -25\,\mathrm{V}$, while with the correction for the signal amplitude results compatible with those of the Spline method are obtained for $V_{\mathrm{bias}} \leq -15\,\mathrm{V}$.

Figure 7.10 shows the time distributions of $t_{\mathrm{pixel}} - \langle t_{\mathrm{MCP-PMT}} \rangle$ obtained with the Leading Edge method (in blue) and with the LE corrected for the amplitude signal (in red) at $V_{\mathrm{bias}} = -50\,\mathrm{V}$. It allows a qualitative comparison between the two distributions, showing how the core distribution becomes narrower and the tail becomes shorter in the distribution obtained after the amplitude-dependent correction of the ToA. Figure 7.11 shows the same two distributions with the fit function, for a quantitative comparison. In this run the effective time resolution improves from $\sigma_t = 26.6 \pm 1.7\,\mathrm{ps}$ to $\sigma_t = 20.0 \pm 0.9\,\mathrm{ps}$ by applying the correction of the ToA for the signals amplitude.

### Comparison with laboratory results

In Chapter 6 it has been explained that the results obtained at the test beam and in laboratory with the $^{90}$Sr source are expected to be different, because of the relevance of multiple scattering at the energies of the electrons emitted by the $^{90}$Sr source, which is negligible at the SPS/H8 beamline energies. The multiple scattering, indeed, is such

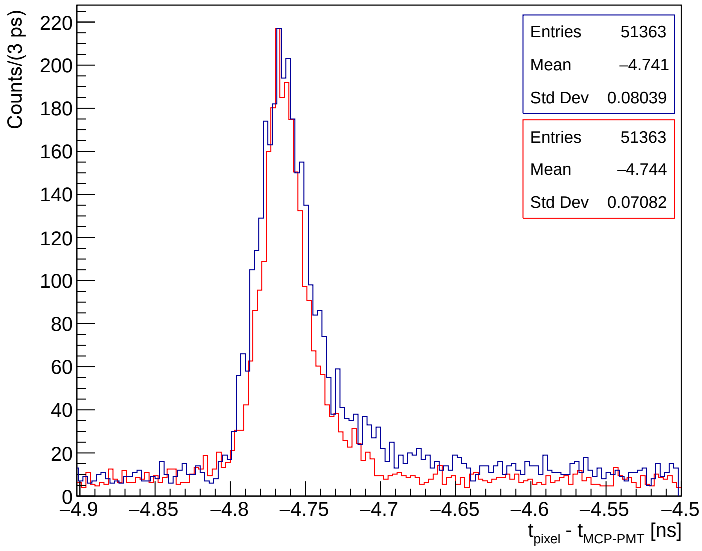

**Fig. 7.10** Distribution of the $t_{\text{pixel}} - \langle t_{\text{MCP-PMT}} \rangle$ for the single pixel at $V_{\text{bias}} = -50\,\text{V}$ with the Leading Edge method (in blue) and with the LE corrected for the signal amplitude (in red). The red distribution has been shifted just to facilitate a visual comparison. The distributions are normalized to the maximum.

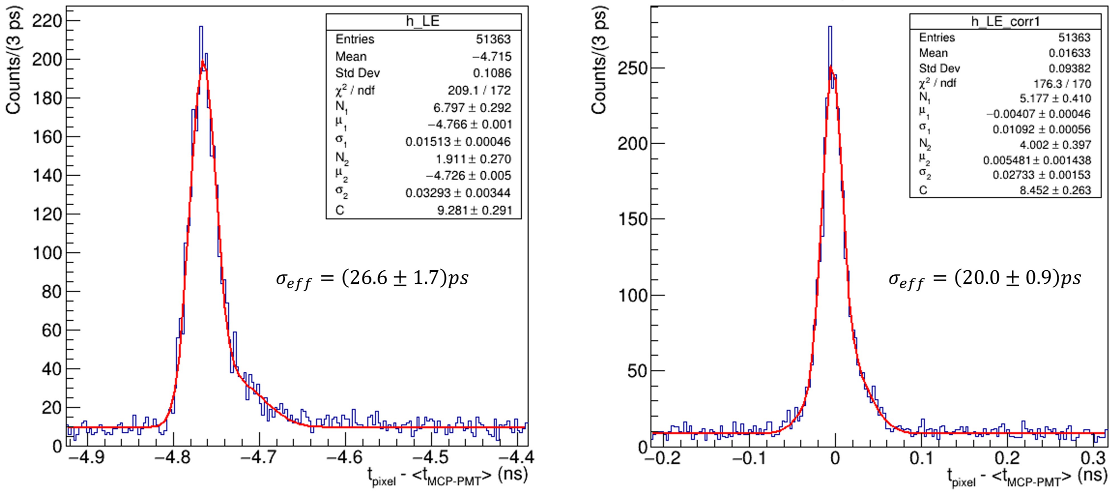

(a) (b)

**Fig. 7.11** Distribution of the $t_{\text{pixel}} - \langle t_{\text{MCP-PMT}} \rangle$ for the single pixel at $V_{\text{bias}} = -50\,\text{V}$ (a) with the *Leading Edge* method and (b) with the LE corrected for the signal amplitude. The distributions are fitted with the sum of two Gaussian functions and a constant.

that the energy deposit in the sensor is smaller in laboratory (Figure 7.12) with respect to the test beam and the signals amplitude distributions are quite different.

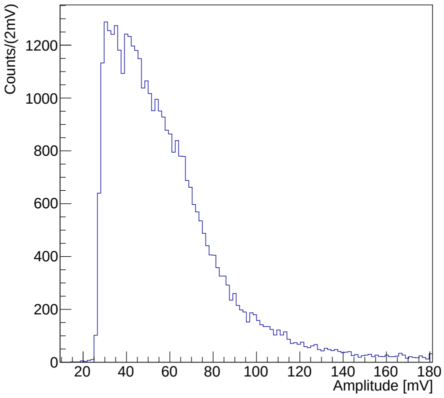

**Fig. 7.12** Single pixel amplitude distribution obtained at $V_{\text{bias}} = -50\,\text{V}$ with the $^{90}$Sr setup.

However, to a first approximation, it is possible to make a comparison by selecting, in the laboratory data, signals with an amplitude larger than 40 mV, in order to reject the signals that are smaller than those measured at the test beam (Figure 7.7). Figure 7.13 shows the effective time resolution measured as a function of the bias voltage in laboratory with the amplitude selection $A > 40\,\text{mV}$ on the single pixel signals and at the test beam. We observe that, with the Spline method, the laboratory results approach test beam results, while still remaining slightly worse, since a simple amplitude selection does not allow to obtain the same Landau-like distribution measured at the test beam. For the same reason, the LE laboratory results deviate even more from those of the test beam; at $V_{\text{bias}} = -7\,\text{V}$ the time resolution measured at the test beam is much higher with respect to that measured at $V_{\text{bias}} = -10\,\text{V}$ with the $^{90}$Sr because in the laboratory the DUT is in the trigger and at this bias voltage a lot of signals have a small amplitude, so a worse time resolution, but in this setup they are rejected by the trigger threshold.

### 7.3.2 Tilted single pixel timing performance

Since it is necessary to operate 3D sensors tilted with respect to the incident particles direction to recover the inefficiency due to the electrodes (see Section 2.5.3), we also performed time resolution measurements on a tilted single pixel sensor, in order to see how much its time resolution is affected by the signal amplitude reduction due to

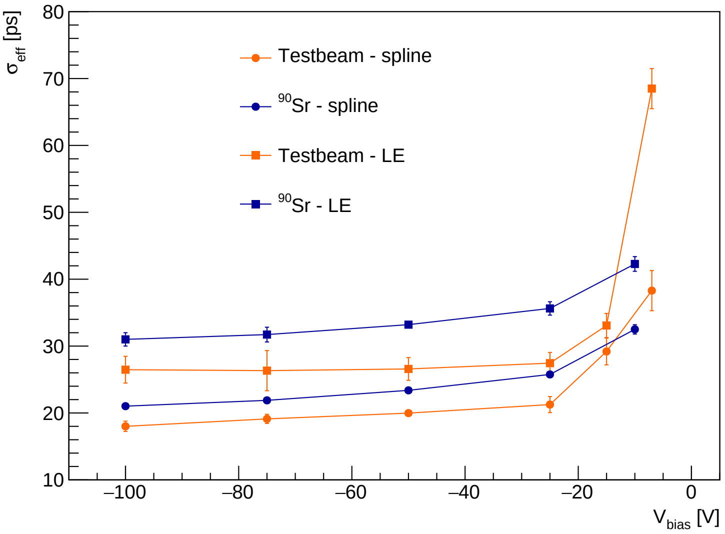

**Fig. 7.13** Effective time resolution of a single pixel measured at different bias voltages in laboratory and at the test beam with Spline and LE methods. The jitter contribution of the time reference detector has been subtracted.

the rotation of the sensor. In fact, for a particle hitting the sensor at an angle $\theta$ with respect to normal incidence, the total track length increases for a fraction of possible hitting positions but decreases whenever the particle crosses a trench, exits or enters into the pixel laterally, consequently the mean particle path length is smaller than at perpendicular incidence. The setup is the same of the measurements performed at normal incidence. The device under test is mounted with the trenches along the vertical axis, that is the rotational axis, as shown in Figure 7.14.

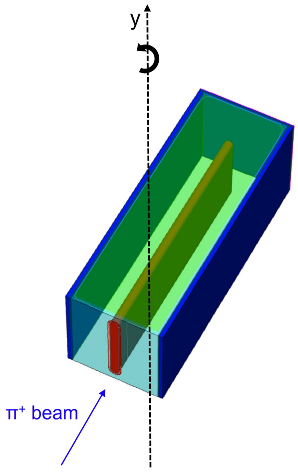

**Fig. 7.14** Rotation scheme of a TimeSPOT pixel.

Figure 7.15 shows the single pixel signals amplitude distributions obtained at normal incidence and at the three tilting angles explored, 5°, 10° and 20°. As expected, as the tilt angle of the sensor increases, the mean amplitude becomes smaller with respect to normal incidence of the particles. For instance, at 10° tilt angle an amplitude reduction of about 30% with respect to normal incidence is observed, so the mean energy loss in the 150 $\mu$m thick TimeSPOT sensor changes from 2 fC (at 0°) to about 1.4 fC. In Figure 7.16 the time resolution of a TimeSPOT single pixel, measured at different incident particle angles and at a bias voltage of $-100$ V, is shown. We observe that the time resolution does not degrade significantly with respect to the normal incidence case and in the worse case, at 20°, the time resolution measured is $\sigma_t = 17.5 \pm 0.9$ ps with the Reference method.

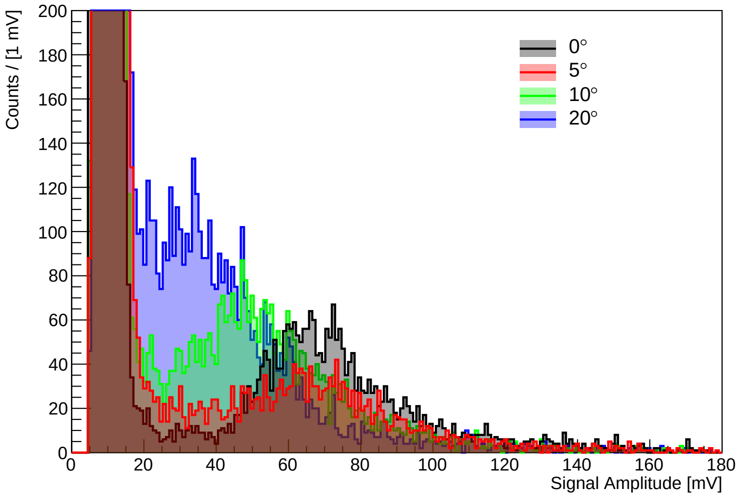

**Fig. 7.15** Amplitude distribution of the single pixel at 0°, 5°, 10° and 20° tilting angles with respect to the beam direction. The single pixel was biased at $V_{bias} = -100$ V.

### 7.3.3 Detection efficiency

Since trenches are non-sensitive volumes of the 3D-trench pixel sensors, if a charged particle goes through a trench it will not be detected. To achieve a full detection efficiency, 3D silicon sensors are usually operated slightly tilted with respect to the beam normal incidence. In this section, measurements of TimeSPOT sensor geometrical efficiency at 0° (normal beam incidence) and at tilting angles of 5°, 10° and 20° with respect to the beam direction are illustrated. For these measurements a triple 3D trench strip, consisting of three adjacent strips, 10 pixels each, connected to the same

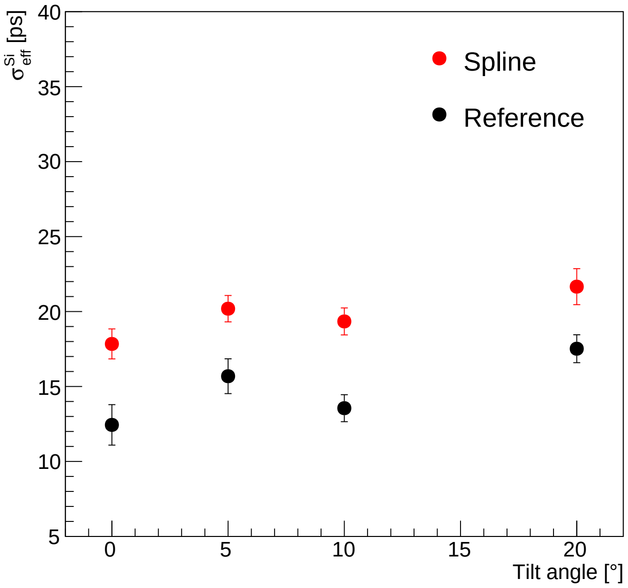

**Fig. 7.16** Time resolution of a single pixel at different tilting angles with the pixel trenches along the $y$ axis. The bias voltage applied to the pixel is $-100$ V.

readout channel of the FEE board (Figure 7.17b), is used as device under test of which we measured the detection efficiency. A single 3D trench pixel has been aligned in the middle of the triple strip active region and it was used as trigger of the acquisition, in AND with one of the MCP-PMTs placed downstream. Moreover, to minimize the overlapping of insensitive volumes, the pixel trenches were oriented perpendicularly to the triple strip trenches. The setup used for these efficiency measurements is shown in Figure 7.17a for the specific tilting angle of 20°.

The efficiency is computed as $\varepsilon = N_{ts}/N_{trks}$, where $N_{ts}$ and $N_{trks}$ are the number of tracks detected by the triple strip and the tracks crossing the triple strip volume, respectively. The number of tracks crossing the triple strip volume, $N_{trks}$, is given by the number of triggered signals with a minimum pulse height both in the single pixel and in the MCP-PMTs in a time window of 200 ps, $N_{trig}$, corrected by the fraction of tracks that miss the triple strip due to the beam divergence, $N_{trks} = N_{\mathrm{trig}} \cdot (1 - f_{\mathrm{miss}})$. This fraction $f_{\mathrm{miss}}$ is estimated using a data sample acquired with the trigger single pixel shifted by 165 $\mu$m along the short side of the triple strip and amounts to $f_{miss} = 1.4 \pm 0.6\,\%$. A particle is considered detected by the triple strip in case the measured ToA relative to the time reference, $t_{\mathrm{3strip}} - \langle t_{\mathrm{MCP-PMT}} \rangle$, is consistent with the expected value given by the time of flight, that means it is in the peak of the time distribution shown in

Figure 7.18a. Such method has been proven to be successful also for small signal amplitudes, consistent with the noise level.

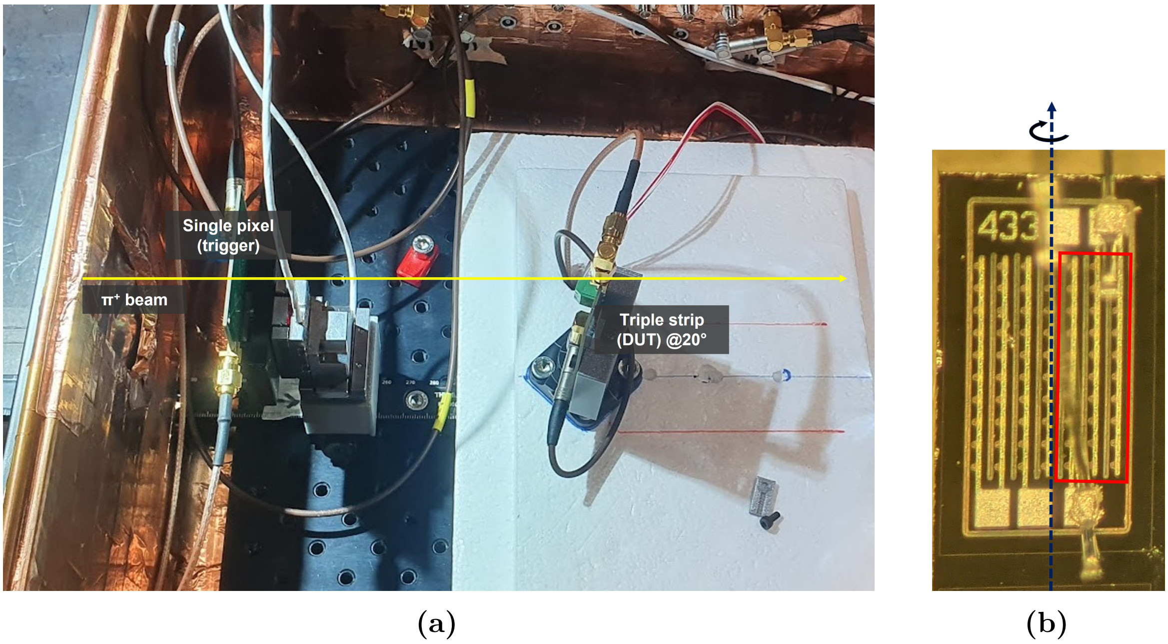

**Fig. 7.17** (a) Setup for detection efficiency measurements. The board with the single pixel used as trigger and mounted on piezoeletric stages upstream and, behind it, the board with the triple strip mounted on the manual rotational stage (in this picture it is rotated 20° with respect to normal incidence). (b) Picture of the test structure used for efficiency measurements. The three strips wire bonded to the FEE board are those in the red box. The rotation axis is also shown.

Figure 7.18a shows the distribution of the difference between the ToA of the triple strip and the time reference detector. The number of tracks detected by the triple strip, $N_{ts}$, is determined by fitting the distribution with a peaking function given by the sum of a Gaussian and an exponential convoluted with a Gaussian, modelling the detected tracks, and a constant function, describing the undetected tracks which have random ToA values. At 0° incident beam angle the efficiency is measured to be $\varepsilon = 79.0 \pm 0.7\,\%$, where the uncertainty accounts for both statistical and systematic contributions. The systematic uncertainty includes uncertainties related to the different methods used to determine the ToA (Section 7.2), to the choice of the fit function to calculate the detected tracks and the uncertainty on the fraction $f_{\text{miss}}$. As a cross check, the efficiency is also calculated by counting the number of events for which the triple strip signal has an amplitude above a certain threshold. For thresholds above 10 mV the results substantially agree with those obtained from the fit to the time distribution,

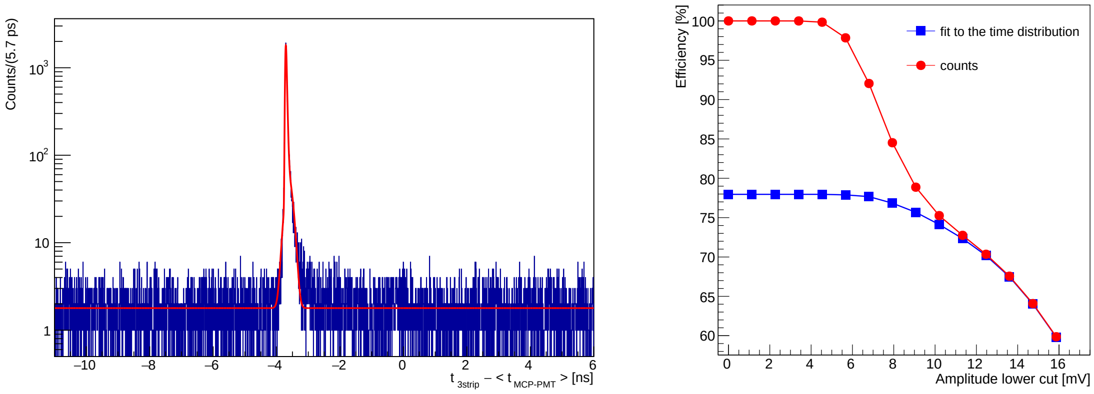

**(a)** **(b)**

**Fig. 7.18** (a) Distribution of the difference between the TOA of the triple strip and the time reference, $t_{3\text{strip}} - \langle t_{\text{MCP-PMT}} \rangle$, for the triggered tracks with a minimum pulse height both in the pixel and in the MCP-PMTs, $N_{trig}$. The red curve represents the result of the fit to the distribution and it is used to determine the yield of detected tracks $N_{ts}$ for the efficiency calculation. (b) Comparison between two methods for the efficiency measurement: the fit of the time distribution to count how many events are in the peaking structure (in blue) and the amplitude cut to determine if an event has been detected by the triple strip (in red). For this comparison the efficiencies are not corrected for the fraction $f_{\text{miss}}$.

as shown in Figure 7.18b. This illustrates that the chosen method for the efficiency measurement allows to include in the $N_{ts}$ count also small signals that would be lost by imposing an amplitude threshold. Figure 7.19 shows the efficiency measured as a function of the triple strip tilting angle with respect to the beamline direction. As expected, the efficiency increases as the incident beam angle increases. The results at 5°, 10° and 20° are $\varepsilon = 90.4 \pm 1.0\,\%$, $98.2 \pm 0.7\,\%$ and $99.1 \pm 0.6\,\%$, respectively. By tilting the sensor around the pixel-strip axis from normal incidence, the contributions due to particles crossing only the inactive volume of the sensor decrease and the full efficiency is restored for tilt angles above 10°.

### 7.3.4 Charge sharing between two adjacent pixels

In this section, the study of the charge sharing between two adjacent TimeSPOT pixels is described. When a charged particle crosses the sensor at an angle different from 0° (normal incidence), it typically crosses the active volume of two, or more, adjacent pixels and, in this cases, the information coming from all the hitted pixels is important in the definition of the overall performance of the system.

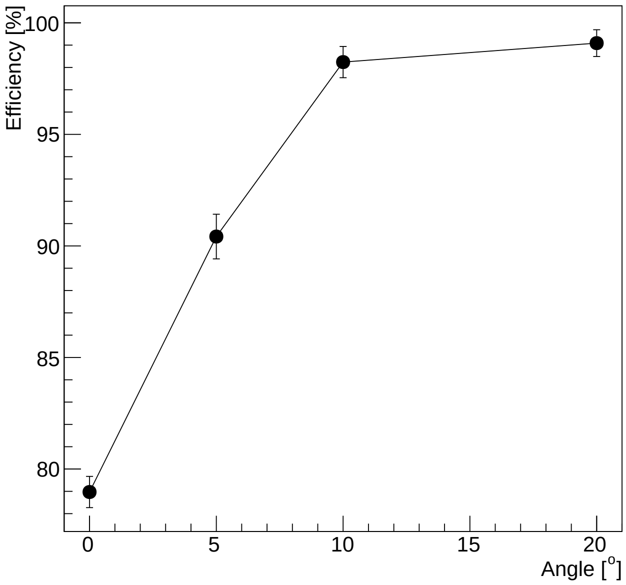

**Fig. 7.19** Triple strip efficiency as a function of the tilt angle with respect to normal sensor incidence. The DUT is rotated around the pixel-strip axis.

In our case, our device under test consists of two neighbour pixels (Figure 7.20a) which are individually readout by using the four-channels front end electronics board (Figure 7.20b), already described in Section 5.2.1. The acquisition was triggered by the coincidence of a signal detected by a single pixel and a signal on one MCP-PMT - representing the time reference of this setup -, placed upstream and downstream the DUT, respectively. The triggering pixel was placed in the middle of the two pixels to equalize the occupancies on the two pixels that were operated at $-100\,\mathrm{V}$. This setup allows to study both the performance of a single pixel alone and that of two pixels considered as a cluster.

In this study the ToA of the silicon sensors signals is evaluated using the *Spline* method, and the following event categories were defined: the *whole pixel*, the *single pixel*, the *shared pixel* and the *cluster*. A *whole pixel* event is that one in which a minimal requirement on the pixel signal amplitude and ToA is asked, to reject most of the noise, and any signal in the neighbour pixel is ignored. Looking also at the neighbour pixel, if there is no signal in it - by applying cuts on its signal amplitude and ToA ($A < 15\,\mathrm{mV}$ OR $|t_{\mathrm{pixel}} - t_{\mathrm{MCP-PMT}}| > 100\,\mathrm{ps}$) - the event is labelled *single pixel*, otherwise if a signal on the neighbour pixel is present ($A > 15\,\mathrm{mV}$ AND $|t_{\mathrm{pixel}} - t_{\mathrm{MCP-PMT}}| < 100\,\mathrm{ps}$), the event is labelled *shared pixel*. In this last case a *cluster* is made by combining the

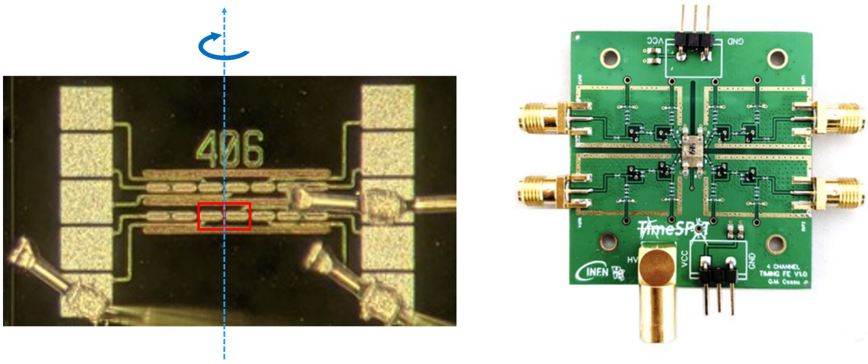

**(a)** **(b)**

**Fig. 7.20** (a) In the red box the two adjacent pixels used for the charge sharing study. (b) The four-channels FEE board used to read two pixels.

information of the two pixels. Clearly, the same event could belong to more than one of the categories above.
Figure 7.21a shows the amplitude distributions obtained at 20° for the different event types. The distribution of the *whole pixel* events deviates from the characteristic Landau shape due to the contribution of the *shared pixel* events, populating the region of small amplitudes $A < 40$ mV. By applying a clusterization algorithm to these events, the resulting amplitude distribution, given by the sum of the amplitudes recorded on the two pixels, recovers the expected Landau shape, as illustrated in Figure 7.21b, where the amplitude distributions of the clusterized events for the measured angles (0°, 5°, 10°, 20°) are shown. The distributions overlap for $A > 45$ mV and peak to consistent values. At low amplitudes, instead, the distributions differ among themselves, in particular at 20°, due to the fact that the larger the angle, the larger the probability to have events with cluster size equal to 3, so a small amount of charge could be lost in our setup composed by only two pixels.

Concerning the cluster timing, the amplitude-weighted ToA of each pixel is corrected by its mean value determined using calibration data samples at 0° with the trigger pixel centered on one of the two DUT pixels alternatively. For the *shared pixel* events, a linear combination of the ToA from both pixels weighted with their amplitude is performed to determine the ToA of the cluster:

$$t_{\text{cluster}} = \frac{t_{\text{pixel,1}}A_{\text{pixel,1}} + t_{\text{pixel,2}}A_{\text{pixel,2}}}{A_{\text{pixel,1}} + A_{\text{pixel,2}}} \tag{7.2}$$

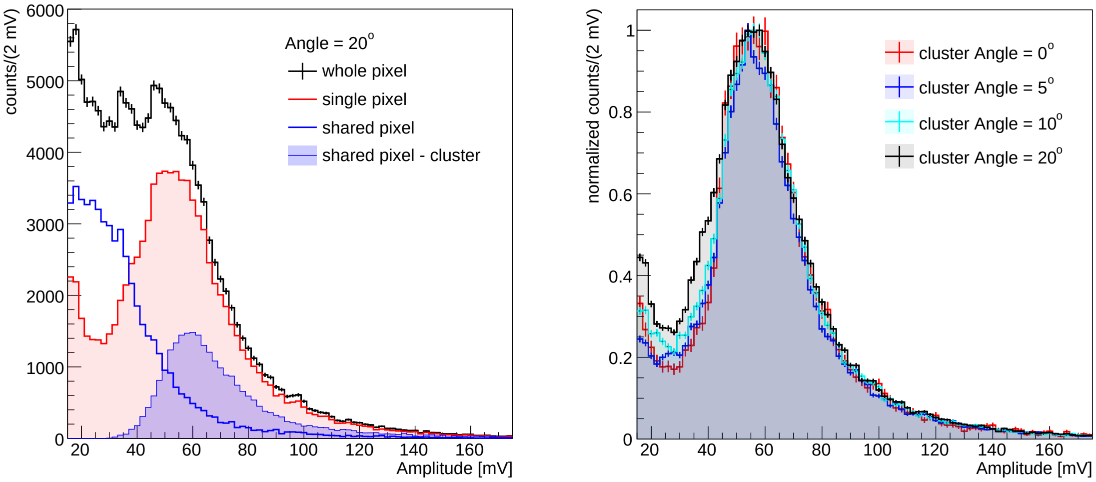

**(a)** **(b)**

**Fig. 7.21** (a) Amplitude distributions at 20° with respect to normal incidence for different event categories. (b) Cluster amplitude distributions at various particle incident angles.

The resulting time resolution, $\sigma^{\mathrm{eff}}_{\mathrm{shared-cluster}} = 16.7 \pm 0.7$ ps, improves the time resolution measured individually for each pixel forming the cluster, as it can be seen in the comparison between the full and empty blue histogram in Figure 7.21a. Similar results are obtained using data at incident beam angles of 5° and 10°.

Figure 7.22 shows the time resolution of the two-pixel cluster as a function of the ratio of amplitudes $A_{\mathrm{pixel,1}}/(A_{\mathrm{pixel,1}} + A_{\mathrm{pixel,2}})$ for each pixel forming the cluster, and the time resolution measured using only the individual pixel information. The largest improvement in time resolution due to the clusterization algorithm is reached when the amplitudes of the two pixels are similar, while in the cases in which one pixel dominates over the other, the time resolution of the combination is similar to that of the dominant pixel. In all cases the time resolution of the cluster is consistent with the combined resolutions of each pixel. Overall, the clustering allows to recover the timing performances at normal incidence when only one pixel is hit. The measured resolutions at 5°, 10° and 20° are all consistent with the value of $20.6 \pm 0.2$ ps at 0° measured with the same setup and analysis method (Spline algorithm).

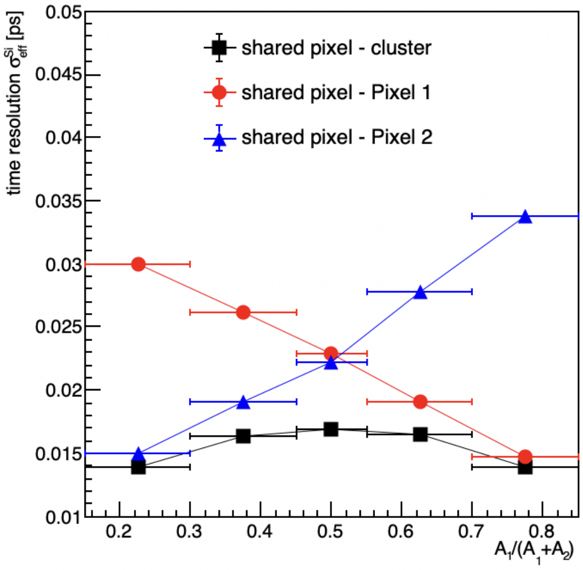

**Fig. 7.22** Two-pixel cluster time resolution as a function of the ratio of the amplitude of one pixel to the sum of the two (black curve). The time resolution estimated using only the individual pixel information is also shown (red and blue curves). Results correspond to an incident beam angle of 20°. The time jitter contribution of the MCP-PMT is not subtracted.

## 7.4 Summary

In this chapter, the results of test beam conducted on non-irradiated TimeSPOT silicon sensors at CERN SPS/H8 beamline in October 2021 and May 2022 have been described. Specifically, time resolution and geometrical efficiency measurements have been performed. Applying a software-based constant fraction discrimination algorithm, a time resolution close to 10 ps has been achieved with a TimeSPOT single pixel. Moreover, the use of a more common leading-edge discrimination method shows also and excellent performance allowing to reach a time resolution close to 25 ps without any amplitude correction. Since the TimeSPOT sensors trenches are inactive, measurements of the geometrical efficiency of such devices has been performed at different particles incidence angles, showing a full recover of the geometrical efficiency by tilting the sensors at 10° or more. On the basis of these measures, TimeSPOT sensors appear as a very promising solution for future upgrade of the tracking systems of many HEP experiments. As illustrated in Chapter 1 another fundamental requirement for these sensors to be used in HEP experiments operating at high luminosity is a high radiation hardness. The characterization of highly irradiated TimeSPOT sensors, performed both in laboratory and at the test beam, will be shown in the next chapter.

# Chapter 8

# Irradiated TimeSPOT sensors characterization

This Chapter presents the first characterization using minimum ionizing particles of irradiated TimeSPOT sensors, both in laboratory and in a test beam at CERN SPS/H8 beamline in May 2022. These measurements are needed to test the radiation hardness of such devices, which is a fundamental requirement for experiments operating in high luminosity conditions. TimeSPOT sensors have been irradiated with neutrons in the TRIGA reactor at the Institut Jožef Stefan in Ljubljana (Slovenia) at different fluences, up to $2.5 \cdot 10^{16}\,1\,\mathrm{MeV}\,\mathrm{n_{eq}}/\mathrm{cm}^2$. Recent results have proven the very high radiation hardness of 3D sensors with columnar electrodes, up to a radiation fluence of $3 \cdot 10^{17}\,1\,\mathrm{MeV}\,\mathrm{n_{eq}}/\mathrm{cm}^2$ tested with Transient Current Technique (TCT) [22]. In this chapter the first characterization of highly irradiated 3D-trench devices is described in detail.

## 8.1 Laboratory characterization

In order to reduce the leakage current of irradiated sensors, irradiated sensors must be operated at low temperatures. To accomplish this, the $^{90}$Sr source setup has been placed inside a climatic chamber (Figure 8.1) that allows to cool down to $-70°$C. All the measurements shown in this Chapter have been performed at a temperature of $-20°$C, sufficient to keep the sensors leakage current to an acceptable level (tens of nA). Figure 8.2 shows two configurations of the setup inside the climatic chamber, with or without the electromagnetically shielded box, respectively. The setup used for timing performance measurements is the same of that used for non-irradiated sensors characterization and described in Chapter 6, and also in this case the MCP3 has been used as time reference. In particular, for the timing measurements, the setup was placed inside the box in order to suppress the noise induced on the detectors by the climatic chamber itself. The DAQ system consists of a 4 GHz analog bandwidth 20 GSa/s 4 channels digital oscilloscope (Rohde & Schwarz RTO1044), used to acquire the signals from the silicon sensor and the MCP-PMT, with the coincidence of the two used as acquisition trigger condition. The acquired waveforms are then analysed offline by applying the Spline and Leading Edge (LE) time-picking methods, previously illustrated in Section 6.1.2. In this case, the optimization of the Spline method parameters resulted in an amplitude fraction of 35% for the measurement of the ToA of the irradiated sensors signals.

**Fig. 8.1** Climatic chamber used for the characterization of the irradiated TimeSPOT sensors in laboratory. The Rohde & Schwarz RTO1044 oscilloscope used for the data acquisition is also visible.

The first characterization measurement performed in laboratory is the measure of the leakage current as a function of the bias voltage for three single-pixel test structure irradiated at three different fluences: $5.0 \cdot 10^{15}\,1\,\mathrm{MeV\,n_{eq}/cm^2}$, $1.0 \cdot 10^{16}\,1\,\mathrm{MeV\,n_{eq}/cm^2}$ and $2.5 \cdot 10^{16}\,1\,\mathrm{MeV\,n_{eq}/cm^2}$. The measurement was performed on the sensors already mounted and wire-bonded to their FEE board. Figure 8.3 shows the resulting IV curves that, as expected (see Section 2.4), exhibit an increase of the leakage current as the fluence increases. A bias voltage down to $-170\,\mathrm{V}$ has been applied to the tested sensors, that have not reached the breakdown up to this value. Moreover, with the increase of

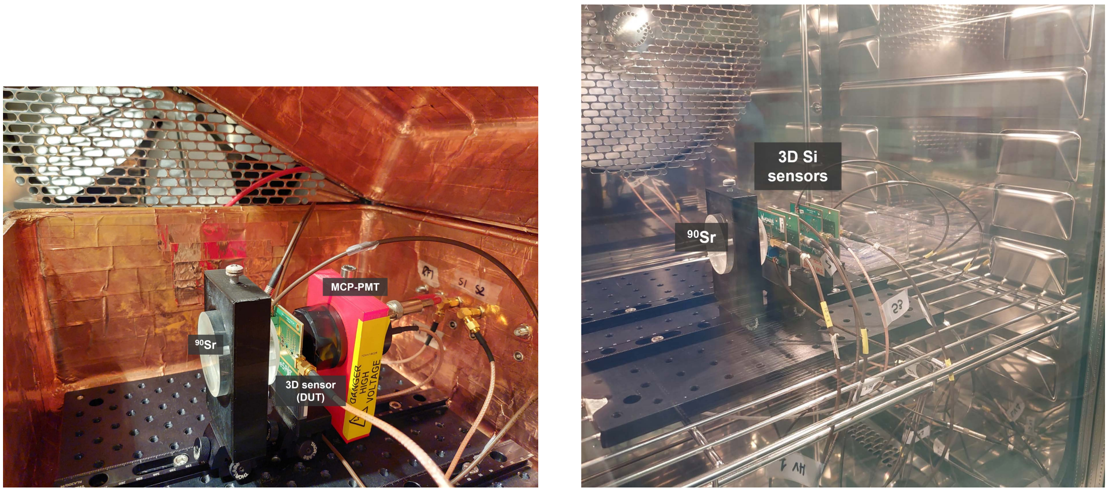

**(a)** **(b)**

**Fig. 8.2** Laboratory setup for characterization of TimeSPOT irradiated sensors with the $^{90}$Sr source (a) inside the electromagnetically shielded black box for time resolution measurements and (b) without the box for preliminary characterizations before the test beam.

the irradiation fluence, an increase of the depletion voltage and a degradation of the charge collection efficiency are expected. Therefore, some indications on the behaviour of the sensors exposed to different irradiation fluences can be provided by the signals rate of the sensor as a function of the bias voltage. This measurement has been performed by placing the sensor in front of the $^{90}$Sr source (Figure 8.2b), triggering on the sensor signal itself at a fixed threshold slightly above the noise and counting the triggers in one minute at different $V_{\text{bias}}$. For this measure pixel-strips test structures are used to have a good rate. Figure 8.4 shows the results obtained for sensors irradiated at $1.0 \cdot 10^{15}\,1\,\text{MeV}\,\text{n}_{\text{eq}}/\text{cm}^2$, $1.0 \cdot 10^{16}\,1\,\text{MeV}\,\text{n}_{\text{eq}}/\text{cm}^2$ and $2.5 \cdot 10^{16}\,1\,\text{MeV}\,\text{n}_{\text{eq}}/\text{cm}^2$ fluences and for a non-irradiated test structure, after a normalization of the rate to the one of the most irradiated sensor operated at $-120\,\text{V}$. The observed behaviour of the $1.0 \cdot 10^{15}\,1\,\text{MeV}\,\text{n}_{\text{eq}}/\text{cm}^2$ sensor is quite similar to the non-irradiated one, while the curves are shifted at higher $V_{\text{bias}}$ and rise slower as the radiation damage increases, reaching the *plateau* at a higher bias voltage.

Regarding the timing performance, as outlined in Chapter 6, the setup with the $^{90}$Sr source provides only an upper limit of the time resolution of the sensor, but still gives useful information preliminary to test beam, in particular it can preliminarily show differences in behaviour of irradiated sensors with respect to those non-irradiated. The devices under test are a single pixel irradiated at $1.0 \cdot 10^{16}\,1\,\text{MeV}\,\text{n}_{\text{eq}}/\text{cm}^2$ and a single

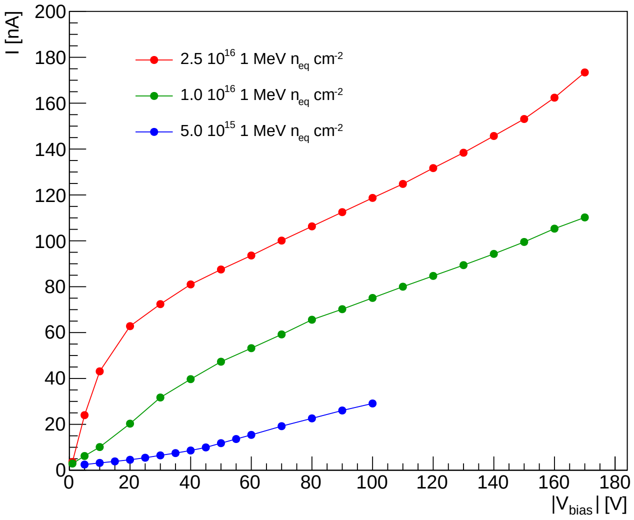

**Fig. 8.3** IV curves of three TimeSPOT single pixels irradiated at $5.0 \cdot 10^{15}\,1\,\mathrm{MeV}\,\mathrm{n_{eq}}/\mathrm{cm}^2$, $1.0 \cdot 10^{16}\,1\,\mathrm{MeV}\,\mathrm{n_{eq}}/\mathrm{cm}^2$ and $2.5 \cdot 10^{16}\,1\,\mathrm{MeV}\,\mathrm{n_{eq}}/\mathrm{cm}^2$.

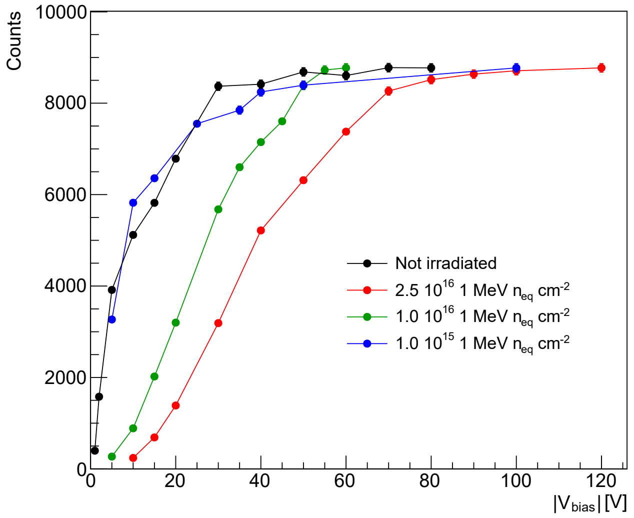

**Fig. 8.4** Rate of signals as a function of the bias voltage for pixel-strips irradiated at $1.0 \cdot 10^{15}\,1\,\mathrm{MeV}\,\mathrm{n_{eq}}/\mathrm{cm}^2$, $1.0 \cdot 10^{16}\,1\,\mathrm{MeV}\,\mathrm{n_{eq}}/\mathrm{cm}^2$ and $2.5 \cdot 10^{16}\,1\,\mathrm{MeV}\,\mathrm{n_{eq}}/\mathrm{cm}^2$ and for a non-irradiated one. The counts are normalized to the rate of the most irradiated pixel-strip at −120 V.

pixel irradiated at $2.5 \cdot 10^{16}\,1\,\mathrm{MeV}\,\mathrm{n_{eq}}/\mathrm{cm}^2$. Figure 8.5 and Figure 8.6 show the overlap of the time distributions, $t_{pixel} - t_{MCP-PMT}$, obtained at different bias voltages with the two algorithms (LE and Spline) for the two irradiated sensors. For both irradiation fluences, very similar distributions are obtained for $V_{\text{bias}} \leq 50\,\text{V}$, while the distribution at $-25$ V is slightly wider for the single pixel irradiated at $1.0 \cdot 10^{16}\,1\,\text{MeV}\,\text{n}_{\text{eq}}/\text{cm}^2$, as seen for non-irradiated sensors, whereas it is narrower for the single pixel irradiated at $2.5 \cdot 10^{16}\,1\,\text{MeV}\,\text{n}_{\text{eq}}/\text{cm}^2$. This is quantified through the effective time resolution, $\sigma_{\text{eff}}$, measured at different bias voltages (Figure 8.7), that, for the most irradiated sensor, results to be smaller at $-25\,\text{V}$. This could seem in contrast to what expected, but the interpretation of this results, supported by the following test beam results, is that at $V_{\text{bias}} = -25\,\text{V}$ the signals of a such irradiated sensor are smaller and below the trigger threshold, consequently only a part of signals, the larger ones, is detected and the time resolution results smaller. This issue is related to this specific acquisition condition in which the DUT is on the trigger, while it is not a problem in the test beam setup. On the other side, the single pixel irradiated at $1.0 \cdot 10^{16}\,1\,\text{MeV}\,\text{n}_{\text{eq}}/\text{cm}^2$ has a behaviour similar to that one observed for the non-irradiated single pixel. For both the irradiated sensors, the time resolution results to be smaller than the one measured for the non-irradiated sensor. Possible explanations will be illustrated in the following section.

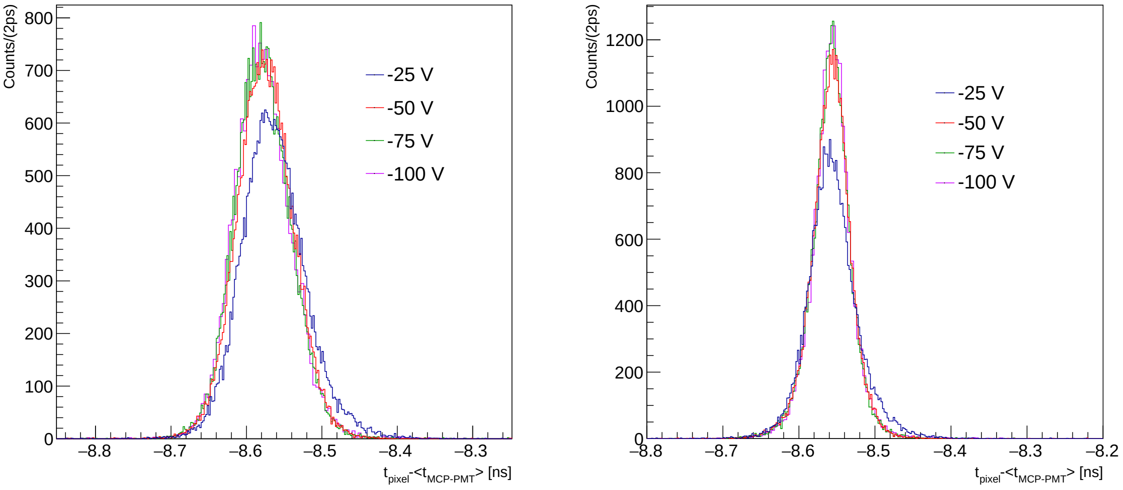

**(a)** **(b)**

**Fig. 8.5** Distribution of the time of arrival of the single pixel irradiated at $1.0 \cdot 10^{16}\,1\,\text{MeV}\,\text{n}_{\text{eq}}/\text{cm}^2$ with respect to the MCP-PMT, $t_{pixel} - t_{MCP-PMT}$, obtained at different bias voltages (a) with the Leading Edge and (b) with the Spline methods.

These preliminary measurements of irradiated sensors made with the laboratory setup have given strong indication that 3D-trench sensors irradiated to high fluences have similar performances to the non irradiated devices if the bias voltage is increased

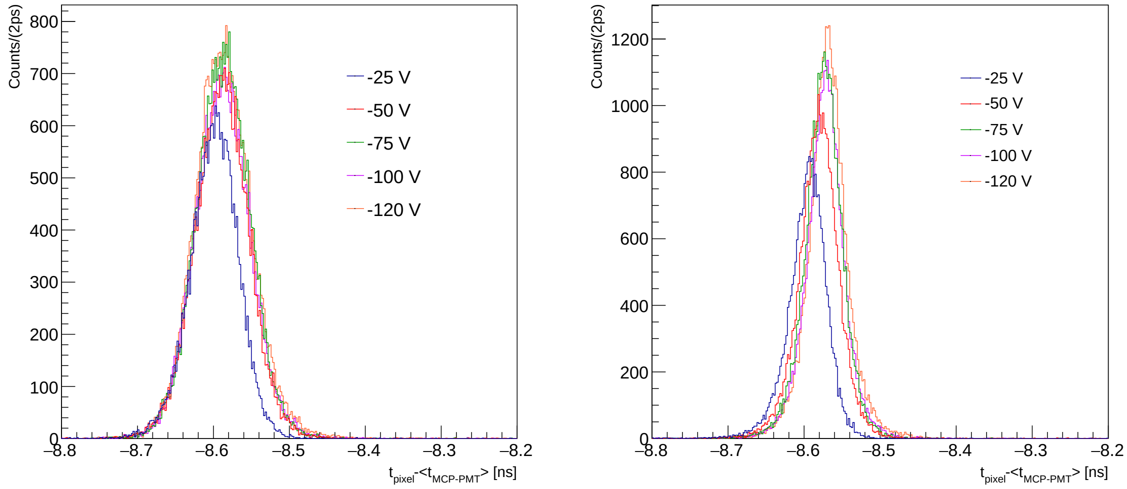

**(a)** **(b)**

**Fig. 8.6** Distribution of the time of arrival of the single pixel irradiated at $2.5 \cdot 10^{16}\,1\,\mathrm{MeV}\,\mathrm{n_{eq}}/\mathrm{cm}^2$ with respect to the MCP-PMT, $t_{pixel} - t_{MCP-PMT}$, obtained at different bias voltages (a) with the Leading Edge and (b) with the Spline methods.

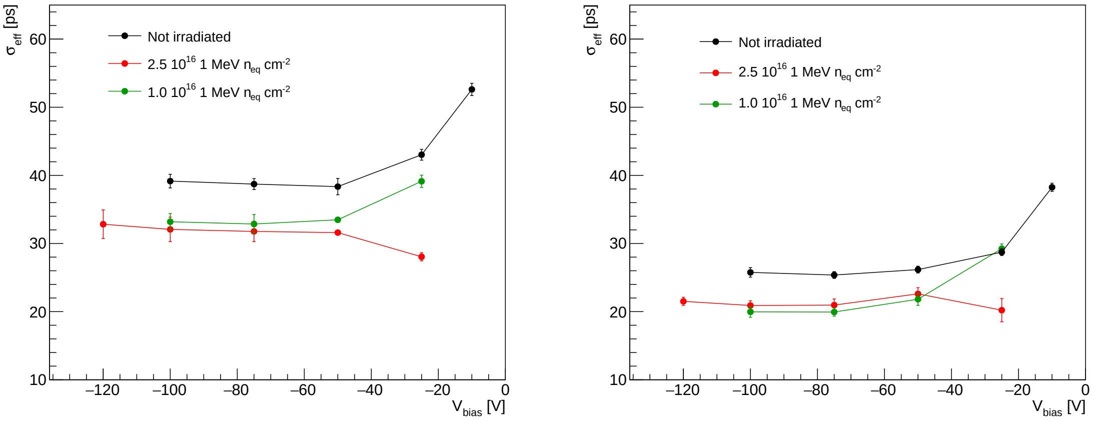

**(a)** **(b)**

**Fig. 8.7** Effective time resolution measured with the $^{90}$Sr setup as a function of the bias voltage for the not irradiated single pixel and for the two irradiated pixels (a) with the LE method and (b) with the Spline method. The time jitter contribution of the MCP-PMT has been subtracted.

of a few tens volts. Further characterizations of these devices by means of a test beam campaign are reported in the next section.

## 8.2 Test beam characterization

The test beam setup used to measure both timing performance and efficiency of irradiated TimeSPOT sensors is very similar to the one used for the characterization of non-irradiated sensors, described in detail in Section 7.1. Two little boxes filled with dry ice next to the irradiated DUT and a polystyrene box to thermally insulate it have been added to the setup (see Figure 8.8). The use of dry ice allows to cool the DUT down to −40°C. The DUT is mounted on a fixed mount that allows to rotate the sensor around the vertical axis and its temperature was constantly monitored by means of a PT100 temperature sensor, in order to switch off the sensor bias voltage when the temperature is higher than −15°C.

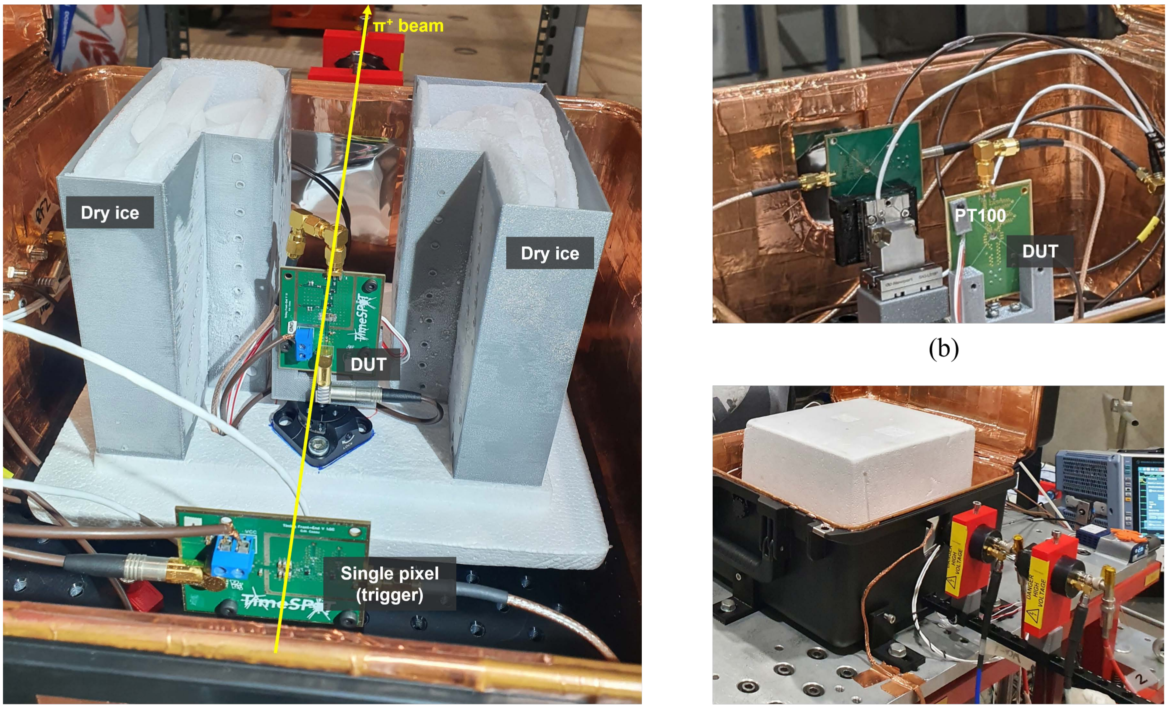

(a)

(b)

(c)

**Fig. 8.8** (a) Test beam setup for the test of TimeSPOT irradiated sensors. The DUT was cool down by means of dry ice. (b) A PT100 temperature sensor was put in contact with the DUT board to monitor the irradiated sensor temperature. (c) The setup with the polystyrene box to thermally insulate the DUT and to avoid condensation on the its surface.

For the characterization of the irradiated single pixels, the trigger condition is the coincidence of a signal of another single pixel, mounted on the piezoelectric linear stages, and one of the two MCP-PMTs that are used as time reference. The same trigger condition is used also for the efficiency measurements, where the DUT is an irradiated triple strip. The single pixels and triple pixel-strip characterized were irradiated at fluences of $1.0 \cdot 10^{16}\,1\,\mathrm{MeV\,n_{eq}/cm^2}$ and $2.5 \cdot 10^{16}\,1\,\mathrm{MeV\,n_{eq}/cm^2}$. The alignment procedure and the DAQ system, for both type of measurements, are the same as those described in Section 7.1. In the analysis for the measurements of the time resolution of these irradiated sensors, the Spline and Reference algorithms have been applied to the sensors signals.

In Figure 8.9 the amplitude distributions obtained at different bias voltages with the single pixels irradiated at $1.0 \cdot 10^{16}\,1\,\mathrm{MeV\,n_{eq}/cm^2}$ and $2.5 \cdot 10^{16}\,1\,\mathrm{MeV\,n_{eq}/cm^2}$ are shown. We observe that the peak of the distribution moves to higher amplitude values as the bias voltage increases, as expected, but at low $V_{\text{bias}}$ the Landau distribution peak is close to the noise peak, especially for the most irradiated sensor, while for the non-irradiated single pixel the Landau distribution was well distinguished from the noise peak even at the very low bias voltage of $-7\,\mathrm{V}$ (see Figure 7.7). The amplitude distribution of the most irradiated single pixel at $V_{\text{bias}} = -20\,\mathrm{V}$ in Figure 8.9b, showing significantly smaller amplitudes with respect to the non-irradiated case, validates the hypothesis illustrated in Section 8.1, according to which in the $^{90}$Sr source setup an important portion of the signals are cut off by the trigger threshold and this explains why in that case (Figure 8.7) an unexpected low time resolution value was obtained for the bias voltage of $-25\,\mathrm{V}$.

The two FEE boards on which the two irradiated pixels were mounted have a different gain, so it is not possible to compare the amplitude values itself, but rather the bias voltage at which the distribution stop to move at higher amplitude values. This happens at about $-100$ V for the single pixel irradiated at $1.0 \cdot 10^{16}\,1\,\mathrm{MeV\,n_{eq}/cm^2}$ and at $V_{\text{bias}} < -100\,\mathrm{V}$ for that one irradiated at $2.5 \cdot 10^{16}\,1\,\mathrm{MeV\,n_{eq}/cm^2}$. For the non-irradiated single pixel, this is observed already at a bias voltage of $-50$ V (see Figure 7.7). Figure 8.10 shows the distribution of the time of arrival of the silicon sensor with respect to the average time measured by the two MCP-PMTs, $t_{\text{pixel}} - \langle t_{\text{MCP-PMT}} \rangle$, obtained with the Reference method at $V_{bias} = -150\,\mathrm{V}$ for the two irradiated pixels.

The distribution is fitted with a function given by the sum of two Gaussian functions, describing the peak of the distribution, and a constant, describing the background, as done in the characterization of non-irradiated sensors (Section 6.1.3). The effective time resolution is then computed by combining the two Gaussian contributions, according to Equation 6.3. The time resolution of the two irradiated single pixels, measured at different bias voltages with the Spline and with the Reference method is shown in Figure 8.11 together to the results obtained for the non-irradiated single pixel. As already

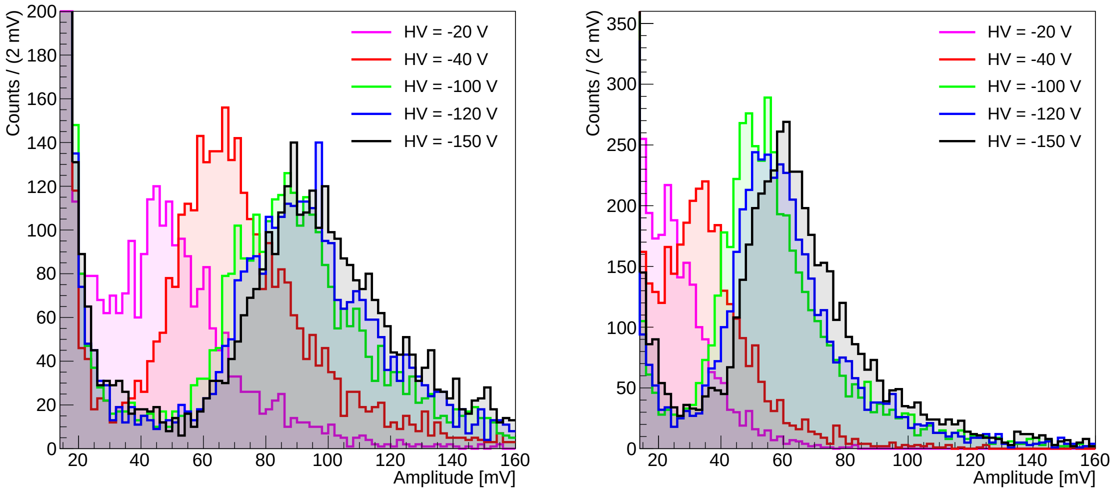

**(a)** **(b)**

**Fig. 8.9** Amplitude distribution of the single pixels irradiated (a) at $1.0 \cdot 10^{16}\,1\,\text{MeV}\,\text{n}_{\text{eq}}/\text{cm}^2$ and (b) at $2.5 \cdot 10^{16}\,1\,\text{MeV}\,\text{n}_{\text{eq}}/\text{cm}^2$ at normal beam incidence and for different bias voltages.

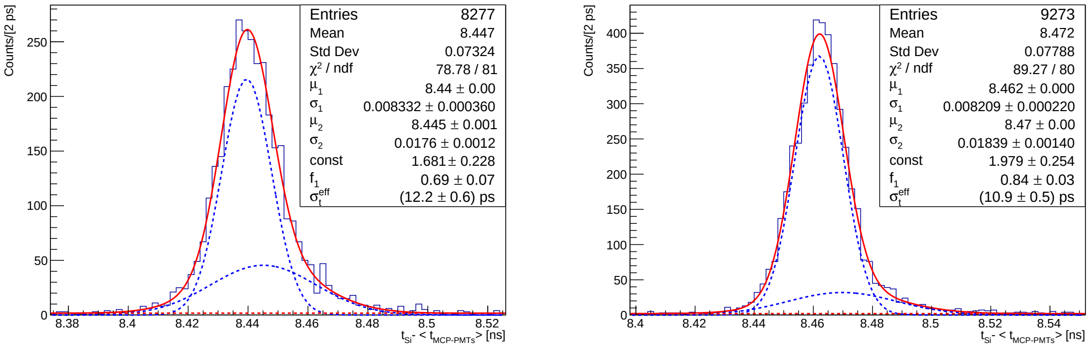

**(a)** **(b)**

**Fig. 8.10** Time distribution of the ToA of the pixel with respect to the average time measured by the two MCP-PMTs, $t_{pixel} - \langle t_{MCP-PMT} \rangle$, obtained with the Reference method at $V_{\text{bias}} = -150$ V (a) for the single pixel irradiated at $1.0 \cdot 10^{16}\,1\,\text{MeV}\,\text{n}_{\text{eq}}/\text{cm}^2$ and (b) for that one irradiated at $2.5 \cdot 10^{16}\,1\,\text{MeV}\,\text{n}_{\text{eq}}/\text{cm}^2$.

observed with the $^{90}$Sr setup, a smaller time resolution is measured for the irradiated sensors with respect to the not irradiated one. This difference is about $(3-4)$ ps and it is not possible to establish the definitive cause of this, based on the measurements made so far only. Such small variations can be due to differences between the three specific FEE boards used for these sensors, but also to the fact that the not irradiated single

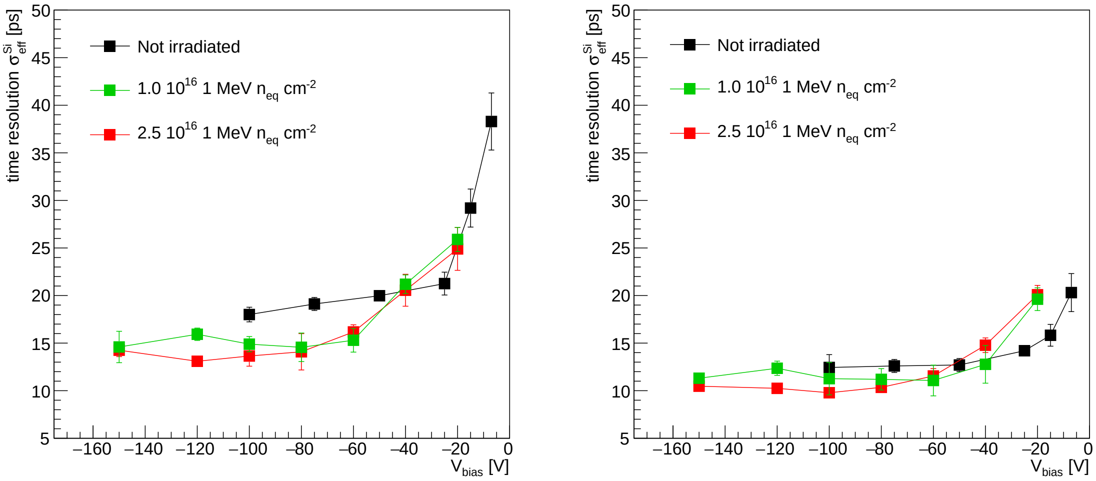

**(a)** **(b)**

**Fig. 8.11** Effective time resolution measured at different bias voltages for the non-irradiated single pixel and for the two irradiated single pixels (a) with the Spline and (b) with the Reference methods.

pixel has been tested at room temperature, unlike the irradiated sensors, and this can impact the timing performance, for the increase of both the charge carriers mobility and the transistor gain as the temperature decreases. Another possibility is that the some regions of the irradiated sensors are not completely efficient and so the sensor seems to have a better timing response. Further studies are necessary to investigate this effect.

As explained in Chapter 7, 3D sensors are usually operated tilted with respect to the normal particle incidence, in order to recover the inefficiency due to the trenches electrodes that are not active. Because of this, we measured the time resolution of the most irradiated pixel also at 20° with respect to the normal beam incidence, as done for the not irradiated single pixel. The results, reported in Table 8.1 for the bias voltage of $-100\,\mathrm{V}$, show that the time resolution does not degrade drastically with the tilting angle.

As explained in Section 2.4, the silicon sensors charge collection efficiency (CCE) is deteriorated by the radiation damage. In particular, the CCE decrease becomes the fundamental problem at irradiation fluences higher than or equal to $1{\cdot}10^{16}\,1\,\mathrm{MeV}\,\mathrm{n_{eq}}/\mathrm{cm}^2$ [40]. The efficiency of TimeSPOT sensors irradiated at $1 \cdot 10^{16}\,1\,\mathrm{MeV}\,\mathrm{n_{eq}}/\mathrm{cm}^2$ and at $2.5{\cdot}10^{16}\,1\,\mathrm{MeV}\,\mathrm{n_{eq}}/\mathrm{cm}^2$ has been measured at the May 2022 test beam at SPS. The data analysis procedure is the same as that followed in the not irradiated case, described in

**Table 8.1** Effective time resolution for not irradiated and irradiated 3D trench single pixels at a bias voltage of $-100\,\mathrm{V}$.

| Fluence | $\sigma_{\mathrm{eff}}^{Si}$ (Reference) [ps] 0° | $\sigma_{\mathrm{eff}}^{Si}$ (Reference) [ps] 20° | $\sigma_{\mathrm{eff}}^{Si}$ (Spline) [ps] 0° | $\sigma_{\mathrm{eff}}^{Si}$ (Spline) [ps] 20° |
|---|---|---|---|---|
| Not irradiated | $12.4 \pm 1.4$ | $17.5 \pm 0.9$ | $17.8 \pm 1.0$ | $21.7 \pm 0.9$ |
| $2.5 \cdot 10^{16}\,1\,\mathrm{MeV}\,\mathrm{n_{eq}}/\mathrm{cm}^{-2}$ | $9.8 \pm 0.4$ | $13.5 \pm 0.6$ | $13.6 \pm 1.1$ | $16.9 \pm 0.9$ |

Chapter 7. For the most irradiated triple strip, the measurement has been performed with the DUT tilted at different angles with respect to the beam direction 0°, 5° and 20°. The results, including those of the non-irradiated sensor, are shown in Figure 8.12. The measured efficiency of irradiated sensors resulted to be compatible with that measured in the not irradiated case, resulting in an efficiency of $98.7 \pm 1.14\%$ at 20° tilting angle with respect to the beam direction. This result was obtained increasing the bias voltage of the irradiated sensor by only 30 V with respect to the non irradiated sensor. It represents a very important result, since it proves the good performance of TimeSPOT sensors also when they are exposed to high radiation fluences, close to the $6 \cdot 10^{16}\,1\,\mathrm{MeV}\,\mathrm{n_{eq}}/\mathrm{cm}^2$ fluence expected in the LHCb VELO during the high luminosity phase (with the Scenario A of the Upgrade II). In Figure 8.13 the efficiency measured at 0° at different bias voltages for both the non irradiated and the irradiated at $1 \cdot 10^{16}\,1\,\mathrm{MeV}\,\mathrm{n_{eq}}/\mathrm{cm}^2$ triple strip is shown. The curves show that while the non irradiated sensor is already fully efficient at $-20\,\mathrm{V}$, the efficiency of the irradiated sensor at the same bias voltage is about 30% smaller and increases with the bias voltage until reaching a plateau. This result is in agreement with the study made with the $^{90}$Sr and reported in Figure 8.4.

Highly irradiated 3D-trench silicon sensors have shown, both in test beam and laboratory measurements, the same performance of the non-irradiated devices in terms of time resolution and efficiency, thus they are good candidates for tracking detectors operating in high luminosity conditions.

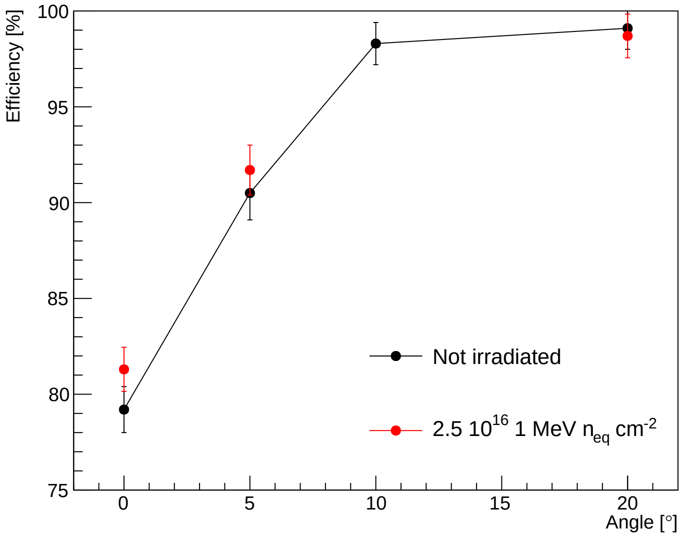

**Fig. 8.12** Efficiency measured at different tilting angles for the non irradiated triple strip and for the triple strip irradiated at a fluence of $2.5 \cdot 10^{16}\,1\,\mathrm{MeV}\,\mathrm{n_{eq}}/\mathrm{cm}^2$.

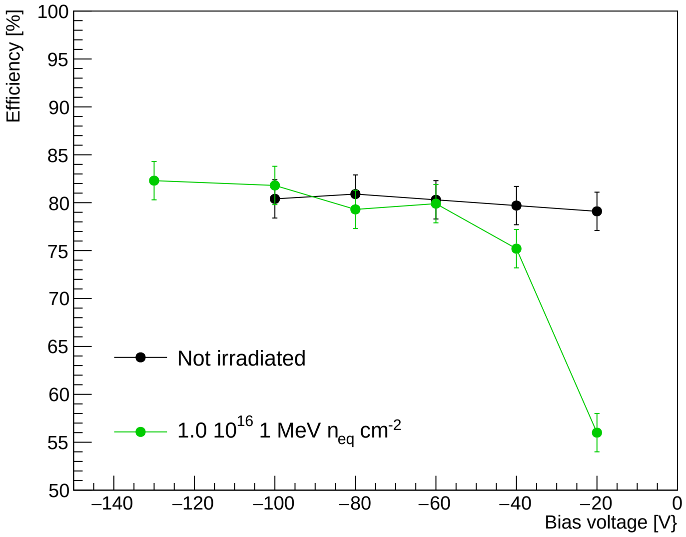

**Fig. 8.13** Efficiency measured at perpendicular beam incidence for the non irradiated triple strip and for the triple strip irradiated at a fluence of $1 \cdot 10^{16}\,1\,\mathrm{MeV}\,\mathrm{n_{eq}}/\mathrm{cm}^2$ at different bias voltages.

# Conclusions

This thesis work was focused on the development of innovative 3D silicon sensors capable to provide at the same time an excellent time resolution ($\mathcal{O}(10\,\mathrm{ps})$) and spatial resolution ($\mathcal{O}(10\,\mu\mathrm{m})$) in the highly radioactive environment of future high luminosity experiments. The design optimization simulations made within the TimeSPOT project have identified the 3D-trench pixel geometry as the best choice to achieve the time resolution goal, since it allows to obtain a very uniform electric and weighting field in its active area. Therefore this geometry design was chosen for TimeSPOT sensors, whose pixels have a $55 \times 55\,\mu\mathrm{m}^2$ area with an active thickness of $150\,\mu\mathrm{m}$ and a central trench collection electrode $135\,\mu\mathrm{m}$ thick and $40\,\mu\mathrm{m}$ long.

These sensors have been characterized in several test beam campaigns and in the laboratory using a $^{90}\mathrm{Sr}$ source. The setup with the $^{90}\mathrm{Sr}$ source represents a handy tool to make preliminary characterizations of the sensors directly in the laboratory, despite its limitations, fully described in this thesis. In particular, it allowed to measure an upper limit of the time resolution of different test structures, both for non-irradiated and irradiated TimeSPOT sensors, in this second case by placing the setup inside a climatic chamber. This setup also allowed to perform a preliminary comparison between sensors exposed to different irradiation fluences, showing indications that as the irradiation fluence increases, the bias voltage has to be increased to recover the detection efficiency of non-irradiated sensors.

In the test beam campaigns both time resolution and geometrical efficiency measurements were performed for the first time. A time resolution close to 10 ps was measured for a TimeSPOT non-irradiated single pixel and comparable results were obtained also for single pixels irradiated at $1 \cdot 10^{16}\,1\,\mathrm{MeV}\,\mathrm{n_{eq}}/\mathrm{cm}^2$ and $2.5 \cdot 10^{16}\,1\,\mathrm{MeV}\,\mathrm{n_{eq}}/\mathrm{cm}^2$, with the latter fluence very close to the maximum expected in the innermost region of the LHCb VELO in the Upgrade II phase. The efficiency measurements performed at perpendicular incident particle beam and at different incident angles have shown that by tilting the 3D-trench sensors, like other columnar 3D sensors, they reach the full efficiency. The results showed that tilting TimeSPOT sensors at more than 10° the efficiency is fully recovered, reaching a value of $99.1 \pm 0.6\%$ at 20° for the non-irradiated sensor tested, at a bias voltage of $-100\,\mathrm{V}$. Applying a bias voltage only $30\,\mathrm{V}$ higher to the sensor irradiated at $2.5 \cdot 10^{16}\,1\,\mathrm{MeV}\,\mathrm{n_{eq}/cm^2}$, a comparable efficiency of $98.7 \pm 1.14\%$ at 20° has been measured.

TimeSPOT sensors have shown an excellent performance in terms of time resolution and radiation hardness and this makes them a very good solution for the detectors of several high energy physics experiments that have to operate in a very high-particle-rate environment, e.g. the LHCb VELO, CMS PPS and the NA62 GTK. Laboratory tests on the TimeSPOT $32 \times 32$ pixels matrix bump-bonded to the Timespot1 ASIC, developed in 28 nm CMOS technology, are ongoing. In the near future it will be tested also in a test beam to evaluate its time resolution and detection efficiency. The test of a complete tracker demonstrator made of four of more detection planes of Timespot1 hybrids is also foreseen during the first half of 2023.

# References

[1] Lyndon Evans and Philip Bryant. LHC Machine. *Journal of Instrumentation*, 3(08):S08001, aug 2008.

[2] The ALICE Collaboration. The ALICE experiment at the CERN LHC. *Journal of Instrumentation*, 3(08):S08002, aug 2008.

[3] The ATLAS Collaboration. The ATLAS Experiment at the CERN Large Hadron Collider. *Journal of Instrumentation*, 3(08):S08003, aug 2008.

[4] The CMS Collaboration. The CMS experiment at the CERN LHC. *Journal of Instrumentation*, 3(08):S08004, aug 2008.

[5] The LHCb Collaboration. The LHCb Detector at the LHC. *Journal of Instrumentation*, 3(08):S08005, aug 2008.

[6] M. Vretenar, Giulia Bellodi, Roland Garoby, Frank Gerigk, Klaus Hanke, Alessandra Lombardi, Stephan Maury, Matteo Pasini, Carlo Rossi, and E. Sargsyan. Linear Accelerator Designs for the Upgrade of the CERN Proton Injector Complex (Linac4, SPL). 01 2007.

[7] O. Aberle et al. *High-Luminosity Large Hadron Collider (HL-LHC): Technical design report*. CERN Yellow Reports: Monographs. CERN, Geneva, 2020.

[8] Nicholas Styles. Collecting and analysing data at high pile-up with ATLAS and CMS. In *50th Rencontres de Moriond on EW Interactions and Unified Theories*, pages 107–112, 2015.

[9] The LHCb Collaboration. Framework TDR for the LHCb Upgrade II - Opportunities in flavour physics, and beyond, in the HL-LHC era. Technical report, CERN, Geneva, 2021.

[10] CMS Collaboration and Thomas Mc Cauley. Collisions recorded by the CMS detector on 14 Oct 2016 during the high pile-up fill. CMS Collection., 2016.

[11] A. Lai, L. Anderlini, M. Aresti, A. Bizzeti, A. Cardini, G.-F. Dalla Betta, G.T. Forcolin, M. Garau, A. Lampis, A. Loi, C. Lucarelli, R. Mendicino, R. Mulargia, M. Obertino, E. Robutti, and S. Vecchi. First results of the TIMESPOT project on developments on fast sensors for future vertex detectors. *Nuclear Instruments and Methods in Physics Research Section A: Accelerators, Spectrometers, Detectors and Associated Equipment*, 981:164491, 2020.

[12] R. Aaij et al. LHCb Collaboration. Measurement of the b-quark production cross-section in 7 and 13 TeV pp collisions. *Physical Review Letters*, 118(5), feb 2017.

[13] I. Bediaga et al. Framework TDR for the LHCb Upgrade: Technical Design Report. Technical report, 2012.

[14] P. R. Barbosa-Marinho et al. *LHCb VELO (VErtex LOcator): Technical Design Report*. Technical design report. CERN, Geneva, 2001, 2001.

[15] LHCb Collaboration. LHCb VELO Upgrade Technical Design Report. Technical report, 2013.

[16] Victor Coco et al. Velo Upgrade Module Nomenclature. Technical report, CERN, Geneva, 2019.

[17] E. Buchanan. The LHCb Vertex Locator (VELO) Pixel Detector Upgrade. *Journal of Instrumentation*, 12(01):C01013, jan 2017.

[18] K. Akiba et al. Considerations for the VELO detector at the LHCb Upgrade II. Technical report, CERN, Geneva, 2022.

[19] E. Bossini. The CMS Precision Proton Spectrometer timing system: performance in Run 2, future upgrades and sensor radiation hardness studies. *Journal of Instrumentation*, 15(05):C05054, may 2020.

[20] The CMS Collaboration. The CMS Precision Proton Spectrometer at the HL-LHC – Expression of Interest. Technical report, CERN, Geneva, 2020. 88 pages.

[21] J. Lange, G. Giannini, S. Grinstein, M. Manna, G. Pellegrini, D. Quirion, S. Terzo, and D. Vázquez Furelos. Radiation hardness of small-pitch 3D pixel sensors up to a fluence of $3{\times}10^{16} n_{eq}/cm^2. Journal\ of\ Instrumentation, 13(09): P09009, sep 2018$.

[22] Maria Manna, Chiara Grieco, Sebastian Grinstein, Salvador Hidalgo, Giulio Pellegrini, David Quirion, and Stefano Terzo. First characterisation of 3d pixel detectors irradiated at extreme fluences. *Nuclear Instruments and Methods in Physics Research Section A: Accelerators, Spectrometers, Detectors and Associated Equipment*, 979:164458, 2020.

[23] A. Lampis, F. Borgato, D. Brundu, A. Cardini, G.M. Cossu, G.-F. Dalla Betta, M. Garau, L. La Delfa, A. Lai, A. Loi, M. Obertino, G. Simi, and S. Vecchi. 10ps timing with highly irradiated 3D trench silicon pixel sensors. *Journal of Instrumentation*, 18(01):C01051, jan 2023.

[24] L. Anderlini, M. Aresti, A. Bizzeti, M. Boscardin, A. Cardini, G.-F. Dalla Betta, M. Ferrero, G. Forcolin, M. Garau, A. Lai, A. Lampis, A. Loi, C. Lucarelli, R. Mendicino, R. Mulargia, M. Obertino, E. Robutti, S. Ronchin, M. Ruspa, and S. Vecchi. Intrinsic time resolution of 3D-trench silicon pixels for charged particle detection. *Journal of Instrumentation*, 15(09):P09029, sep 2020.

[25] F. Borgato, D. Brundu, A. Cardini, G. M. Cossu, G. F. Dalla Betta, M. Garau, L. La Delfa, A. Lai, A. Lampis, A. Loi, M. M. Obertino, G. Simi, and S. Vecchi. Charged-particle timing with 10 ps accuracy using timespot 3d trench-type silicon pixels. *Frontiers in Physics*, 11, 2023.

[26] E. Cortina Gil et al. The beam and detector of the NA62 experiment at CERN. *Journal of Instrumentation*, 12(05):P05025, may 2017.

[27] G. Aglieri Rinella, D. Alvarez Feito, R. Arcidiacono, C. Biino, S. Bonacini, A. Ceccucci, S. Chiozzi, E. Cortina Gil, A. Cotta Ramusino, J. Degrange, M. Fiorini, E. Gamberini, A. Gianoli, J. Kaplon, A. Kluge, A. Mapelli, F. Marchetto, E. Minucci, M. Morel, J. Noël, M. Noy, L. Perktold, M. Perrin-Terrin, P. Petagna, F. Petrucci, K. Poltorak, G. Romagnoli, G. Ruggiero, B. Velghe, and H. Wahl. The NA62 GigaTracker. *Nuclear Instruments and Methods in Physics Research Section A: Accelerators, Spectrometers, Detectors and Associated Equipment*, 845:147–149, 2017. Proceedings of the Vienna Conference on Instrumentation 2016.

[28] G. Aglieri Rinella, E. Cortina Gil, M. Fiorini, J. Kaplon, A. Kluge, F. Marchetto, M. E. Martin Albarran, M. Morel, M. Noy, L. Perktold, S. Tiuraniem, and B. Velghe. Test-beam results of a silicon pixel detector with Time-over-Threshold read-out having ultra-precise time resolution. *Journal of Instrumentation*, 10(12):P12016, dec 2015.

[29] G. Aglieri Rinella, D. Alvarez Feito, R. Arcidiacono, C. Biino, S. Bonacini, A. Ceccucci, S. Chiozzi, E. Cortina Gil, A. Cotta Ramusino, H. Danielsson, J. Degrange, M. Fiorini, L. Federici, E. Gamberini, A. Gianoli, J. Kaplon, A. Kleimenova, A. Kluge, R. Malaguti, A. Mapelli, F. Marchetto, E. Martín Albarrán, E. Migliore, E. Minucci, M. Morel, J. Noël, M. Noy, G. Nüessle, L. Perktold, M. Perrin-Terrin, P. Petagna, F. Petrucci, K. Poltorak, G. Romagnoli, G. Ruggiero, B. Velghe, and H. Wahl. The NA62 GigaTracKer: a low mass high intensity beam 4D tracker with 65 ps time resolution on tracks. *Journal of Instrumentation*, 14(07):P07010, jul 2019.

[30] Matthew Moulson. HIKE: High Intensity Kaon Experiments at the CERN SPS. *arXiv*, 10.48550/ARXIV.2212.00498, 2022.

[31] W. R. Leo. *Techniques for Nuclear and Particle Physics Experiments.* Springer, 1994.

[32] G. F. Knoll. *Radiation Detection and Measurement.* John Wiley and Sons, 1979.

[33] C. Patrignani et al. (Particle Data Group). Chinese Physics C, **40**, 100001 (2016).

[34] J. D. Jackson. *Classical Electrodynamics 2nd Ed.* John Wiley and Sons, New York, 1975.

[35] Gerald R. Lynch and Orin I. Dahl. Approximations to multiple coulomb scattering. *Nuclear Instruments and Methods in Physics Research Section B: Beam Interactions with Materials and Atoms*, 58(1):6–10, 1991.

[36] H. Spieler. *Semiconductor Detector Systems.* Oxford Science Publication, 2005.

[37] W. Shockley. Currents to conductors induced by a moving point charge. *Journal of Applied Physics*, 9(10):635–636, 1938.

[38] S. Ramo. Currents induced by electron motion. *Proceedings of the IRE*, 27(9):584–585, 1939.

[39] A. Holmes-Siedle and L. Adams. *Handbook of Radiation Effects.* Oxford University Press, 2002.

[40] F. Hartmann. *Evolution of Silicon Sensor Technology in Particle Physics.* STMP 231 (Springer Berlin Heidelberg 2009). DOI 10.1007/978-3-540-44774-0.

[41] M. Moll. *Radiation Damage in Silicon Particle Detectors - microscopic defects and macroscopic properties.* PhD thesis, University of Hamburg, Germany, 1999.

[42] G Kramberger, V Cindro, I Mandić, M Mikuž, and M Zavrtanik. Effective trapping time of electrons and holes in different silicon materials irradiated with neutrons, protons and pions. *Nuclear Instruments and Methods in Physics Research Section A: Accelerators, Spectrometers, Detectors and Associated Equipment*, 481(1):297–305, 2002.

[43] G. Pellegrini, P. Fernández-Martínez, M. Baselga, C. Fleta, D. Flores, V Greco, S. Hidalgo, I. Mandić, G. Kramberger, D. Quirion, and M. Ullan. Technology developments and first measurements of low gain avalanche detectors (lgad) for high energy physics applications. *Nuclear Instruments and Methods in Physics Research Section A: Accelerators, Spectrometers, Detectors and Associated Equipment*, 765:12–16, 2014. HSTD-9 2013 - Proceedings of the 9th International "Hiroshima" Symposium on Development and Application of Semiconductor Tracking Detectors.

[44] N. Cartiglia, R. Arcidiacono, M. Baselga, R. Bellan, M. Boscardin, F. Cenna, G.F. Dalla Betta, P. Fernndez-Martnez, M. Ferrero, D. Flores, Z. Galloway, V. Greco, S. Hidalgo, F. Marchetto, V. Monaco, M. Obertino, L. Pancheri, G. Paternoster, A. Picerno, G. Pellegrini, D. Quirion, F. Ravera, R. Sacchi, H.F.-W. Sadrozinski, A. Seiden, A. Solano, and N. Spencer. Design optimization of ultra-fast silicon detectors. *Nuclear Instruments and Methods in Physics Research Section A: Accelerators, Spectrometers, Detectors and Associated Equipment*, 796:141–148, 2015. Proceedings of the 10th International Conference on Radiation Effects on Semiconductor Materials Detectors and Devices.

[45] Chiara Grieco. Low Gain Avalanche Detectors for the ATLAS High Granularity Timing Detector, 2022. Presented 11-07-2022.

[46] Federico Siviero, R. Arcidiacono, G. Borghi, Maurizio Boscardin, N. Cartiglia, M. Vignali, Marco Costa, Gian-Franco Dalla Betta, Maricel Ferrero, F. Ficorella, G. Gioachin, Marco Mandurrino, Scott Mazza, Luca Menzio, Lucio Pancheri, G. Paternoster, H.-F.W. Sadrozinski, A. Seiden, Valentina Sola, and Marta Tornago. Optimization of the gain layer design of ultra-fast silicon detectors. *Nuclear Instruments and Methods in Physics Research Section A: Accelerators, Spectrometers, Detectors and Associated Equipment*, 1033:166739, 04 2022.

[47] N. Cartiglia, A. Staiano, V. Sola, R. Arcidiacono, R. Cirio, F. Cenna, M. Ferrero, V. Monaco, R. Mulargia, M. Obertino, F. Ravera, R. Sacchi, A. Bellora, S. Durando, M. Mandurrino, N. Minafra, V. Fadeyev, P. Freeman, Z. Galloway, E. Gkougkousis, H. Grabas, B. Gruey, C.A. Labitan, R. Losakul, Z. Luce, F. McKinney-Martinez, H.F.-W. Sadrozinski, A. Seiden, E. Spencer, M. Wilder, N. Woods, A. Zatserklyaniy, G. Pellegrini, S. Hidalgo, M. Carulla, D. Flores, A. Merlos, D. Quirion, V. Cindro, G. Kramberger, I. Mandić, M. Mikuž, and M. Zavrtanik. Beam test results of a 16ps timing system based on ultra-fast silicon detectors. *Nuclear Instruments and Methods in Physics Research Section A: Accelerators, Spectrometers, Detectors and Associated Equipment*, 850:83–88, 2017.

[48] R. Arcidiacono, G. Borghi, M. Boscardin, N. Cartiglia, M. Costa, G.F. Dalla Betta, F. Fausti, M. Ferrero, F. Ficorella, M. Mandurrino, S.M. Mazza, E.J. Olave, L. Pancheri, G. Paternoster, H.-F.W. Sadrozinski, V. Sola, A. Staiano, A. Seiden, F. Siviero, M. Tornago, and Y. Zhao. State-of-the-art and evolution of UFSD sensors design at FBK. *Nuclear Instruments and Methods in Physics Research Section A: Accelerators, Spectrometers, Detectors and Associated Equipment*, 978:164375, 2020.

[49] Valentina Sola et al. A compensated design of the LGAD gain layer. *Nucl. Instrum. Meth. A*, 1040:167232, 2022.

[50] L. Menzio et al. DC-coupled resistive silicon detectors for 4D tracking. *Nucl. Instrum. Meth. A*, 1041:167374, 2022.

[51] G. Deptuch, J.-D. Berst, G. Claus, C. Colledani, W. Dulinski, Y. Gornushkin, D. Husson, J.-L. Riester, and M. Winter. Design and testing of monolithic active pixel sensors for charged particle tracking. *IEEE Transactions on Nuclear Science*, 49(2):601–610, 2002.

[52] B Abelev et al and (The ALICE Collaboration). Technical design report for the upgrade of the alice inner tracking system. *Journal of Physics G: Nuclear and Particle Physics*, 41(8):087002, jul 2014.

[53] C. Marinas and M. Vos. The Belle-II DEPFET pixel detector: A step forward in vertexing in the superKEKB flavour factory. *Nuclear Instruments and Methods in Physics Research Section A: Accelerators, Spectrometers, Detectors and Associated Equipment*, 650(1):59–63, 2011. International Workshop on Semiconductor Pixel Detectors for Particles and Imaging 2010.

[54] A. Dorokhov, G. Bertolone, J. Baudot, C. Colledani, G. Claus, Y. Degerli, R. De Masi, M. Deveaux, G. Dozière, W. Dulinski, M. Gélin, M. Goffe, A. Himmi, Ch. Hu-Guo, K. Jaaskelainen, M. Koziel, F. Morel, C. Santos, M. Specht, I. Valin, G. Voutsinas, and M. Winter. High resistivity CMOS pixel sensors and their application to the STAR PXL detector. *Nuclear Instruments and Methods in Physics Research Section A: Accelerators, Spectrometers, Detectors and Associated Equipment*, 650(1):174–177, 2011. International Workshop on Semiconductor Pixel Detectors for Particles and Imaging 2010.

[55] Niklaus Berger. The Mu3e Experiment. *Nuclear Physics B - Proceedings Supplements*, 248-250:35–40, 2014. 1st Conference on Charged Lepton Flavor Violation.

[56] Gianluca Aglieri Rinella. The ALPIDE pixel sensor chip for the upgrade of the ALICE Inner Tracking System. *Nucl. Instrum. Meth. A*, 845:583–587, 2017.

[57] M. Benoit, R. Cardarelli, S. Débieux, Y. Favre, G. Iacobucci, M. Nessi, L. Paolozzi, and K. Shu. 100 ps time resolution with thin silicon pixel detectors and a SiGe HBT amplifier. *Journal of Instrumentation*, 11(03):P03011, mar 2016.

[58] G. Iacobucci, R. Cardarelli, S. Débieux, F.A. Di Bello, Y. Favre, D. Hayakawa, M. Kaynak, M. Nessi, L. Paolozzi, H. Rücker, D.M.S. Sultan, and P. Valerio. A 50 ps resolution monolithic active pixel sensor without internal gain in SiGe BiCMOS technology. *Journal of Instrumentation*, 14(11):P11008, nov 2019.

[59] G. Iacobucci, L. Paolozzi, P. Valerio, T. Moretti, F. Cadoux, R. Cardarelli, R. Cardella, S. Débieux, Y. Favre, D. Ferrere, S. Gonzalez-Sevilla, Y. Gurimskaya, R. Kotitsa, C. Magliocca, F. Martinelli, M. Milanesio, M. Münker, M. Nessi, A. Picardi, J. Saidi, H. Rücker, M. Vicente Barreto Pinto, and S. Zambito. Efficiency and time resolution of monolithic silicon pixel detectors in SiGe BiCMOS technology. *Journal of Instrumentation*, 17(02):P02019, feb 2022.

[60] L. Paolozzi, M. Munker, R. Cardella, M. Milanesio, Y. Gurimskaya, F. Martinelli, A. Picardi, H. Rücker, A. Trusch, P. Valerio, F. Cadoux, R. Cardarelli, S. Débieux, Y. Favre, C.A. Fenoglio, D. Ferrere, S. Gonzalez-Sevilla, R. Kotitsa, C. Magliocca, T. Moretti, M. Nessi, A. Pizarro Medina, J. Sabater Iglesias, J. Saidi, M. Vicente Barreto Pinto, S. Zambito, and G. Iacobucci. Picosecond Avalanche Detector — working principle and gain measurement with a proof-of-concept prototype. *Journal of Instrumentation*, 17(10):P10032, oct 2022.

[61] M. Milanesio, G. Iacobucci, L. Paolozzi, M. Munker, R. Cardella, Y. Gurimskaya, F. Martinelli, A. Picardi, H. Rücker, A. Trusch, P. Valerio, F. Cadoux, R. Cardarelli, S. Debieux, Y. Favre, D. Ferrere, S. Gonzalez-Sevilla, R. Kotitsa, C. Magliocca, T. Moretti, M. Nessi, J. Saidi, M. Vicente Barreto Pinto, and S. Zambito. Gain measurements of the first proof-of-concept PicoAD prototype with a 55Fe X-ray radioactive source. *Nuclear Instruments and Methods in Physics Research Section A: Accelerators, Spectrometers, Detectors and Associated Equipment*, 1046:167807, 2023.

[62] G. Iacobucci, S. Zambito, M. Milanesio, T. Moretti, J. Saidi, L. Paolozzi, M. Munker, R. Cardella, F. Martinelli, A. Picardi, H. Rücker, A. Trusch, P. Valerio, F. Cadoux, R. Cardarelli, S. Débieux, Y. Favre, C.A. Fenoglio, D. Ferrere, S. Gonzalez-Sevilla, Y. Gurimskaya, R. Kotitsa, C. Magliocca, M. Nessi, A. Pizarro-Medina, J. Sabater Iglesias, and M. Vicente Barreto Pinto. Testbeam results of the Picosecond Avalanche Detector proof-of-concept prototype. *Journal of Instrumentation*, 17(10):P10040, oct 2022.

[63] S.I. Parker, C.J. Kenney, and J. Segal. 3d — a proposed new architecture for solid-state radiation detectors. *Nuclear Instruments and Methods in Physics Research Section A: Accelerators, Spectrometers, Detectors and Associated Equipment*, 395(3):328–343, 1997. Proceedings of the Third International Workshop on Semiconductor Pixel Detectors for Particles and X-rays.

[64] Sherwood Parker, Angela Kok, Christopher Kenney, Pierre Jarron, Jasmine Hasi, Matthieu Despeisse, Cinzia Da Via, and Giovanni Anelli. Increased Speed: 3D Silicon Sensors; Fast Current Amplifiers. *IEEE Transactions on Nuclear Science*, 58(2):404–417, April 2011.

[65] C. Da Vià, G.-F. Dalla Betta, and S. Parker. *Radiation Sensors with Three-Dimensional Electrodes*. Taylor Francis Group, LLC, 2019.

[66] B. Abbott et al. Production and integration of the atlas insertable b-layer. *Journal of Instrumentation*, 13(05):T05008, may 2018.

[67] M.M. Obertino. The PPS tracking system: performance in LHC Run2 and prospects for LHC Run3. *Journal of Instrumentation*, 15(05):C05049, May 2020.

[68] Lucio Anderlini, Marco Bellini, Andrea Bizzeti, Alessandro Cardini, Roberto Ciaranfi, Chiara Corsi, Michela Garau, Adriano Lai, Stefano Lagomarsino, Andrea Lampis, Angelo Loi, Chiara Lucarelli, Saverio Mariani, Nicola Minafra, Arianna Morozzi, Roberto Mulargia, Giovanni Passaleva, Daniele Passeri, Silvio Sciortino, Stefania Vecchi, and Michele Veltri. Fabrication and Characterisation of 3D Diamond Pixel Detectors With Timing Capabilities. *Frontiers in Physics*, 8, 2020.

[69] Lucio Anderlini, Marco Bellini, Chiara Corsi, Stefano Lagomarsino, Chiara Lucarelli, Giovanni Passaleva, Silvio Sciortino, and Michele Veltri. Fabrication and First Full Characterisation of Timing Properties of 3D Diamond Detectors. *Instruments*, 5(4), 2021.

[70] Lucio Anderlini, Marco Bellini, Vladimir Cindro, Chiara Corsi, Keida Kanxheri, Stefano Lagomarsino, Chiara Lucarelli, Arianna Morozzi, Giovanni Passaleva, Daniele Passeri, Silvio Sciortino, Leonello Servoli, and Michele Veltri. A Study of the Radiation Tolerance and Timing Properties of 3D Diamond Detectors. *Sensors*, 22(22), 2022.

[71] L. Anderlini, M. Bellini, C. Corsi, S. Lagomarsino, C. Lucarelli, G. Passaleva, S. Sciortino, and M. Veltri. A 4D diamond detector for HL-LHC and beyond. *Nuclear Instruments and Methods in Physics Research Section A: Accelerators, Spectrometers, Detectors and Associated Equipment*, 1040:167230, 2022.

[72] A. Loi. *Design and test of a timing optimized 3D silicon sensor for HL-LHC experiments*. PhD thesis, Università degli Studi di Cagliari, 2020. https://hdl.handle.net/11584/284136.

[73] Synopsys Inc. Synopsys Sentaurus TCAD Version 2018.06 K-2015.06, 2018. https://www.synopsys.com/silicon/tcad.html.

[74] A. Contu and A. Loi. TimeSPOT COde for DEtector Simulation (TCoDe), 2020, Zenodo, doi: 10.5281/zenodo.3686010.

[75] X. Llopart, R. Ballabriga, M. Campbell, L. Tlustos, and W. Wong. Timepix, a 65k programmable pixel readout chip for arrival time, energy and/or photon counting measurements. *Nuclear Instruments and Methods in Physics Research Section A: Accelerators, Spectrometers, Detectors and Associated Equipment*, 581(1):485–494, 2007. VCI 2007.

[76] G.T. Forcolin, R. Mendicino, M. Boscardin, A. Lai, A. Loi, S. Ronchin, S. Vecchi, and G.-F. Dalla Betta. Development of 3d trenched-electrode pixel sensors with improved timing performance. *Journal of Instrumentation*, 14(07):C07011, jul 2019.

[77] A. Montalbano, D. Bassignana, Z. Li, S. Liu, D. Lynn, G. Pellegrini, and D. Tsybychev. A systematic study of bnls 3d-trench electrode detectors. *Nuclear Instruments and Methods in Physics Research Section A: Accelerators, Spectrometers, Detectors and Associated Equipment*, 765:23–28, 2014. HSTD-9 2013 - Proceedings of the 9th International "Hiroshima" Symposium on Development and Application of Semiconductor Tracking Detectors.

[78] Franz Laermer, Sami Franssila, Lauri Sainiemi, and Kai Kolari. *Chapter 21 - Deep Reactive Ion Etching.* Micro and Nano Technologies. William Andrew Publishing, Boston, second edition edition, 2015.

[79] G.T. Forcolin, M. Boscardin, F. Ficorella, A. Lai, A. Loi, R. Mendicino, S. Ronchin, and G.-F. Dalla Betta. 3d trenched-electrode pixel sensors: Design, technology and initial results. *Nuclear Instruments and Methods in Physics Research Section A: Accelerators, Spectrometers, Detectors and Associated Equipment*, 981:164437, 2020.

[80] D.M.S. Sultan, G.-F. Dalla Betta, R. Mendicino, M. Boscardin, S. Ronchin, and N. Zorzi. First production of new thin 3D sensors for HL-LHC at FBK. *Journal of Instrumentation*, 12(01):C01022, jan 2017.

[81] Sandro Cadeddu, Luca Frontini, Adriano Lai, Valentino Liberali, Lorenzo Piccolo, A. Rivetti, Jafar Shojaii, and Alberto Stabile. Timespot1: A 28nm CMOS Pixel Read-Out ASIC for 4D Tracking at High Rates. 09 2022.

[82] M. Garau. Sviluppo di un rivelatore Cherenkov per la misura del tempo di arrivo di particelle ionizzanti ultra-relativistiche. Master's thesis, Università degli Studi di Cagliari, 2019. https://pubblicazioni.dsi.infn.it/tesi/gettesi.php?filename=14211-Garau-magistrale.pdf.

[83] Robert L. Chase. Pulse Timing System for Use with Gamma Rays on Ge(Li) Detectors. *Review of Scientific Instruments*, 39(9):1318–1326, 1968.

[84] S. Meroli, D. Passeri, and L. Servoli. Energy loss measurement for charged particles in very thin silicon layers. *Journal of Instrumentation*, 6:P06013, 06 2011.

[85] Pico-Quant LDH-P-C-650. https://www.picoquant.com/products/category/picosecond-pulsed-sources/ldh-series-picosecond-pulsed-diode-laser-heads.

[86] D. Brundu, A. Cardini, A. Contu, G.M. Cossu, G.-F. Dalla Betta, M. Garau, A. Lai, A. Lampis, A. Loi, M.M. Obertino, B.G. Siddi, and S. Vecchi. Accurate modelling of 3D-trench silicon sensor with enhanced timing performance and comparison with test beam measurements. *Journal of Instrumentation*, 16(09):P09028, sep 2021.

[87] S. Agostinelli et al. Geant4: A simulation toolkit. *Nuclear Instruments and Methods in Physics Research Section A: Accelerators, Spectrometers, Detectors and Associated Equipment*, 506(3):250–303, 2003.

[88] D. Brundu and G. M. Cossu. dbrundu/TFBoost: TFBoost v0.2-alpha. November 2020, Zenodo. doi: 10.5281/zenodo.4291148.

[89] Gian Matteo Cossu and Adriano Lai. Front-end electronics for timing with picoseconds precision using 3d trench silicon sensors. *https://arxiv.org/abs/2209.11147*, 2022.

[90] P. Venkataramaiah, K. Gopala, A. Basavaraju, S. S. Suryanarayana, and H. Sanjeeviah. A simple relation for the fermi function. *Journal of Physics G: Nuclear Physics*, 11(3):359, mar 1985.

[91] J. Dixon et al. Evaluation of a silicon 90sr betavoltaic power source. *Sci. Rep. 6, 38182*, 2016.

[92] Mauro Aresti, Alessandro Cardini, Gian Matteo Cossu, Michela Garau, Adriano Lai, Andrea Lampis, and Angelo Loi. A sub-picosecond precision laser-based test station for the measurement of silicon detector timing performances. In *2020 IEEE Nuclear Science Symposium and Medical Imaging Conference (NSS/MIC)*, pages 1–4, 2020.

[93] Mauro Aresti, Alessandro Cardini, Adriano Lai, Angelo Loi, Gian Matteo Cossu, Michela Garau, Andrea Lampis, Gian-Franco Dalla Betta, and Giulio Forcolin. Laboratory Characterization of Innovative 3D Trench-design Silicon Pixel Sensors Using a Sub-Picosecond Precision Laser-Based Testing Equipment. In *2020 IEEE Nuclear Science Symposium and Medical Imaging Conference (NSS/MIC)*, pages 1–6, 2020.

[94] Origami Onefive 10. https://www.nktphotonics.com/products/femtosecond-lasers/origami-lp/.

[95] Super Agilis CONEX-SAG-LS16P. https://www.newport.com/p/CONEX-SAG-LS16P.